

QUANTUM CHEMISTRY CALCULATIONS OF THE REACTIONS OF GASEOUS
OXYGEN ATOMS WITH CLEAN AND ADSORBATE-TERMINATED Si(100)-(2x1)

By

PAULO EMILIO HERRERA-MORALES

A DISSERTATION PRESENTED TO THE GRADUATE SCHOOL
OF THE UNIVERSITY OF FLORIDA IN PARTIAL FULFILLMENT
OF THE REQUIREMENTS FOR THE DEGREE OF
DOCTOR OF PHILOSOPHY

UNIVERSITY OF FLORIDA

2005

Copyright 2005

by

Paulo Emilio Herrera-Morales

To my late grandmother, Catalina Caal Prado.

ACKNOWLEDGMENTS

I wish to express my sincere appreciation to Dr. Jason F. Weaver (my supervisory committee chair) for all his encouragement and advice throughout my Ph.D. program. I would like to extend my deepest gratitude to the members of my advisory committee (Dr. Gar B. Hoflund, Dr. Vaneica Y. Young, and Dr. Fan Ren) for their assistance, technical support, and guidance. I also thank Dr. David Micha, Dr. Erick Deumens, and Dr. Adrian Roitberg (from the Quantum Theory Project) and Dr. Helena Hagelin-Weaver (from the Chemical Engineering Department) for their valuable support with quantum chemistry matters. I would like to thank my colleagues at Universidad Rafael Landívar in Guatemala, for their support and encouragement.

I would like to express my sincere appreciation and gratitude to my parents, Victor Manuel Herrera and Emma Morales de Herrera; and to my sister, Servanda Virginia Herrera, for supporting me and my parents for the duration of this work. Special thanks go to my fiancée Sonia María García, who supported me more than once. She possesses admirable patience.

I would like to thank the Quantum Theory Project of the University of Florida for the use of its computational facilities; and Brad Shumbera, for his excellent work in setting up the computer network for our research laboratory. I also want to recognize the other Weaver Research Group members, Alex A. Gerrard, Jau Jiun Chen, Sunil Devarajan and Heywood Kan, for their help with different issues through the years.

TABLE OF CONTENTS

	<u>page</u>
ACKNOWLEDGMENTS	iv
LIST OF TABLES	viii
LIST OF FIGURES	x
ABSTRACT	xiii
CHAPTER	
1 INTRODUCTION	1
1.1 Research Objective	1
1.2 The Si(100)-(2x1) Surface	1
1.3 Chemistry of Atomic Oxygen on Si(100)-(2x1)	3
1.4 Important Silicon-based Materials for Microelectronics Industry	4
2 THEORETICAL BACKGROUND OF QUANTUM CHEMISTRY CALCULATIONS	8
2.1 Introduction	8
2.2 Energy Functionals and Early Density Functional Theory (DFT)	10
2.3 Hohenberg-Kohn-Sham Density Functional Theory (KS-DFT)	14
2.3.1 Hohenberg-Kohn Lemmas and Exchange-Correlation Functional Definition	15
2.3.2 Kohn-Sham Self-consistent Field Method	17
2.3.3 Exchange and Correlation Functional Approximations	18
2.3.3.1 Local density approximation (LDA)	19
2.3.3.2 Density gradient corrections	20
2.3.3.3 Hybrid methods	22
2.3.3.4 Empirical DFT methods	24
2.3.4 Kohn-Sham Density Functional Theory Computational Chemistry	25
2.4 Basis Sets	27
2.5 Geometry Optimization and Transition State Search Calculations	31
2.5.1 Geometry Optimization of Energy Minima	33
2.5.2 Transition State Searches	38

3	NITROGEN ATOM ABSTRACTION FROM Si(100)-(2x1).....	41
3.1	Introduction.....	41
3.2	Computational Approach.....	43
3.3	Results.....	45
3.3.1	Bonding Configurations of a Nitrogen Atom on Si(100)-(2x1).....	45
3.3.2	Nitrogen Abstraction by a Gas-Phase Oxygen Atom.....	46
3.3.3	Abstraction of N Adsorbed at the Dangling Bond [R(<i>ad</i>)].....	48
3.3.4	Abstraction of the Nitrogen Bonded Across the Dimer [R(<i>db</i>)].....	51
3.3.5	Abstraction of the Nitrogen Bonded at a Backbond [R(<i>bb</i>)].....	54
3.3.6	Abstraction from the N≡Si ₃ Structure [R(<i>sat</i>)].....	59
3.4	Discussion.....	63
4	CHEMISTRY ON Si(100)-(2x1) DURING EARLY STAGES OF OXIDATION WITH O(³ P).....	66
4.1	Introduction.....	66
4.2	Theoretical Approach.....	69
4.3	Results and Discussion.....	70
4.3.1	Structures with One Adsorbed Oxygen Atom (O ₁ -Si ₉ H ₁₂).....	77
4.3.2	Structures with Two Adsorbed Oxygen Atoms (O ₂ -Si ₉ H ₁₂).....	80
4.3.3	Structures with Three Adsorbed Oxygen Atoms (O ₃ -Si ₉ H ₁₂).....	86
4.3.4	Oxygen Insertion.....	91
4.3.4.1	Thermodynamic considerations.....	91
4.3.4.2	Kinetic considerations.....	94
5	ATOMIC OXYGEN INSERTION INTO ETHYLENE- AND ACETYLENE-TERMINATED Si(100)-(2x1).....	100
5.1	Introduction.....	100
5.2	Theoretical Approach.....	102
5.3	Results and Discussion.....	104
5.3.1	Relative Energies of Oxidized Ethylene-Covered Si(100) Clusters.....	110
5.3.2	Relative Energies of Oxidized Acetylene-terminated Surfaces.....	115
5.3.3	Oxygen Insertion Mechanisms.....	119
5.3.3.1	Thermodynamic considerations.....	119
5.3.3.2	Kinetic considerations.....	120
6	SUMMARY AND CONCLUSIONS.....	124
6.1	Nitrogen Atom Abstraction from Si(100)-(2x1) by Gaseous Atomic Oxygen ..	124
6.2	Initial Step of Si(100)-(2x1) Oxidation by Gaseous Atomic Oxygen.....	125
6.3	Oxidation of C ₂ H ₂ - and C ₂ H ₄ -covered Si(100)-(2x1) by Gaseous Atomic Oxygen.....	127

APPENDIX

A	QUANTUM CHEMISTRY SOFTWARE	128
A.1	File Format .xyz.....	133
A.2	File Format .zmt.....	133
A.3	HyperChem Files (Format .hin).....	136
A.4	Gaussian03 Files (Formats .inp, .log and .chk)	138
B	EXAMPLE OF GAUSSIAN03 OUTPUT FILE.....	141
C	CALCULATION PROTOCOL FOR INITIAL GEOMETRY FOR GEOMETRY OPTIMIZATIONS	157
D	CALCULATION PROTOCOL FOR INITIAL GEOMETRY FOR TRANSITION STATE SEARCHES	159
	LIST OF REFERENCES.....	166
	BIOGRAPHICAL SKETCH	173

LIST OF TABLES

<u>Table</u>	<u>page</u>
1-1 Selected properties of silicon dioxide	6
2-1 Approximations made to correct Thomas-Fermi-DFT before the development of Kohn-Sham DFT	13
2-2 Variables used to express the approximate exchange-correlation functionals $E_{XC}[\rho(\mathbf{r})]$	18
4-1 Suboxide penalty energies for various silicon oxidation states.....	75
4-2 Penalty energies of O ₁ -Si ₉ H ₁₂ isomers	78
4-3 Penalty energies of O ₂ -Si ₉ H ₁₂ isomers	81
4-4 Penalty energies of O ₃ -Si ₉ H ₁₂ isomers	87
4-5 Energy barriers for migration of oxygen atoms in O-Si ₉ H ₁₂ -O _d structures from a dangling bond site to a backbond or dimer bond site in the spin-triplet state.....	96
5-1 E ₁ (SiSi) structure and energy of adsorption compared to those of reported dimerized C ₂ H ₄ -terminated Si(100) structures.....	107
5-2 A ₁ (SiSi) structure and energy of adsorption compared to those of reported dimerized C ₂ H ₂ -terminated Si(100) structures.....	107
5-3 Calculated energy of formation of the different oxidized bridges that form when an oxygen atom inserts into the C ₂ H ₂ - and C ₂ H ₄ -terminated Si ₉ H ₁₂ clusters	109
5-4 Penalty energies of spin-singlet O-C ₂ H ₄ -Si ₉ H ₁₂ isomers	110
5-5 Penalty energies of spin-triplet O-C ₂ H ₄ -Si ₉ H ₁₂ isomers	111
5-6 Penalty energies of spin-singlet O-C ₂ H ₂ -Si ₉ H ₁₂ isomers	115
5-7 Penalty energies of spin-triplet O-C ₂ H ₂ -Si ₉ H ₁₂ isomers	116
A-1 Quantum chemistry programs used in this work.....	132

A-2	File formats used for proper handling of the coordinates systems and results in our geometry optimization calculations	132
A-3	Gaussian03 input files sections	138
C-1	Calculation protocol used to determine the best initial geometry for the geometry optimization, transition state search and frequency calculations.	157

LIST OF FIGURES

<u>Figure</u>	<u>page</u>
1-1 Si(100) -2x1 surface showing the dimer rows.	2
1-2 Metal-oxide-semiconductor field-effect transistor (MOSFET).	6
2-1 Flowchart of the Kohn-Sham SCF procedure	26
2-2 Two-dimensional potential energy surface	31
2-3 Flowcharts for a quasi-Newton algorithm for geometry optimization.....	36
3-1 The Si ₉ H ₁₂ cluster used in our UB3LYP calculations.....	47
3-2 Structural information of N-Si ₉ H ₁₂ clusters	48
3-3 Reaction pathway for the nitrogen abstraction from R(<i>ad</i>).....	49
3-4 Critical point structures of the nitrogen abstraction from R(<i>ad</i>).....	50
3-5 Reaction pathway of nitrogen abstraction from R(<i>db</i>).....	52
3-6 Critical point structures of the nitrogen abstraction from R(<i>db</i>).....	53
3-7 Reaction pathways for the abstraction of the nitrogen atom inserted in a Si-Si backbond	56
3-8 Molecular precursors formed after O-chemisorption onto R(<i>bb</i>)	57
3-9 Structures formed during nitrogen abstraction from MP(<i>bbt</i>)	58
3-10 Structures involved in the nitrogen abstraction from MP(<i>bbs</i>).....	59
3-11 Reaction pathways for N-abstraction from (and O-atom adsorption on) R(<i>sat</i>).....	61
3-12 Structures formed during the direct nitrogen abstraction from R(<i>sat</i>).....	62
3-13 Structures involved in the O-atom chemisorption on R(<i>sat</i>).....	62
4-1 Structural information and highest occupied molecular orbital plot of clean Si ₉ H ₁₂ clusters.....	74

4-2	Relative energies of O ₁ -Si ₉ H ₁₂ isomers.....	77
4-3	Structural characteristics of Si ₉ H ₁₂ clusters with one oxygen atom.....	79
4-4	Relative energies of O ₂ -Si ₉ H ₁₂ isomers.....	83
4-5	Structural information of dangling bond isomers with two oxygen atoms adsorbed on Si(100).....	84
4-6	Structural information of O ₂ -Si ₉ H ₁₂ isomers.....	85
4-7	Relative energies of optimized structures for three oxygen atom incorporation into Si(100).....	88
4-8	Structural information of the dangling bond O ₃ -Si ₉ H ₁₂ isomer DB ₃ (OSiOSiOd) ...	89
4-9	Structural characteristics O ₃ -Si ₉ H ₁₂ isomers.....	90
4-10	Qualitative representation of a minimum energy path for oxygen atom incorporation on Si(100)-(2x1) based on the relative energy of the structures.....	93
4-11	Structural information of transition state structures for oxygen migration in O ₁ -Si ₉ H ₁₂ structures.....	95
4-12	Structural information of transition state structures for oxygen insertion in O ₂ -Si ₉ H ₁₂ structures.....	98
4-13	Structural information of transition state structure TS ₃ (OSiOSiOd-OSiOSiO)	98
4-14	Proposed preferred path for initial steps of oxidation of Si(100)-(2x1) by oxygen atoms	99
5-1	Structural information of optimized clusters for olefin-covered Si(100)-(2x1).....	106
5-2	Relative energies of spin-singlet O-C ₂ H ₄ -Si ₉ H ₁₂ isomers.....	111
5-3	Relative energies of spin-triplet O-C ₂ H ₄ -Si ₉ H ₁₂ isomers.....	112
5-4	Structural information of O-C ₂ H ₄ - Si ₉ H ₁₂ isomers	114
5-5	Structural information of O-C ₂ H ₂ -Si ₉ H ₁₂ isomers	117
5-6	Relative energies of spin-singlet O-C ₂ H ₂ -Si ₉ H ₁₂ structures.....	118
5-7	Relative energies of spin-triplet O-C ₂ H ₂ -Si ₉ H ₁₂ isomers.....	119
5-8	Structural information of clusters involved in oxygen insertion pathways on C ₂ H ₂ - and C ₂ H ₄ -terminated Si(100) surfaces	121

5-9	Potential energy surfaces for insertion of an oxygen atom on an C ₂ H ₂ covered Si(100)-(2x1) surface	123
5-10	Potential energy surfaces for insertion of an oxygen atom on an C ₂ H ₄ covered Si(100)-(2x1) surface	123
A-1	HyperChem 7 interface	129
A-2	Molden visualization interface and main command screens.....	130
A-3	gOpenMol visualization interface	131
A-4	Example of a .xyz file describing a Si ₉ H ₁₂ O ₃ cluster	134
A-5	Z-Matrix file describing a Si ₉ H _{12+x} C _y cluster	135
A-6	HyperChem 7 files describing a Si ₉ H ₁₂ O ₃ cluster.....	137
A-7	Gaussian03 file types	140
D-1	Input file for a transition state search that uses the OPT(QST2) option	160
D-2	Diagram of the structures of reactant and product used to search for a transition state structure using OPT(QST2) or OPT(QST3) in Gaussian03	161
D-3	Z-matrix (.zmt) file generated by Molden.....	162
D-4	Gaussian03 input file for a transition state search where the product structure had to be reordered using Molden.....	163
D-5	Process used to generate an initial guess for the transition state search using OPT(QST3) in Gaussian03	164

Abstract of Dissertation Presented to the Graduate School
of the University of Florida in Partial Fulfillment of the
Requirements for the Degree of Doctor of Philosophy

QUANTUM CHEMISTRY CALCULATIONS OF THE REACTIONS OF GASEOUS
OXYGEN ATOMS WITH CLEAN AND ADSORBATE-TERMINATED Si(100)-(2x1)

By

Paulo Emilio Herrera-Morales

May 2005

Chair: Jason F. Weaver

Major Department: Chemical Engineering

Reactions of gas-phase radicals at solid surfaces are fundamental to the plasma-assisted processing of semiconductor materials. In addition to adsorbing efficiently, radicals incident from the gas-phase can also stimulate several types of elementary processes before thermally accommodating to the surface. Reactions that occur under such conditions may be classified as non-thermal; and examples include atom insertion, direct-atom abstraction and collision-induced reaction and desorption. Indeed, non-thermal surface reactions play a critical role in determining the enhanced surface reactivity afforded by plasma processing. Advancing the fundamental understanding of radical-surface reactions is therefore of considerable importance to improving control in plasma-assisted materials processing. Our study used quantum chemical calculations to investigate the interactions of gas-phase oxygen atoms [$O(^3P)$] with clean and adsorbate-modified Si(100)-(2x1) surfaces. We carefully studied reaction pathways for the oxygen insertion, adsorbate abstraction and adsorbate migration of these

species on reaction with $O(^3P)$ using density functional theory (DFT) and silicon clusters. Knowledge of these reaction pathways helps determine the viability of certain reactions on Si(100)-(2x1) by gas-phase oxygen atoms in plasma-assisted material processing in general.

Another goal of our study was to better understand the chemistry of certain ultrathin silicon-based films. Silicon dioxide has been at the center of the microelectronics industry given its multiple electrical properties. However, as the size of the devices keeps shrinking according to Moore's law predictions of number of transistors, the demands imposed on this material necessitate a detailed understanding of its chemistry at the molecular level urging researchers to look for several alternatives. Materials such as silicon oxynitride (SiO_xN_y) and silicon oxycarbide (SiO_xC_y) have been suggested as possible silicon dioxide substitutes as gate dielectric and interface dielectric, respectively. Silicon oxynitride can be obtained by either inserting nitrogen atoms into silicon dioxide or oxygen atoms into a silicon nitride film, resulting in ultrathin layers that enhance properties of pure silicon dioxide as a gate dielectric. Silicon oxycarbide is one of the products that evolved as an alternative for silicon dioxide as a result of the recent trend of organic functionalization of the silicon surfaces (a process by which hydrocarbon molecules are chemisorbed on top of the silicon surfaces to combine the semiconductor properties of silicon with the organic functionality of carbon). Thus we used quantum chemistry calculations to study the initial steps of oxidation of the clean Si(100)-(2x1) surface, of the abstraction of nitrogen atoms, and for insertion of gaseous oxygen atoms on acetylene- and ethylene-terminated Si(100).

CHAPTER 1 INTRODUCTION

1.1 Research Objective

Our main objective was to advance fundamental understanding of the reactions of gaseous oxygen atoms with clean and adsorbate-modified Si(100)-(2x1) surfaces, motivated by an interest in gaining insights into the possible reaction pathways during the initial steps of oxidation. Our work was also motivated by the potential benefits of fabricating ultrathin silicon-based films and by the need to precisely control the properties of such films. Density functional theory (DFT) quantum chemistry calculations were run to investigate the possible reactions. This chapter provides a brief introduction to the Si(100)-(2x1) surface, an overview of the current state of knowledge of the oxidation process of this surface, and a brief description of the industrially important silicon dioxide, silicon oxynitride, and silicon oxycarbide, semiconductor materials whose production can be deeply impacted by knowledge of oxygen-atom chemistry at the molecular level. Density functional theory and the background of the quantum chemistry calculations are explained in detail in Chapter 2.

1.2 The Si(100)-(2x1) Surface

Because of its numerous industrial applications and model character for semiconductor surface science, the industrially important Si(100) surface has been widely studied, dating back to the early work of Schlier and Farnsworth [1]. It is known that when first formed, the surface reconstructs by forming silicon dimmers, and that the surface adopts a (2x1) orientation (where 2x1 designates the new periodicity of the

surface atoms). The surface forms these dimers so it can reduce the number of dangling bonds per surface atom, from two in the bulk-terminated (1x1) surface to one in the reconstructed (2x1), and also because their formation lowers the surface energy by about 1.0 eV [2] (Figure 1-1).

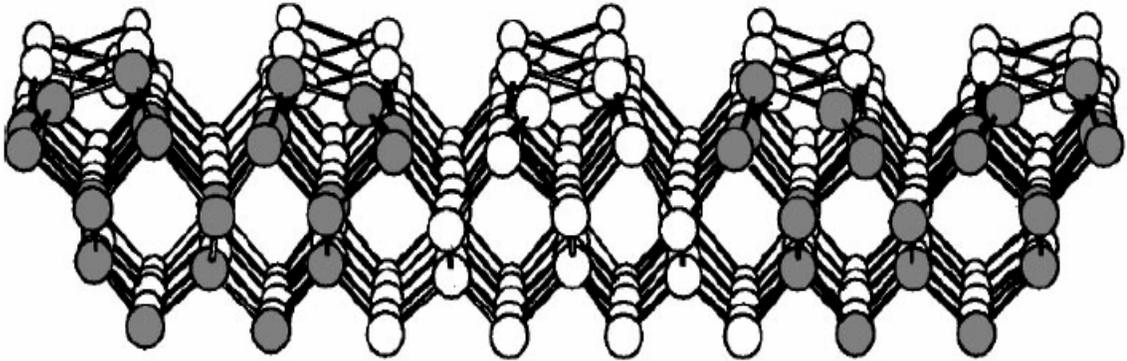


Figure 1-1. Si(100)–(2x1) surface showing the dimer rows.

It is generally accepted [3-8] that the dimers are asymmetric (buckled) and consist of an sp^2 -like bonded down atom, that moves closer to the plane of its three nearest neighbors; and an up atom that moves away from the plane of its neighbors, and possesses an s-like dangling bond. This rehybridization process from the bulk sp^3 to the sp^2 -like configuration of the silicon dimer atoms is accompanied by a charge transfer from the down to the up atom. To minimize this electrostatic effect (and to relieve local stress) the direction of buckling alternates within the dimer rows. The silicon dimer bonds in Si(100)-(2x1) are similar to a C=C double bond [9]. The organic double bond consists of two types of interactions: a σ bond with symmetry around the axis connecting the two atoms, and a π bond with a nodal plane along the axis. Similar interactions exist in the Si-Si dimer bonds, with the difference that the π interaction is sufficiently weak that the dimer is not held in a symmetric configuration, thus adopting the buckled asymmetry that constitutes its more recognizable structural feature [10] (Figure 1-1).

1.3 Chemistry of Atomic Oxygen on Si(100)-(2x1)

Among the most reliable sources of gas-phase radicals such as ground-state atomic oxygen [$O(^3P)$] are plasmas, which typically contain a variety of highly reactive, unstable species (radicals and charged particles) that, in addition to adsorbing efficiently, can also stimulate several types of elementary processes before thermally accommodating to the surface. These elementary processes include atom insertion, direct-atom abstraction, and collision-induced reaction and desorption. It is generally accepted that atom abstraction can occur in several ways, ranging from the Eley-Rideal mechanism (ER) of direct abstraction (in which an atom is abstracted directly from the surface in a single collision with an incident species, without reaching thermal equilibrium with the surface) [11]; and the Langmuir-Hinshelwood mechanism (LH) of collision-induced reaction and desorption (in which the incident species reaches thermal equilibrium with the surface before reacting with the adsorbate and eventually evolving into the gas-phase) [12]. An intermediate reaction mechanism for atom abstraction is the hot atom mechanism (HA) in which the incident species experiences multiple collisions with the surface, but does not fully thermalize before the reactive encounter [13].

To study the aforementioned reaction mechanisms, it is necessary to have a convenient source for all types of radicals. Unfortunately, such a source exists only for hydrogen radicals, which can be produced efficiently by thermal dissociation of molecular H_2 over a hot filament [14]. Thus, abstraction reactions on silicon have been widely investigated only for hydrogen atoms [15-16]; and several kinetic models for the H/Si(100) system have been proposed, most of them favoring the ER mechanism [17-18], the hot atom precursor scenario [19-21], or both [22-25]. Other systems, however (such as those of reactions of oxygen atoms on metal and semiconductor surfaces) have not

been studied as often, despite their industrial and technological importance.

Nevertheless, a few studies on oxidation of silicon surfaces by gaseous oxygen atoms have been reported. Engel *et al.* [26-31] performed a detailed kinetic study of oxidation of clean Si(100) by gaseous oxygen-atoms and reported that O-atom oxidation is facile compared with that caused by molecular oxygen, and that several monolayers of oxide can be formed efficiently via the direct insertion of O atoms into near-surface bonds.

Orellana *et al.* [32] studying the effect of the spin-state of the surface on the oxidation of Si(100) by O₂, found that the oxidation proceeds with a high probability along the triplet potential energy surface (PES), and concluded that the spin state of the surface may be an important factor in determining the quality of the Si/SiO₂ interface.

Despite much study, the reaction mechanism for abstracting hydrogen atoms from Si(100)-(2x1) is still unclear. So the oxygen-atom chemistry on Si(100) is far from understood. Thus, we used quantum chemical calculations to investigate interactions of the O-atoms with clean Si(100), spin-doublet N-covered Si(100), and spin-singlet and spin-triplet C₂H₂- and C₂H₄-terminated Si(100) surfaces. We focused on determining the reaction pathways leading to oxygen insertion or adsorbate direct abstraction from these surfaces, and on the effects that the spin-state has on the processes. This information may be important for the microscopic understanding of the initial steps of the silicon oxidation process by gaseous oxygen atoms. It may also be relevant for developing improved techniques for the fabrication of ultrathin layers of silicon-based industrial materials.

1.4 Important Silicon-based Materials for Microelectronics Industry

Semiconductors are extremely useful for electronic purposes, because they can carry an electric current by electron propagation or hole propagation, and because this

current is generally unidirectional, and the amount of current may be influenced by an external agent [33]. The most widely used insulator is silicon dioxide (SiO_2), which is also one of the most commonly encountered substances in daily life. Modern integrated circuit industry was made possible by the unique properties of silicon dioxide. It is the only native oxide of silicon that is stable in water and at elevated temperatures, is an excellent electrical insulator, is a mask to common diffusing species, and is capable of forming a nearly perfect electrical interface with its substrate (Table 1-1). SiO_2 has strong, directional covalent bonds, and has a well-defined local structure in which four oxygen atoms are arrayed at the corners of a tetrahedron around a central silicon atom. The Si-O-Si bond angles are essentially the tetrahedral angle (109.4°), and the Si-O distance is 1.61 \AA with very little variation. It is these siloxane-bridge bonds between silicon atoms that give SiO_2 many of its unique properties [33].

The Si/ SiO_2 interface is one of the key components of the commonly used metal-oxide-semiconductor field-effect transistor (MOSFET), the building block of integrated circuits (Figure 1-2). This type of transistor continues to be the predominant device in ultralarge scale integrated circuits (USIC) because it is simple to scale down [34]. MOSFETs consists of a source and a drain (regions of doped silicon), a gate dielectric (an extremely thin silicon dioxide layer), and a gate electrode (a layer of polycrystalline silicon), rendered conductive by heavy doping, to bias the gate dielectric. Other MOSFET elements include thin-metal interconnect layers (made of Cu) to connect the transistor electrically to other parts of the circuit, and SiO_2 dielectric layers to provide electrical isolation between the Cu interconnects and other devices. Basically, MOSFETs are switches that allow current to flow from the source to the drain only when the gate electrode supplies the appropriate bias voltage through the gate dielectric [34].

Table 1-1. Selected properties of silicon dioxide.

Oxide native to silicon
Low interfacial defect density ($\sim 10^{10} \text{ eV}^{-1} \text{ cm}^{-2}$)
Melting point = 1713°C
Energy gap = 9 eV
Resistivity $\sim 10^{15} \Omega \text{ cm}$
Dielectric strength $\sim 10^7 \text{ V/cm}$
Dielectric constant relative to air (κ) = 3.9

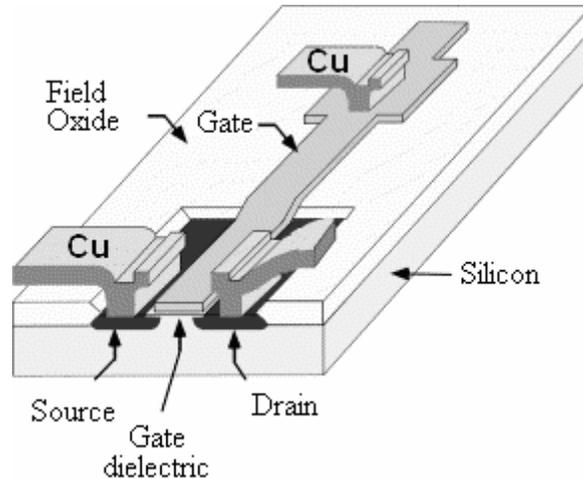


Figure 1-2. Metal-oxide-semiconductor field-effect transistor (MOSFET).

Silicon dioxide has a relatively low-dielectric constant ($\kappa = 3.9$) [33]. Thus, since high gate dielectric capacitance is necessary to produce the required drive currents from submicron devices, and because capacitance is inversely proportional to gate dielectric thickness, the SiO_2 layers have been scaled to extremely thin dimensions where the Si/ SiO_2 interface becomes a more critical (and limiting) part of the gate dielectric. As a result, 1.0 nm SiO_2 layers are commonly found in modern materials. Such a thin silicon dioxide layer is mostly interface, and it contains about five layers of Si atoms (at least two of which reside at the interface). This has given rise to several electrical and performance problems (including impurity penetration through the dioxide, and a lack of convenient insulating properties) that make it necessary to look for alternate gate dielectric materials. Over the past several years, ultrathin silicon oxynitride (SiO_xN_y)

films have been incorporated into metal-oxide-semiconductor (MOS) devices as an alternative for pure SiO₂ [33]. Incorporating nitrogen into SiO₂ is a relatively simple method for fabricating silicon oxynitride films, since the nitrogen atoms tend to aggregate at the Si/SiO₂ interface, and results in dielectric layers that enhance resistance to gate current leakage and inhibit boron penetration into the dielectric [34].

In recent years, surface functionalization also has been intensively investigated [35-36]. This is the process of depositing layers of organic molecules on semiconductor surfaces to impart some property of the organic materials to the semiconductor device [35-36]. The organic molecules might be designed to serve in place of gate oxides in metal-oxide semiconductor field-effect transistor (MOSFET) devices, where the higher wire resistance of smaller metal lines and the crosstalk of closely spaced metal increase the interconnect resistance and capacitance product delay. This requires a low-dielectric constant (low k) material as the interlayer dielectric, and low-resistance conductors (such as aluminum). Until recently, silicon dioxide was the material of choice, but the decrease of the device dimensions and the resulting change of aluminum for copper have necessitated the search for alternative materials. Silicon oxycarbide (SiC_xO_y), a low k hybrid between organic and inorganic materials obtained by organic functionalization, is one of the most favorable candidates for interlayer dielectric in MOSFETs [37-39].

CHAPTER 2
THEORETICAL BACKGROUND OF QUANTUM CHEMISTRY CALCULATIONS

2.1 Introduction

From a chemistry and physics viewpoint three types of systems exist [40]: Systems that possess a very small number of particles where the particles do not interact and that can be studied classically and exactly, systems that have many particles and that require statistical methods to give a nearly exact solution of the properties under study, and systems where only a few particles exist, but where the particles interact considerably with one another. The latter cannot be solved exactly (neither classically nor by statistical modeling) so a different strategy is needed. Electron interactions with other electrons and nuclei within a molecule are an example of these complicated systems for which classical and statistical approaches are insufficient. If one considers that the molecule has N electrons with electronic coordinates \mathbf{r}_i , the total electronic energy of the system is obtained by solving the Schrödinger equation

$$\hat{H}\Psi = E\Psi,$$

where \hat{H} is the Hamiltonian operator, expressed as in Equation 2-1.

$$\hat{H} = -\frac{1}{2} \sum_i^n \nabla^2 + \sum_i^n V(\mathbf{r}_i) + \sum_i^n \sum_{j>i}^n \frac{1}{|\mathbf{r}_i - \mathbf{r}_j|} \quad (2-1)$$

The three terms on the right-hand side of Equation 2-1 correspond to the kinetic energy, the classical Coulomb electrostatic potential between nuclei and electrons, and the electron-electron interactions, respectively. From these, the electron-electron interaction term highly complicates the calculation, given that it describes the highly coupled

motions of the electrons. If one attempts the classical approach, one can ignore the electron-electron interactions completely. This decouples the electronic motions and factorizes the problem into N completely independent problems, one for each electron. However, this approach loses essential elements of the physics of the system. If the statistical approach is attempted there is no need for intuitive simplifications, but a large supercomputer is needed to solve the Schrödinger equation directly. This requires due care in each calculation step, and has the drawback that the result is difficult to interpret and gives little physical insight. Thus, a molecular system is one of those systems for which neither classical nor statistical methods are sufficient. As indicated, these systems require a different approach, and a hybrid between the classical and statistical methods seems the most reasonable. The electron-electron interaction term in Equation 2-1 is replaced by a term that can be solved statistically or computationally, while the first two terms are solved classically. The available methods give a loss of few of the finer details of the system, but they factorize the original problem into N independent one-electron problems that can be solved iteratively (given that usually the one-electron equations depend on the energy, while the energy depends on the one-electron equations) [40].

The two more-widely used iterative computational chemistry methods are Hartree-Fock (HF) and Kohn-Sham density functional theory (Kohn-Sham DFT) [41-44]. Both methods are based on the self-consistent-field (SCF) concept and share many conceptual and computational features. However, they are essentially different because while HF is based on single-electron orbitals $\{\psi_i(\mathbf{r})\}$ and many electron wavefunctions (Ψ) constructed from them, Kohn-Sham DFT is based on the electron density $\rho(\mathbf{r})$ and the fictitious single-particle orbitals $\{\phi_i(\mathbf{r})\}$ [42-45].

This chapter presents the most-common energy functionals (Section 2.2), followed by a detailed description of the Kohn-Sham SCF scheme and its implementation in Gaussian03 (Section 2.3), an introduction to the basis sets (Section 2.4) and an explanation of the geometry optimization schemes used in our study (Section 2.5). Since our main focus is on DFT calculations, we present only the main characteristics of the Hartree-Fock method, and do not discuss the more complex and exact post-Hartree-Fock methods (such as CI and MP2).

2.2 Energy Functionals and Early Density Functional Theory (DFT)

It is useful to express the total electronic energy of a molecular system partitioned in energy functionals, as follows

$$E = E_T + E_V + E_J + E_X + E_C \quad (2-2)$$

given that the computer programs available find the approximate solutions to the Schrödinger equation by calculating each one of the functionals of Equation 2-2 separately. A functional is a mathematical device that maps objects onto numbers, and can be viewed as a function whose argument is also a function. Terms on the right-hand side correspond to the kinetic energy of the electrons, the Coulomb energy of electrons caused by their attraction to the nuclei, the Coulomb energy that the electrons would have in their own field if they moved independently and if each electron repelled itself, a correction for electron exchange, and a correction for electron correlation, respectively.

The last two terms can be combined as

$$E_{XC} = E_X + E_C$$

rendering a correction for the false assumptions involved in E_J (i.e., that electrons do not perturb one another at close approach and that their motions are independent). The exchange energy E_X is the electron stabilization resulting from the Fermi correlation (i.e.,

the dependence of motion arising from the Pauli Principle); while E_C (the correlation energy) arises from the correlation between the motions of electrons with different spins. These five terms have entirely different magnitudes, with E_T , E_V and E_J constituting most of E . The trend is as follows: $E_T > E_V > E_J \gg E_X \gg E_C$. Additionally (as seen later), the expressions for E_V and E_J are common for all SCF methods used in quantum chemistry; while the formulas for E_T , E_X and E_C are the ones that differentiate those methods [40, 45].

The Hartree-Fock approximation (the first SCF method developed) is based on orbital functionals, which are well-defined procedures that take the orbitals of a system and return an energy. The early orbital functionals that were suggested are the Hartree kinetic functional, the self-interaction-correction functional and the Fock exchange functional. In 1928, Hartree [40, 45] presented a model in which the i th electron in an atom moves completely independent of the other in an orbital $\psi_i(\mathbf{r})$. Since all electrons are represented this way, the system is then a collection of uncorrelated electrons, and the total kinetic energy of the atom E_T is the sum of the kinetic energies of the electrons.

$$E_T^{H28} = -\frac{1}{2} \sum_i^N \int \psi_i(\mathbf{r}) \nabla^2 \psi_i(\mathbf{r}) d\mathbf{r} \quad (2-3)$$

Molecular orbital (MO) theory originated when Hartree's model was extended to molecules by delocalizing the $\{\psi_i(\mathbf{r})\}$ over several atoms. However, the model neither gives the exact E_T (given that the electrons do not move independently) nor excludes the self-interactions of electrons (i.e., the exchange energy), and an additional self-interaction-correction functional is required.

A correction functional was presented in 1930 by Fock [40, 45], who indicated that the Hartree wavefunction violates the Pauli Exclusion Principle because it is not properly

antisymmetric. He then solved the problem by rendering the wavefunction antisymmetric as follows

$$E_X^{F30} = -\frac{1}{2} \sum_i^N \sum_j^N \iint \frac{\psi_i(\mathbf{r}_1)\psi_j(\mathbf{r}_1)\psi_i(\mathbf{r}_2)\psi_j(\mathbf{r}_2)}{|\mathbf{r}_1 - \mathbf{r}_2|} d\mathbf{r}_1 d\mathbf{r}_2 \quad (2-4).$$

At this point in the history of quantum chemistry, it was realized that it is cumbersome to work with wavefunctions, given that they have essentially no physical interpretation and have units of probability density to the one-half power. An alternative method was suggested, based on an observable that should allow the construction of the electronic Hamiltonian. Since the Hamiltonian depends on the position and atomic number of nuclei and the total number of electrons N , the best observable for the alternative method is the electron density ρ , given that the total number of electrons N is obtained from

$$N = \int \rho(\mathbf{r}) d\mathbf{r} \quad (2-5)$$

and, since the nuclei correspond to point charges, the nuclei positions are local maxima of ρ . Only the relationship between the atomic number Z_A and the electron density was not clear, but it was found that Z_A is related to the spherically averaged density. With this solved, Eq. 2-2 for the total electronic energy can be expressed in terms of density functionals

$$E[\rho(\mathbf{r})] = E_T[\rho(\mathbf{r})] + E_V[\rho(\mathbf{r})] + E_J[\rho(\mathbf{r})] + E_{XC}[\rho(\mathbf{r})] \quad (2-6)$$

The simplest approximation for the total electron energy was the approach of Thomas-Fermi [46-47], who assumed that the system had classical behavior, and then reduced Equation 2-6 to Equation 2-7.

$$E[\rho(\mathbf{r})] = E_T[\rho(\mathbf{r})] + E_V[\rho(\mathbf{r})] + E_J[\rho(\mathbf{r})] \quad (2-7)$$

In Equation 2-7, the Coulomb interaction terms in the right-hand side are given by Equation 2-8 and 2-9.

$$E_V[\rho(\mathbf{r})] = \sum_a^{\text{nuclei}} \int \frac{Z_a}{|\mathbf{r} - \mathbf{R}_a|} \rho(\mathbf{r}) d\mathbf{r} \quad (2-8)$$

and

$$E_J[\rho(\mathbf{r})] = \frac{1}{2} \iint \frac{\rho(\mathbf{r}_1)\rho(\mathbf{r}_2)}{|\mathbf{r}_1 - \mathbf{r}_2|} d\mathbf{r}_1 d\mathbf{r}_2 \quad (2-9)$$

$E_V[\rho(\mathbf{r})]$ and $E_J[\rho(\mathbf{r})]$ are extremely useful for modern SCF methods, whether based on HF or DFT theories. Equation 2-8 is exact and is used in all the available SCF methods. Equation 2-9 is an approximation that considers that the electrons move independently and that each electron experiences the field caused by all the electrons (including itself).

Thomas and Fermi [46-47] also derived a kinetic functional based on the uniform electron gas, or jellium, which is an idealized system in the limit of N and $V \rightarrow \infty$ of a system of N electrons in a cubical box of volume V , that has a uniformly distributed positive charge that renders the system neutral. Thomas and Fermi chose jellium because although it is a many-electron system, it is completely defined by its electron density ρ [46-47]. The functional is as shown in Equation 2-10.

$$E_T[\rho(\mathbf{r})] = \frac{3}{10} (6\pi^2)^{2/3} \int \rho_\alpha^{5/3}(\mathbf{r}) d\mathbf{r} \quad (2-10)$$

The Thomas-Fermi kinetic energy functional is the only density functional that has an elegant mathematical derivation, but unfortunately, it is not accurate enough to be chemically useful. Also, it was the first DFT functional as such, because it showed that non-electrostatic energy terms can be expressed in terms of the electron density.

Table 2-1. Approximations made to correct Thomas-Fermi-DFT before the development of Kohn-Sham DFT

Functional	Author	Year	Comments
Hole function: $E_J[\rho(\mathbf{r})] = \frac{1}{2} \iint \frac{\rho(\mathbf{r}_1)\rho(\mathbf{r}_2)}{ \mathbf{r}_1 - \mathbf{r}_2 } d\mathbf{r}_1 d\mathbf{r}_2$ $+ \frac{1}{2} \iint \frac{\rho(\mathbf{r}_1)h(\mathbf{r}_1; \mathbf{r}_2)}{ \mathbf{r}_1 - \mathbf{r}_2 } d\mathbf{r}_1 d\mathbf{r}_2$	· Slater · Wigner and Seitz	1930 1933	The hole function $h(\mathbf{r}_1; \mathbf{r}_2)$ is centered on electron 1 and a function of electron 2 coordinates.
Hole exchange energy of jellium: $E_X^{D30}[\rho(\mathbf{r})] = -\frac{3}{2} \left(\frac{3}{4\pi} \right)^{1/3} \int \rho^{4/3}(\mathbf{r}) d\mathbf{r}$	Bloch and Dirac	1930	When combined with the work of Thomas and Fermi, is known as the Thomas-Fermi-Dirac approximation.
Slater exchange hole function: $E_X^{S51}[\rho(\mathbf{r})] = -\frac{9}{8} \left(\frac{3}{\pi} \right)^{1/3} \int \rho^{4/3}(\mathbf{r}) d\mathbf{r}$	Slater	1951	Completely ignores correlation effects. The exchange hole function at any position is calculated as a sphere of constant potential with a radius that depends on the magnitude of the electron density at that position.
X α : $E_X[\rho(\mathbf{r})] = -\frac{9\alpha}{8} \left(\frac{3}{\pi} \right)^{1/3} \int \rho^{4/3}(\mathbf{r}) d\mathbf{r}$ with $\alpha = 1$ for E_X^{S51} and $2/3$ for E_X^{D30}	· Gaspar · Slater and Wood	1954 1971	$\alpha = 3/4$ works better than both 1 and 2/3.

However, these Thomas-Fermi functionals (known as Thomas-Fermi DFT) are no longer widely used, because they predict that molecules are unstable with respect to the dissociation of their constituent atoms. Table 2-1 shows the approximations made to correct for problems with Thomas-Fermi-DFT before Kohn-Sham density functional theory was developed; of these approximations, X α is the only one that still is used in certain scientific endeavours.

2.3 Hohenberg-Kohn-Sham Density Functional Theory (KS-DFT)

The early DFT model presented in Section 2.2 did not have widespread use because it resulted in fairly large errors in molecular calculations, and because the theories were

not rigorously founded. This changed in 1964, when Hohenberg and Kohn (HK) [41] presented two key theorems to the scientific community. Before we further describe the HK theorems, we must clarify that we have limited this description to the simplest systems, that is, N non-relativistic, interacting electrons in a non-magnetic state with Hamiltonian

$$E[\rho(\mathbf{r})] = E_T[\rho(\mathbf{r})] + E_V[\rho(\mathbf{r})] + E_J[\rho(\mathbf{r})] \quad (2-11)$$

$$\text{where } E_T[\rho(\mathbf{r})] \equiv -\frac{1}{2} \sum_j \nabla_j^2, \quad E_V[\rho(\mathbf{r})] \equiv \sum_j v(r_j) \quad \text{and} \quad E_J[\rho(\mathbf{r})] \equiv \frac{1}{2} \sum_{i \neq j} \frac{1}{|r_i - r_j|}.$$

For mathematical reasons, we considered a broad class of Hamiltonians with electrons moving in an arbitrary external potential $v(\mathbf{r})$, besides the physically relevant Coulomb potentials due to point nuclei.

2.3.1 Hohenberg-Kohn Lemmas and Exchange-Correlation Functional Definition

The starting point of KS-DFT is the rigorous, simple-existence lemma of Hohenberg and Kohn (HK) [41] who considered that the specification of the ground-state density, $\rho(\mathbf{r})$, determines the external potential $v(\mathbf{r})$ uniquely (to within an additive constant C). Since $\rho(\mathbf{r})$ also determines N by integration,

$$N[\rho(\mathbf{r})] = \int \rho_c(\mathbf{r}) d\mathbf{r} = N,$$

it determines the full Hamiltonian H (and, implicitly, all the properties determined by H).

Hohenberg and Kohn [41, 45] proved that the ground-state density determines the external potential via *reductio ad absurdum*. They assumed that there were two potentials, $v_a(\mathbf{r})$ and $v_b(\mathbf{r})$, with ground-state wave functions $\Psi_{0,a}$ and $\Psi_{0,b}$, respectively. They also assumed that both wave functions give rise to the same density $\rho(\mathbf{r})$. Unless $[v_b(\mathbf{r}) - v_a(\mathbf{r}) = \text{constant}]$ $\Psi_{0,a}$ and $\Psi_{0,b}$ cannot be equal since they satisfy different

Schrödinger equations. If one denotes the Hamiltonian and ground-state energies associated with $\Psi_{0,a}$ and $\Psi_{0,b}$ by H_a and H_b and $E_{0,a}$ and $E_{0,b}$, then one has by the minimal property of the ground-state,

$$E_{0,b} = \langle \Psi_{0,b} | H_b | \Psi_{0,b} \rangle < \langle \Psi_{0,a} | H_b | \Psi_{0,a} \rangle$$

so that

$$E_{0,a} < E_{0,b} + \int [v_a(\mathbf{r}) - v_b(\mathbf{r})] \rho_0(\mathbf{r}) d\mathbf{r} \quad (2-12)$$

By interchanging a and b , HK found in exactly the same way

$$E_{0,b} < E_{0,a} + \int [v_b(\mathbf{r}) - v_a(\mathbf{r})] \rho_0(\mathbf{r}) d\mathbf{r}, \quad (2-13)$$

Finally, adding Equations 2-12 and 2-13 leads to the inconsistency

$$E_{0,a} + E_{0,b} < E_{0,a} + E_{0,b}. \quad (2-14)$$

With the help of the existence lemma, HK also showed (in a second lemma) that the density obeys a variational (or minimal) principle. For a given $v(\mathbf{r})$, they defined the following energy functional of $\rho(\mathbf{r})$

$$E_{v(\mathbf{r})}[\rho(\mathbf{r})] \equiv \int v(\mathbf{r})\rho(\mathbf{r})d\mathbf{r} + F[\rho(\mathbf{r})], \quad (2-15)$$

$$\text{where } F[\rho(\mathbf{r})] \equiv (\Psi[\rho(\mathbf{r})]E_T + E_J|\Psi[\rho(\mathbf{r})]). \quad (2-16)$$

One should notice that F is a functional of $\rho(\mathbf{r})$, since the wave function itself is a functional of $\rho(\mathbf{r})$. The variational principle is then given by the expression

$$E_{v(\mathbf{r})}[\rho(\mathbf{r})] \geq E_{v(\mathbf{r})}[\rho_0(\mathbf{r})] \equiv E \quad (2-17)$$

where $\rho_0(\mathbf{r})$ and E are the density and energy of the ground-state. The equality in Eq. 2-17 holds only if $\rho_0(\mathbf{r}) = \rho(\mathbf{r})$; in other words, the variational principle states that any calculated energy will be higher than that of the ground-state. Then, Hohenberg and Kohn [41, 45] extracted from $F[\rho(\mathbf{r})]$ its largest and elementary contributions

by writing Equation 2-18,

$$F[\rho(\mathbf{r})] = E_{Ts}[\rho(\mathbf{r})] + \frac{1}{2} \int \frac{\rho(\mathbf{r})\rho(\mathbf{r}')}{|\mathbf{r} - \mathbf{r}'|} d\mathbf{r}d\mathbf{r}' + E_{XC}[\rho(\mathbf{r})] \quad (2-18)$$

where $E_{Ts}[\rho(\mathbf{r})]$ is the kinetic energy of a non-interacting system of electrons with density $\rho(\mathbf{r})$, and the next term is the classical expression for the interaction energy. Equation 2-18 is the KS-DFT definition of $E_{XC}[\rho(\mathbf{r})]$.

2.3.2 Kohn-Sham Self-consistent Field Method

If E_{XC} is ignored in Eq. 2-18, the physical content of the theory becomes identical to that of the Hartree approximation [44]. Kohn and Sham (KS) [42] noticed that and transformed the Euler-Lagrange equation associated with the stationarity of $E_v[\rho(\mathbf{r})]$ into a new set of self-consistent equations, the Kohn-Sham (KS) equations.

$$\left(-\frac{1}{2} \nabla_i^2 + v(\mathbf{r}) + \int \frac{\rho(\mathbf{r}')}{|\mathbf{r} - \mathbf{r}'|} d\mathbf{r}' + V_{XC}(\mathbf{r}) - \varepsilon_j \right) \phi_j(\mathbf{r}) = 0, \quad (2-19a)$$

$$N[\rho(\mathbf{r})] = \sum_{j=1}^N |\phi_j(\mathbf{r})|^2 \quad (2-19b)$$

$$\text{and } V_{XC} = \frac{\delta E_{XC}[\rho(\mathbf{r})]}{\delta \rho(\mathbf{r})} \quad (2-19c).$$

These equations are analogous to Hartree-Fock equations, although they also include correlation effects. They must be solved self-consistently, like the Hartree-Fock equations, calculating V_{XC} in each cycle from Eq. 2-19c, with an appropriate approximation for $E_{XC}[\rho(\mathbf{r})]$ (Section 2.3.3). Despite the appearance of simple, single-particle orbitals, the KS equations are in principle exact provided that the exact E_{XC} is used in Eq. 2-19c; that is, the only error in the theory is due to approximations of

$E_{XC}[\rho(\mathbf{r})]$. Once Equations 2-19 are self-consistently solved, the ground-state energy is obtained by

$$E = \sum_1^v \varepsilon_j - \frac{1}{2} \int \frac{\rho(\mathbf{r})\rho(\mathbf{r}')}{|\mathbf{r}-\mathbf{r}'|} d\mathbf{r}d\mathbf{r}' - \int V_{XC}(\mathbf{r})\rho(\mathbf{r})d\mathbf{r} + E_{XC}[\rho(\mathbf{r})] \quad (2-20)$$

where ε_j and ρ are the self-consistent quantities. The individual eigenfunctions and eigenvalues, φ_j and ε_j , of the Equations 2-19 have no strict physical significance.

2.3.3 Exchange and Correlation Functional Approximations

In principle, the KS-DFT exchange-correlation functional accounts for the classical and quantum mechanical electron-electron repulsion and corrects for the difference in kinetic energy between the fictitious non-interacting system and the real electron system.

Table 2-2. Variables used to express the approximate exchange-correlation functionals $E_{XC}[\rho(\mathbf{r})]$

Variable	Equation	Comments
Energy density (ε_{XC})	$E_{XC}[\rho(\mathbf{r})] = \int \rho(\mathbf{r})\varepsilon_{XC}[\rho(\mathbf{r})]d\mathbf{r}$	Function of the electron density, given by the sum of individual exchange and correlation contributions in the system.
Effective radius [$r_s(\mathbf{r})$]	$r_s(\mathbf{r}) = \left(\frac{3}{4\pi\rho(\mathbf{r})} \right)^{1/3}$	Used when the electron density is expressed for exactly one electron. This electron would be contained within a perfect sphere that has the same density throughout its center.
Normalized spin polarization (ζ)	$\zeta(\mathbf{r}) = \left(\frac{\rho^\alpha(\mathbf{r}) - \rho^\beta(\mathbf{r})}{\rho(\mathbf{r})} \right)$ where: α corresponds to spin-up- and β to spin-down electrons.	Used to express spin densities at any position in open-shell systems. By convention, the spin densities are given by $\rho^\alpha(\mathbf{r}) = \frac{1}{2}\rho(\mathbf{r})(\zeta + 1)$ and $\rho^\beta(\mathbf{r}) = \rho(\mathbf{r}) - \rho^\alpha(\mathbf{r})$.

However, there is no known systematic way to achieve an arbitrarily high level of accuracy for this functional. Therefore, an approximate form for the correct exchange-correlation functional must be selected so that the Kohn-Sham differential equations for the orbitals can be obtained by minimization of the total energy in Eq. 2-20.

These $E_{XC}[\rho(\mathbf{r})]$ approximations can be broadly classified in four major groups: the local density approximation functionals, the gradient-corrected functionals, the hybrid functionals and semi-empirical DFT. Moreover, all these approximate functionals can be expressed in terms of the three variables summarized in Table 2-2.

2.3.3.1 Local density approximation (LDA)

The designation local density approximation originally referred to any DFT functional where the energy density at some position \mathbf{r} was computed exclusively from the value of the electron density at that particular position (i.e., the local value of ρ). However, since the only functionals that follow this definition are those derived based on the uniform electron gas electron density, generally the name LDA is applied only to exchange and correlations functionals derived from jellium.

In the special case when one needs to calculate the exchange energy density for a spin polarized system, LDA can be modified with Equation 2-21.

$$\varepsilon_X[\rho(\mathbf{r}), \zeta] = \varepsilon_X^0[\rho(\mathbf{r})] + \left\{ \varepsilon_X^1[\rho(\mathbf{r})] - \varepsilon_X^0[\rho(\mathbf{r})] \right\} \left[\frac{(1+\zeta)^{4/3} + (1-\zeta)^{4/3} - 2}{2(2^{1/3} - 1)} \right] \quad (2-21)$$

$$\text{where } \varepsilon_X^0[\rho(\mathbf{r})] = -\frac{9\alpha}{8} \left(\frac{3}{\pi} \right)^{1/3} \rho^{1/3}[\mathbf{r}],$$

and $\varepsilon_X^1[\rho(\mathbf{r})]$ is analogous to $\varepsilon_X^0[\rho(\mathbf{r})]$. It describes a uniform electron gas composed of electrons with the same spin. This expression is the local spin density approximation (LSDA) [40, 45].

Since there has been little success in finding analytical expressions for $\varepsilon_c[\rho(\mathbf{r})]$, most of the work available on correlation energy density calculations is approximated by numerical techniques. One of the most widely used functionals is that of Vosko, Wilk and Nusair (VWN) [48]. After Ceperly and Alder used Monte Carlo techniques in 1980 to compute the total energy for jellium of various densities and found their correlation energy by subtracting the exchange, VWN developed a spin polarized correlation local density functional analogous to the exchange functional presented in Eq. 2-21 by fitting these computational results. The VWN proposed expression is Equation 2-22.

$$\varepsilon_c^i(r_s) = \frac{A}{2} \left\{ \begin{array}{l} \ln \frac{r_s}{r_s + b(r_s)^{1/2} + c} + \frac{2b}{(4c - b^2)^{1/2}} \tan^{-1} \left(\frac{(4c - b^2)^{1/2}}{2r_s^{1/2} + b} \right) \\ - \frac{bx_0}{x_0^2 + bx_0 + c} \left\{ \ln \left[\frac{(r_s^{1/2} - x_0)^2}{r_s + br_s^2 + c} \right] + \frac{2(b + 2x_0)}{(4c - b^2)^{1/2}} \tan^{-1} \left(\frac{(4c - b^2)^{1/2}}{2r_s^{1/2} + b} \right) \right\} \end{array} \right\} \quad (2-22)$$

where $i = 0$ or 1 (analogous to $\varepsilon_x^0[\rho(\mathbf{r})]$ and $\varepsilon_x^1[\rho(\mathbf{r})]$), and with different empirical constant sets for $\varepsilon_c^0[\rho(\mathbf{r})]$ and $\varepsilon_c^1[\rho(\mathbf{r})]$. This correlation functional, known as $E_C^{VWN}[\rho(\mathbf{r})]$, is exact for jellium but not for molecular systems and it is a good example of how many empirically optimized constants are required in DFT to approximate the unknown exact $E_{xc}[\rho(\mathbf{r})]$. Furthermore, the semi-empirical flavor of functionals such as $E_C^{VWN}[\rho(\mathbf{r})]$ is the main inspiration for the development of the semi-empirical DFT methods (Section 2.3.3.4).

2.3.3.2 Density gradient corrections

Because the LDA exchange functionals were derived from a HF density matrix constructed with the plane wave orbitals of the uniform electron gas, they typically underestimate the exchange energy by roughly 10 to 15 %, and, consequently, need a

correction for the non-uniformity of atomic and molecular electron densities. An improvement would be the generation of exchange and correlation functionals that depend on the local value of the electron density, and on the extent to which the density is locally changing (i.e., the density gradient). These types of functionals are called gradient-corrected functionals, and the methodology by which they are formed is known as the generalized gradient approximation (GGA). Most of these gradient-corrected functionals are constructed by adding a correction to an LDA functional energy density expression, that is, Equation 2-23.

$$\varepsilon_{X/C}^{GGA}[\rho(\mathbf{r}), \nabla\rho(\mathbf{r})] = \varepsilon_{X/C}^{LSDA}[\rho(\mathbf{r})] + \Delta\varepsilon_{X/C}x(\mathbf{r}) \quad (2-23)$$

where $x(\mathbf{r})$ is the reduced density gradient given by Eq. 2-24,

$$x(\mathbf{r}) = \frac{|\nabla\rho(\mathbf{r})|}{\rho^{4/3}(\mathbf{r})} \quad (2-24),$$

and X/C indicates that this could be either an exchange or a correlation gradient-corrected density functional). The reduced density gradient has small values in bonding regions, larger values in core regions and very large values in Rydberg regions of molecules.

The most widely used GGA exchange functional is the one developed by Becke in 1988 [49], which combines LSDA exchange with a gradient correction, and yields accurate exchange energies for atoms and correct exchange energy density in Rydberg regions. In its simplest form, the functional is given by Equation 2-25,

$$E_X^{B88} = E_X^{D30} - \beta \int (\rho^\sigma)^{4/3} \frac{x_\sigma^2}{1 + 6\beta x_\sigma \sinh^{-1} x_\sigma} d\mathbf{r} \quad (2-25)$$

where the semi-empirical parameter β has a value of 0.0042, obtained by fitting to the E_X^{F30} (Hartree-Fock) exchange energies of six noble gas atoms (He to Rn). Alternative GGA exchange functionals do not include empirically optimized parameters.

With respect to correlation, $E_C^{VWN}[\rho(\mathbf{r})]$ predicts correlation energies that are too large, making it a poor starting point for a gradient-corrected functional. Instead, the most popular GGA correlation functional developed by Lee, Yang and Parr (LYP) [50] computes full correlation energies. LYP abandoned jellium in favor of the He atom, the simplest system with a non-vanishing correlation energy. Their approach was based on earlier work of Colle and Salvetti [51], and it was improved for spin-compensated and spin-polarized versions by Miehlich *et al.* [52]. The expression reported by Miehlich *et al.* for this gradient-corrected correlation functional, denoted as a second-order gradient expansion is Equation 2-26.

$$\begin{aligned}
E_C^{LYP}[\rho, \nabla\rho] = & -a \int \left(\frac{4}{1+d\rho^{-1/3}} \right) \left(\frac{\rho^\alpha \rho^\beta}{\rho} \right) \\
& - ab \int \omega \{ \rho^\alpha \rho^\beta [2^{11/3} C_F ((\rho^\alpha)^{8/3} + (\rho^\beta)^{8/3}) + \left(\frac{47}{18} - \frac{7}{18} \delta \right) |\nabla\rho|^2 \right. \\
& \left. - \left(\frac{5}{2} - \frac{1}{18} \delta \right) (|\nabla\rho^\alpha|^2 + |\nabla\rho^\beta|^2) - \frac{\delta - 11}{9} \left(\frac{\rho^\alpha}{\rho} |\nabla\rho^\alpha|^2 + \frac{\rho^\beta}{\rho} |\nabla\rho^\beta|^2 \right) \right] \\
& \left. - \frac{2}{3} \rho^2 |\nabla\rho|^2 + \left(\frac{2}{3} \rho^2 - (\rho^\alpha)^2 \right) |\nabla\rho^\alpha|^2 + \left(\frac{2}{3} \rho^2 - (\rho^\beta)^2 \right) |\nabla\rho^\beta|^2 \right\}
\end{aligned} \tag{2-26}$$

where $\omega = \frac{\exp(-c\rho^{-1/3})}{1+d\rho^{-1/3}} \rho^{-11/3}$, $\delta = c\rho^{-1/3} + \frac{d\rho^{-1/3}}{1+d\rho^{-1/3}}$, $C_F = \frac{3}{10} (3\pi^2)^{2/3}$ and the

parameters a , b , c and d were obtained from the work of Colle and Salvetti [51]. The

values for the parameters are $a = 0.04918$, $b = 0.132$, $c = 0.2533$ and $d = 0.349$. $E_C^{LYP}[\rho(\mathbf{r})]$

yields better results than $E_C^{VWN}[\rho(\mathbf{r})]$ and is very important in DFT despite some

theoretical deficiencies.

2.3.3.3 Hybrid methods

Given that the basis of the Kohn-Sham approximation is the non-interactive reference system, it was suggested that one can control the conversion from a non-

interacting to a real interacting system. With the Hellmann-Feynman theorem, the DFT exchange-correlation energy can be computed as shown in Equation 2-27.

$$E_{XC} = \int_0^1 \langle \Psi(\lambda) | \bar{V}_{XC}(\lambda) | \Psi(\lambda) \rangle d\lambda \quad (2-27)$$

where λ is the extent of interelectronic interaction, going from 0 (non-interaction system) to 1 (real system). Development of hybrid DFT techniques resulted in methods that are significantly more efficient than *ab initio* methods of comparable accuracy. The relatively good accuracy and computational efficiency of hybrid methods indicate that further improvements might lead to methods that are both highly accurate and relatively efficient. All these methods include Hartree-Fock exchange because a small exact-exchange component is a necessary constituent of any exchange-correlation approximation aiming for accurate molecular energetic. The methods use the conventional mixing method introduced by Becke [53], which expands the functional with respect to the electron density and its gradient according to Eq. 2-23 and adds adjustable coefficients, c_i

$$E_{XC}^B[\rho(\mathbf{r})] = \int \sum_i c_i f(\rho_\alpha, \rho_\beta, \gamma^{\alpha\alpha}, \gamma^{\alpha\beta}, \gamma^{\beta\beta}) d\mathbf{r} \quad (2-28)$$

an approach that is appealing because its application to a new molecule requires only a single Kohn-Sham calculation. Becke developed the B3LYP exchange-correlation functional [53], which is defined by Equation 2-29.

$$E^{B3LYP} = E_T^{H28} + E_V + E_J + (1-c_1)E_X^{D30} + c_1E_X^{F30} + c_2\Delta E_X^{B88} + (1-c_3)E_C^{VWN} + c_3E_C^{LYP} \quad (2-29)$$

where the coefficients c_1 , c_2 and c_3 are semi-empirical coefficients determined by a fit to experimental data. This method cannot be derived rigorously and, at least in its current status, is basically empirical. Nonetheless, it is widely used because its ability to predict

the atomization energies of normal systems is very close to their exact value. Kang and Musgrave [54] proposed a hybrid DFT method in which the exchange functional is a mix of Slater exchange and exact exchange. The KMLYP energy functional is given by Eq. 2-30.

$$E^{KMLYP} = E_T^{H28} + E_V + E_J + (1 - a)E_X^{D30} + aE_X^{F30} + (1 - b)E_C^{VWN} + bE_C^{LYP} \quad (2-30)$$

where $a = 0.557$ and $b = 0.448$ and the subscripts are the same as in Eq. 2-29.

2.3.3.4 Empirical DFT methods

These methods increased the emphasis on empirical parameterization, arguing that by modestly increasing parameterization it may be possible to obtain good functionals. Additionally, empirical DFT methods (EDF) looked for an exchange-correlation functional that was optimized for a relatively small basis set and questioned the need for including Hartree-Fock exchange to obtain good agreement with experiment. Hybrid methods suppose that a small exact-exchange component is a necessary constituent of any exchange-correlation approximation aiming for accurate molecular energetics, but this introduces non-local effects and consequent computational complications that EDF methods tried to eliminate.

Empirical density functional theory 1 (EDF1) [55] developed a DFT functional by linearly combining several existing functionals. It was optimized to yield accurate thermochemistry when used with the 6-31+G* Pople basis set (Section 2.4). Among other variational schemes, it considered linear combinations of different functionals or linear combinations of the same functionals with different parameters. The component functionals used are those of Becke [49] and Lee, Yang and Parr [50], discussed above.

EDF2 [56] was developed following the method used in EDF1 [55], in which a DFT functional is obtained by linearly combining several existing orbital and density

functionals, with a special focus on giving accurate harmonic frequencies when used with the cc-pVTZ [57] basis sets. The expression EDF2 is as shown in Equation 2-31.

$$E_{XC}^{EDF2} = b_1 E_X^{F30}[\psi] + b_2 E_X^{D30}[\rho] + b_3 E_X^{B88}[\rho] + b_4 E_X^{EDF1}[\rho] + b_5 E_C^{VWN}[\rho] + b_6 E_C^{LYP}[\rho] + b_7 E_C^{EDF1}[\rho] \quad (2-31)$$

where $b_1 = 0.1695$, $b_2 = 0.2811$, $b_3 = 0.6227$, $b_4 = -0.0551$, $b_5 = 0.3029$, $b_6 = 0.5998$, and $b_7 = -0.0053$.

2.3.4 Kohn-Sham Density Functional Theory Computational Chemistry

Figure 2-2 summarizes the steps involved in a KS-DFT geometry optimization. For the most part, they are the same as those used in Hartree-Fock theory. First, a basis set is chosen to construct the KS orbitals (Eq. 2-19) and then an initial estimate of the molecular geometry. After that, the overlap integrals and the kinetic energy and nuclear attraction integrals are computed. The latter two kinds of integrals are called one-electron integrals in HF theory to distinguish them from the two-electron Coulomb and exchange integrals. (However, in KS theory all integrals can in some sense be regarded as one-electron integrals since every one reflects the interactions of each one electron with external potentials). To evaluate the remaining integrals, one must guess an initial density, and this density can be constructed as a matrix entirely equivalent to the \mathbf{P} HF density matrix, which describes the degree to which individual basis functions contribute to the many-electron wave function, and thus, how important the Coulomb and exchange integrals should be.

The elements of \mathbf{P} are then computed as indicated in Equation 2-32.

$$P_{\lambda\sigma} = 2 \sum_i^{\text{occupied}} a_{\lambda i} a_{\sigma i} \quad (2-32)$$

where the coefficients $a_{\lambda i}$ and $a_{\sigma i}$ specify the contribution of the basis functions to the molecular orbital i and the factor of two appears because this is a restricted calculation,

Once the guess density is determined one can construct V_{XC} (Eq. 2-19c) and evaluate the remaining integrals in each KS matrix element. New orbitals are determined from solution of the secular equation, the density is determined from those orbitals, and it is compared to the density from the preceding iteration. Once convergence of the SCF is achieved, the energy is computed by plugging the final density into Eq. 2-20. At this point, the calculation proceeds according to the geometry optimization algorithm (i.e., if the geometry does not correspond to the optimal point, a new structure will be found and the KS SCF process will be run again, until the optimum is reached [45]). The geometry optimization algorithm is described in Section 2.5, but first, we present a brief introduction to the basis sets used in this work.

2.4 Basis Sets

As discussed, Equations 2-19 are formally similar to the HF SCF ones, except that the exchange nonlocal one-electron operator is replaced by a local exchange-correlation operator depending on the total electron density. Thus, the KS equations can be efficiently calculated and the single electron wave functions can be represented by several basis functions such as Slater-type orbitals. A basis set is then, a set of mathematical basis functions from which the wave function is constructed in a quantum chemistry calculation.

Slater-type orbitals have a number of attractive features primarily associated with the degree to which they closely resemble hydrogenic atomic orbitals. They suffer, however, from a fairly significant limitation. There is no analytical solution available for the general four-index integral given in Equation 2-33 when the basis functions are STOs. The requirement that such integrals be solved by numerical methods severely limits their utility in molecular systems of any significant size.

$$(\mu\nu | \lambda\sigma) = \iint \phi_\mu(1)\phi_\nu(1) \frac{1}{r_{12}} \phi_\lambda(2)\phi_\sigma(2) d\mathbf{r}(1)d\mathbf{r}(2) \quad (2-33)$$

Alternatives to the use of STOs have been proposed. One of them indicates that for there to be an analytical solution of the general four-index integral (Eq. 2-33) formed from such functions is required that the radial decay of the STOs be changed from e^{-r} to e^{-r^2} . That is, the AO-like functions are chosen to have the form of a Gaussian function. The general functional form of a normalized Gaussian-type orbital (GTO) in atom-centered Cartesian coordinates is as shown in Equation 2-34.

$$\phi(x, y, z; \alpha, i, j, k) = \left(\frac{2\alpha}{\pi}\right)^{3/4} \left[\frac{(8\alpha)^{i+j+k} i! j! k!}{(2i)!(2j)!(2k)!} \right]^{1/2} x^i y^j z^k e^{-\alpha(x^2+y^2+z^2)} \quad (2-34)$$

Small GTO sets can be used for a wider range of chemical problems but involve some loss of flexibility in the resulting molecular orbitals. The simplest level of basis is minimal and corresponds to one basis function per atomic orbital. The next level is split-valence or valence-multiple- ζ in which two basis functions are used for each valence atomic orbital. This second level is known to give a better description of the relative energies and of some geometrical features of molecules. Further improvement of a basis set requires addition of functions of higher angular quantum numbers (polarization functions) [59].

The basis functions are generally contracted (i.e., each basis function is a linear combination of a number of primitive Gaussian functions). The contracted GTOs used in DFT to represent the electronic orbital wave functions, often were originally developed for Hartree-Fock calculations. A considerable increase in computational efficiency can be achieved if the exponents of the Gaussian primitives are shared between different basis functions [60]. At the split-valence level, this has been exploited by sharing

primitive exponents among s and p functions for the valence functions. In particular, a series of basis was defined and designated *K-LMG* by Pople and coworkers [61-68] where *K*, *L*, and *M* are integers. Such a basis for a first-row element (Li to Ne) consists of an s-type inner-shell function with *K* Gaussians, an inner set of valence s- and p-type functions with *L* Gaussians, and another outer sp set with *M* Gaussians. Both valence sets have shared exponents. For hydrogen, only two s-type valence functions (with *L* and *M* Gaussians) are used. Among this basis sets are 3-21G [67-68], 4-31G [64, 69], and 6-31G [63, 65-66]. The original 4-31G and 6-31G split-valence basis sets were obtained by optimizing all Gaussian exponents and contraction coefficients to give the lowest spin-unrestricted Hartree-Fock energy for the atomic ground-state. The Pople basis sets have seen widespread use among the scientific community [45].

A problem with the calculations based on *K-LMG* basis sets is that s and p functions centered on the atoms do not provide sufficient mathematical flexibility to adequately describe the wave function for some geometries. This occurs because the molecular orbitals require more mathematical flexibility than do the atoms. Because of the utility of AO-like GTOs, this flexibility is almost always added in the form of basis functions corresponding to one quantum number higher angular momentum than the valence orbitals. Thus, for a first-row atom the most useful polarization functions are d GTOs, and for hydrogen, p GTOs. A variety of molecular properties prove to be sensitive to the presence of polarization functions; for example, d functions on second-row atoms are absolutely required to make reasonable predictions for the geometries of molecules including such atoms in formally hypervalent bonding situations (e.g., siliconates). Because the total number of functions begins to grow rather quickly with the addition of polarization functions, early calculations typically made use of only a

single set. Pople and coworkers introduced first a simple nomenclature scheme to indicate the presence of the polarization functions, the “*” (star). Thus, 6-31G* implies a set of d functions added to polarize the p functions in 6-31G. A second star implies p functions on H and He (e.g., 6-311G**) [45]. However, realizing the tendency to use more than one set of polarization functions in modern calculations, their basis set nomenclature now typically includes an explicit enumeration of those functions instead of the star nomenclature. Thus, 6-31G(d) is preferred over 6-31G* because the former generalizes to allow names such as, for example, 6-31G(3d2fg,2pd), which implies heavy atoms polarized by three sets of d functions, two sets of f functions, and a set of g functions, and hydrogen atoms by two sets of p functions and one of d.

Finally, we must indicate that the highest energy MOs of anions and highly excited electronic states tend to be much more spatially diffuse than the molecular orbitals described so far. When a basis set does not have the flexibility necessary to allow a weakly bound electron to localize far from the remaining density, significant errors in energies and other molecular properties can occur. To address this limitation, standard basis sets are often augmented with diffuse basis functions. In the Pople family of basis sets, the presence of diffuse functions is indicated by a “+” in the basis set name. Thus, 6-31+G(d) indicates that heavy atoms have been augmented with an additional one s and one set of p functions having small exponents. A second plus indicates the presence of diffuse s functions on H [e.g., 6-311++G(2d,p)]. For the Pople basis sets, the exponents for diffuse functions were variationally optimized on the anionic one-heavy-atom hydrides and are the same for 3-21G, 6-31G and 6-311G [45]. In this work we use the 3-21G*, the double- ζ plus polarization 6-31G(d), and the diffuse triple- ζ plus polarization 6-311++G(2d,p) Pople basis sets.

2.5 Geometry Optimization and Transition State Search Calculations

Before we discuss how to perform geometry optimizations of molecular systems, we must understand the concept of a potential energy surface (PES) since a potential energy surface describes the energy of a particular molecule as a function of its geometry, and a geometry optimization is a process to find minima on a potential energy surface. Finding the total PES is a very complicated task, mainly because molecules have many atoms and many coordinates that describe their geometry. A simplified three-dimensional PES can be represented as a topographic surface with valleys and saddle points (Figure 2-2).

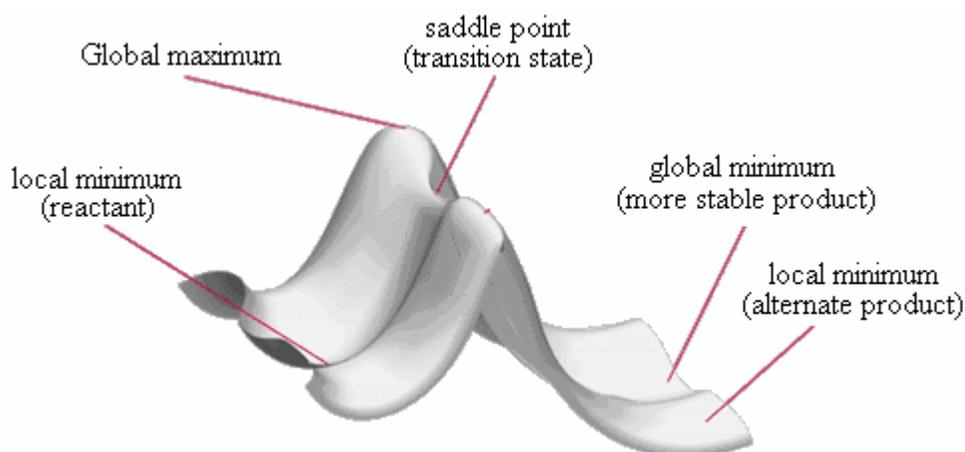


Figure 2-2. Two-dimensional potential energy surface

Generally, calculation of most potential energy surfaces is based on the Born-Oppenheimer approximation which specifies that since the electrons are much lighter than the nuclei, the electronic part of the wave function readjusts almost immediately to any nuclear motion. Thus, potential energy surfaces can be obtained by calculating the total electronic energy for all the possible fixed nuclear positions that the molecule may adopt, an approach that is satisfactory for ground-state systems. On a PES, a reaction path is the movement from a valley of reactants to a valley of products, and a

reaction mechanism is the path across the PES. Then, the important points in the calculated PES are the minima and the saddle points, with the equilibrium geometries corresponding to minima and the saddle points to the highest points on a reaction path that requires the least energy to get from the reactants to the products. Both PES minima and saddle points are called stationary points (or critical points), because for them the gradient (first derivative) is zero, and in classical mechanics, negatives of the first derivatives of the potential energy surface are the forces on the atoms in the molecule, as expressed by Eq. 2-34.

$$\mathbf{F} = -\nabla E_V \quad (2-34)$$

An energy minimum must satisfy two conditions [70]:

- its first derivative (i.e., gradient of the forces) must be zero (critical point).
- its second derivative matrix must be positive definite (i.e., all eigenvalues of the Hessian must be positive or all of the vibrational frequencies must be real).

Because of the difficulty of finding a complete PES, most quantum chemistry geometry optimization methods are focused on finding equilibrium structures and transition states directly. In this work, we performed geometry optimizations of $\text{Si}_9\text{H}_{12+w}\text{O}_x\text{N}_y\text{C}_z$ ($w, x, y, z = 0, 1, 2$, etc.) clusters using the unrestricted hybrid density functional method B3LYP combined with the diffuse triple- ζ plus polarization 6-311++G(2d,p) basis set to expand the molecular orbitals of chemically active atoms (the surface Si atoms, four Si atoms of the first subsurface layer, the carbon atoms, the nitrogen atoms, and the oxygen atoms), and the double- ζ plus polarization 6-31G(d) basis set to describe the remaining subsurface silicon atoms and terminating hydrogen atoms (Section 2.4). Usually, finding equilibrium geometries and transition structures requires application of unconstrained optimization on the PES. However, we imposed constraints

on the hydrogen atoms that terminate broken Si-Si bonds in the clusters, to mimic the constraints that the rest of the solid should impose on the surface dimer under study.

2.5.1 Geometry Optimization of Energy Minima

There are three types of geometry optimization algorithms: Methods that use only the energy, methods that use the first derivatives of the potential energy surface with respect to geometric parameters (i.e., gradient methods), and methods that require second derivatives (i.e., Newton or Newton-Raphson methods). The methods that only use the energy are the most widely applicable, but the slowest to converge, while the second derivative methods converge very fast but, given that analytic second derivatives are not readily available and more costly than the gradient methods. Thus, the gradient algorithms are the preferred methods, and (if analytical gradients are not available) it is usually efficient to calculate them numerically. In this work we performed quantum chemistry calculations with Gaussian03 [71], which uses the gradient method known as the Broyden algorithm [72-73] (Figure 2-3) as the standard method for calculations of both geometry optimizations to a local minimum and transition state searches.

Gradient methods, such as the Broyden algorithm, approximate the potential energy surface as a quadratic function and calculate the energy with the expressions

$$E(\mathbf{r}) = E_0 + \mathbf{g}^t \Delta \mathbf{r} + \frac{1}{2} \Delta \mathbf{r}^t \mathbf{H} \Delta \mathbf{r} \quad (2-35a)$$

$$\mathbf{g} = \mathbf{g}_0 + \mathbf{H} \Delta \mathbf{r} \quad (2-35b)$$

where $\Delta \mathbf{r} = \mathbf{r} - \mathbf{r}_0$, \mathbf{g} is the gradient vector, and \mathbf{H} is the Hessian matrix. Since for an energy minimum $\mathbf{g} = 0$, the minimum structure can be obtained by solving linear equations Eq. 2-36a and Eq. 2-36b.

$$\mathbf{g} = \mathbf{g}_0 + \mathbf{H} \Delta \mathbf{r} = 0 \quad (2-36a)$$

$$\Delta \mathbf{r} = -\mathbf{H}^{-1} \mathbf{g}_0 \quad (2-36b)$$

known as the Newton step. These first derivatives can be found analytically or numerically. The rate of convergence of the Berny algorithm depends predominantly on six factors:

- Initial geometry of the structure to be optimized
- Coordinate system chosen.
- Initial guess for the Hessian matrix.
- Hessian matrix updating method.
- Step size control.

The initial geometry of the structure is a critical issue. It cannot be just any structure that resembles the molecule under study as it would imply that the optimization using a large basis set would require numerous unnecessary steps. Generally, molecular mechanics and semi-empirical methods are used to refine a raw structure and obtain a much better initial guess. In this work, we also ran a DFT/UB3LYP geometry optimization with the 3-21G* Pople basis set after the semi-empirical calculations to get as close as possible to the final minimum energy structure.

Early geometry optimization used non-redundant internal coordinates (e.g., the Z matrix internal coordinates), but later it was shown that Cartesian coordinates and a combination of Cartesian and internal coordinates had some advantages for particular systems [74]. Cartesian coordinates are the simplest and give an unambiguous representation of the structure, but they are also strongly coupled (i.e., to change a bond length one must change the x , y , and z positions of several atoms). Alternatively, internal coordinates (based on bond lengths, valence angles and dihedral angles) avoid problems with rigid body rotations and translations. In internal coordinates, the coupling is much smaller than with Cartesian coordinates, and as a result the Hessian is more diagonal.

(Appendix C reviews the protocol used to determine the initial coordinates for our calculations).

The rate of convergence of a geometry optimization depends also on the initial guess of the nuclear Hessian since a closer guess to the actual Hessian will translate into a faster convergence. Computationally inexpensive empirical methods to generate initial nuclear Hessian have been proposed by Schlegel [75] and Fischer and Almlöf [76], who also compared the effect of different coordinate systems on the geometry optimization.

An initial empirical estimate of a diagonal Hessian can be quite satisfactory for redundant internal coordinates and can be readily transformed to other coordinate systems. However, Baker [77-78] showed that minimizations with Cartesian and redundant internal coordinates were similar if a good initial estimate of the Hessian is used (i.e., a molecular mechanics or semi-empirical Hessian instead of a unit Hessian). The Hessian from an optimization or a frequency calculation previously performed at a lower level of theory is often a very good initial guess for an optimization at a higher level. Some difficult optimizations may require an accurate initial Hessian computed analytically or numerically at the same level of theory as that used for the optimization. The default in Gaussian03 estimates bond stretching force constants from empirical rules, and obtains average angle-bending and torsion constants from vibrational spectra or theoretical calculations, using smaller and less expensive basis sets to calculate the force constants. Finally, since we are interested in constrained structures (given the rigidity that the silicon bulk would impose on the surface dimer chemistry) it is important to know that any components of the gradient vector corresponding to frozen variables are set to zero or projected out, thereby eliminating their direct contribution to the next optimization step.

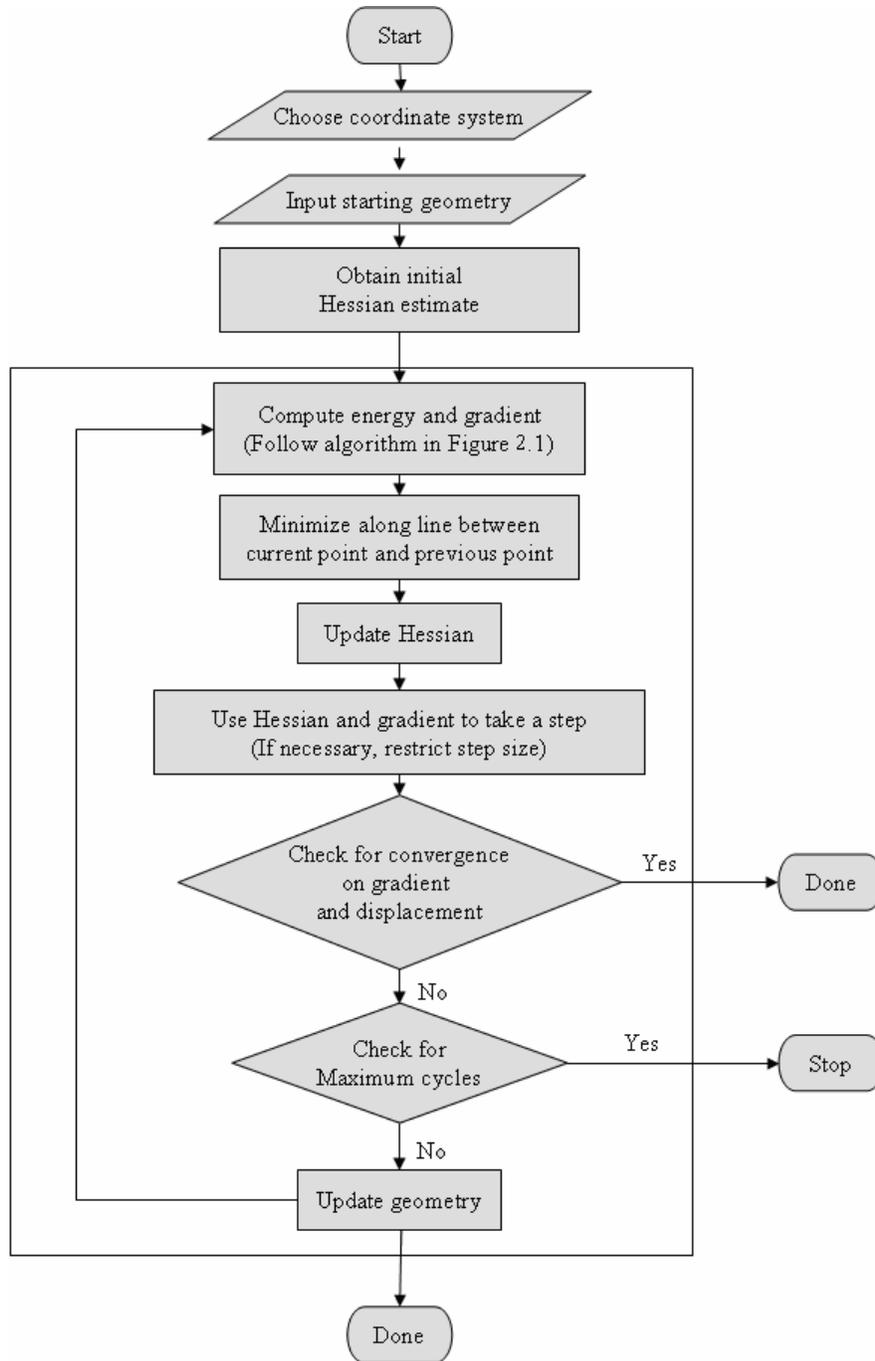


Figure 2-3. Flowcharts for a quasi-Newton algorithm for geometry optimization

Proper update of the Hessian is essential for efficient optimizations, as the quality of the Hessian at each point is critical for the success of the optimization. However, the calculation of the exact Hessian at each point would make the process lengthy and costly. Instead, the Hessian is adjusted in the quadratic approximation represented by Eq. 2-36

so that it fits the gradient \mathbf{g}_i at the current point \mathbf{r}_i and the gradient \mathbf{g}_{i-1} at the previous point. This leads to Equation 2-37.

$$\mathbf{H}_i \Delta \mathbf{r} = \Delta \mathbf{g} \quad (2-37)$$

In Eq. 2-37 $\Delta \mathbf{r} = \mathbf{r}_i - \mathbf{r}_{i-1}$ and $\Delta \mathbf{g} = \mathbf{g}_i - \mathbf{g}_{i-1}$. There are numerous methods to update the Hessian, for example that of Broyden, Fletcher, Goldfab and Shanno (BFGS) [70], which can be written as expressed in Eq. 2-38.

$$\mathbf{H}_i = \mathbf{H}_{i+1} + \Delta \mathbf{g} \Delta \mathbf{g}' / \Delta \mathbf{r}' \Delta \mathbf{g} - \mathbf{H}_{i-1} \Delta \mathbf{r} \Delta \mathbf{r}' \mathbf{H}_{i-1} / \Delta \mathbf{r}' \mathbf{H}_{i-1} \Delta \mathbf{r} \quad (2-38)$$

Eq. 2-38 is symmetric, positive definite, and minimizes the norm of the change in the Hessian. Schlegel *et al.* [74] indicate that most modern updating algorithms give similar results.

Once there is a new dependable Hessian, a Newton step is taken on the model quadratic surface. The Hessian must be positive definite (i.e., all of its eigenvalues must be positive, for the step to be in the downhill direction). If the structure is far from the minimum (e.g., large gradients) or the potential energy surface is very flat (one or more small eigenvalues of the Hessian), then a simple Newton step may be too large, taking the molecule beyond the region where the model quadratic surface is valid. In this case, a shorter step must be taken. One can limit the step to be no larger than a trust radius which can be adjusted as the calculation proceeds, depending on whether the change in the predicted energy compares well with the actual calculated energy difference. In the Berny algorithm of Gaussian03 the trust radius is updated using the method of Fletcher [79].

2.5.2 Transition State Searches

A transition structure is the highest point on the reaction path that requires the least energy to get from the reactant A to the product B. In other words, it is a stationary point that is an energy maximum in one direction and a minimum in all others. For a point to be considered to be a transition state structure the first derivatives must be zero and the energy must be a maximum along the reaction path connecting the valley of reactants with the valley of products on the potential energy surface. The transition state structure must be a critical point of index one (i.e., one of the eigenvalues of the Hessian matrix must be negative and all others must be positive). Energy, structure and vibrational information for transition state structures are obtained from the transition state theory. As the case for minima, transition structures can be found by geometry optimization, although some modifications must be incorporated into the procedure.

Initial estimates for transition structures are more difficult to obtain than for equilibrium structures since transition state geometries vary much more than equilibrium geometries. Moreover, molecular mechanics generally cannot handle transition states involving the making and breaking of bonds. As a result, when searching for transition states, many quasi-Newton methods need to start fairly close to the quadratic region of the transition state. Several techniques have been proposed to search for the initial structure of the transition state, including synchronous transit [80] and eigenvector following [81]. Gaussian03 combines synchronous transit and quasi-Newton methods to find transition states [74, 80, 82]. This method requires two or three structures to start the optimization (one in the reactant valley, the second in the product valley, and an optional third structure as an initial guess for the TS geometry). If there is no third structure, the initial guess is obtained by interpolating between the reactants and products in redundant

internal coordinates. The first few steps search for a maximum along an arc of circle connecting the reactant-like with the product-like structure, and a minimum in all other directions. The initial guess of the points along the reaction path is obtained by interpolating between two input structures; the energy and gradient are calculated at each point and an empirical estimate of the Hessian is obtained also at each point. The highest energy point on the path is chosen to be optimized to the closest TS, dividing the path into two downhill segments. In the remaining optimization steps, a quasi Newton based eigenvector following optimization is guided by the tangent to the arc of circle passing through the presumed TS and minima according to the implementation developed by Baker in 1986 [81].

As in the geometry optimizations, the use of a certain coordinate system can improve the transition state search considerably. Ayala and Schlegel [73] showed that the combined use of redundant internal coordinates and the tangent to the quadratic synchronous transit (QST) path improves considerably the transition state optimization, mainly because a better Hessian is obtained in the first few steps and improves the search direction. These redundant internal coordinates are based on the work of Pulay *et al.* [83-84], who defined a natural internal coordinate system that minimizes the number of redundancies by using local pseudosymmetry coordinates about each atom and special coordinates for ring structures, and Peng *et al.* [74], who reduced the number of special cases of these coordinates by using a simpler set of internal coordinates composed of all bond lengths, bond angles and dihedral angles and applied it successfully for transition state searches. Peng *et al.* [74] defined their coordinates as follows: First, the interatomic distances are examined to determine which atoms are bonded. Then, a bond angle bend coordinate is assigned for any two atoms bonded to the same third atom.

Special attention must be given to linear bond angles; if the bond angle is greater than $\sim 175^\circ$, then two orthogonal linear angle bend coordinates are generated. Finally, a dihedral angle coordinate is assigned for each pair of atoms bonded to opposite ends of a bond. If one or both of the bond angles involved in a dihedral angle is linear, then the dihedral is omitted. In addition to the redundant internal coordinates generated automatically, extra stretch, bend and dihedral angle coordinates can be specified in the input. For regular transition state optimizations starting from one structure, the bonds being made or broken need to be specified in the input.

Some difficult transition state searches may require an accurate initial Hessian computed analytically or numerically at the same level of theory as that used for the optimization instead of an updated one. Furthermore, Hessian update methods are suitable for finding minima for small and medium-sized molecules, but for difficult cases, such as some of the transition state structures investigated in this work, the Hessian has to be recalculated every few steps (or even every step) instead of being updated. This is equivalent to a Newton or Newton-Raphson algorithm. This is a very expensive method, and by default, Gaussian03 avoids it and updates the Hessian; however, its use has the advantage of obtaining an excellent description of the Hessian at each point of the calculation and also, since a vibrational frequency analysis is automatically done at the converged structure there is no need for an additional frequency job to determine the number of positive eigenvalues or zero point vibrational energies. The protocol that we used for transition state searches is presented in Appendix D.

CHAPTER 3
NITROGEN ATOM ABSTRACTION FROM Si(100)-(2x1)

3.1 Introduction

The reactions of gas-phase radicals at solid surfaces are fundamental to the plasma-assisted processing of semiconductor materials. In addition to adsorbing efficiently, radicals incident from the gas-phase can also stimulate several types of elementary processes before thermally accommodating to the surface, including direct-atom abstraction and collision-induced reaction and desorption. Direct-atom abstraction can occur by an Eley-Rideal mechanism in which an atom is abstracted from the surface in a single collision with an incident species [11] or by a hot atom mechanism in which the incident species experiences multiple collisions with the surface but does not fully thermalize before the reactive encounter [13]. Indeed, non-thermal surface reactions such as these play a critical role in determining the enhanced surface reactivity afforded by plasma processing. Advancing the fundamental understanding of radical-surface reactions is therefore of considerable importance to improving control in plasma-assisted materials processing in addition to being of scientific interest.

In the present study, we have used quantum chemical calculations to investigate the interactions of an oxygen atom with nitrogen atoms incorporated into the Si(100)-(2x1) surface, focusing on pathways that lead to direct nitrogen abstraction from the surface by the formation of gaseous NO. This investigation is motivated firstly by an interest in determining the viability of direct nitrogen abstraction from Si(100) by gas-phase oxygen atoms, and to gain insights into the possible pathways for this surface reaction. It is

further motivated by the potential benefits that may be realized by incorporating ultrathin silicon oxynitride films into metal-oxide-semiconductor (MOS) devices and the need to precisely control the properties of such films. Over the past several years, ultrathin silicon oxynitride (SiO_xN_y) films have been incorporated into MOS devices as an alternative for SiO_2 , which is no longer suitable as an insulator for MOS devices because of the decreasing dimensions of microelectronic devices imposed by Moore's law [33, 85]. Incorporating nitrogen into SiO_2 is a relatively simple method for fabricating silicon oxynitride films, and results in dielectric layers that enhance resistance to gate current leakage and inhibit boron penetration into the dielectric [86]. However, as the sizes of semiconductor devices continue to decrease, it is becoming critical to develop processing methods that afford control of film properties and composition at the monolayer level.

Low-temperature remote plasma processing offers distinct advantages over other ultrathin silicon oxynitride film preparation methods [33]. For example, researchers [87-88] have reported that the concentration profiles of nitrogen and oxygen atoms within SiO_xN_y films grown by remote plasma processing on Si(100) can vary significantly with both the feed gas composition and processing protocol that is used. Of particular interest is the observation that the exposure of Si(100) to an N_2O or N_2/O_2 plasma produces a film with a highly heterogeneous composition profile in which the nitrogen atoms accumulate at the film-Si interface and the oxygen atoms remain close to the film-vacuum interface. It was suggested that this composition profile results, at least in part, by chemical reactions in which gaseous oxygen atoms efficiently scavenge nitrogen atoms located closest to the film-vacuum interface. In a separate study, Watanabe and Tatsumi [89] also observed a decrease in surface nitrogen concentration after exposing a nitrated Si(100) surface to an oxygen plasma, and asserted that nitrogen atoms are removed from

the surface through reactions with gaseous oxygen atoms. While thermally activated reactions between accommodated oxygen and nitrogen atoms could have taken place at the surface temperature of 750 °C used in the work of Watanabe and Tatsumi, the other investigations cited were conducted with the substrate held at 300 °C, which is well below the temperature for appreciable thermal decomposition of silicon oxide [30] and nitride surfaces [90-91]. It is therefore likely that the oxygen-induced removal of nitrogen from the surfaces of these films occurs by non-thermal processes such as Eley-Rideal abstraction. In the present study, we find that direct nitrogen abstraction by gaseous oxygen atoms is energetically favorable when nitrogen is bound at the Si(100) surface in coordinatively unsaturated configurations, but less so when the nitrogen is triply coordinated with surrounding silicon atoms.

3.2 Computational Approach

Quantum chemical calculations of oxygen induced abstraction of a nitrogen atom from the Si(100)-(2x1) surface were performed using density functional theory (DFT) and cluster models of the surface. Cluster energies were computed using the unrestricted, hybrid three-parameter Becke method (UB3LYP), which combines the gradient-corrected exchange functional of Becke [49, 53] with the Lee-Yang-Parr (LYP) correlation functional [50]. An unrestricted approach was used for all calculations because the reactants, products and transition states are open shell structures. Geometry optimization methods based on the Broyden algorithm were used for calculating local minima [73-74], while transition state structures were obtained using a multiple step procedure. In this approach, an initial transition structure is obtained using the quadratic synchronous transit-guided quasi-Newton method (QSTN) [74, 82]. A frequency analysis is then performed to determine the normal mode of vibration that has the largest imaginary

frequency. In the final step, this normal mode is selected to search for a transition structure using an eigenvector following method. This extensive approach was found to be more robust than the standard search routines available in the Gaussian03 package for identifying transition structures for the open shell systems we investigated. After convergence, a final frequency analysis was performed to confirm that the local minima and transition structures were zero or first order saddle points, respectively [92].

Figure 3-1 shows the Si_9H_{12} one-dimer cluster that was used to model the $\text{Si}(100)\text{-(}2\times 1\text{)}$ surface in these calculations. This cluster model has been widely used to study chemical reactions on $\text{Si}(100)\text{-(}2\times 1\text{)}$ using DFT [10, 93-101], mainly because it is the smallest structure that adequately represents the main structural characteristics of the $\text{Si}(100)\text{-(}2\times 1\text{)}$ surface such as the tilted silicon dimer bond and well-oriented sp^3 covalent bonds. DFT calculations using the one-dimer cluster have been found to accurately predict bond energies and barriers for several reactions on $\text{Si}(100)\text{-(}2\times 1\text{)}$ [10, 99] for which non-local electronic effects [98] are of minor importance. Hydrogen atoms are used to terminate the bonds of the Si cluster (i.e., hydrogen atoms are used as substituents for the bulk silicon atoms that are removed by truncation of Si-Si bonds at the exterior of the cluster). These H atoms preserve the tetrahedral sp^3 bonding environment of subsurface Si atoms, mimic strain that the bulk silicon atoms would impose on the boundary of the cluster, and generally have a negligible effect on the quantum chemistry calculation itself [99, 102]. Geometric constraints are imposed on the hydrogen atoms to improve the simulation of bulk strain effects as follows: All H atoms in place of bulk Si atoms are held fixed in their ideal tetrahedral configurations, while those replacing silicon atoms in neighboring dimers are fixed in positions that mimic the buckled dimer structure [96, 99]. The third and fourth layer Si atoms are not directly constrained, although their

displacements are hindered by the constraints imposed on their neighbors and terminating hydrogen atoms; the fourth layer Si atom is practically held fixed in space due to the limited displacement of the third layer silicon atoms. Finally, all chemically active atoms, which include the silicon dimer atoms, the second layer Si atoms, and the nitrogen and oxygen atoms, are allowed to fully relax during the geometry optimizations.

To reduce the computational expense of the calculations, a mixed basis set was used to expand the electronic wave function. A diffuse triple- ζ plus polarization 6-311++G(2d,p) basis set was used to describe the chemically active atoms while the remaining subsurface silicon atoms and terminating hydrogen atoms are described with a double- ζ plus polarization 6-31G(d) basis set [92]. All the structures investigated have a spin doublet multiplicity and the calculations were done using the Gaussian03 program [71].

3.3 Results

3.3.1 Bonding Configurations of a Nitrogen Atom on Si(100)-(2x1)

We investigated the pathways for nitrogen abstraction from four different configurations of a nitrogen atom bonded on the Si(100)-(2x1) surface to explore the influence of the local surface bonding environment on these reactions. The N-Si(100) structures that we examined were recently predicted by Widjaja *et al.* [98] to be possible equilibrium structures resulting from incorporating a single nitrogen atom into the silicon surface. To benchmark our calculations, we optimized the N-Si(100) structures using the same computational procedure as used by those authors.

The structures and the corresponding energies of formation that we predicted are shown in Figure 3-2, where the zero of energy is taken to be the energy of the nitrogen atom and silicon cluster at infinite separation. Each structure has a spin multiplicity of

two. The lowest energy structure, which has an energy of formation of 2.69 eV, is obtained when the nitrogen atom bonds to a single dimer atom [R(*ad*)]. The remaining structures are the N atom bonded with both dimer atoms in an epoxide-like structure [R(*db*)], the N atom inserted into a Si-Si backbond [R(*bb*)] and finally the N atom bonded with one dimer atom and two second layer Si atoms [R(*sat*)]. The geometrical properties of these structures are in excellent agreement with those reported by Widjaja *et al.* [98], and the energies of structures R(*ad*), R(*db*) and R(*sat*) differ by less than 0.11 eV from their results. However, the energy of formation of structure R(*bb*) is found to be higher by 0.38 eV from the prediction of Widjaja *et al.* The differences in the energies predicted in these studies most likely arise from slight differences in the way geometric constraints are imposed in the calculations. It is noted that the energy of structure R(*bb*) is particularly sensitive to the positions of the terminating hydrogen atoms. Despite this difference, the geometries and trends in the relative energies of the N-Si(100) structures are very close to those reported in the study of Widjaja *et al.* [98]. Finally, each of the structures (Figure 3-2) is predicted to be a local minimum on the doublet N-Si(100) potential energy surface, and the lowest barrier for interconversion between the structures is 0.48 eV [98]. These characteristics suggest that at moderate surface temperature each structure could exist in appreciable concentrations during the initial stages of nitridation.

3.3.2 Nitrogen Abstraction by a Gas-Phase Oxygen Atom

We investigated reactions between species only in their respective electronic ground-states. All of the reactions occur on a doublet potential energy surface and

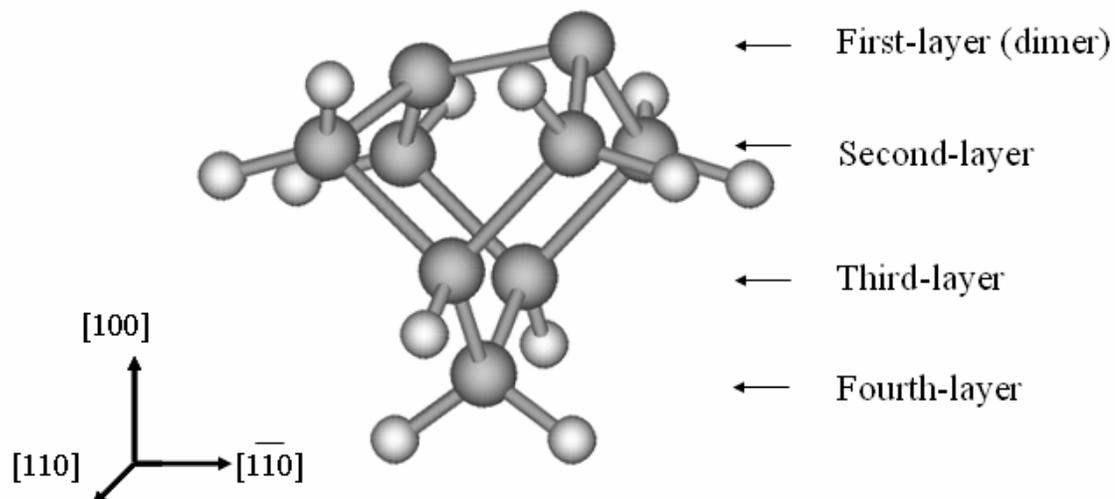
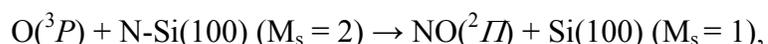


Figure 3-1. The Si_9H_{12} cluster used in our UB3LYP calculations. Si atoms are represented by dark spheres and H atoms are shown as light-colored spheres.

may be represented by the general equation,



where M_s is the initial spin multiplicity of the surface cluster. For each of the N-Si(100) structures investigated, nitrogen abstraction by a gas-phase O-atom was found to be highly exothermic. This conclusion is reached by considering that the bond energy of NO in its doublet ground-state is about 6.5 eV, whereas the energies of formation of the N-Si(100) structures range from about 2.7 to 4.7 eV (Figure 3-2). We initially explored direct pathways for abstraction in which the N-O bond forms and the Si-N bonds break in a single elementary step, as depicted by the reaction equation shown above. Extensive searches revealed a transition structure for only one single-step abstraction process, namely, direct abstraction from the R(*sat*) structure. For structures R(*ad*), R(*db*) and R(*bb*), the abstraction pathways exhibit energy wells between the reactants and products due to the formation and interconversion of adsorbed NO species. These molecular precursor structures are produced when the $\text{O}({}^3P)$ atom attaches directly to a nitrogen dangling bond, yielding an NO species that is bound to the surface.

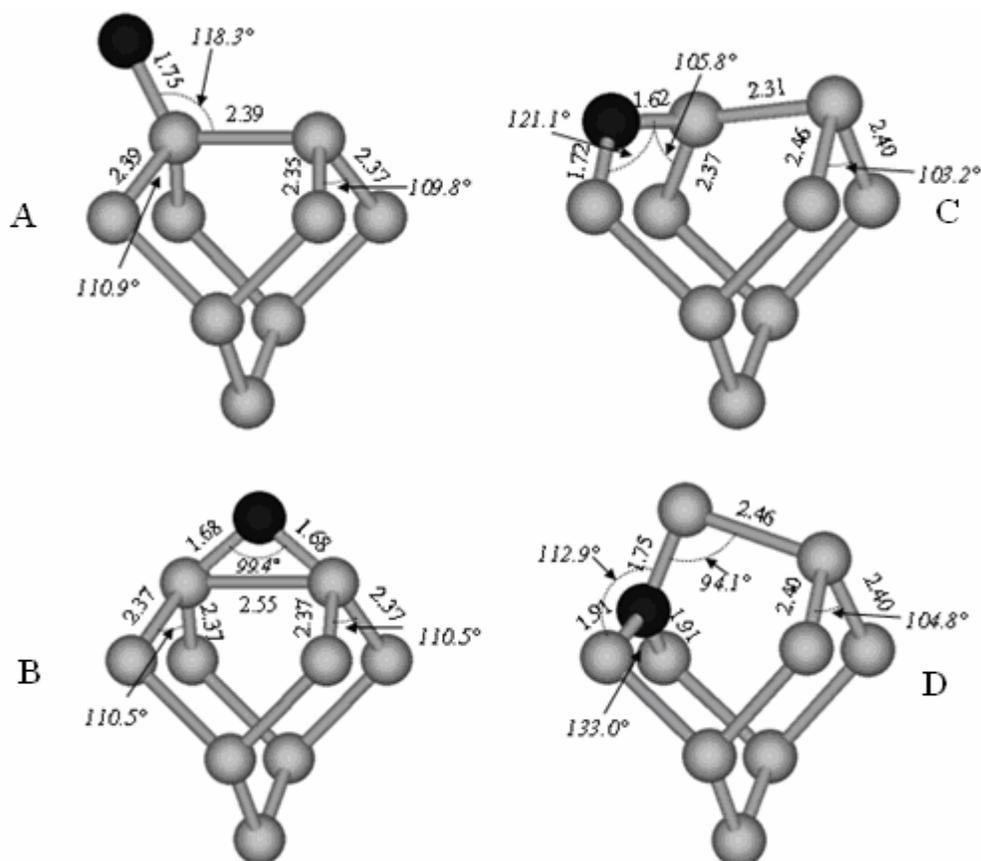


Figure 3-2. Structural information of N-Si₉H₁₂ clusters. A) R(*ad*). B) R(*db*). C) R(*bb*). D) R(*sat*). All distances are in Å. Terminating hydrogen atoms have been excluded for clarity. Si atoms are shown as light-colored spheres and N atoms as darker spheres.

3.3.3 Abstraction of N Adsorbed at the Dangling Bond [R(*ad*)]

Figure 3-3 shows the predicted pathway by which an oxygen atom abstracts a nitrogen atom that is adsorbed on a single Si atom of the surface dimer [R(*ad*)]. The reaction involves the initial formation of molecular precursor MP(*ad*) (Figure 3-4B), which then decomposes to produce a gaseous NO molecule and the bare Si cluster, structure P (Figure 3-4C). The production of MP(*ad*) is highly exothermic (4.84 eV), since this reaction involves the formation of a strong N-O double bond without cleavage of other bonds in the cluster. The subsequent decomposition of MP(*ad*) via the formation of a gaseous NO molecule is endothermic by 0.91 eV. A transition structure could not be

found along the path from structure $MP(ad)$ to P so only the thermochemical barrier must be overcome in this step. Although the molecular precursor lies at a lower energy than the abstraction product, a minimum of 3.93 eV of energy would need to be dissipated to the solid for the molecular precursor to stabilize. Moreover, since the NO species couples to the solid mainly through the Si-N bond, it is likely that the Si-N bond

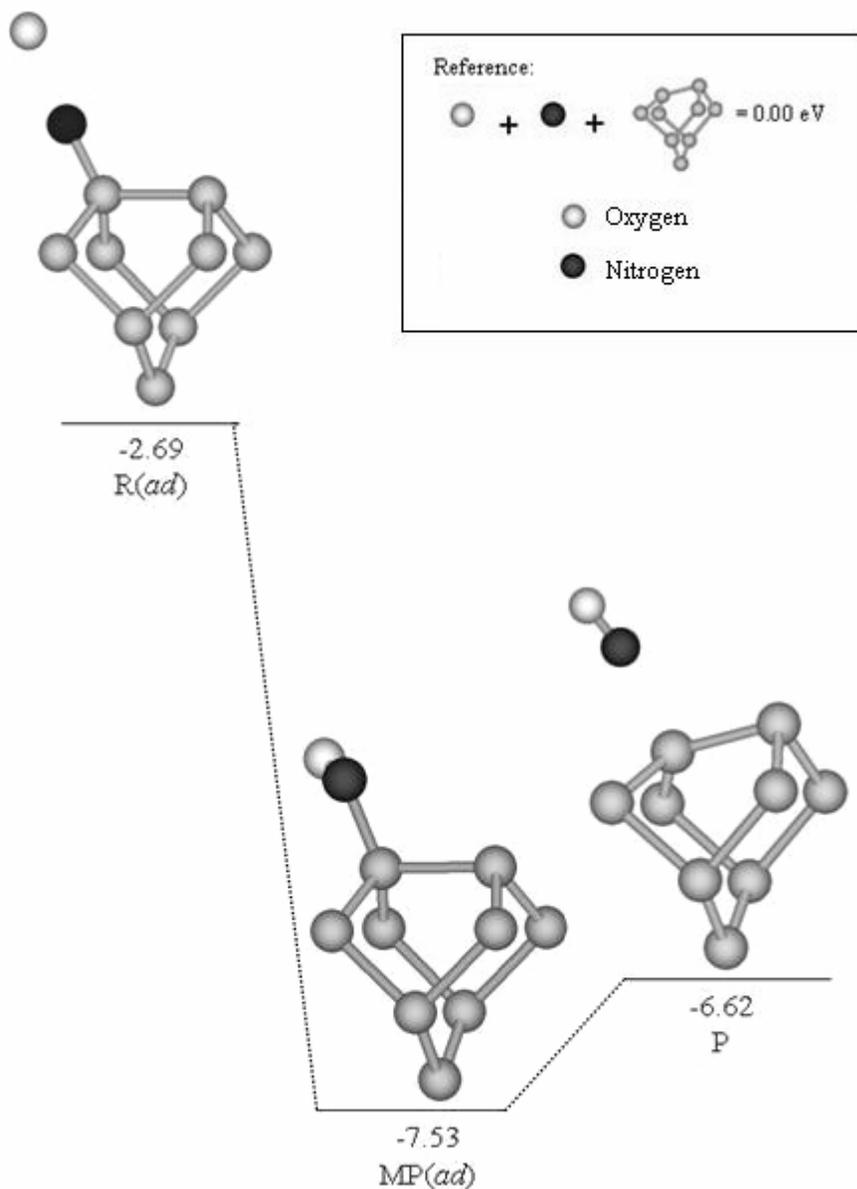


Figure 3-3. Reaction pathway for the nitrogen abstraction from $R(ad)$. Energies are in units of eV and the zero of energy is taken to be the ground-state nitrogen atom, the $O(^3P)$ atom and the singlet Si cluster at infinite separation.

will become highly excited and break during N-O bond formation since only 0.91 eV are needed to detach the NO molecule from the structure. This result therefore suggests that nitrogen abstraction from structure R(*ad*) will be highly facile, occurring effectively in a single atom-surface collision.

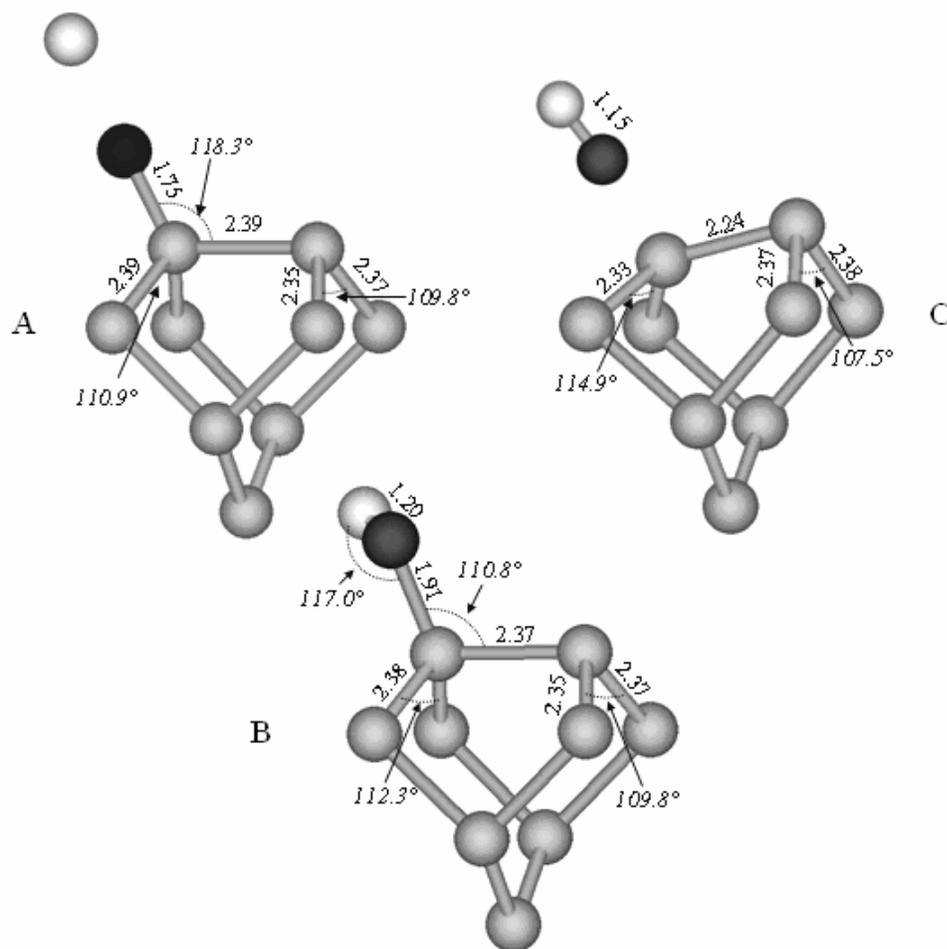


Figure 3-4. Critical point structures of the nitrogen abstraction from R(*ad*). A) R(*ad*) B) MP(*ad*). C) P (final product). All distances are in Å and the terminating hydrogen atoms have been excluded for clarity.

The geometric and electronic changes that occur during the reaction shown in Figure 3-3 provide additional insights for understanding this reaction. In reactant R(*ad*), two unpaired alpha electrons are localized on the N atom, and one beta electron resides mainly on the triply coordinated Si atom of the surface dimer. Since the O(³*P*) atom also

has two unpaired electrons, its interaction with the adsorbed N atom results in the highly exothermic formation of an NO double bond. The N-O bond in structure MP(*ad*) is close in length to that of the N-O bond of an isolated NO molecule (1.20 vs. 1.15 Å, respectively, Figure 3-4). The predominant change in the relative positions of the Si and N atoms that occurs during the first reaction step is elongation of the Si-N bond from 1.75 to 1.91 Å, which indicates a weakening of the Si-N bond when the N-O double bond of MP(*ad*) is formed. In the final reaction step, the molecular precursor decomposes by cleavage of the Si-N bond, with one electron transferring to a π^* orbital of the NO molecule and the other remaining at the surface. This remaining electron experiences a weak π -interaction with the initially unpaired electron on the opposing dimer atom since the bare Si surface in these calculations is taken to be the singlet, buckled dimer structure that is thought by many to be the ground-state of the Si(100)-(2x1) surface [103-104].

3.3.4 Abstraction of the Nitrogen Bonded Across the Dimer [R(*db*)]

Shown in Figure 3-5 is the pathway predicted for the abstraction of a nitrogen atom bonded across the surface dimer [R(*db*), Figure 3-6(A)]. The first step in this pathway is N-O bond formation, resulting in structure MP(*db*). The exothermicity of this reaction is 3 eV, which is quite significant but is still lower by 1.84 eV than N-O bond formation in the analogous reaction R(*ab*) \rightarrow MP(*ab*) (Figure 3-3). Formation of structure MP(*db*) is followed by NO migration from the bridging site to the dangling bond site from which NO desorbs. The migration path is predicted to have an energy barrier of 0.48 eV, and the final desorption step presents a thermochemical barrier of 0.91 eV as discussed. Each of these barriers is significantly less than the energy released in the initial formation of the N-O bond. Thus, unless energy is efficiently dissipated away from the initial collision zone, NO desorption can occur rapidly by this pathway as well.

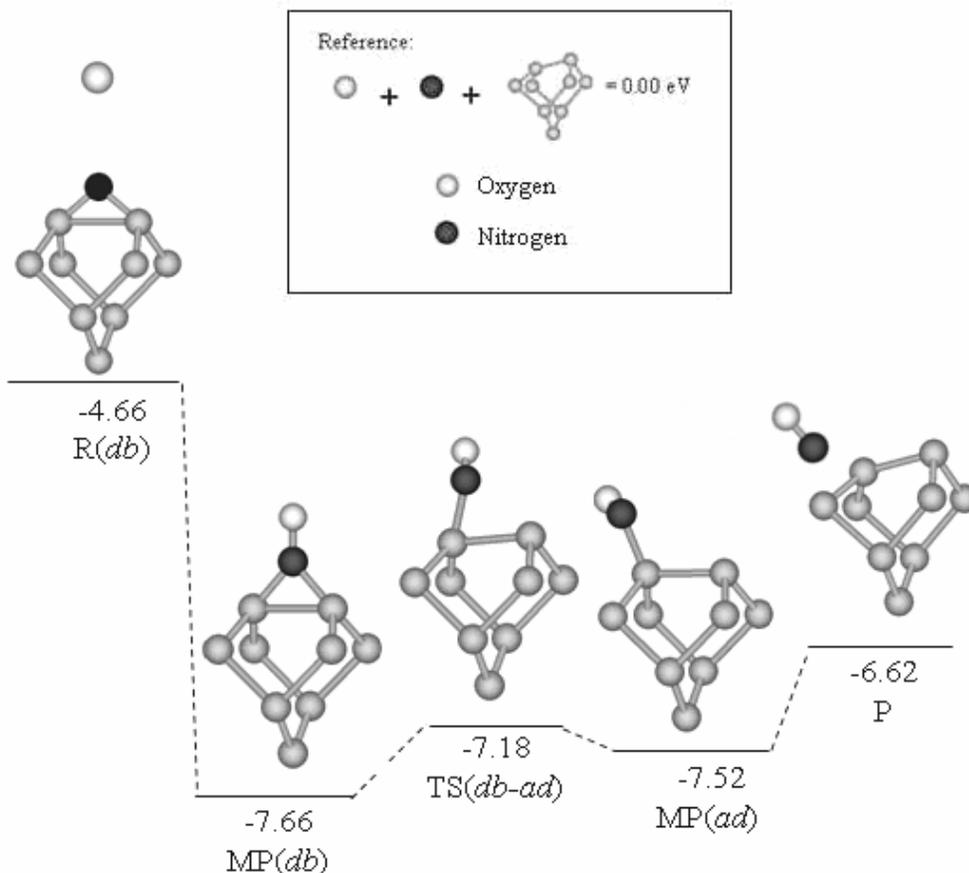


Figure 3-5. Reaction pathway of nitrogen abstraction from R(*db*). Energies expressed are in eV.

The geometric changes that the cluster undergoes during these reactions steps are illustrated in Figure 3-6. N-O bond formation to produce MP(*db*) causes each Si-N bond to stretch from 1.68 to 1.80 Å, and the Si-Si dimer bond to contract from 2.55 to 2.37 Å, which is indicative of weaker Si-N bonds and a stronger Si dimer bond. Also, the N-O bond in MP(*db*) is longer than that in MP(*ad*) (1.27 vs. 1.20 Å), suggesting a weaker N-O bond in the former. These changes may be understood by considering the corresponding changes in the alpha spin densities on the surface atoms. In the initial reactant R(*db*), an unpaired electron is distributed mainly between the Si atoms of the epoxide-like ring. The alpha spin density on these Si atoms decreases to zero upon formation of molecular precursor MP(*db*), and an unpaired electron is distributed almost evenly between the N

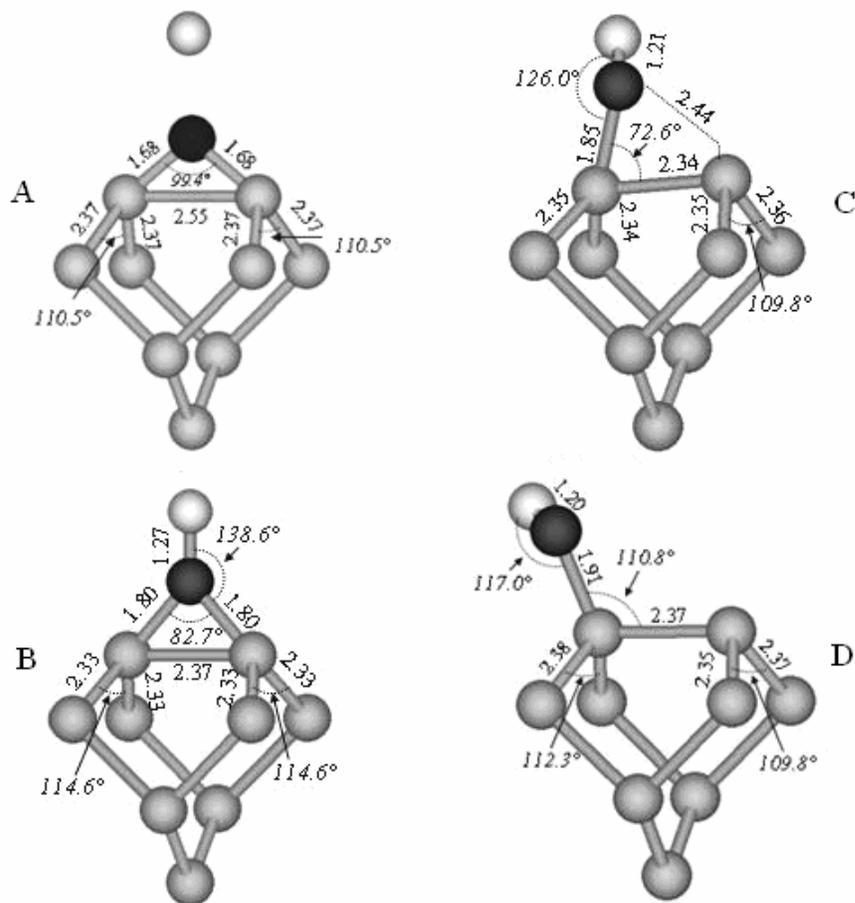


Figure 3-6. Critical point structures of the nitrogen abstraction from $R(db)$. Structural information and relative energy. A) $R(db)$. B) $MP(db)$. C) $TS(db-ad)$. D) $MP(ad)$. All distances are in Å. The terminating hydrogen atoms were excluded for clarity. The final product is shown in Figure 3-4(C).

and O atoms in the $MP(db)$ structure. These changes indicate that NO bond formation leading to $MP(db)$ involves a pairing between the lone electron on the reactant $R(db)$ and an unpaired electron on the incident $O(^3P)$ atom. The second lone electron on the $O(^3P)$ atom is transferred to a π^* -like orbital between the N and O atoms. The resulting N-O bond effectively has a bond order of 1.5 and is therefore weaker and longer than the NO double bond of $MP(ad)$.

The migration of the NO species from the bridging to the dangling bond position is activated by 0.48 eV, since it involves the simultaneous cleavage of a Si-N bond and the

formation of an NO double bond. In this reaction, an electron from the initial Si-N bond is transferred to the NO species to form the double bond, while the second electron remains localized on the Si atom. The transition structure TS(*db-ad*) for this reaction is shown in Figure 3-6(C). To reach TS(*db-ad*) from MP(*db*), the NO species tilts away from one of the Si dimer atoms, causing the Si-N bond to stretch to 2.44 Å. At TS(*db-ad*), the NO bond contracted to 1.21 Å, and the remaining Si-N bond is elongated from 1.68 to 1.85 Å. On the path from TS(*db-ad*) to MP(*ad*), the structure adopts a more stable configuration as the NO species tilts farther away from the opposing Si dimer atom, and the N-O bond contracts to its final value of 1.20 Å.

3.3.5 Abstraction of the Nitrogen Bonded at a Backbond [R(*bb*)]

We found two pathways for nitrogen abstraction from the backbonded position [structure R(*bb*)] (Figure 3-7). For each path, the oxygen atom is predicted to first bond directly with the nitrogen atom of structure R(*bb*) to generate molecular precursor MP(*bbs*) (Figure 3-8B) in which the N-O bond is nearly parallel to the bisector of the Si-N-Si bond angle. In one pathway, the O atom tilts toward the Si atom to form an Si-O bond resulting in structure MP(*bbt*) which can then decompose by sequential N-Si bond cleavage, forming MP(*ad*) and then a gaseous NO molecule. The alternative pathway involves direct N-Si bond cleavage, causing the symmetric structure MP(*bbs*) to convert directly to MP(*ad*) from which the NO molecule detaches (Figure 3-7, inset). The reaction to produce MP(*bbs*) from the nitrogen backbonded structure is exothermic by 2.68 eV, and only a small energy barrier of 0.03 eV must be overcome for MP(*bbs*) to transform into the more stable molecular precursor MP(*bbt*). An energy barrier of 0.38 eV must be overcome for MP(*bbt*) to transform to MP(*ad*), while a barrier of 0.55 eV is predicted for the direct conversion of MP(*bbs*) to the MP(*ad*) structure. The

overall reaction is exothermic by 2.25 eV, and the energy released during the initial N-O bond formation is much greater than the barriers that must be surmounted for the NO molecule to desorb from the cluster.

The general bonding characteristics of the MP(*bbs*) structure (Figure 3-8B) are similar to those of the MP(*db*) structure (Figure 3-6B) discussed above. In particular, formation of the N-O bond in MP(*bbs*) involves a pairing between lone electrons on the N and O atoms, with the second lone electron of the O atom transferring to a π^* -like orbital localized along the N-O bond. Despite these similarities, however, structure MP(*bbs*) is less energetically favorable than MP(*db*) by 0.61 eV. A comparison of the structures (Figures 3-6B and 3-8B) suggests that MP(*bbs*) is more strained since its formation is accompanied by an increase of the Si-N-Si bond angle and elongation of the Si-N bonds. The N-O bond in MP(*bbs*) is also longer than in MP(*db*), which suggests that additional strain would be imposed if the N-O bond were to achieve its optimum length.

One of the pathways for N abstraction involves the conversion of structure MP(*bbs*) to MP(*bbt*) (Figure 3-8D), which is exothermic by 0.25 eV and presents a barrier of only 0.03 eV (Figure 3-7). Although the energy barrier is quite small for this reaction, vibrational analysis indicates that structures MP(*bbs*) and TS(*bbs-bbt*) do correspond to zero and first order saddle points, respectively. The exothermicity for this reaction step is also relatively small mainly because unfavorable structural changes offset the energy gained in forming the strong Si-O bond.

The predominant structural changes include stretching of the N-O bond from 1.32 to 1.51 Å and an increase of the Si-N-Si bond angle from 132.6° to 164.5°. Elongation of the N-O bond indicates a weakening of this bond, and the substantial increase in the

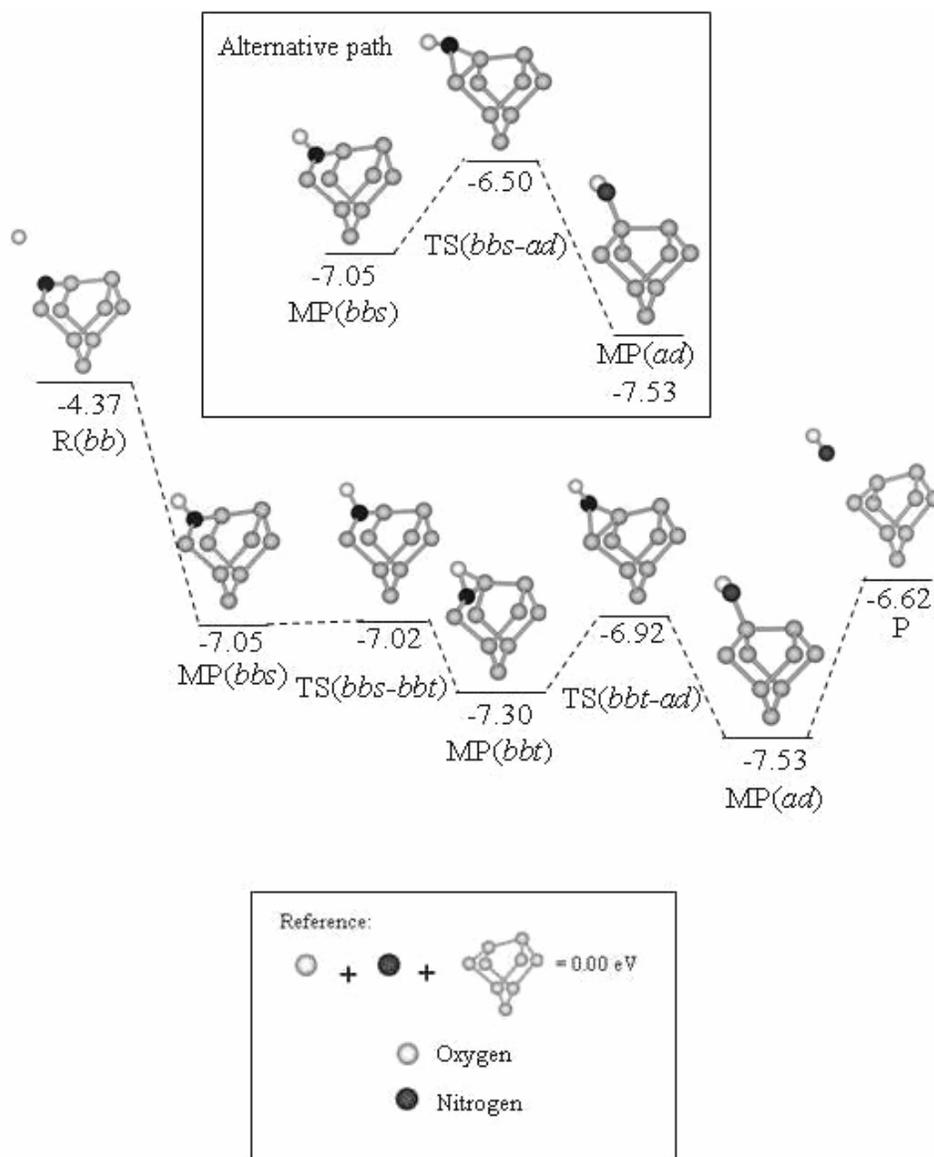


Figure 3-7. Reaction pathways for the abstraction of the nitrogen atom inserted in a Si-Si backbond. Main panel: $O + R(bb) \rightarrow MP(bbs) \rightarrow TS(bbs-bbt) \rightarrow MP(bbt) \rightarrow TS(bbt-ad) \rightarrow MP(ad) \rightarrow P$. Top inset: $O + R(bb) \rightarrow MP(bbs) \rightarrow TS(bbs-ad) \rightarrow MP(ad) \rightarrow P$. Energies are in units of eV.

Si-N-Si bond angle imparts strain on the Si-Si bonds in underlying layers. Energy is also required for this reaction because an electron must be removed from a π -like bond along the Si surface dimer for the Si-O bond to form. The remaining steps in this abstraction pathway include migration of the NO species of structure MP(bbt) to the dangling bond position, and then NO desorption from MP(ad). The migration reaction $MP(bbt) \rightarrow$

MP(*ad*) is exothermic by 0.23 eV and has an energy barrier of 0.38 eV (Figure 3-7). The geometry of the transition structure TS(*bbt-ad*) (Figure 3-9B) reveals that the NO species tilts away from the Si dimer atom, causing the Si-O bond to break and the N-O bond to strengthen and contract early along the reaction path. Concurrently, the Si-N-Si bond angle decreases to allow the Si-Si backbond to begin forming and the lower Si-N bond to break. Formation of the Si-Si backbond and the N-O bond is completed on the MP(*ad*) side of the barrier.

In the second abstraction pathway for N(*bb*), the symmetric MP(*bbs*) structure converts directly to MP(*ad*) by the path shown in the inset of Figure 3-7. This reaction step is exothermic by 0.48 eV and has an energy barrier of 0.55 eV. The corresponding transition structure TS(*bbs-ad*) for this path is shown in Figure 3-10(B). The bond

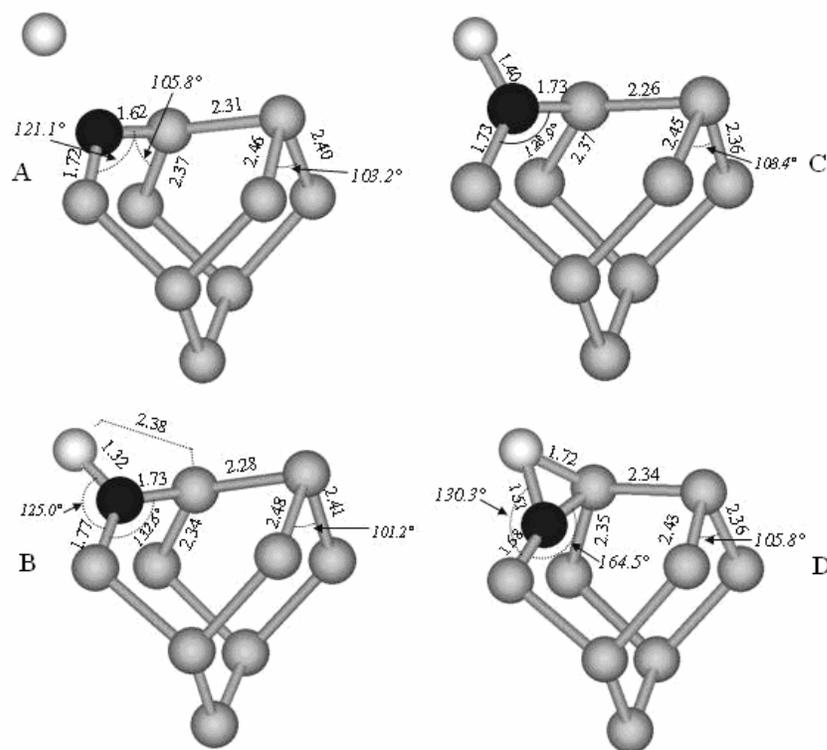


Figure 3-8. Molecular precursors formed after O-chemisorption onto R(*bb*). Structural information of the structures involved in the reaction pathway. A) R(*bb*). B) MP(*bbs*). C) TS(*bbs-bbt*). D) MP(*bbt*). All distances are in Å. The terminating hydrogen atoms were excluded for clarity.

lengths in TS(*bbs-ad*) are nearly identical to those in TS(*bbt-ad*) (Figure 3-9B), which is not surprising since the reactions that proceed through these transition states have a common product. Nevertheless, the energies of these transition structures, referenced to the same initial state, differ by 0.42 eV. The most striking structural difference is that in TS(*bbt-ad*) the NO bond is nearly parallel with the plane defined by the Si-N-Si ring, whereas the NO bond is significantly tilted out of this plane in TS(*bbs-ad*). This suggests that overlap of the π -like orbitals in the NO species with those in the Si-N-Si ring is enhanced in the planar configuration of TS(*bbt-ad*), thereby lowering the energy of the structure relative to that of TS(*bbs-ad*).

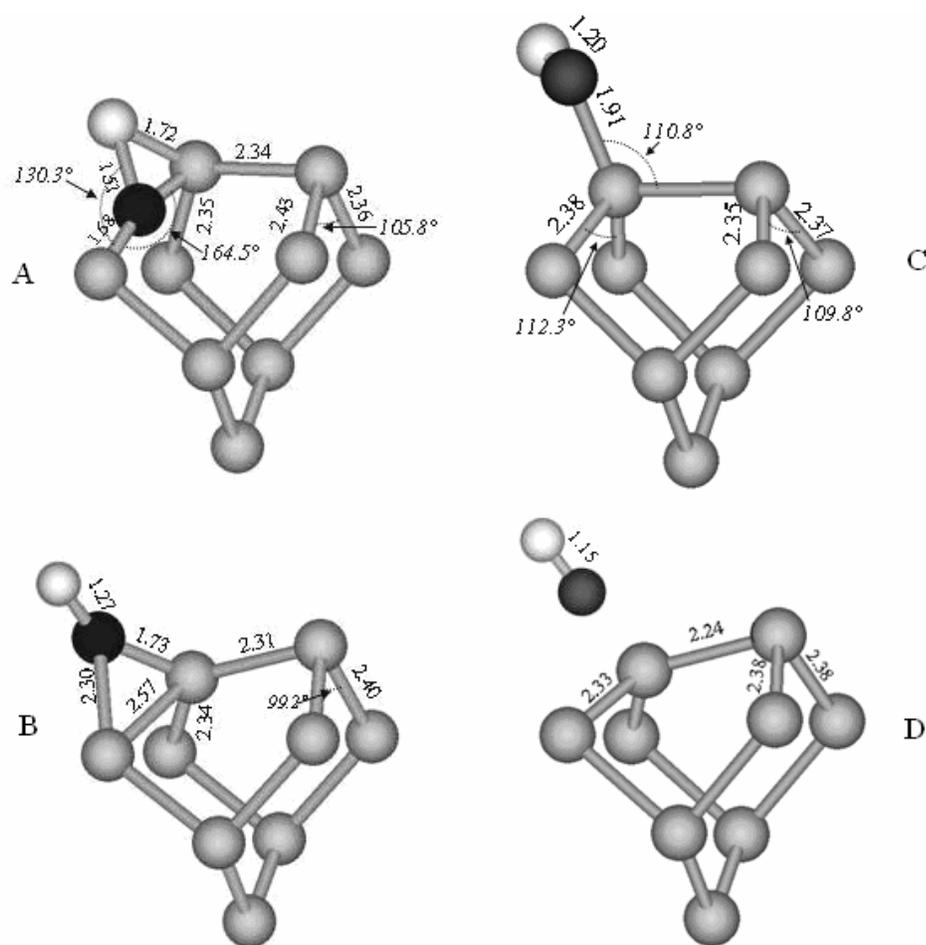


Figure 3-9. Structures formed during nitrogen abstraction from MP(*bbt*). A) MP(*bbt*). B) TS(*bbt-ad*). C) MP(*ad*). D) P. All distances are in Å.

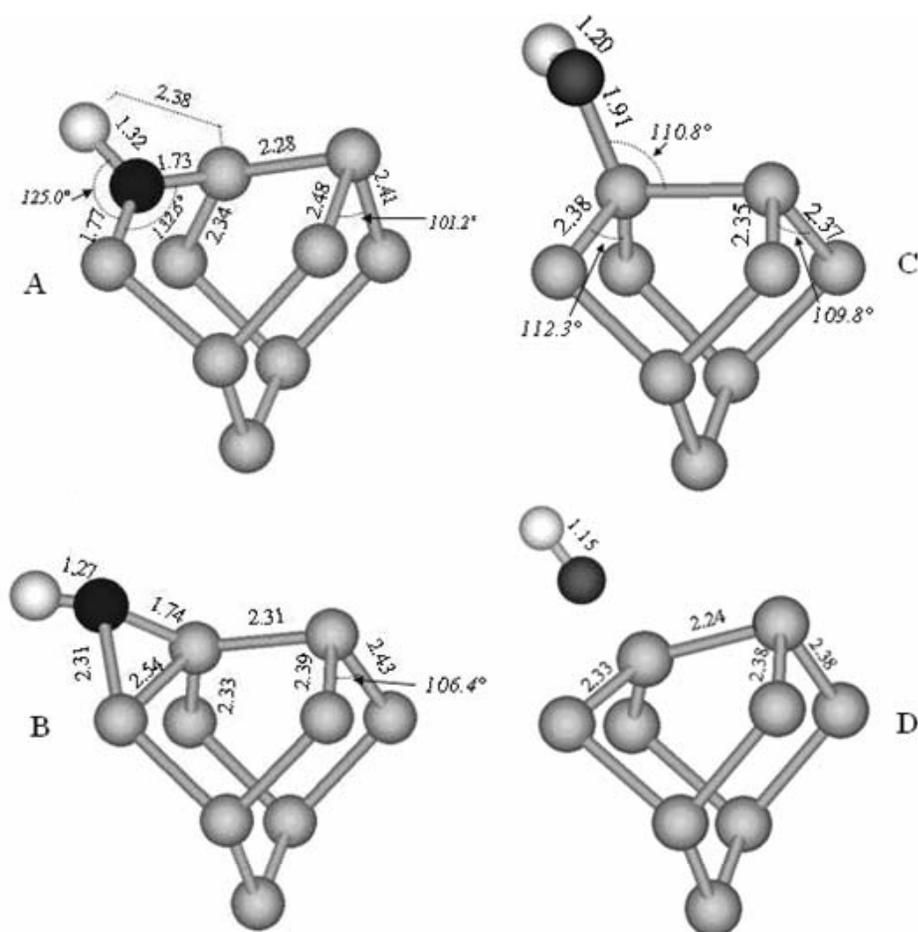


Figure 3-10. Structures involved in the nitrogen abstraction from MP(*bbs*). A) MP(*bbs*). B) TS(*bbs-ad*). C) MP(*ad*). D) P. All distances are in Å

3.3.6 Abstraction from the $\text{N}\equiv\text{Si}_3$ Structure [R(*sat*)]

Figure 3-11 shows two possible pathways for N abstraction from the $\text{N}\equiv\text{Si}_3$ structure [R(*sat*), Figure 3-12(A)] by an incoming $\text{O}({}^3P)$ atom, and one pathway for the adsorption of the O atom at a Si dangling bond site. The first abstraction pathway is a direct process wherein the incident O atom removes the N atom from the surface in a single step. This reaction is the only single-step abstraction process that was identified in the study. Direct N abstraction from the $\text{N}\equiv\text{Si}_3$ structure is predicted to be exothermic by 2.57 eV and presents a relatively small energy barrier of 0.20 eV. The N-O separation at the transition structure is 1.23 Å (TS(*sat-P*)) (Figure 3-12B), which is only 0.12 Å longer

than the NO bond of the isolated NO molecule. In addition, each second-layer Si-N bond has broken and two Si-Si backbonds have formed on the path to the transition structure. This indicates that direct abstraction from $\text{N}\equiv\text{Si}_3$ is a concerted process in which three Si-N bonds break while two Si-Si backbonds and a N-O bond simultaneously form during a single gas-surface collision. This reaction would require the upper Si dimer atom to move toward the second layer Si atoms by a considerable distance, and the N atom to simultaneously move out of the plane defined by these three Si atoms as the O atom approaches the cluster and the N-O bond begins to form. The other possible pathway for N abstraction from the $\text{N}\equiv\text{Si}_3$ structure is also a concerted process in which the interaction of the O-atom with the cluster produces molecular precursor $\text{MP}(bbs)$ (Figure 3-8B), which then decomposes by the pathways shown in Figure 3-7. However, neither an intermediate structure nor a transition structure could be found for the reaction $\text{O}(^3P) + \text{R}(sat) \rightarrow \text{MP}(bbs)$. Thus, for this reaction to occur, an N-O bond and a Si-Si backbond must form, and a Si-N bond must break during a single collision of the O-atom with the cluster.

Although neither of these abstraction pathways is energetically prohibitive, they each involve the formation and scission of multiple bonds in a single gas-surface collision. Moreover, these reactions require that the O-atom come in close proximity to the dangling bond of the Si dimer atom where it could adsorb. Indeed, adsorption of the O-atom at the dangling bond site (Figure 3-11) is predicted to be barrierless and highly exothermic (6.35 eV), and is therefore concluded that to be the predominant outcome of the interaction between an $\text{O}(^3P)$ atom and the $\text{N}\equiv\text{Si}_3$ structure. As may be seen in Figure 3-12, adsorption of an $\text{O}(^3P)$ atom at the Si dangling bond causes the local $\text{N}\equiv\text{Si}_3$ configuration to change negligibly, but it does result in contraction of the Si-Si dimer

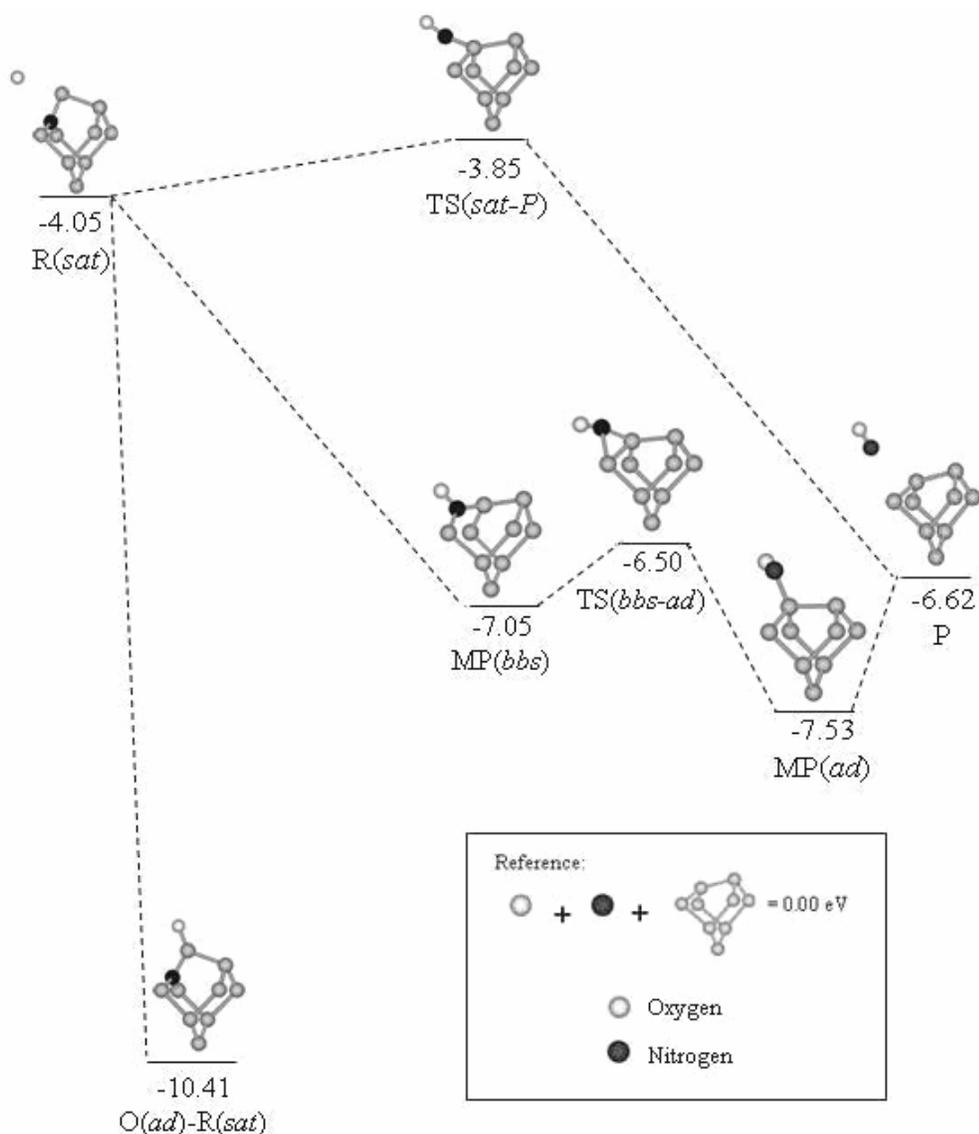


Figure 3-11. Reaction pathways for N-abstraction from (and O-atom adsorption on) $R(sat)$. Energies are in units of eV and the zero of energy is taken to be the ground-state nitrogen atom, the $O(^3P)$ atom and the singlet Si cluster at infinite separation.

bond. This contraction indicates that O-Si formation alleviates repulsive interactions between the two unpaired electrons that are present on the silicon dimer atoms of the $N\equiv Si_3$ structure. In fact, we find that the energy of O-atom adsorption at the Si dangling bond site of $R(sat)$ is 1.9 eV higher than that for O-adsorption on the clean Si(100)-(2x1) surface. This indicates that significant electronic repulsion exists along the dimer of the $R(sat)$ structure, and that O-atom adsorption is highly favorable on this surface.

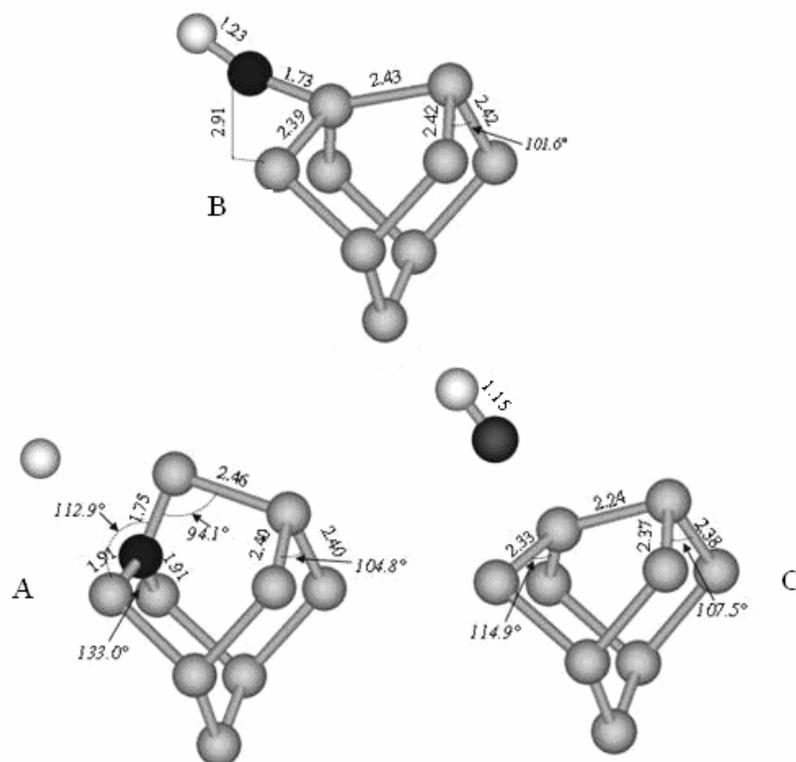


Figure 3-12. Structures formed during the direct nitrogen abstraction from R(*sat*). A) O(³P) attacks the nitrogen atom of R(*sat*). B) Transition structure [TS(*sat*-P)]. C) NO molecule desorbed into the gas phase and bare Si surface (P). All distances are in Å. The terminating hydrogen atoms were excluded for clarity.

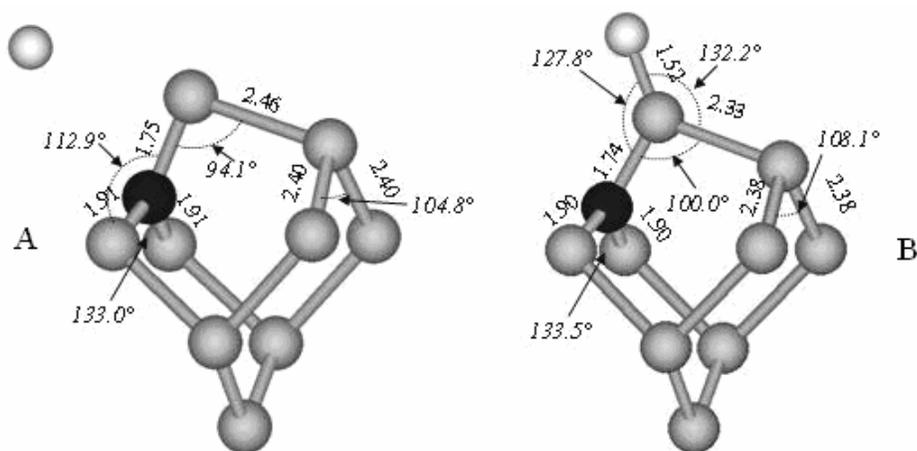


Figure 3-13. Structures involved in the O-atom chemisorption on R(*sat*). Structural information and relative energy. A) O(³P) atom approaching structure R(*sat*) and B) O-atom adsorbed at the Si dangling bond site [O(*ad*)-R(*sat*)] All distances are in Å. The terminating hydrogen atoms were excluded for clarity.

3.4 Discussion

Nitrogen abstraction by a gas-phase $O(^3P)$ atom is highly exothermic for each of the N-Si(100) structures investigated in this study. However, abstraction is predicted to occur in a single step only for the reaction of $O(^3P)$ with the coordinatively saturated N-atom of the $N\equiv Si_3$ structure, and (in this case) single-step abstraction appears to be much less probable than O adsorption due to the energetic differences in these reactions and because multiple bonds must break and form for single-step abstraction to occur. For each of the coordinatively unsaturated N-Si(100) structures, N abstraction is predicted to occur by a precursor-mediated pathway that is initiated by the formation of an N-O bond and the release of between 2.7 and 4.8 eV into the surface. Since the subsequent elementary steps leading to NO desorption have barriers that are less than 1.0 eV, NO bond formation provides the system with excess energy that could readily promote local bond rearrangements and ultimately NO desorption. Indeed, nitrogen abstraction by such a pathway would effectively be an Eley-Rideal process since the NO product would evolve into the gas-phase within no more than a few vibrational periods after the initial gas-surface collision. Alternatively, the energy released during NO bond formation could be dissipated away from the surface bonds, allowing the adsorbed NO species to equilibrate in one of the configurations predicted. However, considering the significant amount of energy (~ 2 to 4 eV) that would need to be channeled away from the initial collision zone for a precursor to stabilize, it is reasonable to expect NO desorption to be the more likely outcome of initial N-O bond formation in these systems. Nevertheless, calculations of the dynamics for abstraction, and particularly the efficiency of energy dissipation to the solid, are needed to explore the propensity for $O(^3P)$ atoms to abstract nitrogen from Si(100) by the pathways predicted here.

Prior experimental studies have provided indirect evidence for nitrogen abstraction from Si surfaces by gaseous atomic oxygen. For example, exposure of Si(100) to plasmas containing both O and N atoms results in a surface that is depleted of nitrogen [87, 88, 105]. Similarly, treating nitrated Si(100) with an oxygen plasma has been reported to lower the surface nitrogen concentration [89, 106]. We recently conducted reactive scattering experiments in UHV to directly examine the abstraction of nitrogen from Si(100) by an atomic oxygen beam, but we did not observe the evolution of gaseous NO using mass spectrometry or nitrogen depletion from the surface [107]. However, the absence of measurable nitrogen abstraction in our experiments can be attributed to the bonding state of nitrogen that was investigated. In that work, nitrogen was incorporated into Si(100) by thermally decomposing NH_3 on the surface at a substrate temperature of 900 K; adsorption at this high surface temperature is necessary to ensure the complete desorption of hydrogen. Above about 700 K, however, nitrogen has been found to diffuse into the subsurface region of Si(100) [108] and is apparently inaccessible for direct abstraction by gaseous O-atoms. Our experimental observations therefore suggest that the N-Si(100) structures considered in the present computational study are not stable at temperatures greater than about 700 K. In fact, recent quantum chemical investigations predict that a single nitrogen atom does have an energetic preference to bond in the subsurface of Si(100) [109-110].

Nevertheless, the N-Si(100) structures investigated in the present study, which were reported originally by Widjaja *et al.* [98], may be stable at surface temperatures lower than 700 K since, to our knowledge, barriers for the migration of nitrogen into the Si(100) subsurface have not been reported, and may be high enough to enable nitrogen atoms to stabilize at the surface at low to moderate temperatures. Hence, nitrogen

abstraction by gaseous O-atoms may indeed occur during plasma-enhanced oxynitridation of Si(100) if the surface temperature is maintained sufficiently low. Another possibility is that the barriers for nitrogen diffusion to the subsurface are small, which would imply that the N-Si(100) structures that we investigated in this computational study (Figure 3-2) do not exist in appreciable concentrations at low to moderate surface temperature. In this case, a mechanism other than direct abstraction by gaseous oxygen atoms would be needed to explain observations of nitrogen depletion at the Si(100) surface by reaction with oxygen plasmas. Experiments to directly investigate nitrogen abstraction by atomic oxygen will require a method for adsorbing N atoms onto Si(100) at low surface temperature, which should be possible using an active nitrogen source such as gaseous N-atoms or through non-thermal activation of nitrogen-containing adsorbates.

CHAPTER 4
CHEMISTRY ON Si(100)-(2x1) DURING EARLY STAGES OF OXIDATION WITH
O(³P)

4.1 Introduction

Oxygen adsorption on Si(100)-(2x1) is an important process because it corresponds to the initial stages of the formation of the Si/SiO₂ interface, a system of high technological relevance in microelectronic devices, especially in the metal-oxide-semiconductor field-effect transistor (MOSFET) gate dielectrics. Because of the demands imposed by Moore's law, the thickness of the silicon dioxide gate dielectrics grown on Si(100) is crucial for the future of the microelectronic industry. As these layers approach the sub nanometer region (it is now possible to fabricate devices with SiO₂ gate thickness of 1.3 nm [34], which correspond to about ten silicon atoms across the Si/SiO₂ interface) it is important to understand the detailed mechanism of initial oxidation of silicon surfaces. This small thickness is a limit for the use of SiO₂ gate dielectrics given that the concentration of undesirable silicon suboxides (Si⁺, Si²⁺ and Si³⁺) in the Si/SiO₂ interface becomes increasingly greater. Because of this, aggressive research for alternative gate dielectric materials is taking place, but even for these new gate high- κ dielectric materials, knowledge of the initial steps of SiO₂ formation is critical given that many of them still involve one or two monolayers of SiO₂ deposited over the gate channel region.

Several methods to fabricate silicon dioxide have been used successfully over the year [33-34]. However, because of the continuous scaling of the devices, these

traditional methods are becoming increasingly less efficient. Furthermore, as the size of the silicon dioxide layers approach molecular and atomic dimensions, it would be ideal to have a fabrication method based on molecular chemistry and low temperature, so the product obtained by the manufacturing process remains in a given configuration and is not affected by thermal changes of the system. One of these methods is plasma processing of silicon substrates. The interactions of radical species such as oxygen atoms, which can be present in large fractions in plasma environment, with silicon surfaces are relatively poorly understood. Engel and coworkers [26-31] reported detailed kinetics studies of the O atom oxidation of clean silicon using a plasma-based atomic beam source. Also, Yasuda *et al.* [111] studied the O atom oxidation of hydrogen-terminated silicon using a hot-filament source. These studies revealed that O atom oxidation is favorable compared with that due to O₂, and that several monolayers of oxide can be formed efficiently via the direct insertion of O atoms into near-surface bonds.

We explore the structures formed during the initial steps of O(³P) incorporation on clean Si(100)-(2x1) using small Si₉H₁₂ cluster models and gradient-corrected density functional theory (DFT). From the time when early studies of asymmetric dimer descriptions [112] and initial adsorption of hydrogen on Si(100) [94] were made, the Si₉H₁₂ cluster has been proven a very useful tool for performing theoretical studies of local chemistry on Si(100)-(2x1). Recent comprehensive oxidation studies which combine Si₉H₁₂ clusters with gradient-corrected density functional theory (DFT) techniques yielded accurate energetics and vibrational frequencies for several oxidation products, although none of them has treated oxidation by O(³P) specifically. Most of previous work has focused on the water-induced oxidation of the clean Si(100)-(2x1)

surface [34, 95, 96, 104, 113, 114], and some on oxidation by molecular oxygen [100]. What has been found so far using the DFT/cluster approach can be summarized as follows: Initially, water adsorbs dissociatively on top of single silicon dimer and forms H and OH fragments which are most stable when they are bonded with the hydroxyl oriented away from the surface dimer bond [95, 104]. Thermodynamic [96] and mechanistic studies [113–114] revealed a strong tendency for O to agglomerate on the dimers of Si(100) and predicted that the three- and five-oxygen agglomerated structures were the most stable. Formation of epoxide-like rings upon dehydrogenation of the surface in the event of oxygen agglomeration was also reported. This tendency for O to agglomerate was found to be thermodynamically driven since it is energetically more favorable to have one dimer with n oxygens, for $n=2-5$, and $(n-1)$ oxygen-free dimers, than it is to have n dimers each with one oxygen.

In this work, we performed DFT/cluster calculations to determine minimum energy geometries to elucidate the relative thermodynamic energies of the possible oxidation products that can form by insertion of up to three $O(^3P)$ atoms, and we use this result to predict a minimum energy reaction path. These oxidized Si_9H_{12} clusters were classified in three different sets of isomers ($O_1-Si_9H_{12}$, $O_2-Si_9H_{12}$ or $O_3-Si_9H_{12}$) depending on the number of oxygen atoms adsorbed on the surface. The energy of these isomers was then compared to one another to determine how it was affected by the formation of the two Si–O bonds in place of one Si–Si bond, by the oxidation state of the surface silicon atoms, by the spin-state of the surface (spin-singlet vs. spin-triplet) and by strain effects (all quantified by using a bond energy model that assumes that they are independent and additive). Finally, we investigated transition states for the insertion process, to develop a model for the preferred mechanism of the initial steps of Si(100) oxidation by $O(^3P)$.

4.2 Theoretical Approach

Our theoretical approach was based on Kohn-Sham density functional theory (DFT) calculations of clusters of silicon that represent the local bonding arrangement of the surface. The silicon cluster used was the Si_9H_{12} (Figure 3-1) which is the smallest structure that appropriately represents the main structural characteristics of the Si(100)-(2x1) surface (i.e., covalent tetrahedral sp^3 arrangement of Si-Si bonds and a tilted dimer). This cluster has twelve H atoms to terminate all dangling bonds resulting from truncation of Si-Si bonds at the exterior of the cluster; these terminating hydrogen atoms preserve the tetrahedral bonding and have a negligible effect on the predicted energies of the different clusters [102, 115]. The clusters were constrained by imposing boundary conditions that mimic the strain that the bulk silicon would impose on the surface dimer under study. In particular, the hydrogen atoms were fixed in their positions along the directions of truncated Si-Si bonds that they terminate. Two types of hydrogen atoms can be found in this cluster. The bulk hydrogen atoms, fixed along tetrahedral directions, and the neighboring dimer hydrogen atoms, constrained in positions that mimic nearest silicon dimers. The third and fourth layer silicon atoms were not directly constrained, but the displacement of these atoms is minimal because they are surrounded by fixed H atoms. All the chemically active atoms including the first and second layer silicon atoms were allowed to relax completely unconstrained.

Kohn-Sham density functional theory [41-44] is used for the electronic structures calculations. Specifically, we use the B3LYP hybrid-gradient-corrected method [53, 116] which calculates the exchange correlation term by means of a linear combination of local, gradient-corrected and exact Hartree-Fock exchange terms with the Becke gradient-corrected term (B88) [49], and the local and gradient-corrected correlations

terms of Vosko-Wilk-Nusair (VWN) [48] and Lee-Yang-Parr (LYP) [50], respectively.

The electronic wave function was expanded using mixed Gaussian basis sets. Diffuse triple- ζ plus polarization 6-311++G(2d,p) was used for the oxygen atoms and first and second layer silicon atoms, while subsurface silicon and terminating H atoms were expanded with a double- ζ plus polarization 6-31G(d) basis set. This approach, used successfully in similar studies [97-100], focuses basis functions on the chemically active portion of the cluster and accurately describes orbitals involved in the reaction while minimizing the computational expense. All calculations were run using an unrestricted approach to calculate the open-shell structures of the spin-triplet systems. Comparison between restricted and unrestricted calculation results for closed shell systems (i.e., spin-singlet state clusters) showed negligible differences. The commercial program Gaussian03 [71] was used to run all the calculations.

4.3 Results and Discussion

A primary goal of this study was to assess the factors which influence the thermodynamic stability of local structures formed in the early stages of Si(100) oxidation. Toward this end, we performed energy minimization for each possible isomer in which one, two or three oxygen atoms are inserted into the first and second layer Si-Si bonds of the Si_9H_{12} cluster. Since these calculations generated many structures, a shorthand notation of capital letters followed by a subscript and a code in parenthesis is used for labeling the clusters to facilitate discussion. The first capital letters –which are DB, ME or TS- stand for dangling bond, minimum energy, and transition state structure, respectively. Subscripts 1 or 3 appear after the capital letter to indicate whether the structure is a spin singlet or triplet. Finally, the code in parenthesis is based on the notation used by Stefanov and Raghavachari [96] in which SiSi corresponds to a non-

oxidized cluster, SiOSi is a cluster with the O atom inserted into the dimer bond, SiSiO₂ is a structure with two oxygen atoms inserted into the two backbonds of the same dimer silicon atom, OSiSiO has two oxygen atoms inserted in a backbond pair at the same side of the dimer Si-Si bond, OxSiSiO has the two oxygen atoms in opposite-side backbonds, and SiSiOd is a cluster with an oxygen atom bonded to a single silicon atom of the dimer.

Several factors determine the heat of formation of an oxidized cluster, including the Si oxidation states, bond strain and the spin state of the cluster. We investigated clusters in both singlet and triplet spin states since the lowest energy structures of the clean Si(100) correspond to these spin states. The spin has two primary effects on the energy of the cluster. Firstly, a singlet cluster has one extra Si-Si bond compared with a triplet cluster, which tends to lower the energy of the structure. However, the formation of this extra bond also alters the geometric structure of a cluster and hence the strain energy. The strain is typically higher in a singlet cluster than in the analogous triplet structure for the one-dimer model. To directly compare the energies of singlet and triplet clusters, the energy of an oxidized cluster is defined with respect to a common reference state, which was taken to be the energy of the appropriate number of isolated oxygen atoms plus that of the clean (unoxidized) cluster in its singlet ground-state, [structure ME₁(SiSi)].

The singlet bare cluster was chosen as the reference state because DFT predicts that this structure minimizes the energy of the clean Si(100) surface. The dangling bonds on the Si dimer atoms are unpaired in the spin-triplet state of the bare cluster, [ME₃(SiSi), Figure 4-1(a)], but they pair to form a weak π bond along the dimer in the spin-singlet state, [ME₁(SiSi), Figure 4-1(B)]. This extra bond in ME₁(SiSi) shortens and tilts the silicon dimer bond along the $[\bar{1}10]$ direction, resulting in an asymmetric structure that is

0.37 eV more stable than its symmetric $\text{ME}_3(\text{SiSi})$ counterpart. The highest occupied molecular orbitals (HOMO) of both $\text{ME}_1(\text{SiSi})$ and $\text{ME}_3(\text{SiSi})$ were also calculated (Figure 4-1). The 0.37 eV energy difference, labeled as ΔE_{spin} , reflects the energy gained by the π interaction, which has been reported to be 1.24 eV [117]. It also reflects the difference in strain energies between the singlet and triplet bare clusters. Since the initial surface is taken to be the singlet bare cluster, the production of an oxidized cluster in the triplet spin state may be considered to occur in two steps, namely, conversion of the bare cluster from the singlet to the triplet ground-state, and then insertion of oxygen atoms into the triplet bare cluster. Thus, when comparing the energies of the oxidized clusters, it is important to recognize that the singlet to triplet conversion step contributes an energy penalty of 0.37 eV to the heat of formation of a triplet cluster. This energy is taken into account in our analysis of other factors that determine the cluster energies as discussed below.

We quantified factors which contribute to the energy of an oxidized cluster by invoking a bond energy model, which has previously been shown to provide a reasonable representation of the heats of silicon suboxide formation [118]. In the bond energy model, bond strain and distinct Si-O bond strengths for Si^{+1} , Si^{+2} and Si^{+3} oxidation states are treated as separable effects that contribute additively to the total heat of formation. In cases for which each oxygen atom in the cluster is inserted into a Si-Si bond, the bond energy model yields the following expression for the energy of an oxidized cluster,

$$\Delta E_{\text{UB3LYP}} = N(2\varepsilon_{\text{SiO}} - \varepsilon_{\text{SiSi}}) + \Delta E_{\text{suboxide}} + \delta(\Delta E_{\text{spin}}) + \Delta E_{\text{strain}} \quad (4-1)$$

where ΔE_{UB3LYP} is the energy of the oxidized cluster calculated by DFT, N is the total number of oxygen atoms in the cluster, ε_{SiO} is the Si-O bond energy in stoichiometric β

quartz crystal and ε_{SiSi} is the Si-Si bond energy in bulk silicon. In addition, $\Delta E_{suboxide}$ is the total suboxide penalty energy, ΔE_{spin} is the 0.37 eV energy difference between the triplet and singlet bare clusters, where δ is zero for the spin-singlet and one for the spin-triplet clusters, and ΔE_{excess} is the excess energy that is mainly related to changes in strain that result from oxygen insertion into the bare cluster. The suboxide energy penalty is defined by the Equation 4-2.

$$\Delta E_{suboxide} = \sum_x N_{Si^{+x}} (\Delta_x) \quad (4-2)$$

where $N_{Si^{+x}}$ is the number of silicon atoms bonded to x oxygen atoms (with $x = 1, 2$ or 3), and Δ_x is the energy penalty of a Si atom in the $+x$ oxidation state.

The concept of suboxide penalty energies was introduced in the bond energy model of Hamman [119] to take into account the effective increase in Si-O bond strength as the Si oxidation state increases. This effect originates mainly from the greater amount of ionic character in Si-O bonds involving Si atoms in higher oxidation states, but quantum resonance has also been suggested to enhance the bond strengths [119]. To quantify the differences in suboxide Si-O bond strengths, penalty energies were computed by Hamann [119] and Bongiorno and Pasquarello [118] for each Si suboxide state, under the assumption that the penalty energies can simply be added to the $(2\varepsilon_{SiO}-\varepsilon_{SiSi})$ term to compute the heats of formation of suboxide structures. Since the quantity ε_{SiO} is defined as the Si-O bond energy in crystalline SiO_2 , the penalty energies have positive values so that their contribution reduces the energy change in forming Si-O suboxide bonds. Table 4-1 shows the values of the suboxide penalty energies determined in the separate studies of Hamann [119] and Bongiorno and Pasquarello [118].

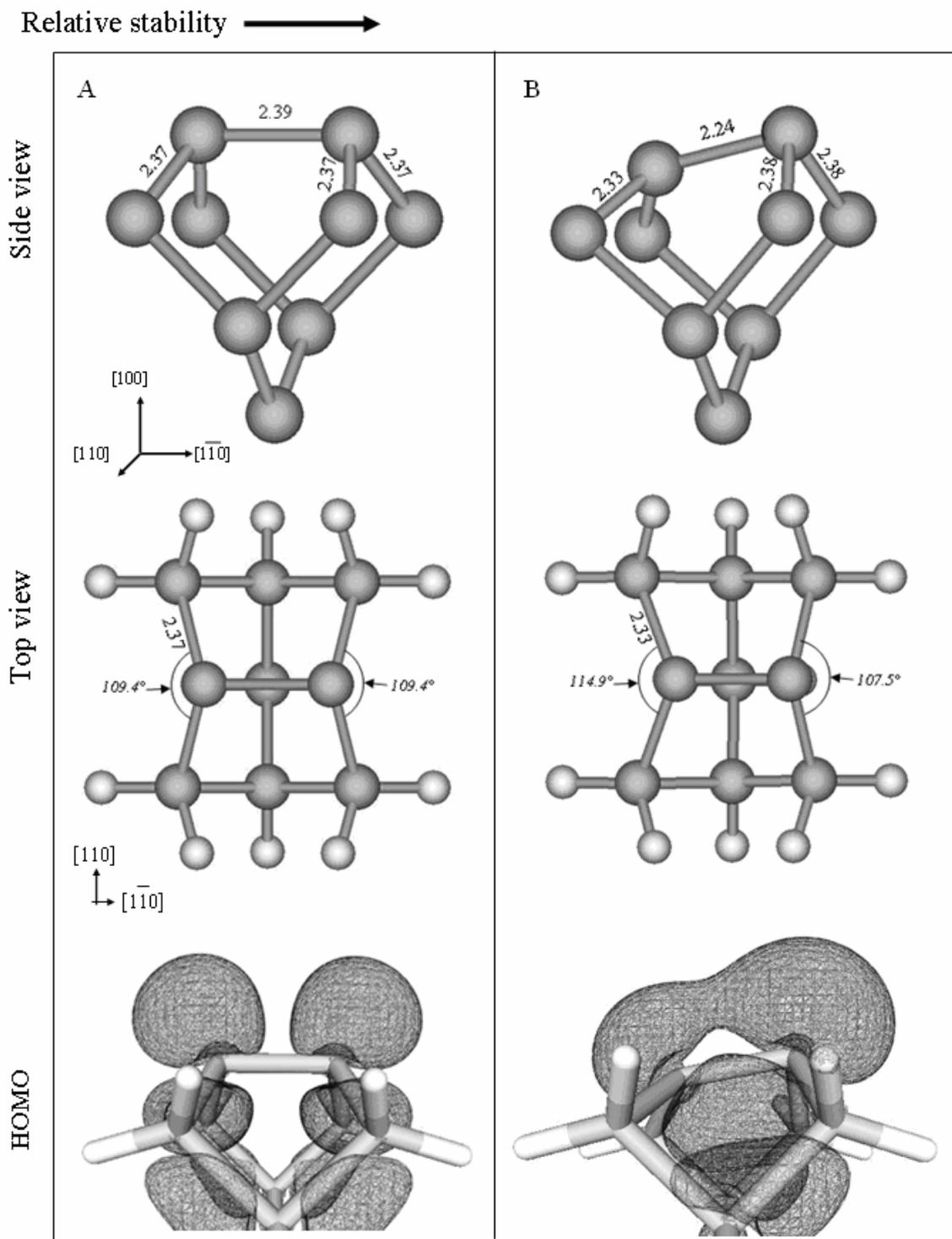


Figure 4-1. Structural information and highest occupied molecular orbital plot of clean Si_9H_{12} clusters. A) Symmetric spin-triplet surface $\text{ME}_3(\text{SiSi})$. B) asymmetric spin-singlet surface $\text{ME}_1(\text{SiSi})$. $\text{ME}_1(\text{SiSi})$ is calculated to be more stable than $\text{ME}_3(\text{SiSi})$ by 0.37 eV. Silicon and hydrogen are represented by grey and white balls, respectively. Bond lengths are expressed in Å.

Table 4-1. Suboxide penalty energies for various silicon oxidation states. The superscripts denote the number of oxygen atoms bonded to a particular silicon atom. Energies are given in eV.

Oxidation state	Energy penalty	Ref. 118	Ref. 119
Si ⁺¹	Δ_1	0.50	0.47
Si ⁺²	Δ_2	0.51	0.51
Si ⁺³	Δ_3	0.22	0.24

The penalty energies determined in these studies by Hamann [119] and Bongiorno and Pasquarello [118] are in good agreement with one another and are significant in value (Table 4-1), which suggests that maximizing the Si oxidation states is an important driving force that determines the types of local structures that form on Si(100) during initial oxidation.

We used the bond energy model given in Eq. 4-2 to quantify changes in strain energy resulting from the insertion of oxygen atoms into Si-Si bonds of the bare cluster. We chose to use an average of the suboxide penalty energies reported by Hamann [119] and Bongiorno and Pasquarello [118] in our analysis. This approach appears justified considering the close agreement in the penalty energies determined in those investigations. In addition, the values of ε_{SiO} and ε_{SiSi} were taken to be -4.35 and -2.02 eV, respectively, as reported for the Si-O bond energy in crystalline SiO₂ (β quartz, the lowest-energy form), and for the Si-Si bond energy in bulk silicon [96, 117]. Additionally, for spin-singlet structures where the oxygen atom inserts into the silicon dimer, the appropriate value of ε_{SiSi} in Eq. 4-2 corresponds to the energy for Si-Si π bond cleavage (-1.24 eV) [117]. These choices introduce some uncertainty in the absolute strain energies that are calculated because ε_{SiO} and ε_{SiSi} are experimentally determined values and are, therefore, not subject to the systematic errors that may affect the energies predicted by DFT.

We also investigated clusters in which one of the oxygen atoms adsorbs on a single Si atom of the surface dimer and forms only one Si-O bond, which we label as Si-O_d. These structures can serve as precursors to the formation of Si-O-Si linkages which form when the adsorbed O atom inserts into Si-Si bonds near the surface. In fact, a recent experimental study by Gerrard *et al.* [107] shows that gaseous O(³P) atoms initially adsorb at surface dangling bond sites on Si(100), forming Si-O_d bonds, before incorporating into the solid. Hence, investigating these dangling bond structures is essential for developing a mechanistic understanding of Si(100) oxidation by gaseous oxygen atoms. For the dangling bond structures, the following variation of Eq. 4-2 was used to quantify strain energies,

$$\Delta E_{UB3LYP} = (N - 1)(2\varepsilon_{SiO} - \varepsilon_{SiSi}) + \varepsilon_{SiO_d} + \Delta E_{suboxide} + \delta(\Delta E_{spin}) + \Delta E_{excess} \quad (4-3)$$

where all quantities have the same definitions as given above except for ε_{SiO_d} which is the energy of the Si-O_d bonds. We find that Si-O_d bonds have a more delocalized character than the Si-O bonds in Si-O-Si linkages due to the lone electron from the oxygen atom. One consequence of this delocalization is that the bond energy model with the parameters defined above, yields excessive values for the relative strain energies for the dangling bond structures (Section 4.3.2). In virtue of this, the value of ε_{SiO_d} has been defined by the difference in energy between the DB₃(SiSiOd) and ME₁(SiSi) structures.

Finally, it is important to point out that charge transfer involved in the incorporation of adsorbed species on Si(100)-(2x1) can exhibit nonlocal effects (i.e., charge transfer to a neighboring dimer on the surface) which may limit the overall usefulness of the O_x-Si₉H₁₂ clusters in estimating heats of formation. However, Widjaja and Musgrave [100] reported that the electron density in the similar system of O₂

adsorbed on Si(100)-(2x1) remains localized within the one-dimer environment. This observation supports the use of the small Si₉H₁₂ cluster for our investigation.

4.3.1 Structures with One Adsorbed Oxygen Atom (O₁-Si₉H₁₂)

Since we are interested in structures formed during the early stages of oxidation of the Si(100)-(2x1) surface, we considered only oxygen atom insertion into the surface dimer bond, one or more backbonds or a dangling bond. Optimized total energies of the different oxidized clusters are used to evaluate their stability relative to that of the clean clusters. For now, we postpone discussing the mechanistic aspects (i.e., reaction barriers) of these reactions and focus exclusively on the relative thermodynamic stabilities of the different isomers.

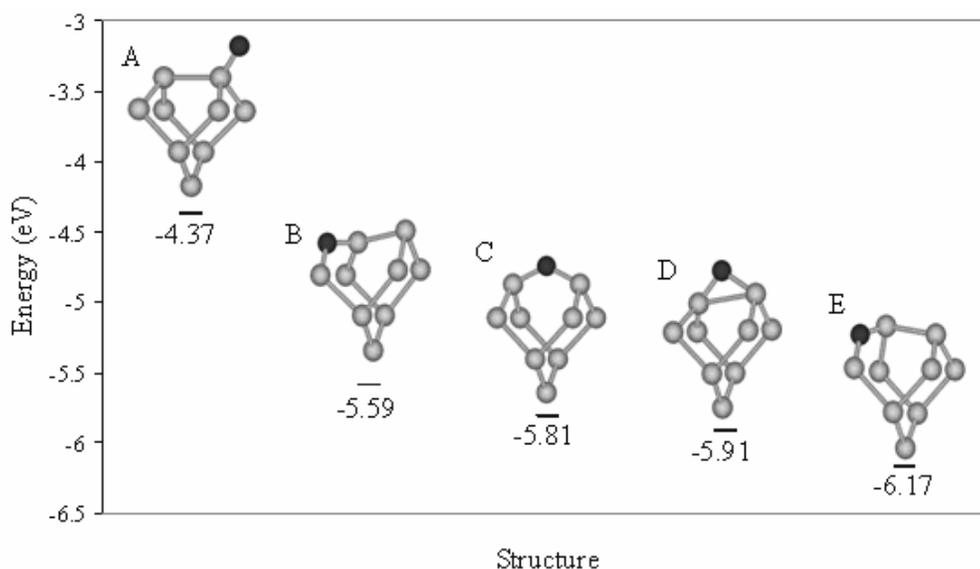
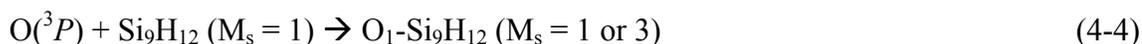


Figure 4-2. Relative energies of O₁-Si₉H₁₂ isomers. A) DB₃(SiSiOd). B) ME₃(SiSiO). C) ME₃(SiOSi). D) ME₁(SiOSi). E) ME₁(SiSiO). Energy reference: ME₁(SiSi) + O(³P) = 0.00 eV. Oxygen and silicon atoms are represented by black and gray balls, respectively.

For the minimum energy analysis, the energies of the O₁-Si₉H₁₂ isomers are referenced to the reaction



where M_s is the spin multiplicity. Table 4-2 shows the different energies that contribute to the calculated UB3LYP energies of the O_1 - Si_9H_{12} clusters, in order of ascendant stability. The $DB_3(SiSiOd)$ structure (Figure 4-3A) is the least favorable cluster because it only has one new Si-O bond. According to the bond energy model for dangling bond structures (Eq. 4-3) and the definition of the ϵ_{SiOd} energy, there is not any stress associated to $DB_3(SiSiOd)$. This value is not surprising, since the only difference in the geometric characteristics of the $DB_3(SiSiOd)$ and $ME_3(SiSi)$ structures (Figure 4-1A) is an 0.02 Å elongation of each of the backbonds that are located on the oxygen side of the dimer.

Table 4-2. Penalty energies of O_1 - Si_9H_{12} isomers. Contributions of the different factors to the calculated DFT/UB3LYP energies, according to the bond energy model. Energies are given in eV. For all structures: $N = 1$. Isomers are listed in order of increasing thermodynamic stability. Energy reference: $ME_1(SiSi) + 2O(^3P) = 0.00$ eV.

Structure	$N(2\epsilon_{SiO}-\epsilon_{SiSi})^a$	ϵ_{SiOd}	$\Delta E_{suboxide}$	$\delta(\Delta E_{spin})$	ΔE_{excess}	ΔE_{UB3LYP} (Eq. 4-3)
Dangling Bond Isomers						
$DB_3(SiSiOd)$	0.00	-4.74	0.00	0.37	0.00	-4.37
Minimum Energy Isomers						
$ME_3(SiSiO)$	-6.68	N/A	1.00	0.37	-0.28	-5.59
$ME_3(SiOSi)$	-6.68	N/A	1.00	0.37	-0.50	-5.80
$ME_1(SiOSi)^b$	-7.46	N/A	1.00	0.00	0.56	-5.90
$ME_1(SiSiO)$	-6.68	N/A	1.00	0.00	-0.49	-6.17

a: corresponds to $(N-1)(2\epsilon_{SiO}-\epsilon_{SiSi})$ for dangling bond clusters.

b: uses a value of -1.24 eV for the ϵ_{SiSi} , which corresponds to the Si-Si π bond

In the remaining O_1 - Si_9H_{12} structures, two Si-O bonds are formed at the expense of one Si-Si bond, so each structure has the same suboxide energy penalty. Thus, differences in the relative energies arise from the spin penalty energy and the different amounts of strain in the structures. Firstly, the spin-singlet isomers $ME_1(SiOSi)$ (Figure 4-3D) and $ME_1(SiSiO)$ (Figure 4-3E) are predicted to be the more energetically favorable structures, indicating that strain relief in the triplet structures is insufficient to

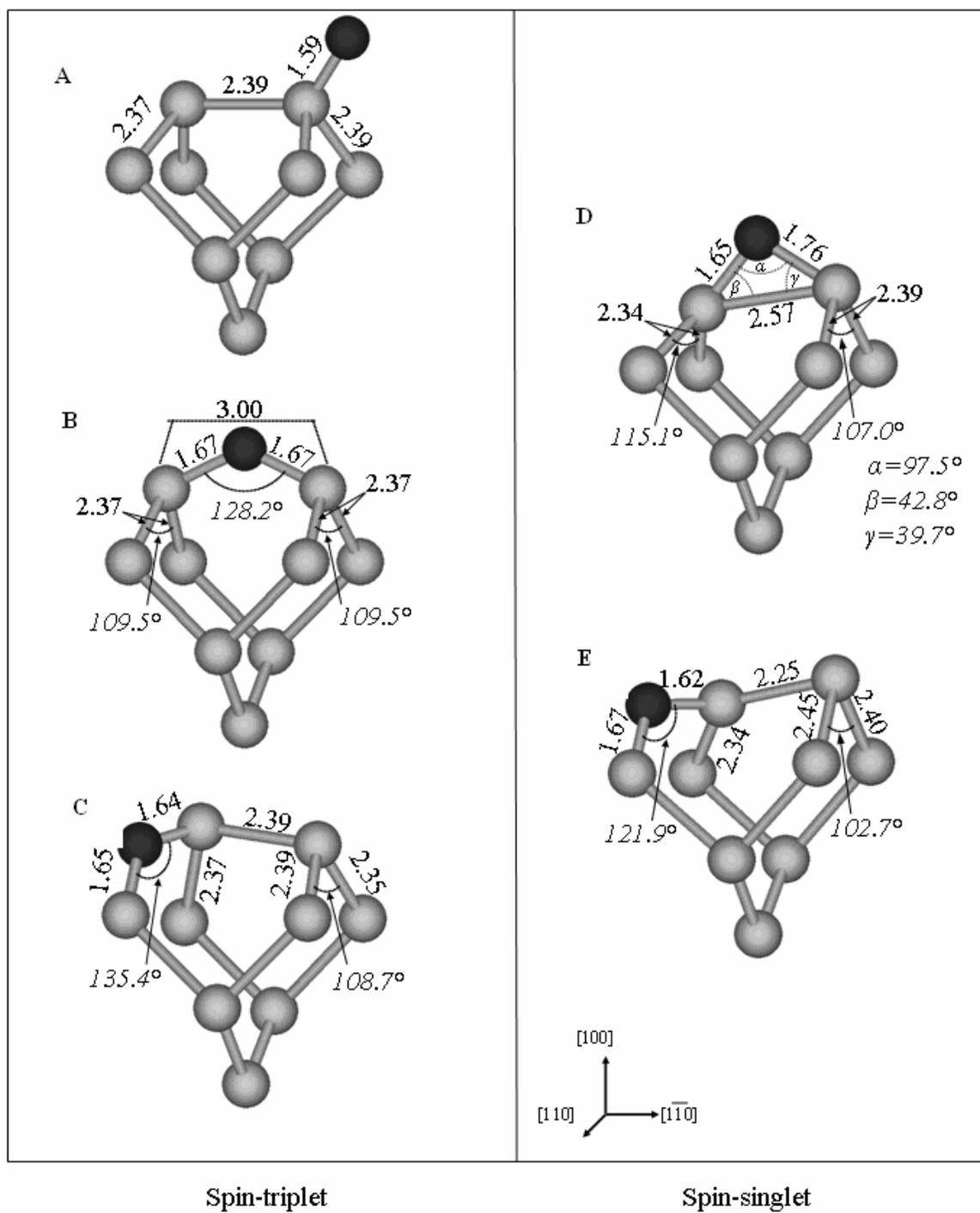


Figure 4-3. Structural characteristics of Si_9H_{12} clusters with one oxygen atom. A) $\text{DB}_3(\text{SiSiOd})$. B) $\text{ME}_3(\text{SiOSi})$. C) $\text{ME}_3(\text{SiSiO})$. D) $\text{ME}_1(\text{SiOSi})$. E) $\text{ME}_1(\text{SiSiO})$. Oxygen and silicon atoms are represented by black and gray balls, respectively. Bond lengths are expressed in Å. The crystallographic coordinate origin gives the orientation of the clusters. The surface is along the $[100]$ plane.

compensate the spin penalty energy. Structure $\text{ME}_1(\text{SiOSi})$ is more strained, and therefore less favorable than $\text{ME}_1(\text{SiSiO})$ by 0.27 eV, since formation of the epoxide-like ring stretches and weakens the Si-Si dimer bond. This result agrees with observations made by Weldon *et al.* [113-114], who were the first researchers to report the epoxide-like ring structures and suggested that they were the thermodynamically favored products after oxygen agglomeration (i.e., after three or more oxygen atoms adsorb on the Si(100) surface). For the triplet structures, $\text{ME}_3(\text{SiOSi})$ is more favorable than $\text{ME}_3(\text{SiSiO})$ by 0.22 eV since oxygen insertion breaks the dimer bond and thereby relieves the strain that the dimer bond imposes on the bare cluster. Notice in Figure 4-3(B) that the silicon dimer atoms are separated by 3.00 Å in the $\text{ME}_3(\text{SiOSi})$ structure. Finally, the bond energy model predicts negative strain energy (i.e. strain relief, for almost all of the $\text{O}_1\text{-Si}_9\text{H}_{12}$ structures, suggesting that each structure possesses less strain than the corresponding bare cluster). The only exception is the $\text{ME}_1(\text{SiOSi})$ structure, in which the predominant structural change is a significant elongation of the silicon dimer bond to a length of 2.57 Å, that increases the strain in the cluster by 0.56 eV. Nevertheless, the silicon dimer bond is not cleaved in this structure given that the formation of the Si-O bond only disrupts the weak Si-Si π interaction along the dimer. This formation does not break the stronger Si-Si σ bond, although it elongates the bond considerably.

4.3.2 Structures with Two Adsorbed Oxygen Atoms ($\text{O}_2\text{-Si}_9\text{H}_{12}$)

Figure 4-4 shows the relative thermodynamic stability of all the isomers with two oxygen atoms ($\text{O}_2\text{-Si}_9\text{H}_{12}$), and the various contributions to these relative stabilities are presented in Table 4-3, in order of ascendant stability. The energies of the isomers are referenced to the reaction expressed in Eq. 4-5.



where, as before, M_s is the spin multiplicity. As in the case of the $\text{O}_1\text{-Si}_9\text{H}_{12}$ clusters, the dangling bond structures are the least favorable structures, because they only have three Si-O bonds instead of the four that form on all the other isomers given that one of the oxygen atoms bonds to a silicon dangling bond. An interesting structural effect is predicted by the DFT/UB3LYP calculations for the dangling bond structures which significantly influences the heats of Si-O_d bond formation. We find that Si-O_d bond Si-Si bond lengths and angles relative to the reactant $\text{ME}_3(\text{SiSi})$. In contrast, formation of an Si-O_d bond on the $\text{ME}_3(\text{SiOSi})$ and $\text{ME}_3(\text{SiSiO})$ structures causes one Si-Si bond length to increase, thereby weakening the structure. In particular, with respect to the reactant structures, the dimer Si-Si bond is stretched by about 0.07 Å in $\text{DB}_3(\text{OSiSiOd})$ and $\text{DB}_3(\text{SiSiO2d})$, and one of the Si-Si backbonds on the O_d side of the dimer is

Table 4-3. Penalty energies of $\text{O}_2\text{-Si}_9\text{H}_{12}$ isomers. Contributions of the different factors to the calculated DFT/UB3LYP energies, according to the bond energy model. Energies are given in eV. For all structures: $N = 2$. Isomers are listed in order of increasing thermodynamic stability. Energy reference: $\text{ME}_1(\text{SiSi}) + 2\text{O}(^3P) = 0.00$ eV

Structure	$N(2\varepsilon_{\text{SiO}} - \varepsilon_{\text{SiSi}})^a$	$\varepsilon_{\text{SiOd}}$	$\Delta E_{\text{suboxide}}$	$\delta(\Delta E_{\text{spin}})$	ΔE_{excess}	ΔE_{UB3LYP} (Eq. 4-3)
Dangling Bond Isomers						
$\text{DB}_3(\text{OSiSiOd})$	-6.68	-4.74	1.00	0.37	0.23	-9.82
$\text{DB}_3(\text{SiSiO2d})$	-6.68	-4.74	1.00	0.37	-0.27	-10.32
$\text{DB}_3(\text{SiOSiOd})$	-6.68	-4.74	1.00	0.37	-0.38	-10.43
Minimum Energy Isomers						
$\text{ME}_1(\text{OSiSiO})$	-13.37	N/A	2.00	0.00	0.33	-11.04
$\text{ME}_3(\text{OxSiSiO})$	-13.37	N/A	2.00	0.37	-0.26	-11.25
$\text{ME}_1(\text{OxSiSiO})$	-13.37	N/A	2.00	0.00	0.06	-11.31
$\text{ME}_3(\text{SiSiO2})$	-13.37	N/A	1.51	0.37	0.05	-11.44
$\text{ME}_3(\text{OSiSiO})$	-13.37	N/A	2.00	0.37	-0.70	-11.69
$\text{ME}_3(\text{SiOSiO})$	-13.37	N/A	1.51	0.37	-0.57	-12.05
$\text{ME}_1(\text{SiOSiO})^b$	-14.15	N/A	1.51	0.00	0.48	-12.15
$\text{ME}_1(\text{SiSiO2})$	-13.37	N/A	1.51	0.00	-0.30	-12.16

a: corresponds to $(N-1)(2\varepsilon_{\text{SiO}} - \varepsilon_{\text{SiSi}})$ for dangling bond clusters.

b: uses a value of -1.24 eV for the $\varepsilon_{\text{SiSi}}$, which corresponds to the Si-Si π bond.

stretched by 0.10 Å in the $\text{DB}_3(\text{SiOSiOd})$ structure. As expected, this Si-Si bond elongation lowers the heat of Si-O_d bond formation. For example, the heat of the reaction $\text{ME}_3(\text{SiSi}) + \text{O}({}^3P) = \text{ME}_3(\text{SiSiOd})$ is 0.50 eV greater than the heat of the reaction $\text{ME}_3(\text{SiSiO}) + \text{O}({}^3P) = \text{ME}_3(\text{OSiSiOd})$. This energy difference may be attributed almost entirely to the observed Si-Si bond weakening since the Si-O_d bonds in both structures involve a Si^{+1} species, and the only appreciable structural difference between reactants and products is the longer Si-Si dimer bond in $\text{ME}_3(\text{OSiSiOd})$. It is tempting to conclude that Si-Si bond weakening occurs in the $\text{O}_2\text{-Si}_9\text{H}_{12}$ structures because the Si atoms in these bonds have higher partial positive charges than in $\text{ME}_3(\text{SiSiOd})$. For example, the dimer bond in $\text{ME}_3(\text{SiSiOd})$ involves an Si^0 and Si^{+1} species, whereas in $\text{ME}_3(\text{OSiSiOd})$ the dimer Si atoms are both nominally in the +1 oxidation state. However, similar Si-Si bond stretching is not observed in $\text{O}_2\text{-Si}_9\text{H}_{12}$ structures in which each oxygen atom is present in an Si-O-Si linkage (Figure 4-6). Hence, delocalization of the unpaired electron of the O_d atom must play an important role in weakening Si-Si bonds in the $\text{O}_2\text{-Si}_9\text{H}_{12}$ dangling bond structures.

The remaining $\text{O}_2\text{-Si}_9\text{H}_{12}$ isomers result from the formation of Si-O bonds in siloxane bridges or epoxide-like rings in place of the dimer bond or backbonds (Figure 4-6). The relative energies of these structures are determined by a combination of effects, though the suboxide energy penalty generally has the largest influence. The overall trend is that the structures possessing four Si^{+1} species are less favorable than those with a combination of two Si^{+1} and one Si^{+2} species, and that the spin-singlet structures are more favorable than their spin-triplet counterparts. Indeed, three of the four isomers possessing a Si^{+2} atom are the most energetically favorable among the two O-atom isomers and, in order of increasing stability, the most favorable structures are $\text{ME}_3(\text{SiOSiO}) <$

$\text{ME}_1(\text{SiOSiO}) < \text{ME}_1(\text{SiSiO}_2)$. The $\text{ME}_3(\text{SiSiO}_2)$ structure falls out of this trend as it is 0.25 eV less favorable than the $\text{ME}_3(\text{OSiSiO})$ structure which has four Si^{+1} species and, consequently, should be less stable. After accounting for the suboxide penalties, the bond energy model suggests a substantial 0.75 eV difference in the excess energies of these two structures, which probably arises from a combination of strain effects associated to the bonding site of the oxygen atom. The results suggest that forming two siloxane-bridges with two different silicon dimer atoms is the favored product.

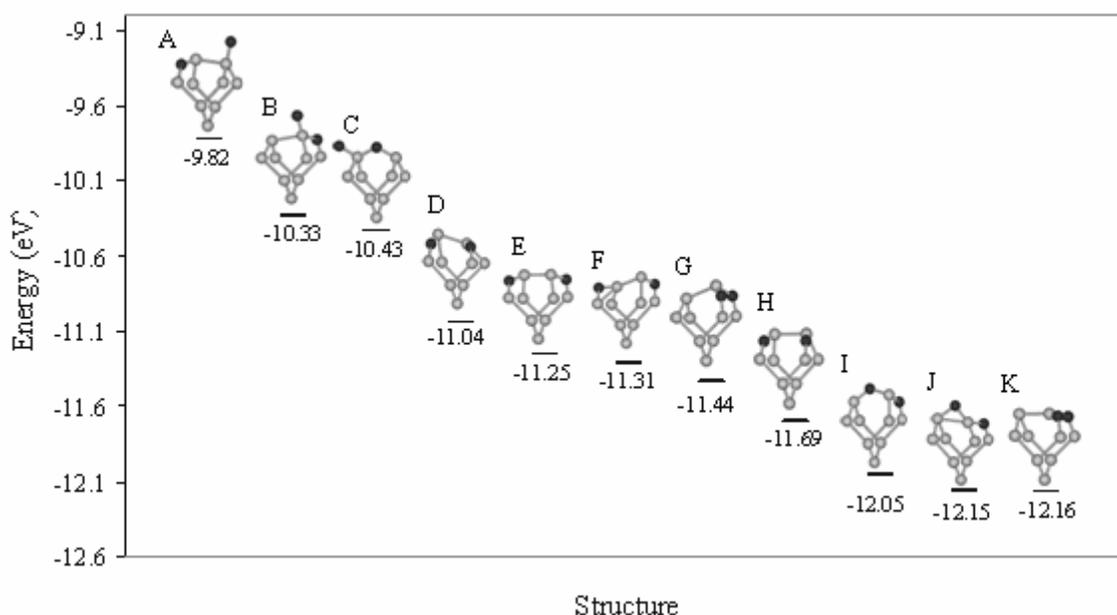


Figure 4-4. Relative energies of $\text{O}_2\text{-Si}_9\text{H}_{12}$ isomers. A) $\text{DB}_3(\text{OSiSiOd})$. B) $\text{DB}_3(\text{SiSiO}_2\text{d})$. C) $\text{DB}_3(\text{SiOSiOd})$. D) $\text{ME}_1(\text{OSiSiO})$. E) $\text{ME}_3(\text{OxSiSiO})$. F) $\text{ME}_1(\text{OxSiSiO})$. G) $\text{ME}_3(\text{SiSiO}_2)$. H) $\text{ME}_3(\text{OSiSiO})$. I) $\text{ME}_3(\text{SiOSiO})$. J) $\text{ME}_1(\text{SiOSiO})$. K) $\text{ME}_1(\text{SiSiO}_2)$. Energy reference: $\text{ME}_1(\text{SiSi}) + 2\text{O}({}^3P) = 0.00$ eV. Oxygen and silicon atoms are represented by black and gray spheres, respectively.

Another substantial effect of strain is the observation that structure $\text{ME}_3(\text{OSiSiO})$ (Figure 4-6A) is significantly lower in energy than structure $\text{ME}_1(\text{OSiSiO})$ (Figure 4-6E), despite the spin penalty energy that applies to the triplet structure. After taking into account the spin penalty energy, the bond energy model suggests that $\text{ME}_1(\text{OSiSiO})$ has 1.02 eV more strain than $\text{ME}_3(\text{OSiSiO})$. In both of these structures, the formation of two

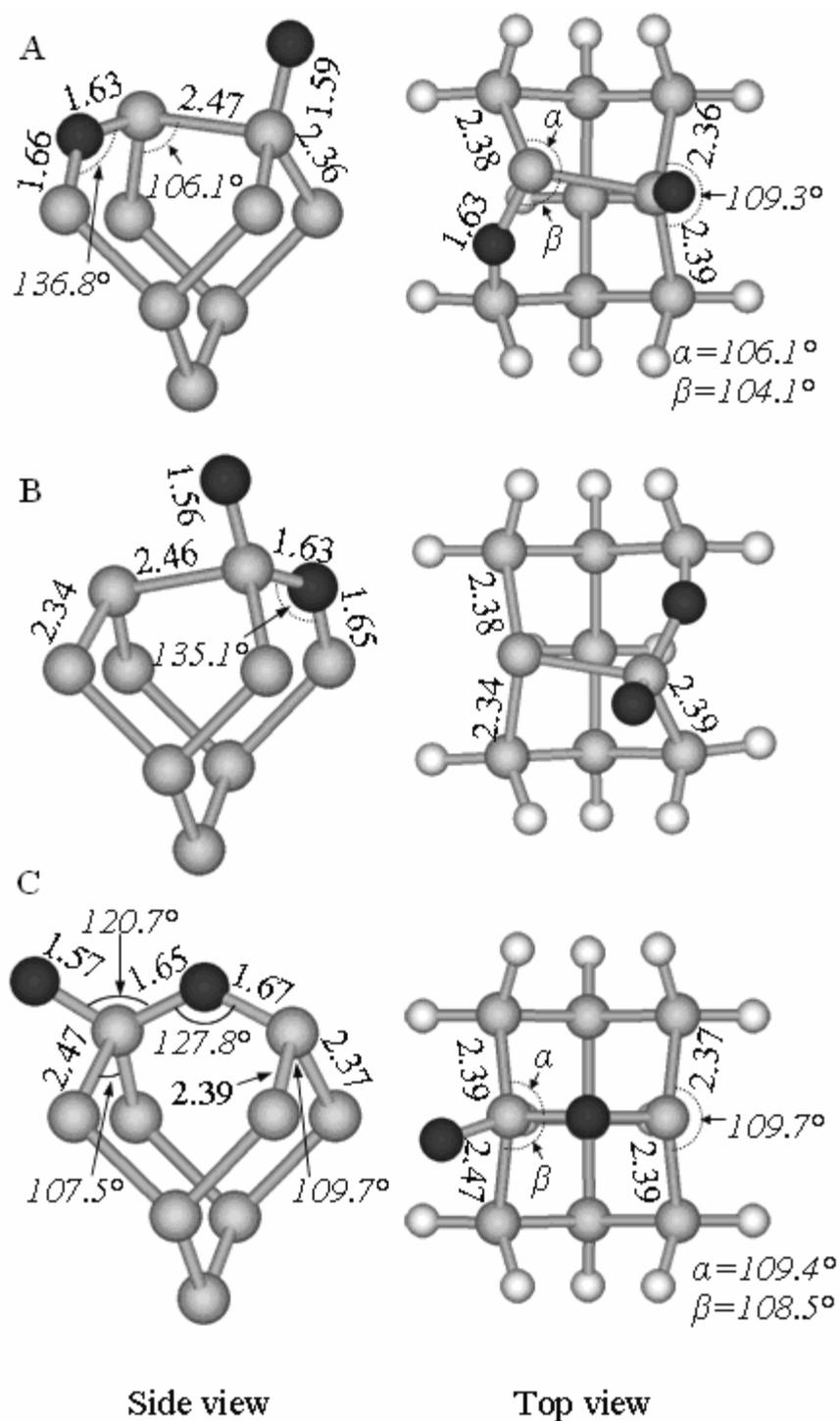


Figure 4-5. Structural information of dangling bond isomers with two oxygen atoms adsorbed on Si(100). A) $\text{DB}_3(\text{OSiSiOd})$. B) $\text{DB}_3(\text{SiSiO}_2\text{d})$. C) $\text{DB}_3(\text{SiOSiOd})$. Bond lengths are expressed in Å. Oxygen atoms are represented with black balls. Silicon and hydrogen atoms are represented in gray and white balls, respectively.

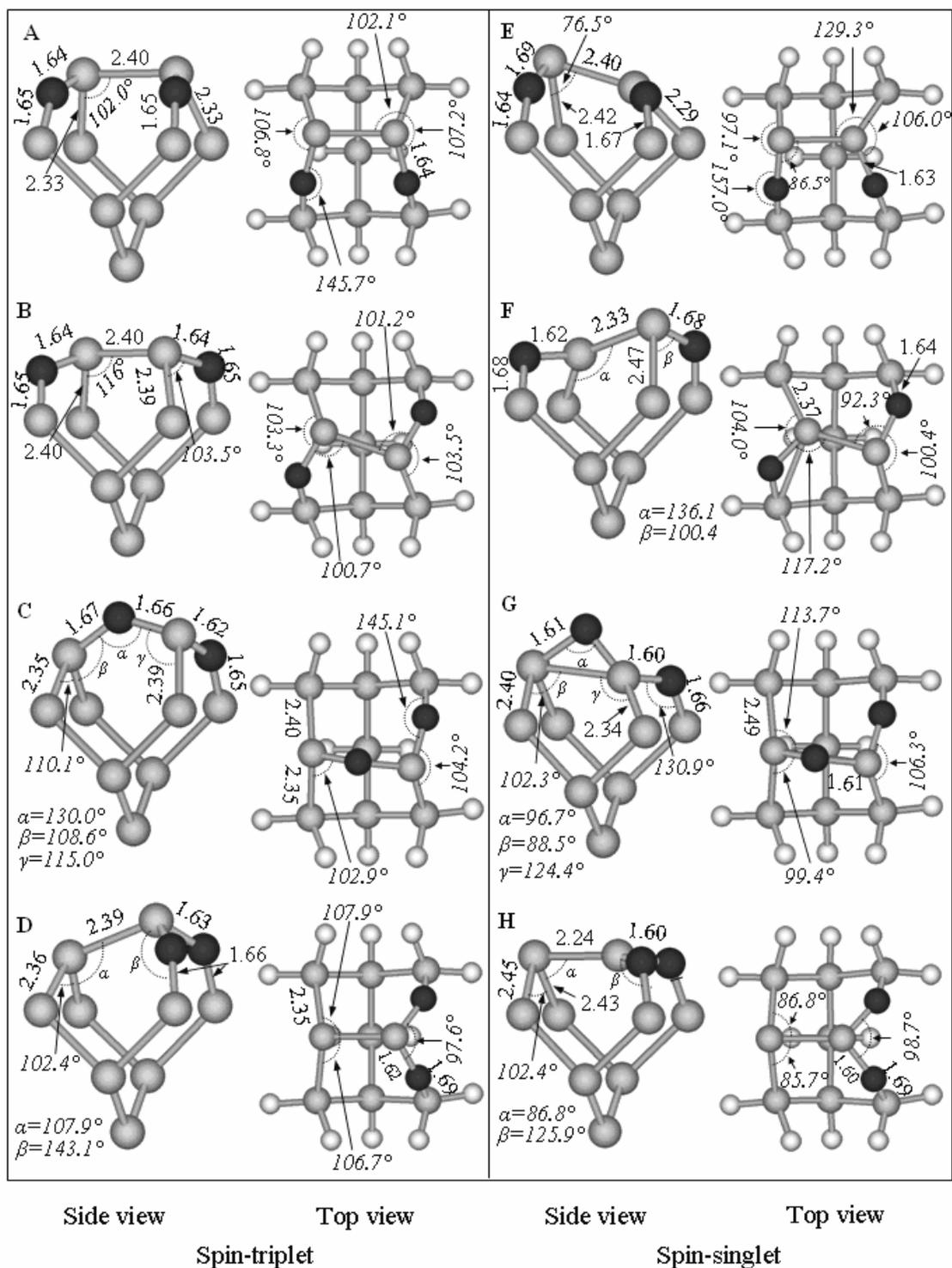


Figure 4-6. Structural information of $O_2-Si_9H_{12}$ isomers. Structures are listed by increasing relative stability of the spin-singlet isomers. A) $ME_3(OSiSiO)$. B) $ME_3(OxSiSiO)$. C) $ME_3(SiOSiO)$. D) $ME_3(SiSiO_2)$. E) $ME_1(OSiSiO)$. F) $ME_1(OxSiSiO)$. G) $ME_1(SiOSiO)$. H) $ME_1(SiSiO_2)$. Bond lengths are expressed in Å. Oxygen atoms are represented with black balls. Silicon and hydrogen atoms are represented in gray and white balls, respectively.

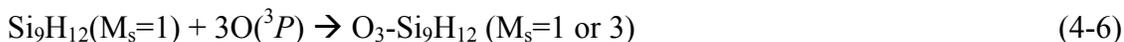
siloxane bridges on the same side of the silicon dimer bond shifts the dimer out of its original symmetry plane, without changing its orientation along the $[\bar{1}\bar{1}0]$ direction.

However, these structures experience markedly different strain effects due to the different bonding interactions along their respective Si-Si dimers. In $\text{ME}_3(\text{OSiSiO})$, the formation of the two siloxane bridges alleviates strain in the remaining Si-Si backbonds, which each shorten by 0.04 Å. Aside from being shifted out of plane, the dimer bond remains largely unaltered by the formation of $\text{ME}_3(\text{OSiSiO})$. These structural changes are predicted to relieve about 0.70 eV of strain from the cluster, and result in considerable stabilization of the structure, making it the most energetically favorable of all the structures with four Si^{+1} species. In contrast, the formation of the siloxane bridges significantly weakens the π interaction across the silicon dimer in $\text{ME}_1(\text{OSiSiO})$, causing the dimer bond to stretch by 0.16 Å, resulting in an 0.33 eV increase in strain relative to the singlet bare cluster, according to the bond energy analysis.

4.3.3 Structures with Three Adsorbed Oxygen Atoms ($\text{O}_3\text{-Si}_9\text{H}_{12}$)

Figure 4-7 shows relative energies of isomers with three oxygen atoms and table 4-4 shows the different contributions to the relative energies of the structures, as determined from the bond energy model.

As in the previous two cases discussed above, the energies of the isomers are defined with respect to the reaction described by Equation 4-6.



We calculated the relative energies and structural characteristics of the $\text{O}_3\text{-Si}_9\text{H}_{12}$ isomers (Figures 4-8 and Figure 4-9). We found that the relative energy of the structures is determined by a combination of effects, including strain and suboxide formation.

Table 4-4. Penalty energies of O_3 - Si_9H_{12} isomers. Contributions of the different factors to the calculated DFT/UB3LYP energies, according to the bond energy model. Energies are given in eV. For all structures: $N = 3$. Isomers are listed in order of increasing thermodynamic stability. Energy reference: $ME_1(SiSi) + 3O(^3P) = 0.00$ eV.

Structure	$N(2\varepsilon_{SiO}-\varepsilon_{SiSi})^a$	ε_{SiOd}	$\Delta E_{suboxide}$	$\delta(\Delta E_{spin})$	ΔE_{excess}	ΔE_{UB3LYP}
Dangling Bond Isomer						
DB ₃ (OSiOSiOd)	-13.37	-4.74	1.51	0.37	0.72	-15.51
Minimum Energy Isomers						
ME ₃ (OSiSiO2)	-20.05	N/A	2.51	0.37	0.19	-16.97
ME ₁ (OSiSiO2)	-20.05	N/A	2.51	0.00	0.20	-17.34
ME ₃ (OxSiOSiO)	-20.05	N/A	2.02	0.37	0.14	-17.52
ME ₃ (SiOSiO2)	-20.05	N/A	1.74	0.37	0.34	-17.60
ME ₁ (OxSiOSiO)	-20.83	N/A	2.02	0.00	1.13	-17.68
ME ₁ (SiOSiO2)	-20.83	N/A	1.74	0.00	1.18	-17.93
ME ₃ (OSiOSiO)	-20.05	N/A	2.02	0.37	-0.44	-18.10
ME ₁ (OSiOSiO) ^b	-20.83	N/A	2.02	0.00	0.25	-18.57

a: corresponds to $(N-1)(2\varepsilon_{SiO}-\varepsilon_{SiSi})$ for dangling bond clusters.

b: uses a value of -1.24 eV for the ε_{SiSi} , which corresponds to the Si-Si π bond.

The least favored of the O_3 - Si_9H_{12} isomers are the structures ME₃(OSiSiO2) and ME₁(OSiSiO2). These structures have the highest suboxide energy penalty of 2.51 eV, so their energetic positions are governed mainly by the suboxide penalty, with the spin penalty separating the energies of these two isomers. In contrast, however, the lowest energy structures, ME₁(OSiOSiO) and ME₃(OSiOSiO) (Figure 4-9D and 4-9F), each have a suboxide penalty of 2.02 eV, which is not the lowest (1.74 eV) among the O_3 - Si_9H_{12} isomers. These two structures owe their high relative stabilities to strain minimization. In fact, according to the bond energy model, only the formation of ME₃(OSiOSiO) lowers the strain energy, relative to that of the bare clusters; all the other structures have higher strain energies than the bare clusters. And in ME₁(OSiOSiO), the strain increases by 0.25 eV, but in this cluster only a weak Si-Si π bond (1.24 eV) is broken by the oxygen incorporation rather than the stronger crystalline SiSi bond (2.02 eV). It appears that by shifting the dimer out of its original symmetry plane, the cluster is able to accommodate the oxygen atoms and also relieve strain.

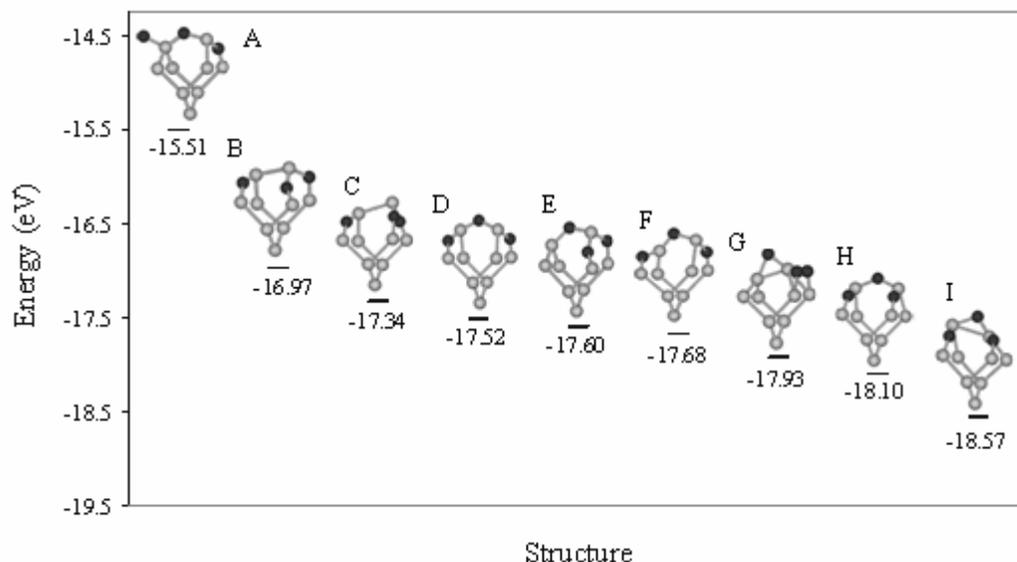


Figure 4-7. Relative energies of optimized structures for three oxygen atom incorporation into Si(100). A) $\text{DB}_3(\text{OSiOSiO})$. B) $\text{ME}_3(\text{OSiSiO}_2)$. C) $\text{ME}_1(\text{OSiSiO}_2)$. D) $\text{ME}_3(\text{OxSiOSiO})$. E) $\text{ME}_3(\text{SiOSiO}_2)$. F) $\text{ME}_1(\text{OxSiOSiO})$. G) $\text{ME}_1(\text{SiOSiO}_2)$. H) $\text{ME}_3(\text{OSiOSiO})$. I) $\text{ME}_1(\text{OSiOSiO})$. Energy reference: $\text{ME}_1(\text{SiSi}) + 3\text{O}({}^3P) = 0.00 \text{ eV}$.

The energy positions of the remaining clusters are determined by a combination of effects as well. For example, the third and fourth most favorable structures, $\text{ME}_1(\text{SiOSiO}_2)$ and $\text{ME}_1(\text{OxSiOSiO})$, respectively, are in the same spin state and their strain energies differ by only 0.05 eV. So, the lower energy of $\text{ME}_1(\text{SiOSiO}_2)$, can be attributed to its lower suboxide energy penalty. Notice, however, that the strain associated to these two structures is considerably high, as a direct result of the fact that the oxygen atom adsorbs by breaking a weak Si-Si π bond and forming an epoxide-like ring on top of the dimer bond. This ring imposes considerable strain on the silicon dimer, which stretches from 2.24 to 2.92 Å in $\text{ME}_1(\text{OxSiOSiO})$, and shrinks in $\text{ME}_1(\text{SiOSiO}_2)$ from 2.24 to 2.17 Å. The next two isomers, $\text{ME}_3(\text{SiOSiO}_2)$ and $\text{ME}_3(\text{OxSiOSiO})$, are higher in energy than their spin-singlet counterparts due to the spin energy penalty, and structure $\text{ME}_3(\text{SiOSiO}_2)$ is lower in energy than $\text{ME}_3(\text{OxSiOSiO})$ by only 0.08 eV. According to the bond energy model, the lower suboxide penalty in $\text{ME}_3(\text{SiOSiO}_2)$

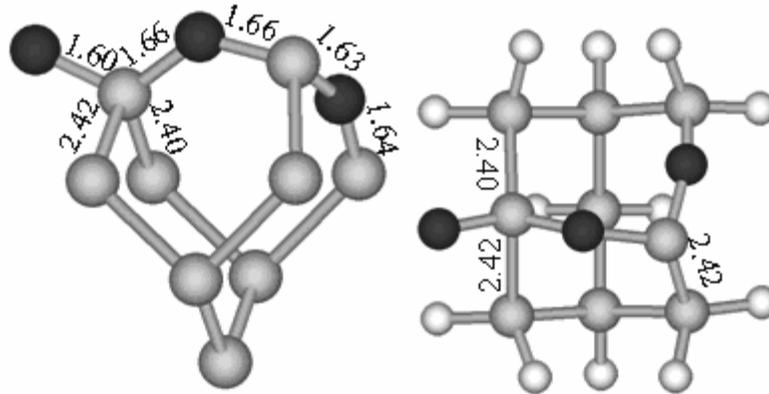


Figure 4-8. Structural information of the dangling bond $O_3\text{-Si}_9\text{H}_{12}$ isomer $DB_3(OSiOSiOd)$. Bond lengths are expressed in Å. Oxygen atoms are represented with black balls. Silicon and hydrogen atoms are represented in gray and white balls, respectively.

compensates its higher strain energy relative to $ME_3(O_xSiOSiO)$, making $ME_3(SiOSiO_2)$ the more favorable of the two. Finally, each spin-singlet structure is lower in energy than its spin-triplet counterpart, demonstrating the importance of the spin state in determining the relative energies of the $O_3\text{-Si}_9\text{H}_{12}$ isomers. Of the possible $O_3\text{-Si}_9\text{H}_{12}$ isomers with a single $Si-O_d$ bond, we optimized only the $DB_3(OSiOSiOd)$ structure. This structure was chosen firstly because it is a precursor to the $ME_3(OSiOSiO)$ structure, which is the most favorable of the triplet $O_3\text{-Si}_9\text{H}_{12}$ isomers and is only higher in energy than one other three O-atom cluster, $ME_1(OSiOSiO)$. In addition, $DB_3(OSiOSiOd)$ is generated by the adsorption of an oxygen atom at a dangling bond site of $ME_3(SiOSiO)$ (Figure 4-7C), which is the most favorable of the triplet $O_2\text{-Si}_9\text{H}_{12}$ isomers, and is only higher in energy by 0.11 eV than the lowest energy, two O-atom cluster. Assuming that the equilibrium energy of a local structure is important in determining its formation probability, the $DB_3(OSiOSiOd)$ structure can be expected to be a prevalent precursor in the early stages of Si(100) oxidation since it enables the conversion between the most stable $O_2\text{-Si}_9\text{H}_{12}$ and $O_3\text{-Si}_9\text{H}_{12}$ isomers.

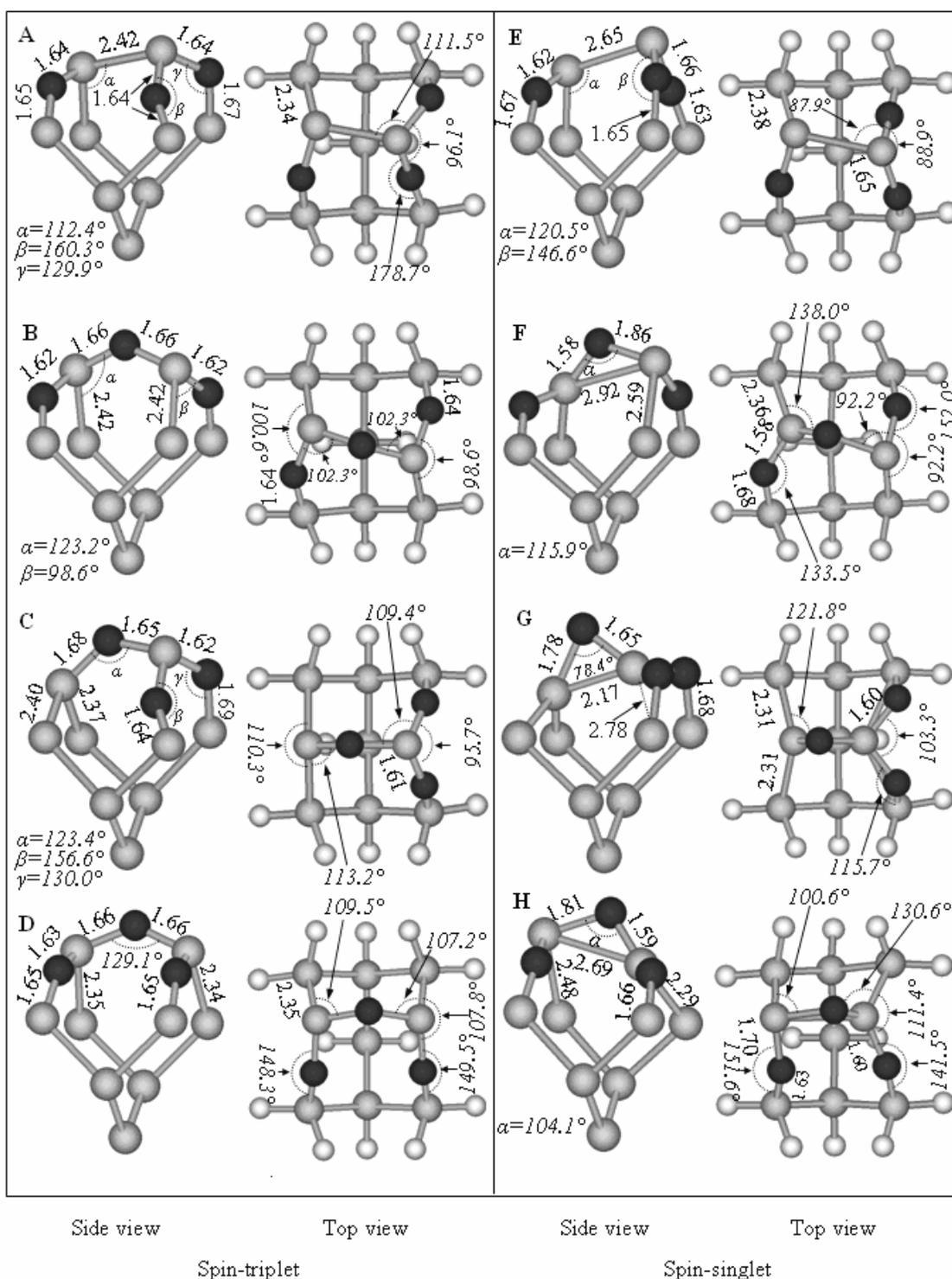


Figure 4-9. Structural characteristics $O_3-Si_9H_{12}$ isomers. Isomers are listed by increasing relative stability of the spin-singlet isomers. A) $ME_3(OSiSiO_2)$. B) $ME_3(OxSiOSiO)$. C) $ME_3(SiOSiO_2)$. D) $ME_3(OSiOSiO)$. E) $ME_1(OSiSiO_2)$. F) $ME_1(OxSiOSiO)$. G) $ME_1(SiOSiO_2)$. H) $ME_1(OSiOSiO)$. Bond lengths are expressed in Å. Oxygen atoms are represented with black balls. Silicon and hydrogen atoms are represented in gray and white balls, respectively.

Oxygen adsorption on $\text{ME}_3(\text{SiOSiO})$ to produce $\text{DB}_3(\text{OSiOSiOd})$ is significantly less exothermic than Si-O_d bond formation in the isomers with one and two oxygen atoms. In particular, the heat of the $\text{ME}_3(\text{SiOSiO}) + \text{O}({}^3P) = \text{DB}_3(\text{OSiOSiOd})$ reaction is 3.46 eV, whereas oxygen adsorption on the triplet bare cluster is exothermic by 4.74 eV. The heat of Si-O_d bond formation on clusters containing one Si-O-Si linkage was found to be lower than on the bare cluster due to weakening of an Si-Si bond in the $\text{O-Si}_9\text{H}_{12}\text{-O}_d$ structures (Section 4.3.2). There appears to be a similar effect in the $\text{DB}_3(\text{OSiOSiOd})$ structure (Figure 4-8), where the presence of two siloxane-bridges in combination with the Si-O_d bond formation weaken the three remaining Si-Si bonds, which is evident by the similar elongation of all of them. This stretching further translates into the reduction of formation energy. Finally, notice that the three spin-singlet most stable structures present an epoxide-like ring. This is in agreement with the observations of Weldon *et al.* [113-114], who suggested that the epoxide-like rings were the thermodynamically favored products when three or more oxygen atoms absorb on the $\text{Si}(100)$ surface.

4.3.4 Oxygen Insertion

4.3.4.1 Thermodynamic considerations

Recent experimental results [107] showed that gaseous $\text{O}({}^3P)$ atoms incorporate into the $\text{Si}(100)\text{-(}2\times 1\text{)}$ surface by first adsorbing at dangling bond sites and then inserting in Si-Si bonds in the near-surface region. Thus, the dangling bond structures serve as precursors for oxygen atom insertion into the $\text{Si}(100)$ surface. Because the dangling bond structures are all of triplet spin multiplicity, the insertion of an oxygen atom into a cluster is considered to occur on the triplet potential energy surface. Interconversion between singlet and triplet spin states is not explicitly taken into account in our calculations, but such state-crossing processes are certain to occur during $\text{Si}(100)$ oxidation, and may

impose additional energy barriers on the oxidation process. According to our calculations, the most energetically favorable structures exist in spin-singlet states, so the generation of these structures via dangling bond precursors necessitates a triplet to singlet conversion. Nevertheless, the relative energies determined for the oxidized clusters do provide critical information for assessing likely pathways for the initial stages of Si(100)-(2x1) oxidation. Before discussing mechanistic aspects of oxidation, it is useful to consider the likely progression of local structures that will form based on their relative energies.

We investigated the thermodynamic feasibility of several insertion reactions in the spin-triplet state, which may be represented by reaction Equation 4-7.



In Eq. 4-7 M_s corresponds to the multiplicity state, -O_d indicates that the oxygen atom is bonded at a dangling bond, and $x = 0, 1$ or 2 . An $\text{O}({}^3P)$ atom will initially adsorb on the clean surface to generate the structure $\text{DB}_3(\text{SiSiOd})$. The adsorbed oxygen atoms can then insert into either the Si-Si dimer bond or a backbond to generate either $\text{ME}_3(\text{SiSiO})$ or $\text{ME}_3(\text{SiOSi})$, with formation of the latter being more exothermic by 0.23 eV. Since the singlet $\text{O}_1\text{-Si}_9\text{H}_{12}$ isomers are lower in energy, the triplet structures will eventually convert to the spin-singlet state, unless the barriers for state-crossing are prohibitively high. Interestingly, the more thermodynamically favored singlet structure, $\text{ME}_1(\text{SiSiO})$, is the less favored of the triplet structures (i.e., $\text{ME}_3(\text{SiSiO})$ must first form via the $\text{DB}_3(\text{SiSiOd})$ precursor). Based only on the relative energies, structure $\text{ME}_3(\text{SiOSi})$ should form preferentially over $\text{ME}_3(\text{SiSiO})$, and will then convert to $\text{ME}_1(\text{SiOSi})$ to further lower the energy of the system.

Oxygen adsorption onto the $O_1\text{-Si}_9\text{H}_{12}$ isomers can result in three distinct dangling bond structures (Figure 4-5). Although the heats of formation of these structures vary by as much as 0.50 eV, oxygen adsorption is non-activated so each dangling bond structure should form with roughly equal probability, assuming that the $\text{ME}_1(\text{SiOSi})$ and $\text{ME}_1(\text{OSiSi})$ reactants are present in equal concentrations. The $\text{ME}_3(\text{SiOSiO})$ structure is the most likely product of the oxygen insertion reactions that can originate from the $O_1\text{-Si}_9\text{H}_{12}\text{-O}_d$ structures. Firstly, the $\text{ME}_3(\text{SiOSiO})$ structure has the lowest energy of all the triplet $O_2\text{-Si}_9\text{H}_{12}$ isomers, and can further lower the energy of

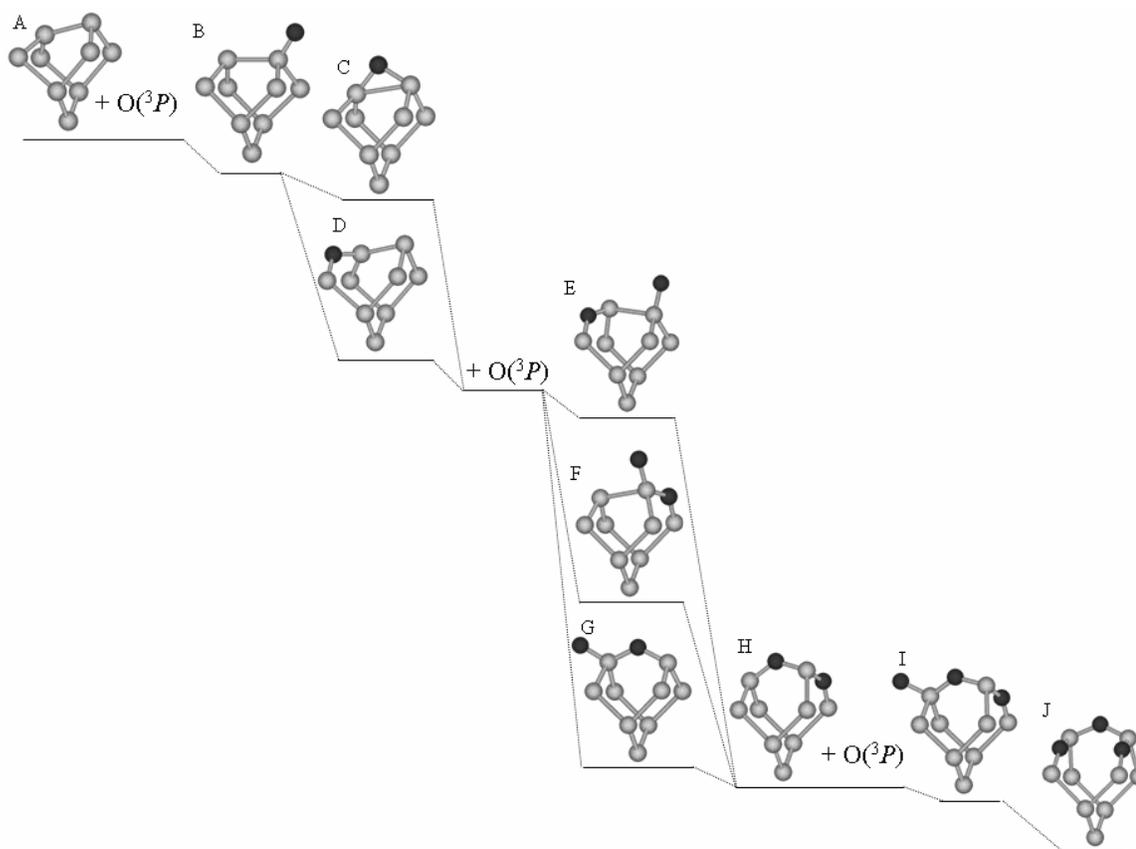


Figure 4-10. Qualitative representation of a thermodynamic preferred path for oxygen atom incorporation on $\text{Si}(100)\text{-(}2\times 1\text{)}$ based on relative thermodynamic stability of the structures. Relative energies are not at scale. A) $\text{ME}_1(\text{SiSi})$. B) $\text{DB}_3(\text{SiSiOd})$. C) $\text{ME}_1(\text{SiOSi})$. D) $\text{ME}_1(\text{SiSiO})$. E) $\text{DB}_3(\text{OSiSiOd})$. F) $\text{DB}_3(\text{SiSiO}2d)$. G) $\text{DB}_3(\text{SiOSiOd})$. H) $\text{ME}_3(\text{SiOSiO})$. I) $\text{DB}_3(\text{OSiOSiOd})$. J) $\text{ME}_3(\text{OSiOSiO})$.

the system by converting to the $\text{ME}_1(\text{SiOSiO})$ structure through a state-crossing event. In addition, each of the three $\text{O}_1\text{-Si}_9\text{H}_{12}\text{-O}_d$ structures can transform directly to the $\text{ME}_3(\text{SiOSiO})$ structure, thereby increasing the likelihood that this structure will be formed.

The lowest energy $\text{O}_2\text{-Si}_9\text{H}_{12}$ isomer is $\text{ME}_1(\text{SiSiO}_2)$, which is favored by a mere 0.01 eV over $\text{ME}_1(\text{SiOSiO})$. However, the formation of $\text{ME}_1(\text{SiSiO}_2)$ appears to be less likely than $\text{ME}_1(\text{SiOSiO})$ for several reasons. It can only be produced from the $\text{DB}_3(\text{SiSiO}_2d)$ isomer via the production of $\text{ME}_3(\text{SiSiO}_2)$, and the $\text{ME}_3(\text{SiSiO}_2)$ structure is 0.61 eV higher in energy than the alternate $\text{ME}_3(\text{SiOSiO})$ product. Finally, the most stable triplet $\text{O}_3\text{-Si}_9\text{H}_{12}$ cluster, $\text{ME}_3(\text{OSiOSiO})$ (Figure 4-9D), can form directly from $\text{DB}_3(\text{OSiOSiOd})$, and $\text{ME}_3(\text{OSiOSiO})$ can then transform into the lowest energy $\text{O}_3\text{-Si}_9\text{H}_{12}$ isomer via a state-crossing process. These thermodynamic considerations suggest that the progression of structures shown in Figure 4-10 represent the preferred path for the incorporation of three oxygen atoms into a single dimer unit of the Si(100) surface.

4.3.4.2 Kinetic considerations

We computed transition structures and energy barriers for oxygen insertion from several dangling bond structures into Si-Si bonds of the cluster. Specifically, transition states for each possible insertion reaction from the one and two O-atom dangling bond structures were calculated to determine kinetically favored pathways at these oxygen concentrations, and also to identify factors that govern the magnitudes of the energy barriers. On the other hand, a transition state was determined for the insertion reaction involving only the most energetically favorable $\text{O}_3\text{-Si}_9\text{H}_{12}$ isomer [i.e. conversion of $\text{DB}_3(\text{OSiOSiOd})$ to $\text{ME}_3(\text{OSiOSiO})$].

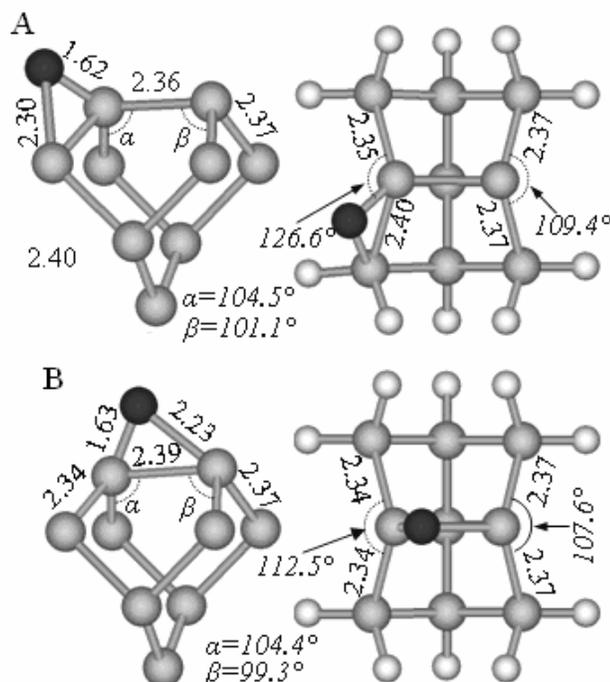


Figure 4-11. Structural information of transition state structures for oxygen migration in $O_1\text{-Si}_9\text{H}_{12}$ structures. (a) $\text{TS}_3(\text{SiSiOd-SiSiO})$. (b) $\text{TS}_3(\text{SiSiOd-SiOSi})$. Barriers for these transition states are 0.30 and 0.45 eV, respectively. Bond lengths are expressed in Å. Oxygen atoms are represented with black balls. Silicon and hydrogen atoms are represented in gray and white balls, respectively.

We calculated the transition structures for oxygen insertion from the $O_1\text{-Si}_9\text{H}_{12}$ dangling bond isomer $\text{DB}_3(\text{SiSiOd})$ into both a backbond and the dimer bond (Figure 4-11). Both transition structures have an epoxide-like ring in which the original Si-O bond is only slightly elongated, a second Si-O bond begins to form (although weak and elongated) and the Si-Si bond length barely changes, suggesting that the barriers for oxygen insertion occur early along the reaction path. The barrier for insertion into the backbond is predicted to be 0.30 eV, whereas the barrier for insertion into the dimer bond is 50% higher at 0.45 eV. This difference indicates that insertion into the backbond is the kinetic preference, even though the overall reaction is less exothermic than insertion into the dimer bond (1.22 vs. 1.47 eV). Interestingly, however, the product of the more

kinetically-favored reaction can transform, via a state-crossing event, into the lowest energy $O_1\text{-Si}_9\text{H}_{12}$ isomer, $ME_1(\text{SiSiO})$.

Table 4-5. Energy barriers for migration of oxygen atoms in $O\text{-Si}_9\text{H}_{12}\text{-O}_d$ structures from a dangling bond site to a backbond or dimer bond site in the spin-triplet state.

Reactant	Product	Barrier (eV)	Structure in Figure 4-12
$DB_3(\text{SiOSiOd})$	$ME_3(\text{SiOSiO})$	0.07	(a)
$DB_3(\text{SiSiO2d})$	$ME_3(\text{SiSiO2})$	0.36	(B)
$DB_3(\text{SiSiO2d})$	$ME_3(\text{SiOSiO})$	0.25	(C)
$DB_3(\text{OSiSiOd})$	$ME_3(\text{OxSiSiO})$	0.23	(D)
$DB_3(\text{OSiSiOd})$	$ME_3(\text{OSiSiO})$	0.21	(E)
$DB_3(\text{OSiSiOd})$	$ME_3(\text{SiOSiO})$	0.11	(f)

The energy barriers for insertion from $O\text{-Si}_9\text{H}_{12}\text{-O}_d$ structures into more stable $O_2\text{-Si}_9\text{H}_{12}$ isomers are listed in Table 4-5 and the corresponding transition structures are shown in Figure 4-12. The geometric properties of these transition structures are generally similar in that the top of the barrier is reached after only a slight stretching of the Si-Si bond into which the oxygen inserts, and at a fairly large separation between the Si and O atoms that are forming a bond. An interesting observation is that, with one exception, the insertion barriers are lower from the $O\text{-Si}_9\text{H}_{12}\text{-O}_d$ structures than from $DB_3(\text{SiSiOd})$. For example, the barriers for backbond insertion are 0.07, 0.21, 0.23 and 0.36 eV for the two O-atom structures, whereas a barrier of 0.30 eV is predicted for backbond insertion from $DB_3(\text{SiSiOd})$. Similarly, the barriers for insertion into the dimer bond are 0.11 and 0.25 eV for the $O\text{-Si}_9\text{H}_{12}\text{-O}_d$ structures, but is 0.45 eV for the one O-atom cluster. The lower insertion barriers appear to originate from the weakened Si-Si bond that is present in the $O\text{-Si}_9\text{H}_{12}\text{-O}_d$ structures. In fact, the lowest barrier is predicted for each $O\text{-Si}_9\text{H}_{12}\text{-O}_d$ structure when the oxygen atoms inserts into the elongated Si-Si bond of the cluster, and eliminates this destabilized bond from the cluster. A similar result is predicted for oxygen insertion from $DB_3(\text{OSiOSiOd})$ (Figure 4-13) to produce $ME_3(\text{OSiOSiO})$ for which a barrier of only 0.05 eV is predicted.

Coupling the thermodynamic and kinetic information determined to this point, we can begin to refine the preferred reaction pathway (Section 4.3.4.1). The preferred oxidation pathway, based on the lowest energy barriers and the relative energies of the clusters is shown in Figure 4-14. Neglecting significant differences in the preexponential factors, oxygen insertion into a Si-Si backbond is the kinetically preferred pathway from the initial $\text{DB}_3(\text{SiSiOd})$ structure, and will ultimately result in the $\text{ME}_1(\text{SiSiO})$ structure. Oxygen adsorption onto $\text{ME}_1(\text{SiSiO})$ will then produce either $\text{DB}_3(\text{OSiSiOd})$ or $\text{DB}_3(\text{SiSiO}_2\text{d})$, and the minimum energy insertion pathways from these structures, with barriers of 0.11 and 0.25 eV, respectively, both produce the $\text{ME}_3(\text{SiOSiO})$ structure. Oxygen adsorption onto the $\text{ME}_3(\text{SiOSiO})$ structure will produce $\text{DB}_3(\text{OSiOSiOd})$, which converts to $\text{ME}_3(\text{OSiOSiO})$ after overcoming a barrier of only 0.05 eV. Notice that oxygen adsorption onto $\text{ME}_3(\text{SiOSiO})$ can also generate $\text{DB}_3(\text{SiOSiOd}_2)$, which can then convert ultimately to the thermodynamically favorable $\text{ME}_1(\text{SiOSiO}_2)$ structure. A barrier for this process was not computed. An alternative route to the favorable $\text{ME}_3(\text{SiOSiO})$ structure is for $\text{DB}_3(\text{SiSiOd})$ to overcome a 0.45 eV barrier to generate $\text{ME}_3(\text{SiOSi})$, followed by a state crossing to $\text{ME}_1(\text{SiOSi})$ and then oxygen adsorption to produce $\text{DB}_3(\text{SiOSiOd})$. Finally, the oxygen atom attached at the dangling bond structure must overcome a small 0.07 eV barrier to insert into a backbond and generate the $\text{ME}_3(\text{SiOSiO})$ structure. Based on the predicted insertion barriers, the bottleneck for the second route to $\text{ME}_3(\text{SiOSiO})$ is the production of $\text{ME}_1(\text{SiOSi})$ since the formation of this species competes with the formation of $\text{ME}_1(\text{SiSiO})$. Unless the preexponential factors differ significantly, the insertion barriers suggest that $\text{ME}_1(\text{SiSiO})$ will be produced preferentially over $\text{ME}_1(\text{SiOSi})$.

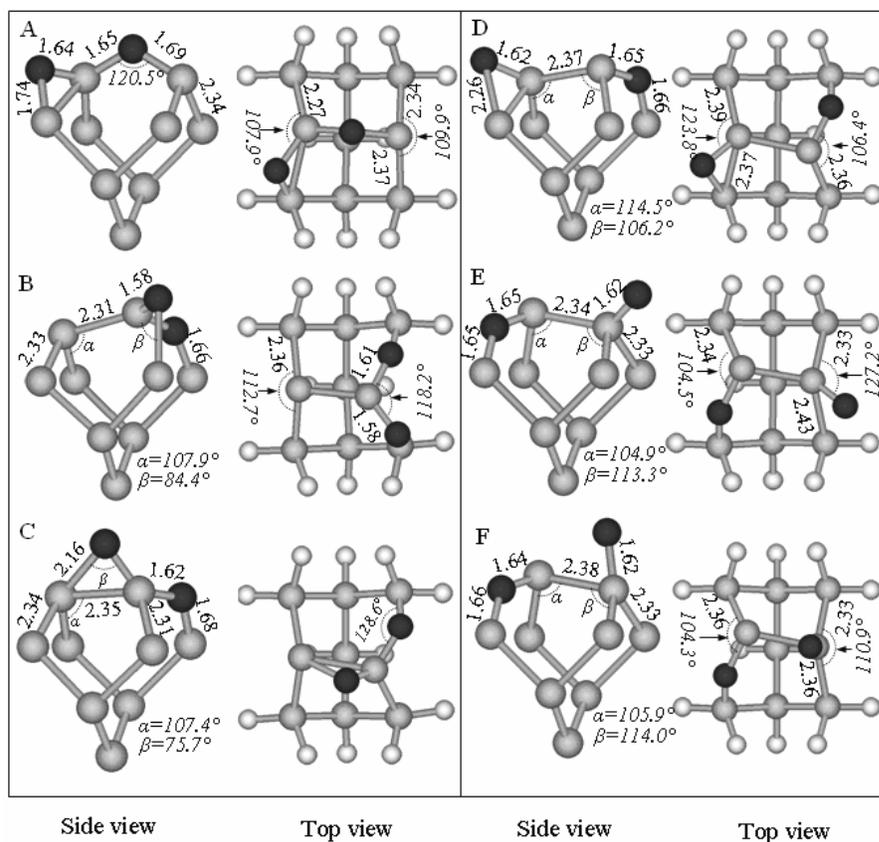


Figure 4-12. Structural information of transition state structures for oxygen insertion in O_2 - Si_9H_{12} structures. A) $TS_3(SiOSiOd-SiOSiO)$. B) $TS_3(SiSiO_2d-SiSiO_2)$. C) $TS_3(SiSiO_2d-SiOSiO)$. D) $TS_3(OSiSiOd-OxSiSiO)$. E) $TS_3(OSiSiOd-OSiSiO)$. F) $TS_3(OSiSiOd-SiOSiO)$. Bond lengths are expressed in Å. Oxygen atoms are represented with black balls. Silicon and hydrogen atoms are represented in gray and white balls, respectively.

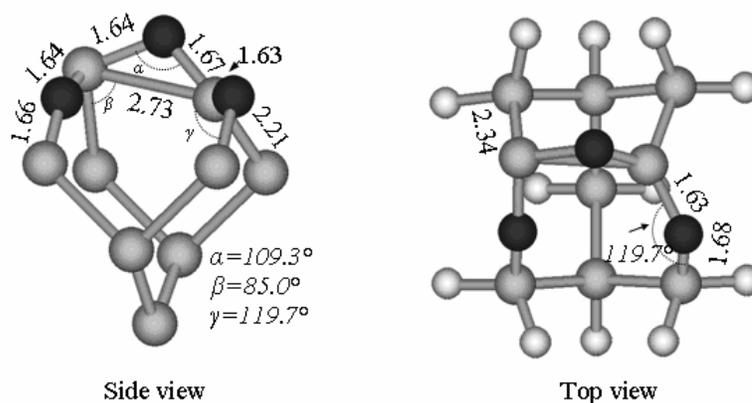


Figure 4-13. Structural information of transition state structure $TS_3(OSiOSiOd-OSiSiO)$. Bond lengths are expressed in Å. Oxygen atoms are represented with black balls. Silicon and hydrogen atoms are represented in gray and white balls, respectively.

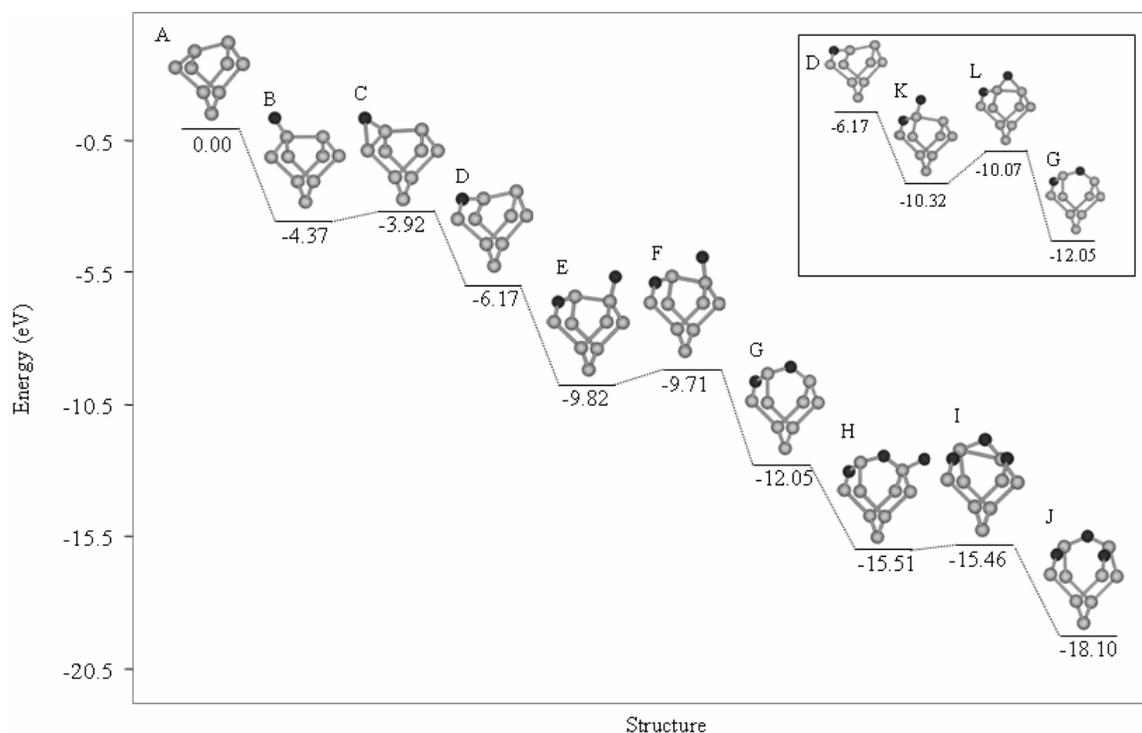


Figure 4-14. Proposed preferred path for initial steps of oxidation of Si(100)-(2x1) by oxygen atoms. Energy of structures are relative to that of $ME_1(\text{SiSi})$ plus three $O(^3P)$ at infinite separation. A) $ME_3(\text{SiSi})$. B) $DB_3(\text{SiSiOd})$. C) $TS_3(\text{SiSiOd-SiSiO})$. D) $ME_1(\text{SiSiO})$. E) $DB_3(\text{SiOSiOd})$. F) $TS_3(\text{SiOSiOd-SiOSiO})$. G) $ME_3(\text{SiOSiO})$. H) $DB_3(\text{OSiOSiOd})$. I) $TS_3(\text{OSiOSiOd-OSiOSiO})$. J) $ME_3(\text{OSiOSiO})$. Insert: alternative path.

CHAPTER 5
ATOMIC OXYGEN INSERTION INTO ETHYLENE- AND
ACETYLENE-TERMINATED Si(100)-(2x1)

5.1 Introduction

Surface functionalization, also known as organic modification, is the process of depositing layers of organic molecules on semiconductor surfaces [36]. This process stems from a desire to impart some property of the organic materials to the semiconductor device, especially since the rich chemistry of carbon can be used to provide new capabilities in optical, electronic and mechanical functions to the semiconductor surfaces. For instance, hydrocarbon films may be useful as low-dielectric materials for microelectronics, and would be especially useful if such films can form covalent bonds to the surface that chemically and electrically passivate the surface. Furthermore, covalently bound monolayers may serve as an interface between silicon and other organic materials, particularly if monolayers with a variety of chemical functionality can be produced. The C=C bond in olefins has been found to be very reactive at silicon dangling bond sites, as observed, for example, in early studies of propylene and ethylene chemisorption on the Si(100) surface [35, 120-121]. Based on such results, it has been suggested that the attachment of a variety of bifunctional organic molecules to Si(100) can be achieved by using C=C groups to achieve bonding to the surface while preserving the second bond functionality for further surface reactions [35]. These organic molecules might be designed to serve in place of gate oxides in metal-oxide semiconductor field-effect transistor (MOSFET) devices, for example.

In MOSFETs, the high wire resistance of smaller metal lines and the crosstalk between closely spaced metal increase the interconnect resistance and capacitance product delay. This requires a low-dielectric constant (low k) material as the interlayer dielectric and low resistance conductors such as copper. Silicon oxycarbide (SiC_xO_y), a low k hybrid between organic and inorganic materials, is one of the most favorable candidates for an interlayer dielectric in MOSFETs [39]. In addition to its low k value, silicon oxycarbide offers resistance to diffusion of copper and exhibits the desirable material and integration properties of silicon dioxide (SiO_2) [39].

SiC_xO_y thin films are generally deposited at high temperature by chemical vapor deposition (CVD) [37-38]. However, plasma-assisted deposition at low temperature may provide greater control over the properties of silicon oxycarbide films and other oxidized organic layers since thermally activated reactions would be inhibited. For example, thin films of organic oxygenates could be prepared by oxidizing adsorbed hydrocarbon layers using an oxygen plasma. Since plasma-assisted oxidation occurs efficiently at low temperature, it may be possible to introduce specific oxygen-containing chemical functionality into the organic thin film, depending on the reaction selectivity of the active oxygen species toward the organic adsorbate. However, the interactions of gaseous radicals with adsorbate-covered silicon surfaces are relatively poorly understood, mainly because few fundamental studies of radical-surface interactions have been conducted under well-controlled ultrahigh vacuum (UHV) conditions. It is therefore unclear how gaseous atomic oxygen will react with adsorbate-modified Si(100) surfaces.

To our knowledge, only a single UHV investigation of the interactions between gaseous O-atoms and organic adsorbates on Si(100) has been reported. In this work,

Auger electron spectroscopy (AES) was used to study the oxidation of acetylene (C_2H_2)-, and ethylene (C_2H_4)-covered Si(100) by gaseous oxygen atoms [14]. Oxygen plasma species were replicated by generating a 50/50 mixture of ground-state $O(^3P)$ and electronically excited $O(^1D)$ by the 157 nm photolysis of O_2 . From AES measurements, it was found that the O atom adsorption probability for oxygen coverages in the 1-3 monolayer regime is on the order of 0.1 on these olefin-covered surfaces. In addition, the investigators did not observe loss of carbon on either surface and suggested that there first must be extensive oxidation of the near-surface region of silicon before the removal of carbon chemisorbed on Si(100). However, these authors were unable provide chemical state information about the oxidized products so details about the oxidation mechanism remain uncertain.

In this work, we used gradient-corrected density functional theory (DFT) to investigate oxygen incorporation into model C_2H_2 - and C_2H_4 -terminated Si(100) surfaces. We focused on determining the relative energies of the products that result from oxygen atom insertion into the different bonds that are available on the olefin-terminated surfaces, and on elucidating the predominant factors that determine the reaction energetics. We also calculated energy barriers for the oxygen insertion reactions that yield the most energetically favorable products. We find that the formation of siloxane bridges is both thermodynamically and kinetically favored over other insertion pathways on both surfaces.

5.2 Theoretical Approach

We used Kohn-Sham density functional theory (DFT) calculations of silicon clusters that represent the local bonding arrangement of the Si(100)-(2x1) surface. We chose to use the Si_9H_{12} cluster (Figure 3-1) which is the smallest structure that

appropriately represents the key structural characteristics of Si(100)-(2x1) (i.e., covalent tetrahedral sp^3 arrangement of Si-Si bonds and a tilted dimer). Truncated Si-Si bonds in this cluster were terminated with hydrogen atoms; which preserve the tetrahedral bonding and have negligible effect on the predicted energies [102, 115]. The clusters were constrained by imposing boundary conditions that mimic the strain that the bulk silicon atoms would impose on the surface dimer under study. This was attained by fixing the hydrogen atoms in their positions. Two types of hydrogen atoms, depending on the Si-Si bond type that they are terminating can be found in a Si_9H_{12} cluster: The bulk atoms that were fixed along tetrahedral directions, and the neighboring dimer atoms, that were constrained in positions that mimic nearest silicon dimer bonds. Third and fourth layer silicon atoms were not directly constrained, while the first and second layer atoms were allowed to completely relax without any constraint, other than the small constraints place on them by the few Si-H bonds that they have. All the chemically active atoms were also allowed to relax completely unconstrained.

Kohn-Sham density functional theory (DFT) [41-44] was used for the electronic structures calculations. We used here the B3LYP hybrid-gradient-corrected method [53, 116] which calculates the exchange correlation term of the electronic energy by means of a linear combination of local, gradient-corrected and Hartree-Fock exact exchange terms with the Becke gradient-corrected term (B88) [49], and the local and gradient-corrected correlation terms of Vosko-Wilk-Nusair (VWN) [48] and Lee-Yang-Parr (LYP) [50], respectively. A mixed approach was used for the basis sets that expand the electronic wave function. A diffuse triple- ζ plus polarization 6-311++G(2d,p) Pople basis set was used to describe the chemically active atoms (i.e.: the surface Si atoms, four Si atoms of

the first subsurface layer, the oxygen atom and the adsorbed olefin), while the remaining subsurface silicon atoms and terminating hydrogen atoms were described with a double- ζ plus polarization 6-31G(d) Pople basis set. All calculations used an unrestricted approach to calculate the open-shell structures of the spin-triplet states.

In all these calculations we did not impose symmetry constraints on the structures, since experimental results [122-124] indicate that the C-C bond of adsorbed ethylene is twisted by 11.4° with respect to the Si dimer axis, resulting in a 23 meV increase of the binding energy. The quantum chemistry package Gaussian03 [71] was used to run the calculations.

5.3 Results and Discussion

A primary goal of this study was to characterize the reaction products that result when gaseous $O(^3P)$ atoms interact with C_2H_2 - and C_2H_4 -covered Si(100). Toward this end, we performed energy minimization for various products of O incorporation into the C_2H_2 - and C_2H_4 -modified surfaces. We specifically considered the relative energies of the products that result when the oxygen atom inserts into a C-C bond, a Si-C bond, a C-H bond or a Si-Si backbond. Since we investigated several structures for both spin-singlet and spin-triplet surfaces, we developed a shorthand notation of capital letters followed by a subscript and a code in parenthesis to label the clusters to facilitate discussion. In this notation the letters A or E designate the surface as either acetylene- or ethylene-covered Si(100), respectively. This letter is followed by a subscript (1 for the spin-singlet and 3 for the spin-triplet states) and a combination of three atomic symbols in parenthesis. These atomic symbols represent the bridge bond that is formed after the oxygen atom inserts into the surface. Four types of oxidized bridges may form: C-O-C, C-O-H, C-O-Si and Si-O-Si in which the oxygen breaks a C-C, C-H, Si-C or Si-Si bond,

respectively; and one case of a single bond formation, in which the oxygen atom adsorbs on a dangling bond. In the latter case, the symbol Od is in parenthesis and it represents that the oxygen atom is attached at dangling bonding site. In the case of the bare clusters or clusters with only olefins adsorbed, the symbols included in parenthesis are SiSi to symbolize that no oxygen atom has reacted with the surface.

We ran quantum chemical calculations to analyze the relative energies of the oxidized structures and transition states to determine the preferred products and details of their formation. The relative energies are defined with respect to the energies of the spin-singlet C₂H₄- and C₂H₂-terminated Si(100) clusters, which we labeled as A₁(SiSi) (Figure 5-1A) and E₁(SiSi) (Figure 5-1C), respectively. For oxygen insertion into the ethylene-covered Si(100) structures, we defined the zero of energy as in Equation 5-1a,

$$E_1(\text{SiSi}) + \text{O}({}^3P) = 0.00 \text{ eV} \quad (5-1a)$$

while for oxygen insertion into the C₂H₂-terminated clusters, the energy reference was defined in Equation 5-1b.

$$A_1(\text{SiSi}) + \text{O}({}^3P) = 0.00 \text{ eV} \quad (5-1b)$$

Before presenting our results for oxygen atom incorporation into the olefin-modified Si(100) surfaces, we explain some details of the chemistry of formation of A₁(SiSi) and E₁(SiSi) and how our results compare to those available in the literature. Given the similarity between a C=C bond and the silicon dimer bond structure with the Si-Si π interaction, it has been reported that the formation of A₁(SiSi) and E₁(SiSi) is analogous to [2s+2s] cycloaddition reactions [125]. In organic systems, cycloadditions are reactions in which two π bonded molecules come together to form a new cyclic molecule, losing two π bonds and making two new σ bonds in the process [36].

Specifically, in a $[2_s+2_s]$ reaction two alkenes come together to form a new four-membered ring, subject to the Woodward-Hoffman selection rules [126]. However, while this $[2s+2s]$ cycloaddition model is well accepted for C_2H_4 , chemisorption of C_2H_2 on Si(100) is still controversial, with some researchers [123, 127] reporting that the unsaturated hydrocarbon molecule is bonded to two surface Si atoms, but that these Si atoms do not necessarily belong to the same dimer. Others [121] even suggest that when C_2H_2 adsorbs on top of the dimer bond of the Si(100) surface, the silicon dimer bond is cleaved.

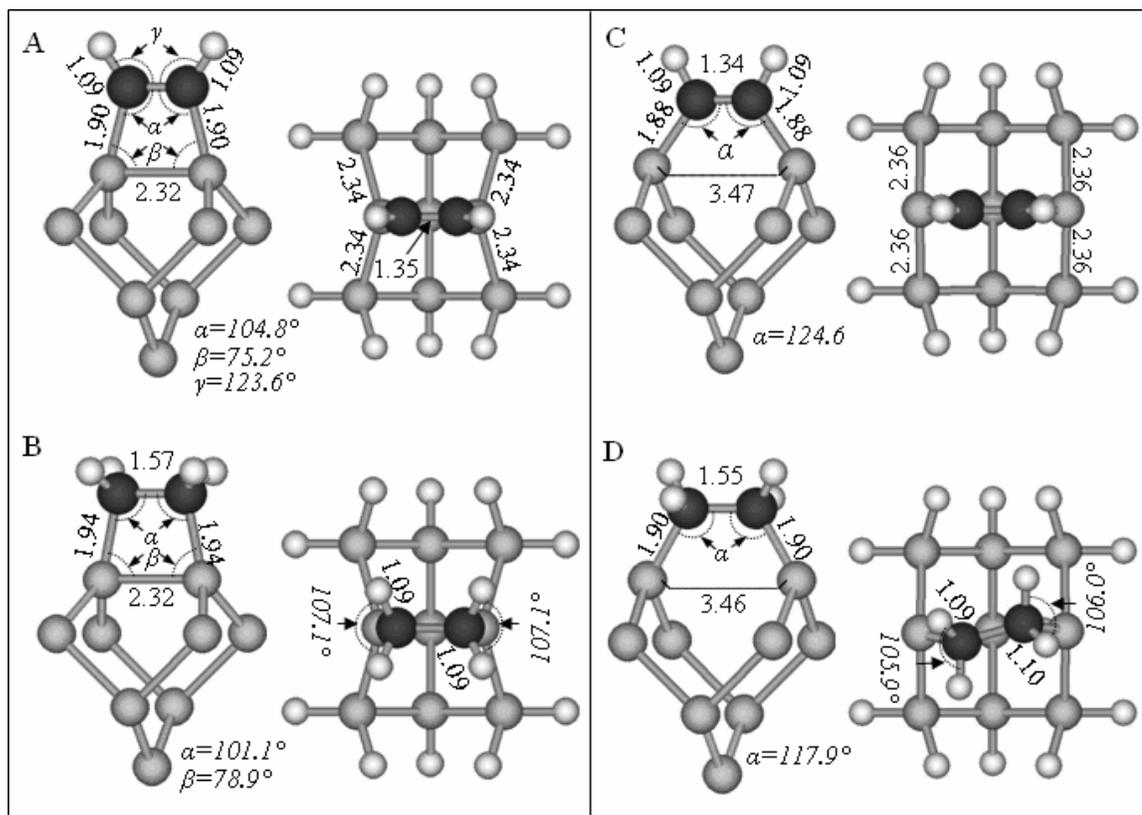


Figure 5-1. Structural information of optimized clusters for olefin-covered Si(100)-(2x1). Top views include terminating hydrogen atoms to stress adsorbate orientation with respect to the silicon grid. A) $A_1(\text{SiSi})$. B) $A_3(\text{SiSi})$. C) $E_1(\text{SiSi})$. D) $E_3(\text{SiSi})$. Carbon atoms are in black, silicon atoms in gray and hydrogen atoms in white. Bond lengths are expressed in Å.

Table 5-1. $E_1(\text{SiSi})$ structure and energy of adsorption compared to those of reported dimerized C_2H_4 -terminated $\text{Si}(100)$ structures.

Reference	$E_{\text{ads}}(\text{eV})$	C-C (Å)	C-Si (Å)	Si-Si (Å)	Si-C-C (°)
This work	1.80	1.57	1.94	2.32	101.1
123	1.89	1.56	1.96	2.37	N/A
125	1.87	1.57	1.953	2.36	101.4
128	1.81	1.52	1.93	2.33	N/A

Table 5-2. $A_1(\text{SiSi})$ structure and energy of adsorption compared to those of reported dimerized C_2H_2 -terminated $\text{Si}(100)$ structures.

Reference	$E_{\text{ads}}(\text{eV})$	C-C (Å)	C-Si (Å)	Si-Si (Å)	Si-C-C (°)
This work	2.58	1.32	1.90	2.32	104.8
123	2.74	1.37	1.91	2.37	N/A
125	2.61	1.353	1.909	2.368	105.5
129	2.81	1.36	1.90	2.36	N/A

The energy of adsorption and the main structural characteristics of $E_1(\text{SiSi})$ and $A_1(\text{SiSi})$ are compared to theoretical results available in the literature in Tables 5-1 and 5-2, respectively. We calculated the structures of $E_1(\text{SiSi})$ and $A_1(\text{SiSi})$ (Figure 5-1), and we predict that in $E_1(\text{SiSi})$ the ethylene C-C bond stretches upon adsorption from the molecular value of 1.34 to 1.57 Å as a result of the C-C π bond cleavage, and that two identical Si-C σ bonds (1.90 Å) form as well. Also, according to our calculations, the silicon dimer bond is symmetric with respect to the underlying Si atoms and its bond length is 2.32 Å. For $A_1(\text{SiSi})$, we predict that acetylene forms a di- σ bonded adsorbate complex on the $\text{Si}(100)$ surface, retaining a C-C double bond (1.32 Å) and decreasing the Si-Si-C bond angle from its optimal value of 109.5° to 104.8°. Our results compare reasonably well with the values available in the literature, with the differences attributed to the fact that the other values were obtained using different computational methods.

We also optimized the $E_3(\text{SiSi})$ and $A_3(\text{SiSi})$ structures, which correspond to the spin-triplet isomers for the C_2H_4 - and C_2H_2 -covered $\text{Si}(100)$, respectively, in which the Si-Si dimer bond is cleaved upon olefin adsorption. These cleaved structures were

investigated to compare their energies to those the spin-singlet counterparts. We find that the energies of olefin adsorption are 0.01 eV for $E_3(\text{SiSi})$ and 0.83 eV for $A_3(\text{SiSi})$, which are 1.79 and 1.74 eV less favorable than their corresponding spin-singlet olefin-terminated structures. These results support the $[2s+2s]$ cycloaddition model for ethylene and acetylene adsorption on the Si(100) surface dimer. Additionally, we observed that the C-C bond of adsorbed C_2H_4 remains aligned with the silicon dimer bond in $E_1(\text{SiSi})$ and that the $-\text{CH}_2$ groups remain symmetric with another. In contrast, the C-C bond in the $E_3(\text{SiSi})$ structure rotates out of the $[\bar{1}\bar{1}0]$ direction and the $-\text{CH}_2$ groups also rotate in opposite directions about the C-C bond axis. These structural changes act to relieve strain in the cluster and are possible because the $E_3(\text{SiSi})$ structure is less rigid than $E_1(\text{SiSi})$ structure due to the absence of a constrained ring.

After confirming that $E_1(\text{SiSi})$ and $A_1(\text{SiSi})$ are the minimum energy structures of the adsorbed olefins, we used a bond energy model to estimate the main factors that contribute to the energy of formation of an oxidized cluster. In this model, the calculated energy of an oxidized cluster (ΔE_{UB3LYP}) is assumed to be given by Equation 5-2.

$$\Delta E_{UB3LYP} = \Delta E_{bond} + \delta \Delta E_{cleavage} + \Delta E_{excess} \quad (5-2)$$

In Eq. 5-2 ΔE_{bond} is the energy of formation of the oxidized bridge in a representative molecule, $\Delta E_{cleavage}$ is the energy required to cleave the dimer bond in the olefin-Si(100) complex, where δ equals zero or one for spin-singlets and triplets, respectively, and ΔE_{excess} represents the energy contributions to ΔE_{UB3LYP} that are not taken into account through ΔE_{bond} and $\Delta E_{cleavage}$. The excess energy is primarily determined by the change in strain energy upon oxygen insertion into the cluster, but it also represents the intrinsic error in this simple model. A key assumption in the bond energy model is that the bonds

being broken and formed are localized and have well-defined energies. The model therefore implies that oxygen insertion modifies other bonds in the cluster only indirectly by altering the geometric structure and hence the strain energy of the cluster.

Table 5-3. Calculated energy of formation of the different oxidized bridges that form when an oxygen atom inserts into the C₂H₂- and C₂H₄-terminated Si₉H₁₂ clusters. Energy is expressed in eV.

Bridge	Reaction	ΔE_{bond}
C-O-C (epoxide)	$\text{H}_2\text{C}=\text{CHSiH}_3 + \text{O}({}^3P) \rightarrow \text{H}_2\text{COCHSiH}_3$	-3.54
C-O-C (ether)	$\text{H}_3\text{C}-\text{CH}_2\text{SiH}_3 + \text{O}({}^3P) \rightarrow \text{H}_3\text{COCH}_2\text{SiH}_3$	-3.65
C-O-H (alkyl)	$\text{H}_3\text{C}-\text{CH}_3 + \text{O}({}^3P) \rightarrow \text{H}_3\text{C}-\text{CH}_2\text{OH}$	-4.08
C-O-H (vinyl)	$\text{H}_2\text{C}=\text{CH}_2 + \text{O}({}^3P) \rightarrow \text{H}_2\text{C}=\text{CH}_2\text{OH}$	-4.34
Si-O-C	$\text{H}_3\text{CH}_2\text{C}-\text{SiH}_3 + \text{O}({}^3P) \rightarrow \text{H}_3\text{CH}_2\text{COSiH}_3$	-5.14
Si-O-Si	$\text{H}_3\text{Si}-\text{SiH}_3 + \text{O}({}^3P) \rightarrow \text{H}_3\text{SiOSiH}_3$	-6.68

To estimate the bond energy terms, we calculated the energies of formation of oxidized bridges in small, linear molecules that do not experience the changes in bond strain that occur in the surface clusters upon oxygen insertion. We performed DFT/UB3LYP energy minimization calculations using diffuse triple- ζ plus polarization 6-311++G(2d,p) basis sets for each of the representative molecules before and after an oxygen atom is inserted into a bond to form the oxidized bridge of interest. The molecular formation reactions and their corresponding ΔE_{bond} values are shown in Table 5-2. Our calculated values compare well with results obtained using values reported by Norman [117] for the crystalline Si-O and Si-Si bonds and by Lide and coworkers [130] for the organic molecule bonds. The $\Delta E_{cleavage}$ term is included in the bond energy model because the energies of formation are referenced to the energies of the spin-singlet olefin-surface complexes in which the dimer bond is intact. Thus, the formation of an oxidized cluster of triplet spin may be considered to occur in two steps, namely, cleavage of the dimer bond of the olefin-surface complex, followed by oxygen insertion. The values of $\Delta E_{cleavage}$ are 1.74 and 1.79 eV for the ethylene- and acetylene-covered surfaces,

respectively, and represent the difference in energy of the singlet and triplet structures of those reactants. By explicitly including the $\Delta E_{cleavage}$ term, the excess energy ΔE_{excess} represents the change in strain resulting from oxygen insertion into either the singlet or triplet reactant.

5.3.1 Relative Energies of Oxidized Ethylene-Covered Si(100) Clusters

We obtained the energies of the singlet and triplet oxidized products that result from oxygen insertion into different bonds of the C₂H₄-covered surface (Figures 5-4 and 5-5). For each set of products, the trend in relative energies is determined by the strengths of the different oxidized bridges, as given by the bond energy term (Table 5-2). Structures with a C-O-C bridge are the highest energy products, followed by the alcohols, and the incorporation of oxygen into a Si-C bond. The formation of a siloxane-bridge at a silicon backbond results in the minimum energy structure. Additionally, a comparison of Figures 5-4 and 5-5 reveals that the singlet clusters are more favorable than their triplet counterparts in all cases. Thus, the calculations predict that the dimer bond will remain intact during oxygen insertion into any of the available surface bonds. This prediction indicates that any strain relief that may occur by cleaving the dimer bond to accommodate an oxygen atom does not compensate the energy required to cleave the dimer bond.

Table 5-4. Penalty energies of spin-singlet O-C₂H₄- Si₉H₁₂ isomers. Contributions of the different energy effects to the relative energies calculated using DFT/UB3LYP (ΔE_{UB3LYP}). Reference: E₁(SiSi) + O(³P) = 0.00 eV. Energies are given in eV. Column for $\Delta E_{cleavage}$ omitted, since it is 0 for all structures.

Structure	ΔE_{bond}	ΔE_{excess}	ΔE_{UB3LYP} [Eq. (5-2)]
E ₁ (COC)	-3.65	0.00	-3.65
E ₁ (COH)	-4.08	-0.07	-4.15
E ₁ (SiOC)	-5.14	-0.69	-5.83
E ₁ (SiOSi)	-6.68	0.45	-6.23

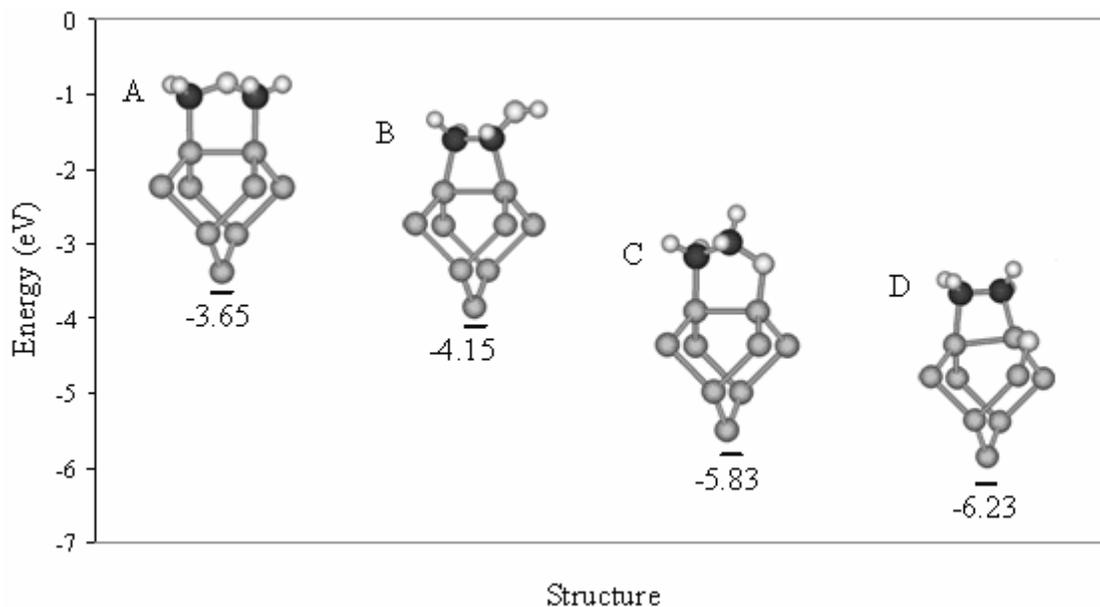


Figure 5-2. Relative energies of spin-singlet $\text{O-C}_2\text{H}_4\text{-Si}_9\text{H}_{12}$ isomers. A) $E_1(\text{COC})$. B) $E_1(\text{COH})$. C) $E_1(\text{SiOC})$. D) $E_1(\text{SiOSi})$. Reference: $E_1(\text{SiSi}) + \text{O}(^3P) = 0.00 \text{ eV}$. Carbon atoms are in black, silicon atoms in gray, oxygen atoms are the large white balls and hydrogen atoms are the small white balls.

The bond energy model provides additional insights for understanding the energetic changes that occur upon oxygen insertion and reveals effects that are not evident from chemical intuition only. For example, the formation of ether and alcohol groups produces relatively small changes in the strain energy (Tables 5-4 and 5-5), although these reactions do alter the adsorbate structure (Figure 5-4). For each ether isomer, the CH_2 groups rotate about their respective Si-C bonds and the C-O-C plane is tilted significantly away from the Si-C-C-Si ring. According to the bond energy model that we use in this work, these changes introduce no strain into the dimerized structure $E_1(\text{COC})$, but cause an 0.18 eV increase in strain for the $E_3(\text{COC})$ structure. Alcohol formation has only a small effect on the strain as well (Figure 5-4C), which is perhaps more easily anticipated since COH formation occurs on the periphery of the adsorbate molecule and does not affect appreciably the rest of the structure..

Table 5-5. Penalty energies of spin-triplet O-C₂H₄- Si₉H₁₂ isomers. Contributions of the different energy effects to the relative energies calculated using DFT/UB3LYP (ΔE_{UB3LYP}). Reference: $E_1(\text{SiSi}) + \text{O}(^3P) = 0.00$ eV. Energies are given in eV.

Structure	ΔE_{bond}	$\Delta E_{cleavage}$	ΔE_{excess}	ΔE_{UB3LYP} (Eq. 5-2)
E ₃ (COC)	-3.65	1.74	0.19	-1.72
E ₃ (COH)	-4.08	1.74	0.05	-2.29
E ₃ (SiOC)	-5.14	1.74	0.09	-3.31
E ₃ (SiOSi)	-6.68	1.74	0.24	-4.70

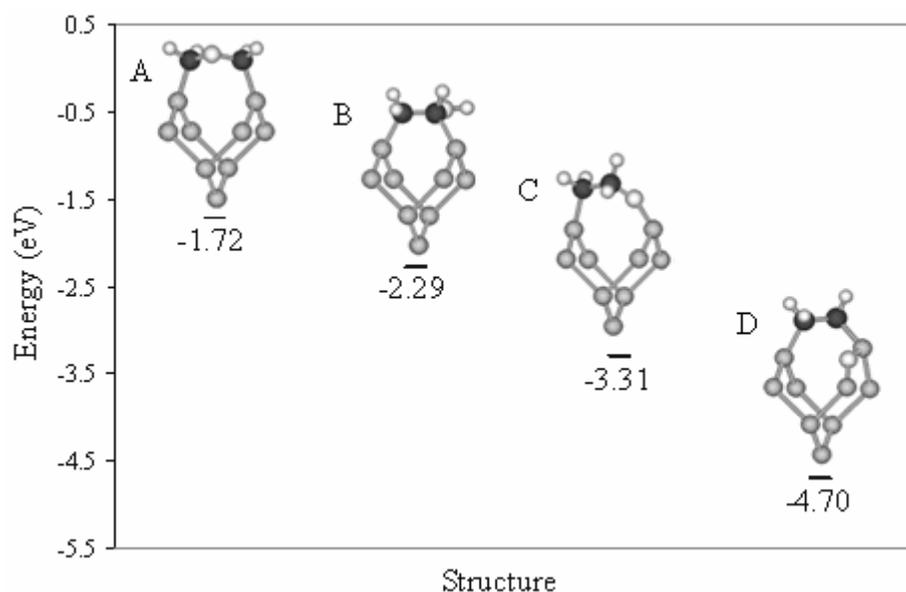


Figure 5-3. Relative energies of spin-triplet O-C₂H₄-Si₉H₁₂ isomers. A) E₃(COC). B) E₃(COH). C) E₃(SiOC). D) E₃(SiOSi). Reference: $E_1(\text{SiSi}) + \text{O}(^3P) = 0.00$ eV.

Strain effects are more pronounced in the formation of the Si-O-C and Si-O-Si linkages. Specifically, the spin-triplet Si-O-Si and Si-O-C clusters each have smaller ΔE_{excess} values than their spin-singlet isomers (Tables 5-4 and 5-5), which indicates that structures with a cleaved dimer bond are subject to smaller changes in strain during oxygen insertion. This occurs because the triplet clusters are less constrained than the singlets, since they lack a silicon dimer bond, and can therefore more easily adopt geometric configurations that minimize surface strain when oxygen is inserted into the structure. This difference is most evident for the E₃(SiOC) (Figure 5-4F) and E₁(SiOC)

(Figure 5-4B) structures. For the triplet cluster, the strain energy increases by only 0.09 eV upon oxygen insertion into the Si-C bond, whereas the formation of $E_1(\text{SiOC})$ is accompanied by strain relief of 0.69 eV. This substantial decrease in the strain energy can be attributed to the release of ring strain since the formation of $E_1(\text{SiOC})$ involves the conversion of a four-membered ring to a five-membered ring, and it is well known that three- and four-membered rings are highly strained, while five-membered ring are much less strained [131].

The strain energy accompanying oxygen insertion into a Si-Si backbond is also influenced by the presence of the Si-Si dimer bond. In the formation of $E_1(\text{SiOSi})$, the strain energy increases by 0.45 eV, because the four-membered ring remains intact but is pushed out of its original symmetry plane by the Si-O-Si bridge at the backbond (Figure 5-4). The strain also increases during the formation of $E_3(\text{SiOSi})$ but only by 0.24 eV, since this structure is better able to accommodate the Si-O-Si bridge. In addition to rotation of the C-C bond out of the original plane of symmetry, a rotation about the C-C axis also occurs, enabling the hydrogen atoms to achieve a staggered conformation in the $E_3(\text{SiOSi})$ structure (Figure 5-4). Interestingly, the energy of formation of $E_1(\text{SiOSi})$ is close to that for the incorporation of an oxygen atom into a spin-singlet bare cluster Si_9H_{12} (Table 4-2), which suggests that these structures experience similar amounts of strain. Overall, the binding energy model that we have used appears to adequately capture the dominant contributions to the formation energies of oxidized products on the ethylene-covered Si(100) clusters, despite the initial assumption made regarding the localization of the bond formation, and considering the different penalty energies as isolated, independent and additive contributors to the total energy.

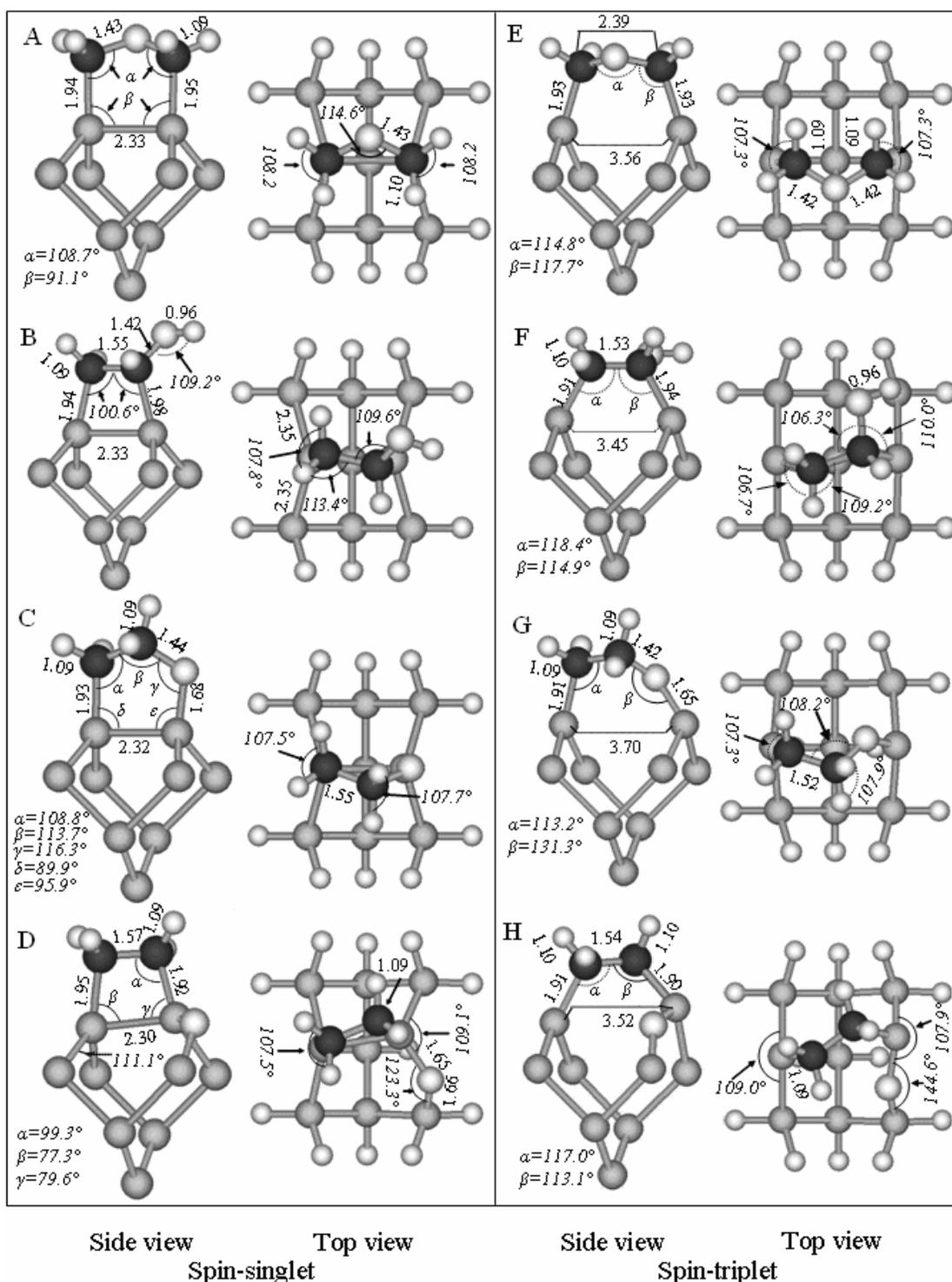


Figure 5-4. Structural information of O-C₂H₄-Si₉H₁₂ isomers. Spin-singlet structures: A) E₁(COC). B) E₁(COH). C) E₁(SiOC). D) E₁(SiOSi). Spin-triplet structures: E) E₃(COC). F) E₃(COH). G) E₃(SiOC). H) E₃(SiOSi). Oxygen and hydrogen atoms are represented by large and small white balls, respectively. Carbon and silicon atoms are represented by black and gray balls, respectively. Bond lengths are expressed in Å.

5.3.2 Relative Energies of Oxidized Acetylene-terminated Surfaces

The relative energies of the products resulting from oxygen incorporation into the C₂H₂-terminated surface (Figures 5-7 and 5-8) follow the same general trend as predicted for the C₂H₄-terminated surface. For each type of oxidized bridge, the singlet structure is predicted to be energetically favored over the triplet, indicating that the dimer bond will remain intact during oxygen insertion into any of the bonds on these olefin-terminated surfaces. Also, for each spin state, the relative energies of the products are dictated by the strengths of the oxidized bridges that form; the relative energies of the products are COC > COH > COSi > SiOSi. Similar changes in bond strain are also predicted for oxygen insertion into the C₂H₂-terminated surface as found for the C₂H₄-terminated surface. For example, upon Si-O-Si formation at the backbond, more strain is introduced into the singlet than the triplet C₂H₂-terminated surface (Tables 5-6 and 5-7). Also, oxygen insertion into the Si-C bond results in significantly more strain relief when the dimer bond remains intact than if this bond is cleaved; the excess energies for the formation of A₁(SiOC) and A₃(SiOC) are $\Delta E_{excess} = -0.95$ and -0.02 eV, respectively. In fact, the strain relief is so significant for A₁(SiOC) that its energy is only 0.07 eV higher than that of A₁(SiOSi), for which the strain increase is 0.52 eV.

Table 5-6. Penalty energies of spin-singlet O-C₂H₂- Si₉H₁₂ isomers. Contributions of the different energy effects to the relative energies calculated using DFT/UB3LYP (ΔE_{UB3LYP}). Reference energy: A₁(SiSi) + O(³P) = 0.00 eV. Energies are given in eV. Column for $\Delta E_{cleavage}$ omitted, since it is 0.00 eV for all the spin-singlet structures.

Structure	ΔE_{bond}	ΔE_{excess}	ΔE_{UB3LYP} (Eq. 5-2)
A ₁ (COC)	-3.54	0.54	-3.00
A ₁ (COH)	-4.34	-0.28	-4.62
A ₁ (SiOC)	-5.14	-0.95	-6.09
A ₁ (SiOSi)	-6.68	0.52	-6.16

Table 5-7. Penalty energies of spin-triplet O-C₂H₂- Si₉H₁₂ isomers. Contributions of the different energy effects to the relative energies calculated using DFT/UB3LYP (ΔE_{UB3LYP}). Reference energy: A₁(SiSi) + O(³P) = 0.00 eV. Energies are given in eV.

Structure	ΔE_{bond}	$\Delta E_{cleavage}$	ΔE_{excess}	ΔE_{UB3LYP} (Eq. 5-2)
A ₃ (COC)	-3.54	1.74	-0.03	-1.83
A ₃ (COH)	-4.34	1.74	-0.16	-2.76
A ₃ (SiOC)	-5.14	1.74	-0.02	-3.42
A ₃ (SiOSi)	-6.68	1.74	0.39	-4.55

While the trends in oxygen insertion chemistry are very similar on the olefin-terminated surfaces investigated, the C-C π bond does have a distinct influence on the relative energies and structures of the oxygen insertion products on the C₂H₂-terminated surface. Firstly, the change in strain energy is generally greater for oxygen insertion into the acetylene-terminated surface, as may be seen by comparing the excess energies for Si-O-C and Si-O-Si formation on both surfaces (Tables 5-4 to 5-7). Inspection of the corresponding surface structures provides insights for understanding these differences. For example, for each oxidized product on the C₂H₄-terminated surface, the C-C bond is predicted to rotate away from the $[\bar{1}\bar{1}0]$ direction, and the CH₂ groups also rotate about the Si-C bonds, with these structural changes acting to reduce strain introduced by oxygen insertion (Figure 5-4). In contrast, rotation of and about the C-C double bond of the C₂H₂-terminated structures is strongly hindered and, consequently, this bond remains parallel with either the $[\bar{1}\bar{1}0]$ direction, for most structures, or with the Si-Si dimer bond.

Oxygen insertion into the C-C double bond is a particularly interesting case. This reaction produces an epoxide-like structure, A₃(COC), on the triplet surface, for which the C-O-C bond is tilted significantly out of the Si-C-C-Si plane. Interestingly, an

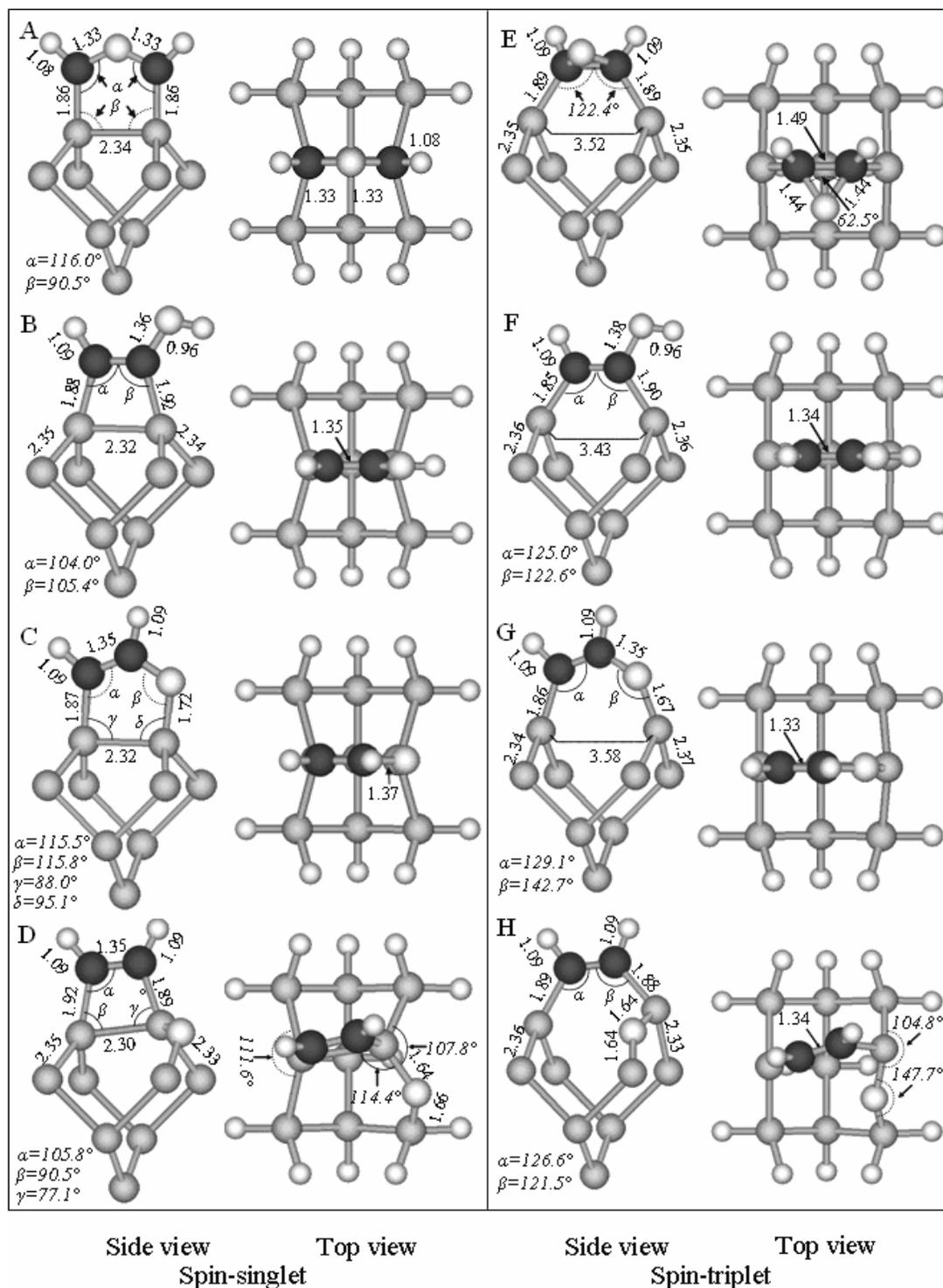


Figure 5-5. Structural information of $\text{O-C}_2\text{H}_2\text{-Si}_9\text{H}_{12}$ isomers. Spin-singlet structures: A) $A_1(\text{COC})$. B) $A_1(\text{COH})$. C) $A_1(\text{SiOC})$. D) $A_1(\text{SiOSi})$. Spin-triplet structures: E) $A_3(\text{COC})$. F) $A_3(\text{COH})$. G) $A_3(\text{SiOC})$. H) $A_3(\text{SiOSi})$. Oxygen and hydrogen atoms are represented by large and small white balls, respectively. Carbon and silicon atoms are represented by black and gray balls, respectively. Bond lengths are expressed in Å.

epoxide does not form when an oxygen atom inserts into the C-C double bond of the singlet C_2H_2 -terminated surface. Oxygen insertion into the C-C double bond of the singlet cleaves the double bond and produces an C-O-C bridge that lies within a planar, five-membered ring that is parallel with the $[\bar{1}10]$ direction (Figure 5-7). The C-O-C bridge of the $A_1(COC)$ structure involves a π interaction in addition to the C-O σ bonds, and is therefore stronger than an ether-like linkage. Notice that the C-O bond lengths are 1.33 Å in the $A_1(COC)$ structure, whereas the C-O bonds are about 1.43 Å long in the ether linkages of the $E_1(COC)$ and $E_3(COC)$ structures. Although the C-O-C linkage of structure $A_1(COC)$ appears to involve stronger bonding than either an ether or epoxide linkage, its formation also involves cleavage of a C-C double bond. Thus, it is unclear whether the high excess energy of 0.54 eV for $A_1(COC)$ structure should be viewed as an upper or lower bound of the change in strain energy during $A_1(COC)$ formation.

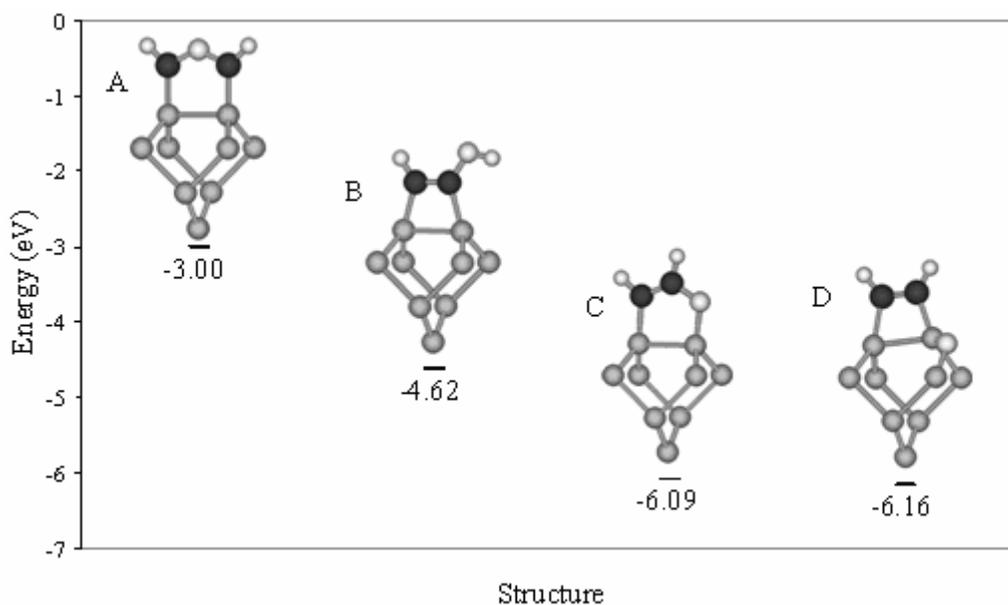


Figure 5-6. Relative energies of spin-singlet $O-C_2H_2-Si_9H_{12}$ structures. A) $A_1(COC)$. B) $A_1(COH)$. C) $A_1(SiOC)$. D) $A_1(SiOSi)$. Reference energy: $A_1(SiSi) + O(^3P) = 0.00$ eV. Oxygen and silicon atoms are represented by black and gray spheres, respectively. Carbon and hydrogen atoms are represented by large and small white spheres, respectively.

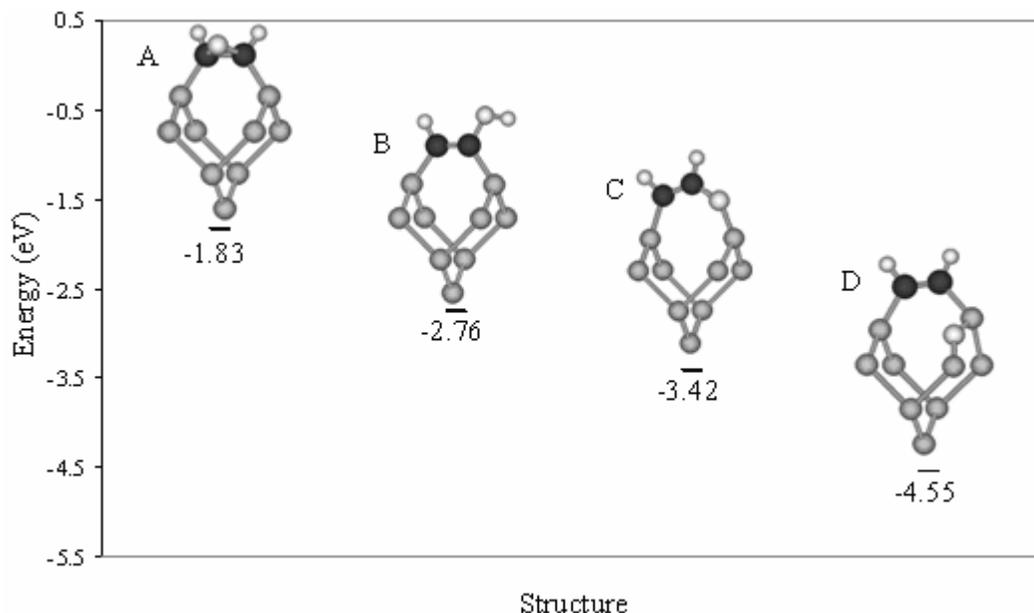


Figure 5-7. Relative energies of spin-triplet $\text{O-C}_2\text{H}_2\text{-Si}_9\text{H}_{12}$ isomers. A) $A_3(\text{COC})$. B) $A_3(\text{COH})$. C) $A_3(\text{SiOC})$. D) $A_3(\text{SiOSi})$. Reference energy: $A_1(\text{SiSi}) + \text{O}(^3P) = 0.00$ eV. Oxygen and silicon atoms are represented by black and gray spheres, respectively. Carbon and hydrogen atoms are represented by large and small white spheres, respectively.

5.3.3 Oxygen Insertion Mechanisms

5.3.3.1 Thermodynamic considerations

Our relative energy calculations predict that the oxygen atom has an energetic preference for inserting into a Si-Si backbond over all other bonds that are available on the olefin-covered surfaces. This finding is consistent with an insertion mechanism proposed for oxidation of H-terminated Si(100) by gaseous O-atoms, in which oxygen atoms prefer to insert into Si-Si bonds over abstraction hydrogen atoms [111]. Our results also support the conclusions made by Litorja and Buntin [14] that oxidation of acetylene and ethylene-terminated Si(100) proceeds initially by oxidation of the Si atoms. However, this agreement is based only on the prediction that Si-O-Si formation results in the lowest energy reaction products. It is necessary to also consider the energy barriers for oxygen insertion to confirm that the lowest energy products are kinetically preferred.

5.3.3.2 Kinetic considerations

According to recent experimental results [107], oxidation of Si(100) by gaseous $O(^3P)$ atoms is initiated by the adsorption of the O-atom onto a Si dangling bond, followed by oxygen insertion into a Si-Si bond. The precursor structures in this mechanism are spin-triplets since the $O(^3P)$ atom bonds with only one Si atom of the surface dimer. This interaction leaves one unpaired electron localized on the adsorbed oxygen atom, and the other localized on the opposing Si dimer atom. Similar to our previous study of oxygen insertion into the Si(100) surface, we considered oxygen insertion into the olefin-terminated surfaces as occurring in the triplet spin-state according to the general reaction described in Equation 5-3.



In Eq. 5-3 M_s is the spin multiplicity, O_d indicates that the oxygen atom is bonded at a Si dangling bond and $x = 2$ or 4 (Figure 5-8). The heats of O-atom adsorption onto the triplet ethylene and acetylene-terminated surfaces, resulting in $E_3(O_d)$ and $A_3(O_d)$, are found to be 4.86 and 4.95 eV, respectively, and are each slightly higher than the 4.74 eV value found previously for O-atom adsorption onto the bare Si(100) cluster. The O_d -Si bond is strengthened on the olefin-terminated surfaces since the adsorbed olefins withdraw charge from the Si atom, resulting in a more polar O-Si bond.

We found two energy pathways and the transition state structures for insertion of an oxygen atom into an Si-Si backbond and an Si-C bond of the C_2H_2 terminated Si(100)-(2x1) surface (Figure 5-9). Oxygen insertion into the silicon backbond to form $A_3(SiOSi)$ from $A_3(O_d)$ is by far the more kinetically preferred pathway. This reaction has a barrier of 0.31 eV, which is very close to that predicted for the analogous insertion

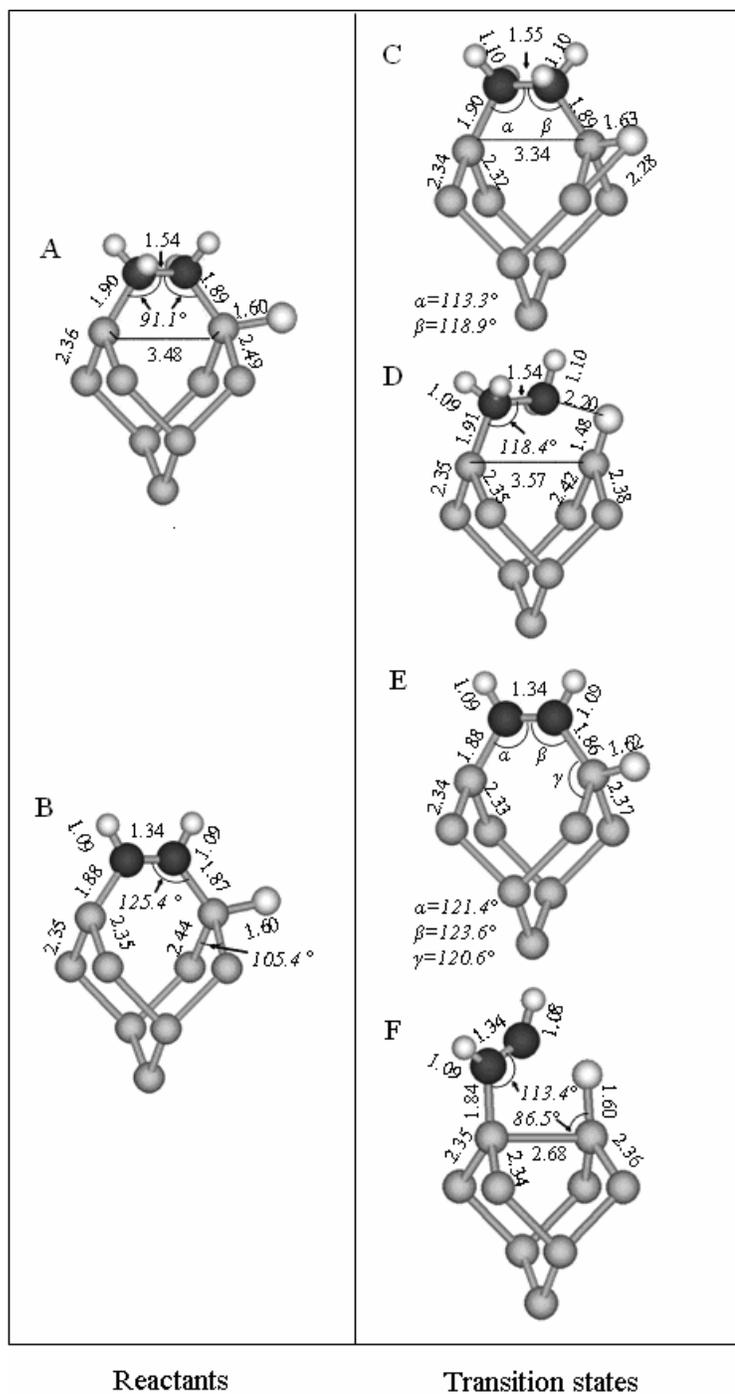


Figure 5-8. Structural information of clusters involved in oxygen insertion pathways on C₂H₂- and C₂H₄-terminated Si(100) surfaces. Reactants: A) E₃(Od). B) A₃(Od). Transition state structures: C) TSE₃(Od-SiOSi). D) TSE₃(Od-SiOC). E) TSA₃(Od-SiOSi). F) TSA₃(Od-SiOC). Oxygen and hydrogen atoms are represented by large and small white balls, respectively. Carbon and silicon atoms are represented by black and gray balls, respectively. Bond lengths are expressed in Å.

reaction on the clean Si(100) surface (Chapter 4). The barrier for oxygen insertion into the Si-C bond is predicted to be 1.42 eV, which is significantly higher than that for insertion into the Si-Si bond and therefore suggests that Si-O-C formation does not compete effectively with Si-O-Si formation, at least in the initial stages of oxidation of the C₂H₂-terminated surface.

The difference between the energy barriers for oxygen insertion into a Si-Si backbond versus into a Si-C bond is even more dramatic for the ethylene-terminated surface. An energy barrier of only 0.10 eV is predicted for oxygen insertion into the silicon backbond of E₃(Od), which is lower than that computed for the C₂H₂-terminated surface (Figure 5-10). In contrast, a barrier of 2.77 eV is predicted for oxygen insertion into the Si-C bond of the ethylene-terminated surface, whereas a lower barrier, but still quite high, was predicted for the same reaction on the C₂H₂-terminated surface. Based on the magnitudes of the predicted reaction barriers, our calculations suggest that oxidation of olefin-terminated Si(100)-(2x1) by O(³P) atoms will be initiated exclusively by oxygen insertion into Si-Si backbonds, which is consistent with the conclusions reached by Litorja and Buntin [14].

Indeed, the barriers for oxygen insertion into Si-C bonds would need to be significantly reduced by the presence of siloxane bridges for Si-O-C bond formation to become a viable reaction pathway at higher oxygen coverages. Additionally, our prediction that the barrier for Si-O-Si formation on the ethylene-terminated surface is lower than that on the acetylene-terminated surface (0.10 vs. 0.31 eV) is also consistent with experimental observations of higher oxidation rates of the C₂H₄- versus C₂H₂-terminated surface by gaseous oxygen atoms [14].

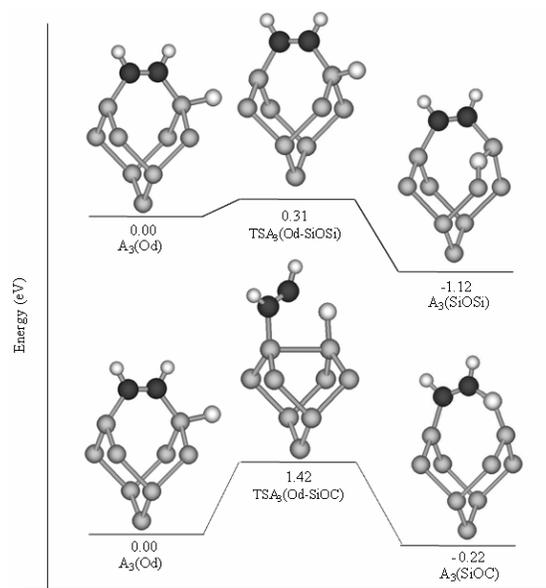


Figure 5-9. Potential energy surfaces for migration of an oxygen atom on an C_2H_2 covered $Si(100)-(2 \times 1)$ surface. Bond lengths are expressed in \AA and energies in eV. Oxygen and hydrogen atoms represented by large and small white balls, respectively. Carbon and silicon atoms represented by black and gray balls, respectively.

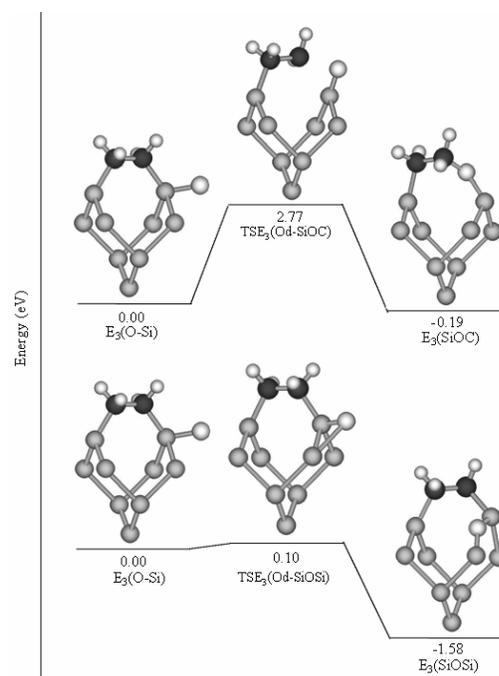


Figure 5-10. Potential energy surfaces for migration of an oxygen atom on an C_2H_4 covered $Si(100)-(2 \times 1)$ surface. Energies expressed in eV. Oxygen and hydrogen atoms represented by large and small white balls, respectively. Carbon and silicon atoms represented by black and gray balls, respectively.

CHAPTER 6 SUMMARY AND CONCLUSIONS

6.1 Nitrogen Atom Abstraction from Si(100)-(2x1) by Gaseous Atomic Oxygen

The abstraction of nitrogen atoms from Si(100)-(2x1) by gas-phase O(3P) atoms was investigated using DFT for different bonding configurations of nitrogen on the surface. Abstraction in a single elementary step was predicted only for nitrogen bound in a coordinatively saturated configuration, and a barrier of 0.20 eV was determined for this reaction. Despite this relatively low abstraction barrier, oxygen adsorption on a Si dangling bond site appears to be preferred over direct abstraction of coordinatively-saturated nitrogen due to both energetic differences between adsorption and abstraction and the requirement that multiple bonds must break and form during single step abstraction. Abstraction of coordinatively unsaturated nitrogen atoms is predicted to occur by precursor-mediated pathways in which the incident oxygen atom first bonds directly with a surface nitrogen atom to form an adsorbed NO species. A series of elementary steps must then occur for NO to desorb from the surface. Since N-O bond formation releases at least 1.7 eV more energy into the surface than is required to activate the subsequent steps leading to NO desorption, the calculations indicate that gaseous O(3P) atoms can efficiently abstract coordinatively-unsaturated nitrogen atoms from Si(100). Although the prediction of facile nitrogen abstraction by gaseous oxygen atoms is consistent with previous observations that nitrogen is depleted from Si surfaces by reaction with oxygen plasma, additional work is needed to clarify the conditions under

which atomic nitrogen exists on Si(100) in coordinatively unsaturated configurations, and is therefore susceptible to direct attack by incident oxygen atoms.

6.2 Initial Step of Si(100)-(2x1) Oxidation by Gaseous Atomic Oxygen

We studied the incorporation of $O(^3P)$ atoms onto the Si(100)-(2x1) surface to assess the factors which influence the thermodynamic stability of local structures formed in the early stages of Si(100) oxidation by atomic oxygen. Specifically, since we were interested in structures formed during the early stages of oxidation we considered only oxygen atom insertion into the surface dimer bond, one or more backbonds or a dangling bond. Special attention was given to the effects that the spin-state of the surface, the oxidation state of the surface silicon atoms and the strain resulting from oxygen incorporation have on the final energy of the oxidized products. These factors were quantified using a bond energy model that assumes that each one of them contributes additively to the total heat of formation of the products. Transition states for the insertion process were also investigated, to develop a model for the preferred mechanism of the initial steps of Si(100) oxidation by $O(^3P)$ adsorption.

For clusters with one-oxygen atom, the dangling bond structure is the least favorable because it only has one Si-O bond. In all the other more stable one O-atom isomers, two Si-O bonds are formed at the expense of one Si-Si bond, and all the structures have the same suboxide energy penalty. Thus, the differences in the relative energies of these clusters arise from the different spin-states and amounts of strain in them. We found that the spin-singlet isomers are predicted to be more energetically favorable than the spin-triplet isomers. Oxygen adsorption onto the one-atom isomers can result in three distinct dangling bond structures and each of them should form with roughly equal probability. These dangling bond structures have different relative energies

despite their similar structures. These differences are due to delocalization effects associated to the Si-O_d bond.

The relative energies of the isomers with two and three-adsorbed oxygen atoms are determined by a combination of effects, though the suboxide energy penalty generally has the largest influence. Generally, structures possessing four Si⁺¹ species are less favorable than those with a combination of two Si⁺¹ and one Si⁺² species, and the spin-singlet structures are more favorable than their spin-triplet counterparts. It was noticed, though, that the formation of a dangling bond structure with three adsorbed oxygen atoms is 1.28 eV less exothermic than oxygen adsorption on the triplet bare cluster.

Based on our kinetic studies we complemented the thermodynamic analysis and propose the following preferred reaction path for oxidation of Si(100)-(2x1) via O(³P) adsorption. Initially, an oxygen atom adsorbs onto a clean cluster at a dangling bond of the silicon dimer. Then, that oxygen atom inserts into a Si-Si backbond by overcoming an energy barrier of 0.30 eV and ultimately reaches the spin-singlet state, which is more stable than its spin-triplet counterpart by 0.58 eV. A second oxygen atom will adsorb again at a dangling bond site, either with the same or the opposite silicon dimer atom as the first O-atom. Either way, the second O-atom eventually inserts into the dimer bond by overcoming small activation barriers. The reaction barrier for going from having the two oxygen atoms attached at the same silicon dimer is 0.25 eV, and it is only 0.11 eV in the other case. A third oxygen atom adsorbs at the dangling bond of the silicon dimer atom that does not have any backbonded siloxane bridge, eventually inserting into the Si-Si backbond that is on the same side of the dimer as the siloxane-bridge already

present in the structure after overcoming a 0.05 eV activation barrier. Additional oxygen atoms will adsorb following a similar mechanism in which the O-atom first adsorbs at a dangling bond and eventually inserts into a backbond.

6.3 Oxidation of C₂H₂- and C₂H₄-covered Si(100)-(2x1) by Gaseous Atomic Oxygen

We used DFT to investigate the reaction energetics of oxygen atom insertion into different bonds of the C₂H₂- and C₂H₄-terminated Si(100) surfaces. Our calculations predict that the Si-Si dimer bond will remain intact when a single oxygen atom inserts into any of the bonds that are available on the olefin-terminated surfaces investigated. In addition, the trend in the relative energies of the oxidized products is found to be determined by the formation energies of the oxidized bridges that form, with changes in strain energy having a secondary influence on the energetics. Specifically, a Si-O-Si bridge at a Si-Si backbond is found to be the most energetically favored product of oxygen insertion, followed by Si-O-C, C-O-H and C-O-C bridge formation. For the C₂H₂- and C₂H₄-terminated surfaces, respectively, the barriers for the insertion of an adsorbed oxygen atom into a Si-Si backbond are predicted to be 0.31 and 0.10 eV, whereas the barriers for oxygen insertion into a Si-C bond are found to be significantly higher at 1.42 and 2.77 eV. This prediction suggests a strong kinetic preference for siloxane formation over Si-O-C formation during the initial stages of oxidation of olefin-terminated Si(100) by gaseous O(³P) atoms. The present computational results are consistent with the findings of a recent experimental study [14] which suggest that oxidation of the Si(100) substrate precedes other reaction processes that are stimulated by the interactions between gaseous oxygen atoms and acetylene and ethylene-terminated Si(100).

APPENDIX A QUANTUM CHEMISTRY SOFTWARE

Four computational packages (QCP) were used in this work to properly perform geometry optimization calculations. These programs are Gaussian03 [71], HyperChem 7, Molden, and gOpenMol. Gaussian03 is a program system for *ab initio* electronic structure calculations created by late John Pople and his collaborators. It is available through the Quantum Theory Project at the University of Florida (QTP), which has all the environment variables set by default. Gaussian03 is the latest in the Gaussian series of electronic structure programs, which have been successfully used for research in established and emerging areas of chemical interest. Based on the basic laws of quantum mechanics, the program predicts the energies, molecular structures, and vibrational frequencies of molecular systems, along with numerous molecular properties derived from these basic computation calculations. Gaussian03 stores all the information relevant to a particular calculation in a binary checkpoint (.chk) file and generates a simplified report of it for the user in an output (.log) file (in text format).

To visualize our Gaussian03 computational results and generate initial guesses for geometry optimization or transition state search calculations, we used HyperChem 7 (Figure A-1), which is available on the Windows NT server of QTP. This is a molecular modeling program that is easy to use thanks to its user-friendly Windows interface. The program combines advanced 3D visualization and animation with quantum chemical calculations. All these features made HyperChem 7 our program of choice to perform all our molecular mechanics and semi-empirical geometry optimization calculations,

visualize input and output structures, create images of final optimized structures and generate most of our Gaussian03 input files. It was also useful in determine the starting guess structure for transition state calculations.

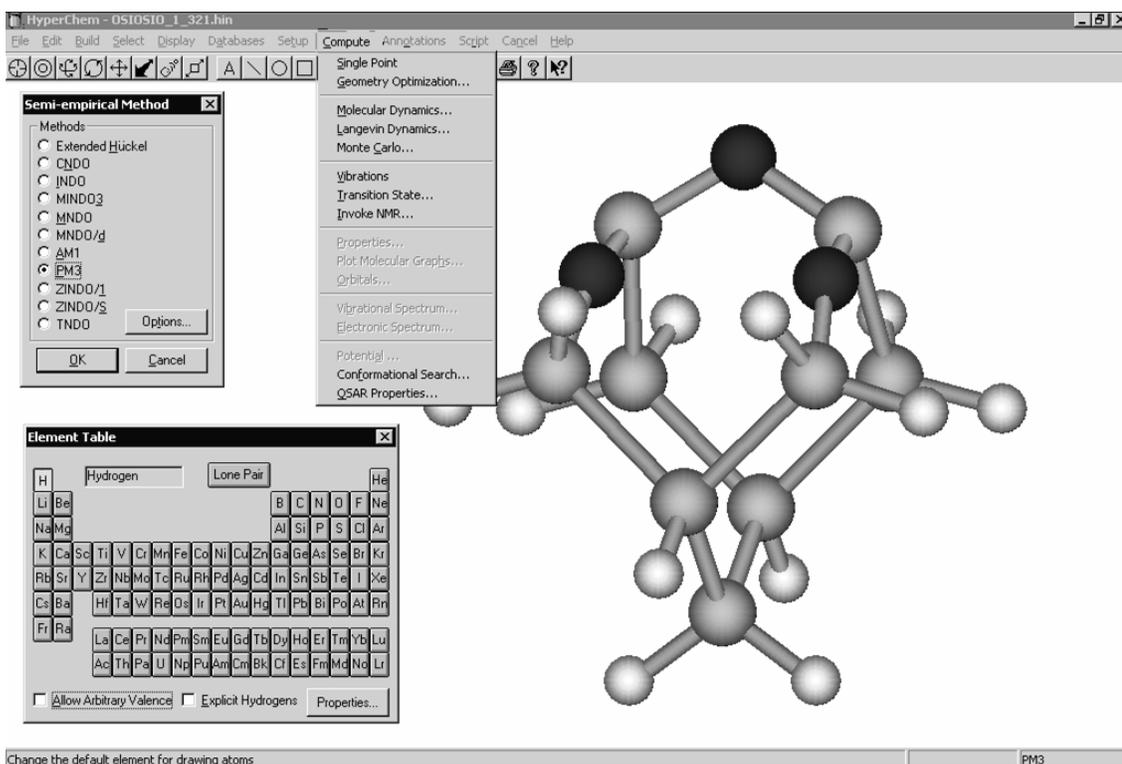


Figure A-1. HyperChem 7 interface.

Molden is a software that is mainly used for visualizing molecular densities and orbitals calculated with *ab initio* packages such as Gaussian03 [71]. The program reads all the required information directly from Gaussian03 output (.log) files and displays molecular orbitals, electron density, molecular-atomic density of optimized structures and convergence plots. These capabilities made it the ideal choice to check the day-to-day status of the different optimization calculations that were running at any given time (Figure A-2). Moreover, it also can animate reaction paths and molecular vibrations and, thanks to its advanced Z-matrix editor, it can be used to reorder the Z-matrices (an option that is very useful when creating input files for transition state searches, where several

structures are required, including those of the reactant, the product and, quite often, an initial guess for the transition state).

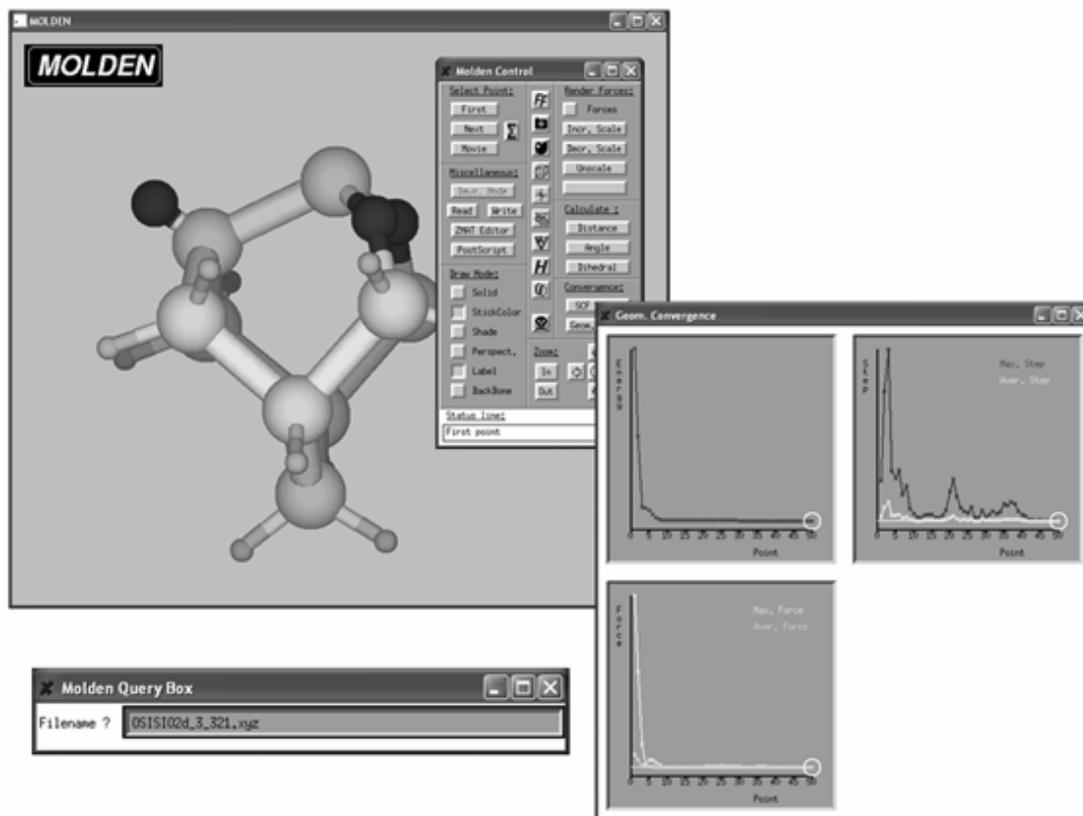


Figure A-2. Molden visualization interface and main command screens.

Finally, to plot highest occupied molecular orbitals (HOMO) –or any other type of molecular orbital- from the information contained in the Gaussian03 checkpoint file we used gOpenMol (Figure A-3), which is a program for the visualization and analysis of molecular structures and their chemical properties. The software was written by Leif Laaksonen and it is available from him on the internet. Since the program can import, display and analyze several different input coordinates and binary trajectory file formats, we also used it to visualize molecular structures available in different file formats. Table A-1 summarizes the information of the different quantum chemistry programs used in this work.

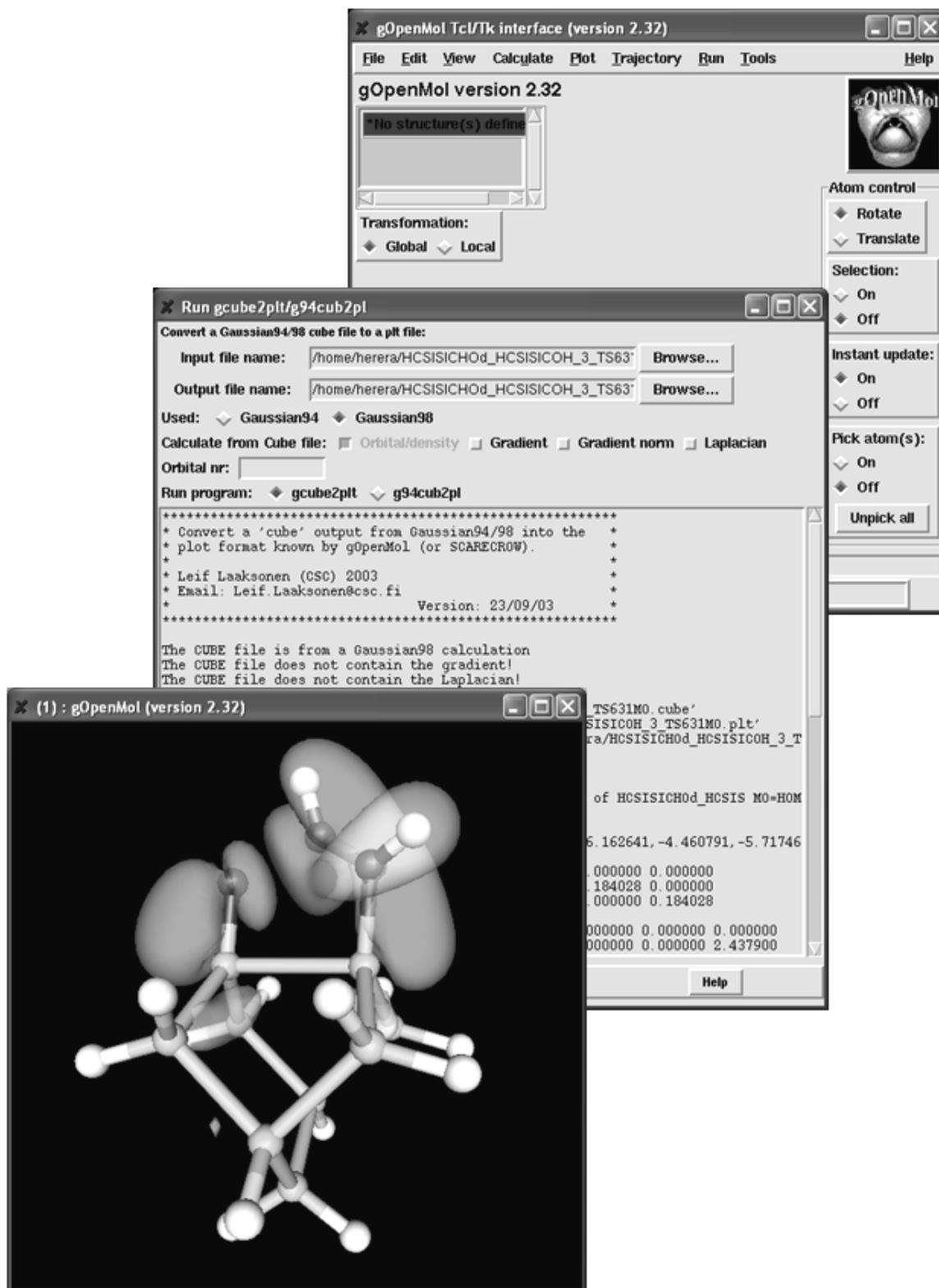


Figure A-3. gOpenMol visualization interface. Main window and command screens. The main screen includes an image of the structure HOMO.

Table A-1. Computational software used in this work

Program	Platform	Applications
Gaussian03	UNIX/Linux	<ul style="list-style-type: none"> · DFT geometry optimizations · DFT transition state searches · DFT frequency calculations
HyperChem 7	Windows	<ul style="list-style-type: none"> · MM geometry optimizations · Semi-empirical geometry optimizations · Gaussian03 input file generation · Generation of initial guess for TS searches · Final structure visualizations · Final structure image creation
Molden	Linux	<ul style="list-style-type: none"> · Preliminary optimized structure visualization · Periodic check of optimization calculations status · Creation of transition state movies · Z-matrix reordering
gOpenMol	Linux	<ul style="list-style-type: none"> · HOMO visualization · Creation of transition state movies

Table A-2. File formats used for proper handling of the coordinates systems and results in our geometry optimization calculations. All these files, except .chk, are plain text and can be easily modified by standard text editors. We used EMACS for text editing.

File Suffix	Format Description	Generated by	Read by
.xyz	Cartesian coordinates with no special format	<ul style="list-style-type: none"> · Molden · gOpenMol · HyperChem · Babel (from .hin) 	
.zmt	Z-Matrix in internal coordinates	<ul style="list-style-type: none"> · Molden · Babel (from .hin or .xyz) 	
.hin	Cartesian coordinates with HyperChem format	<ul style="list-style-type: none"> · HyperChem · Babel (from .xyz) 	HyperChem 7
.inp	Gaussian03 input	<ul style="list-style-type: none"> · Molden · Text editor (based on .zmt) 	Gaussian03
.log	Gaussian03 output	Gaussian03	<ul style="list-style-type: none"> · Molden · gOpenMol · Text editor
.chk	Gaussian03 checkpoint file	Gaussian03	Molden (requires use of cubegen and formchk gaussian utilities)

Six different file formats were used in this work (Table A-2). Most of these file formats can be converted into one another by means of the commercial software Babel, or edited using a text editor, such as the commercial UNIX based Emacs. Babel is a program specifically designed to interconvert file formats commonly in molecular modeling. The following sections briefly describe each one of these file types.

A.1 File Format .xyz

The .xyz file format is the simplest one of all the formats used in this work. It is found in plain text files and consists of four columns: atom identification, and Cartesian x , y and z positions, with each row corresponding to the identification and coordinates of a single atom. The files have a two-line header with the number of atoms in the first line, and a brief description of the file in the second. Even though the order in which the atoms appear in this file format is not important because the coordinates of one atom are completely independent of those of other atoms, the special order shown in Figure A-4 is kept throughout this work. This is all the information that most quantum chemistry programs need to recognize the structure in Cartesian coordinates.

A.2 File Format .zmt

The order in which the $\text{Si}_9\text{H}_{12+w}\text{O}_x\text{N}_y\text{C}_z$ cluster components are in the .xyz file presented in Figure A-4 is not coincidental. Given that the most effective way to specify Gaussian input files is by using a Z-Matrix format (where the atom positions are specified by bond lengths, bond angles and torsion angles with respect to other atoms in the system [74]) it is necessary to list first all those atoms that remain fixed during the calculation, followed by the bulk atoms, and the surface and chemically active atoms. In other words, the XYZ matrix described in the .xyz files is constructed in order of decreasing constraints imposed on the atoms.

atom label	x position	y position	z position
24 — Number of atoms			
scf done: -2824.260681			
H	0.000000	0.000000	0.000000
H	0.000000	0.000000	2.439200
H	3.405407	0.000000	1.179228
H	-2.364395	2.446693	1.218924
H	2.952147	2.469978	-1.907356
H	4.706251	3.000198	-0.251935
H	4.740128	3.058559	2.454324
H	3.254646	2.398272	4.316089
H	-0.435065	3.862356	4.363306
H	-1.124524	5.471041	2.621688
H	-0.445963	4.008533	-1.867615
H	-1.126575	5.530258	-0.033742
Si	0.326490	0.809610	1.217773
Si	2.609131	1.244201	1.221026
Si	-0.844456	2.832190	1.173905
Si	3.312197	2.631790	-0.476281
Si	3.320468	2.787460	2.876853
Si	-0.276359	4.269230	2.939289
Si	-0.243682	4.522248	-0.481422
Si	2.397524	5.573673	0.505651
Si	2.030692	4.844675	2.760889
O	0.974438	5.683461	-0.327222
O	2.579160	3.976724	0.097904
O	2.745370	5.492015	4.068503

Hydrogen atoms

Third and fourth layer

First and second layer

Chemically active atoms

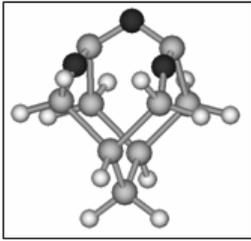
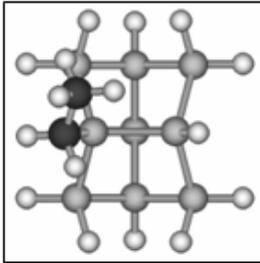


Figure A-4. Example of a .xyz file describing a $\text{Si}_9\text{H}_{12}\text{O}_3$ cluster. Molecular geometry expressed in Cartesian coordinates. Insert: The cluster described by the file corresponds.

It is important to emphasize that all the files that describe the same structures in a particular geometry optimization calculation keep the same atom order independently of the file format. In this work, the main constraint imposed on the clusters is on all the terminating hydrogen atoms which are fixed in their positions; thus, they must be specified first in the molecule matrix. By doing this, it is guaranteed that all the bond lengths, bond angles and torsion angles that define the hydrogen atoms will remain unchanged during the whole geometry optimization calculation. Following the hydrogen atoms, we list those atoms that are affected the least by the surface reactions (i.e., the third and fourth layer silicon atoms). These atoms will barely move because all of their coordinates are defined relative to those of the hydrogen atoms. The surface silicon atoms and the chemically active atoms are the last to be specified because these atoms are relatively free to move.

atom label	bond lengths	bond angles	torsion angles	
H				
H	1 r2			
H	1 r3	2 a3		
H	2 r4	1 a4	3 d4	
H	3 r5	1 a5	2 d5	
H	5 r6	3 a6	1 d6	
H	6 r7	5 a7	3 d7	
H	7 r8	6 a8	5 d8	
H	8 r9	7 a9	6 d9	
H	9 r10	8 a10	7 d10	
H	5 r11	3 a11	1 d11	
H	11 r12	5 a12	3 d12	
Si	1 r13	2 a13	3 d13	
Si	3 r14	1 a14	2 d14	
Si	4 r15	2 a15	1 d15	
Si	6 r16	5 a16	3 d16	
Si	7 r17	6 a17	5 d17	
Si	10 r18	9 a18	8 d18	
Si	12 r19	11 a19	5 d19	
Si	19 r20	12 a20	11 d20	
Si	20 r21	19 a21	12 d21	
C	21 r22	20 a22	19 d22	
H	22 r23	21 a23	20 d23	
C	22 r24	21 a24	20 d24	
H	22 r25	21 a25	20 d25	
H	24 r26	22 a26	21 d26	
H	24 r27	22 a27	21 d27	
H	24 r28	22 a28	21 d28	
H	22 r29	21 a29	20 d29	
Variables:				
r2= 2.4398				
r3= 3.6156				
a3= 70.29				
r4= 3.6178				
a4= 70.46				
d4= 132.97				
r5= 3.9563				
a5= 70.61				
:				
:				



Hydrogen atoms

Third and fourth layer

First and second layer

Silicon atoms

Chemically active atoms

Variable definitions

Figure A-5. Z-Matrix file describing a $\text{Si}_9\text{H}_{12+x}\text{C}_y$ cluster. Insert: Top view of $\text{Si}_9\text{H}_{18}\text{C}_2$ cluster described by this file. Since this file is used in a geometry optimization calculation, the coordinates are specified as variables, whose values are listed below the matrix in the variable section.

A Z-Matrix file (Figure A-5) consists of a structure matrix with four columns (corresponding to atom labels, bond lengths, bond angles and torsion angles) followed by a variables section. This variable section shows the values of those coordinates that were specified by a variable name in the structure matrix. Some of these values can also be specified as constants. If that is the case, then a constants section follows immediately

below the variables. Since all the coordinates in a Z-matrix need at least two reference atoms, the first three atom descriptions are incomplete, rendering a non-redundant internal coordinate system that contains only $3N-6$ internal coordinates for an N -atom molecule.

A.3 HyperChem Files (Format .hin)

HyperChem 7 results can be presented in a long and a short file format. Both of them are easily edited using a program like Emacs. HyperChem 7 automatically generates the long file format every time work is saved by the user. This format includes a heading with the quantum chemistry platform used and references for molecule display, which are instructions that the program needs to display the structure the next time it is required by the user.

Immediately after the header, the Cartesian coordinate matrix of the structure is presented in the HyperChem matrix format. In addition to the Cartesian coordinates, the format includes the type of atom, the energy associated to it, the order numbers of the atoms to which each atom is bonded and the type of bonding. The file ends with a section displaying all the atoms selected and named by the user. HyperChem short files only have the HyperChem matrix of the structure and are usually generated from .xyz files using Babel, as these files are only mere translations of .xyz files to a format that HyperChem 7 can handle.

We used the two HyperChem file formats in two different instances. The .hin long format files are used when exploring for a best initial guess for an optimization calculation (Appendix C). They result from a combination of molecular mechanics and semi-empirical geometry optimization calculations.

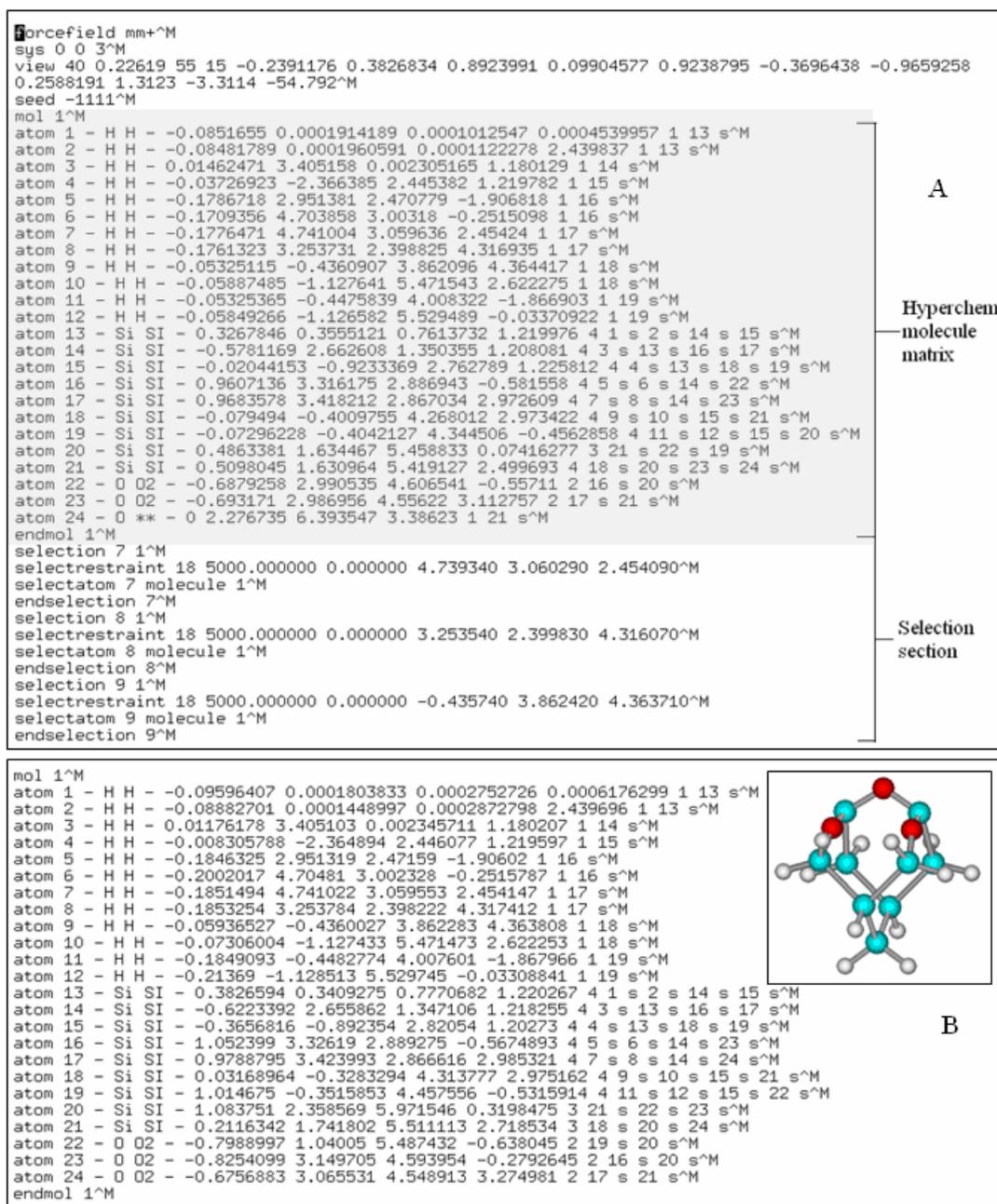


Figure A-6. HyperChem 7 files describing a $\text{Si}_9\text{H}_{12}\text{O}_3$ cluster. A) .hin long format. B) .hin short format. Insert: Side view of the cluster that these files describe.

The files are then converted into a Z-matrix format using Babel and used to generate an input file for a UB3LYP/3-21G* calculation in Gaussian03 [71]. The .hin short format files are usually obtained from .xyz files that are generated using Molden from Gaussian03 output files and are always used to visualize the final results and

generate the optimized structure images in HyperChem 7 that are presented in the results section of this dissertation.

A.4 Gaussian03 Files (Formats .inp, .log and .chk)

There are three Gaussian03 files: the input (.inp), checkpoint (.chk), and output (.log) files [71]. Contrary to the HyperChem 7 files, the differences among these files go beyond mere formatting. Gaussian03 input files (.inp) (Figure A-7A) are very simple ASCII text files that contain the structure specification (generally in Z-Matrix format) and the Gaussian commands for the simulation that the user wants. The basic structure of an input file includes several sections, which are summarized in Table A-3.

Table A-3. Gaussian03 input files sections. An example of an input file is shown in Figure A-1.

Section	Description
Link 0 commands	<ul style="list-style-type: none"> • Locates and names scratch files • Specifies required memory and number of processors
Route section (# lines)	Specify desired calculation type, model chemistry and options to keywords. The latter may be specified in any of the following forms: <ul style="list-style-type: none"> • keyword = option • keyword(option) • keyword=(option1, option2, etc.) • keyword(option1, option2, etc.)
Title section	Brief description of the calculation
Molecule specification	Specify molecular system to be studied in XYZ or Z-matrix formats
Optional additional sections	Additional input needed for specific job types

Figure A-7(a) is an example of an input file that requests a geometry optimization of a $\text{Si}_9\text{H}_{12}\text{O}_3$ cluster using the UB3LYP/3-21G* model chemistry. In this job, the route and title sections each consist of a single line. The molecule specification section begins with a line giving the charge and spin multiplicity for the molecule: 0 charge (neutral molecule) and spin multiplicity 3 (triplet) in this case. The charge and spin multiplicity line is followed by lines describing the location of each atom in the molecule (in internal

coordinates in this example). This particular job requests a geometry optimization and the input section including redundant coordinates that follows the molecule specification is used by the Opt(ModRedundant) keyword, as it serves to add constraints in the geometry optimization. The file also includes two Link 0 commands that specify the memory (%Mem) and the number of computer processors (%NProc) that the job requires.

Gaussian03 output (.log) files are log ASCII text files that register the optimization calculation main results in user format. A detailed and commented example is presented in Appendix B. These output files includes information such as the energy of the system, the initial structure in several coordinate systems, intermediate structures specification, final structure specification in several coordinate systems, the number of primitive Gaussians, dipole moment, and spin and charge Mulliken analysis, among others. The file is of considerable length but it includes a briefing of the relevant information at the end, so the user can see the main results at a glance (Figure A-7B). Gaussian03 output files are the most important ones in this study, but due to their complexity, the other file formats are required to extract and visualize the information from them.

Finally, to generate plots of the highest occupied molecular orbitals (HOMO) using the gOpenMol interface, the Gaussian03 checkpoint file (.chk) is needed. This is a binary file that includes all the information generated by the optimization calculation. The required information is extracted with the Gaussian03 Unix utilities formchk and cubegen [71]. Formchk converts a checkpoint file into an ASCII form that visualization programs can read, while cubegen is a standalone utility that generates cubes of electron density and electrostatic potential.

```

%Mem=250MB | Machine RAM and number of processors
%Nproc=2
#ub3lyp/3-21G* Opt(ModRedundant) Nosymm — Procedure: Geometry optimization using internal
OSISI02d_3_321.inp — Title, description and history
0 3 — Molecule charge and spin
H
H 1 r2
H 1 r3 2 a3
H 1 r4 2 a4 3 d4
.
.
.
0 20 r22 19 a22 12 d22
0 20 r23 19 a23 12 d23
0 21 r24 18 a24 9 d24
Variables:
r2= 2.4392
.
.
d24= 317.96

1 B
2 B
3 B
4 B
5 B
6 B
7 B
8 B
9 B
10 B
11 B
12 B
* F

```

Procedure: Geometry optimization using internal redundant coordinates and the b3lyp/3-21G* level of theory. The unrestricted option for B3LYP used because this is an open shell calculation. Symmetry simplifications have been turned off to improve accuracy.

Z-Matrix (From zmt file)

Redundant coordinates: the hydrogen atoms are fixed in their x,y,z positions.

A

```

1\1\GINC-THOR\F0pt\UB3LYP\3-21G*\H1203Si9(3)\PHERRERA\21-Oct-2004\0\#\#
UB3LYP/3-21G* OPT(MODREDUNDANT) NOSYMM\OSISI02d_3_321.inp\0,3\H,0.,0
..0.\H,0.,0.,2.4392\H,3.4054068896,0.,1.1792278643\H,-2.3643946794,2.4
466926331,1.2189235411\H,2.9521470944,2.469978285,-1.9073559495\H,4.70
62506697,3.0001981197,-0.2519352102\H,4.7401281557,3.0585591051,2.4543
235951\H,3.2546462792,2.3982720338,4.3160891921\H,-0.435064546,3.86235
62401,4.3633064294\H,-1.1245236214,5.4710406556,2.6216878016\H,-0.4459
634634,4.0085326199,-1.8676148497\H,-1.1265747899,5.5302583028,-0.0337
418829\Si,0.326489575,0.8096097047,1.2177732044\Si,2.6091310721,1.2442
009692,1.2210256078\Si,-0.8444558262,2.8321897038,1.173904814\Si,3.312
1966439,2.6317903679,-0.4762806252\Si,3.3204678575,2.7874598237,2.8768
532788\Si,-0.2763593483,4.2692300723,2.9392890161\Si,-0.243682408,4.52
22481259,-0.4814220781\Si,2.3975235386,5.5736734997,0.5056510624\Si,2.
0306915626,4.8446751906,2.7608889582\O,0.9744375704,5.6834610711,-0.32
72215189\O,2.5791595567,3.9767244404,0.0979038487\O,2.7453703057,5.492
0145066,4.0685026139\Version=x86-Linux-G03RevB.04\HF=-2824.2606814\S2
=2.013446\S2-1=0.\S2A=2.000087\RMSE=3.699e-09\RMSF=6.837e-03\Dipole=-0
.1934417,-1.1454323,-0.7209343\PG=C01 [X(H1203Si9)]\@

WAR ES EIN GOTT DER DIESE ZEICHEN SCHRIEB?
- LUDWIG BOLTZMANN, QUOTING GOETHE, ABOUT MAXWELL'S EQUATIONS.
Job cpu time: 0 days 22 hours 14 minutes 51.5 seconds.
File lengths (MBytes): RWF= 69 Int= 0 D2E= 0 Chk= 11
1
Normal termination of Gaussian 03 at Thu Oct 21 07:39:55 2004.

```

Procedure and user

Atomic positions

Energetic information

Computer time required

B

Figure A-7. Gaussian03 file types. A) Sample input file (.inp) for a geometry optimization run. B) View of end section of an output file (.log) showing the most relevant results of the calculation. A schematic of a complete output file is presented in Appendix B

APPENDIX B EXAMPLE OF GAUSSIAN03 OUTPUT FILE

The following is a commented example of a typical geometry optimization Gaussian03 output file. Some explanatory comments were included for the different sections (link outputs) of the file.

The first part of the Gaussian output file states in considerable detail the contents of the license agreement. Gaussian03 is no public domain software and University of Florida user must sign an agreement of non-disclosure.

```
Entering Gaussian System, Link 0=g03
Input=OSISIO2d_3_321.inp
Output=OSISIO2d_3_321.log
Initial command:
/usr/local/Gaussian/g03/l1.exe /storage/Gau-21781.inp -scrdir=/storage/
Entering Link 1 = /usr/local/Gaussian/g03/l1.exe PID=      21782.
```

```
Copyright (c) 1988,1990,1992,1993,1995,1998,2003, Gaussian, Inc.
All Rights Reserved.
```

```
This is the Gaussian(R) 03 program. It is based on the
the Gaussian(R) 98 system (copyright 1998, Gaussian, Inc.),
the Gaussian(R) 94 system (copyright 1995, Gaussian, Inc.),
the Gaussian 92(TM) system (copyright 1992, Gaussian, Inc.),
the Gaussian 90(TM) system (copyright 1990, Gaussian, Inc.),
the Gaussian 88(TM) system (copyright 1988, Gaussian, Inc.),
the Gaussian 86(TM) system (copyright 1986, Carnegie Mellon
University), and the Gaussian 82(TM) system (copyright 1983,
Carnegie Mellon University). Gaussian is a federally registered
trademark of Gaussian, Inc.
```

```
This software contains proprietary and confidential information,
including trade secrets, belonging to Gaussian, Inc.
```

```
This software is provided under written license and may be
used, copied, transmitted, or stored only in accord with that
written license.
```

```
The following legend is applicable only to US Government
contracts under DFARS:
```

RESTRICTED RIGHTS LEGEND

```
Use, duplication or disclosure by the US Government is subject
to restrictions as set forth in subparagraph (c)(1)(ii) of the
Rights in Technical Data and Computer Software clause at DFARS
252.227-7013.
```

```
Gaussian, Inc.
Carnegie Office Park, Building 6, Pittsburgh, PA 15106 USA
```

The following legend is applicable only to US Government contracts under FAR:

RESTRICTED RIGHTS LEGEND

Use, reproduction and disclosure by the US Government is subject to restrictions as set forth in subparagraph (c) of the Commercial Computer Software - Restricted Rights clause at FAR 52.227-19.

Gaussian, Inc.
Carnegie Office Park, Building 6, Pittsburgh, PA 15106 USA

Warning -- This program may not be used in any manner that competes with the business of Gaussian, Inc. or will provide assistance to any competitor of Gaussian, Inc. The licensee of this program is prohibited from giving any competitor of Gaussian, Inc. access to this program. By using this program, the user acknowledges that Gaussian, Inc. is engaged in the business of creating and licensing software in the field of computational chemistry and represents and warrants to the licensee that it is not a competitor of Gaussian, Inc. and that it will not use this program in any manner prohibited above.

Cite this work as:

Gaussian 03, Revision B.04,
M. J. Frisch, G. W. Trucks, H. B. Schlegel, G. E. Scuseria,
M. A. Robb, J. R. Cheeseman, J. A. Montgomery, Jr., T. Vreven,
K. N. Kudin, J. C. Burant, J. M. Millam, S. S. Iyengar, J. Tomasi,
V. Barone, B. Mennucci, M. Cossi, G. Scalmani, N. Rega,
G. A. Petersson, H. Nakatsuji, M. Hada, M. Ehara, K. Toyota,
R. Fukuda, J. Hasegawa, M. Ishida, T. Nakajima, Y. Honda, O. Kitao,
H. Nakai, M. Klene, X. Li, J. E. Knox, H. P. Hratchian, J. B. Cross,
C. Adamo, J. Jaramillo, R. Gomperts, R. E. Stratmann, O. Yazyev,
A. J. Austin, R. Cammi, C. Pomelli, J. W. Ochterski, P. Y. Ayala,
K. Morokuma, G. A. Voth, P. Salvador, J. J. Dannenberg,
V. G. Zakrzewski, S. Dapprich, A. D. Daniels, M. C. Strain,
O. Farkas, D. K. Malick, A. D. Rabuck, K. Raghavachari,
J. B. Foresman, J. V. Ortiz, Q. Cui, A. G. Baboul, S. Clifford,
J. Cioslowski, B. B. Stefanov, G. Liu, A. Liashenko, P. Piskorz,
I. Komaromi, R. L. Martin, D. J. Fox, T. Keith, M. A. Al-Laham,
C. Y. Peng, A. Nanayakkara, M. Challacombe, P. M. W. Gill,
B. Johnson, W. Chen, M. W. Wong, C. Gonzalez, and J. A. Pople,
Gaussian, Inc., Pittsburgh PA, 2003.

Actual program output specific to a certain calculation starts with a statement of the date, program version, Gaussian revision (here B.4), and system software (here LINUX). Subsequently the keywords used in the input file are repeated together with other general settings such as the amount of main memory needed for the calculations (here 250 MB), and the location of a binary checkpoint file for storage of important results (here OSISIO2d_3_321.chk). The OPT keyword used here specifies geometry optimization and the quantum mechanical method used is UB3LYP. The “U” in UB3LYP stands for unrestricted, an approach that is used any time one is dealing with open-shell systems such as the spin-triplet of spin-double cluster in this work.

```

*****
Gaussian 03:  x86-Linux-G03RevB.04 2-Jun-2003
              19-Oct-2004
*****
%Mem=250MB
%Nproc=2
Will use up to    2 processors via shared memory.
-----
#ub3lyp/3-21G* Opt(ModRedundant) Nosymm
-----

```

The keywords are transformed by Gaussian into a sequence of subroutine calls termed links. The links are given together with the corresponding options set for each link in a proprietary format.

```

1/14=-1,18=120,26=3,38=1/1,3;
2/9=110,15=1,17=6,18=5,40=1/2;
3/5=5,7=1,11=2,16=1,25=1,30=1,74=-5/1,2,3;
4/7=2/1;
5/5=2,38=5/2;
6/7=2,8=2,9=2,10=2,28=1/1;
7/30=1/1,2,3,16;
1/14=-1,18=20/3(1);
99/99;
2/9=110,15=1/2;
3/5=5,7=1,11=2,16=1,25=1,30=1,74=-5/1,2,3;
4/5=5,7=2,16=3/1;
5/5=2,38=5/2;
7/30=1/1,2,3,16;
1/14=-1,18=20/3(-5);
2/9=110,15=1/2;
6/7=2,8=2,9=2,10=2,19=2,28=1/1;
99/9=1/99;

```

In link101 the program reads in or retrieves from the checkpoint file the structure of the system together with other parameters and prints the structure (in a slightly modified format) together with overall charge and spin multiplicity and the comments supplied in the input file. It is good practice to include the name of the input file in the comments of the job. It is also convenient to keep a log of all the unsuccessful attempts that one might have had to do in order to accomplish a successful initial geometry or a successful geometry optimization. The system chosen here for optimization is a $\text{Si}_9\text{H}_{12}\text{O}_3$ cluster in its triplet electronic ground-state with one of the oxygen atoms bonded at a dangling bond site.

```
-----
OSISIO2d_3_321.inp
-----
```

```
Symbolic Z-matrix:
```

```
Charge = 0 Multiplicity = 3
```

```
H
H          1   r2
H          1   r3       2   a3
H          1   r4       2   a4       3   d4       0
H          3   r5       1   a5       2   d5       0
H          5   r6       3   a6       1   d6       0
H          6   r7       5   a7       3   d7       0
H          7   r8       6   a8       5   d8       0
H          4   r9       1   a9       2   d9       0
H          9   r10      4   a10      1   d10      0
H          5   r11      3   a11      1   d11      0
H          11  r12      5   a12      3   d12      0
Si         2   r13      1   a13      3   d13      0
Si         3   r14      1   a14      2   d14      0
Si         4   r15      1   a15      2   d15      0
Si         6   r16      5   a16      3   d16      0
Si         8   r17      7   a17      6   d17      0
Si         9   r18      4   a18      1   d18      0
Si        12   r19     11   a19      5   d19      0
Si        19   r20     12   a20     11   d20      0
Si        18   r21      9   a21      4   d21      0
O         20   r22     19   a22     12   d22      0
O         20   r23     19   a23     12   d23      0
O         21   r24     18   a24      9   d24      0
O         22   r25     18   a25      9   d25      0
```

```
Variables:
```

```
r2          2.4392
r3          3.6038
a3          70.9
r4          3.6142
a4          70.29
d4          225.98
r5          3.9791
a5          68.81
d5          221.74
r6          2.4695
a6          62.12
d6          151.1
r7          2.7071
a7          133.13
d7          313.47
r8          2.4716
a8          137.71
d8          8.98
[...]
```

```
The following ModRedundant input section has been read:
```

```
X   1 B
X   2 B
X   3 B
X   4 B
X   5 B
X   6 B
X   7 B
X   8 B
X   9 B
X  10 B
X  11 B
X  12 B
X   * F
```

In link103 the program selects a coordinate system in which the geometry optimization will be performed. The string GradGradGrad... delimits the output from the Berny optimization procedures. On the first, initialization pass, the program prints a table giving the initial values of the variables to be optimized. Notice that for optimizations in redundant internal coordinates, all coordinates in use are displayed in the table and not merely those present in the molecule specification section. Also, observe that the manner in which the initial second derivative are provided is indicated under the heading Derivative Info (in this case the second derivatives are frozen for all the coordinates of the constrained hydrogen atoms, while they are estimated for all the other coordinates).

```

GradGradGradGradGradGradGradGradGradGradGradGradGradGradGradGrad
Berny optimization.
Initialization pass.
-----
!      Initial Parameters      !
! (Angstroms and Degrees)    !
-----
! Name  Definition              Value      Derivative Info.      !
-----
! X1    R(1,-1)                 0.0       Frozen                !
! Y1    R(1,-2)                 0.0       Frozen                !
! Z1    R(1,-3)                 0.0       Frozen                !
! X2    R(2,-1)                 0.0       Frozen                !
! Y2    R(2,-2)                 0.0       Frozen                !
! Z2    R(2,-3)                 2.4392    Frozen                !
! X3    R(3,-1)                 3.4054    Frozen                !
! Y3    R(3,-2)                 0.0       Frozen                !
! Z3    R(3,-3)                 1.1792    Frozen                !
! X4    R(4,-1)                 -2.3644   Frozen                !
! Y4    R(4,-2)                 2.4467    Frozen                !
! Z4    R(4,-3)                 1.2189    Frozen                !
! X5    R(5,-1)                 2.9521    Frozen                !
! Y5    R(5,-2)                 2.47      Frozen                !
! Z5    R(5,-3)                 -1.9074   Frozen                !
! X6    R(6,-1)                 4.7063    Frozen                !
! Y6    R(6,-2)                 3.0002    Frozen                !
! Z6    R(6,-3)                 -0.2519   Frozen                !
! X7    R(7,-1)                 4.7401    Frozen                !
.
.
.
! D80   D(22,20,21,18)          -9.5614   estimate D2E/DX2     !
! D81   D(22,20,21,24)          -144.608  estimate D2E/DX2     !
! D82   D(23,20,21,17)          6.2737   estimate D2E/DX2     !
! D83   D(23,20,21,18)          -113.1856 estimate D2E/DX2     !
! D84   D(23,20,21,24)          111.7678 estimate D2E/DX2     !
! D85   D(21,20,22,19)          -26.2057 estimate D2E/DX2     !
! D86   D(23,20,22,19)          81.7555  estimate D2E/DX2     !
! D87   D(21,20,23,16)          50.02    estimate D2E/DX2     !
! D88   D(22,20,23,16)          -62.7957 estimate D2E/DX2     !
-----
Trust Radius=3.00D-01 FncErr=1.00D-07 GrdErr=1.00D-06
Number of steps in this run= 144 maximum allowed number of steps= 144.

```

Link202 determines, among others, the symmetry of the system, decides on the symmetry properties that will be used in the actual quantum mechanical calculations and rotates the molecule such that the center of mass is located in the origin of the cartesian coordinate system, the principal axis (if present) points along the z-axis, and the principal plane of symmetry is located in the yz-plane. The resulting orientation is printed as standard orientation, which is then assumed for all information regarding the wavefunction and first and second derivatives of the energy with respect to structural parameters.

GradGradGradGradGradGradGradGradGradGradGradGradGradGradGradGradGradGrad

Input orientation:

Center Number	Atomic Number	Atomic Type	Coordinates (Angstroms)		
			X	Y	Z
1	1	0	0.000000	0.000000	0.000000
2	1	0	0.000000	0.000000	2.439200
3	1	0	3.405407	0.000000	1.179228
4	1	0	-2.364395	2.446693	1.218924
5	1	0	2.952147	2.469978	-1.907356
6	1	0	4.706251	3.000198	-0.251935
7	1	0	4.740128	3.058559	2.454324
8	1	0	3.254646	2.398272	4.316089
9	1	0	-0.435065	3.862356	4.363306
.					
.					
.					
20	14	0	2.346874	5.611148	0.481206
21	14	0	2.013479	4.776043	2.699130
22	8	0	0.991805	5.409444	-0.396979
23	8	0	3.242276	4.465825	-0.239658
24	8	0	2.521716	5.336089	3.523604

Distance matrix (angstroms):

		1	2	3	4	5
1	H	0.000000				
2	H	2.439200	0.000000			
3	H	3.603800	3.631023	0.000000		
4	H	3.614200	3.614657	6.267255	0.000000	
5	H	4.295809	5.805903	3.979100	6.167640	0.000000
.						
.						
.						
		21	22	23	24	
21	Si	0.000000				
22	O	3.321281	0.000000			
23	O	3.200415	2.445360	0.000000		
24	O	1.118800	4.209154	3.929212	0.000000	

Symmetry turned off by external request.

Stoichiometry H12O3Si9(3)

Framework group C1[X(H12O3Si9)]

Deg. of freedom 66

Full point group

Rotational constants (GHZ): C1 NOp 1 0.3685978 0.3641897 0.3294472

Link 301 loads all components necessary for the actual quantum mechanical part of the calculation.

```
Standard basis: 3-21G* (6D, 7F)
Integral buffers will be 262144 words long.
Raffenetti 2 integral format.
Two-electron integral symmetry is turned off.
  222 basis functions, 378 primitive gaussians, 222 cartesian basis functions
  82 alpha electrons 80 beta electrons
    nuclear repulsion energy 1911.7608705331 Hartrees.
NAtoms= 24 NActive= 24 NUniq= 24 SFac= 1.00D+00 NATFMM= 60 Big=F
One-electron integrals computed using PRISM.
NBasis= 222 RedAO= T NBF= 222
NBsUse= 222 1.00D-06 NBFU= 222
```

Before the actual energy calculation is performed a guess for the wavefunction is obtained using the Harris method. Alternatively, a guess could also be read from the checkpoint or input file.

```
Harris functional with IExCor= 402 diagonalized for initial guess.
ExpMin= 9.33D-02 ExpMax= 9.11D+02 ExpMxC= 9.11D+02 IAcc=2 IRadAn= 4 AccDes= 0.00D+00
HarFok: IExCor= 402 AccDes= 0.00D+00 IRadAn= 4 IDoV=1
ScaDFX= 1.000000 1.000000 1.000000 1.000000
<S**2> of initial guess= 2.0000
```

The UB3LYP energy of the system is calculated with link 502. The heat of formation of the system is given relative to the corresponding elements in their standard states at 298K and 1bar pressure. The energy is given in atomic units (a.u., Hartree).

```
Requested convergence on RMS density matrix=1.00D-08 within 128 cycles.
Requested convergence on MAX density matrix=1.00D-06.
Requested convergence on energy=1.00D-06.
No special actions if energy rises.
Integral accuracy reduced to 1.0D-05 until final iterations.
EnCoef did 1 forward-backward iterations
Initial convergence to 1.0D-05 achieved. Increase integral accuracy.
SCF Done: E(UB+HF-LYP) = -2823.75111938 A.U. after 24 cycles
      Conv = 0.4891D-08 -V/T = 2.0092
      S**2 = 2.0088
Annihilation of the first spin contaminant:
S**2 before annihilation 2.0088, after 2.0000
```

Selected information on the optimized wavefunction is printed along with a Mulliken population analysis in link601.

Population analysis using the SCF density.

Alpha occ. eigenvalues -- -65.77906 -65.77859 -65.77530 -65.77283 -65.76357
 Alpha occ. eigenvalues -- -65.75541 -65.75457 -65.75179 -65.68641 -19.03988
 Alpha occ. eigenvalues -- -19.03842 -18.98261 -5.30490 -5.29808 -5.29518

.

.

Alpha virt. eigenvalues -- 2.00237 2.12797 2.18049 2.27291 2.39592
 Alpha virt. eigenvalues -- 2.40934 2.43628 2.54564 2.56050 2.57939
 Alpha virt. eigenvalues -- 2.63137 2.68744 3.11002 3.20990 3.23101
 Beta occ. eigenvalues -- -65.77858 -65.77692 -65.77518 -65.77049 -65.76320
 Beta occ. eigenvalues -- -65.75539 -65.75457 -65.75085 -65.68568 -19.03825
 Beta occ. eigenvalues -- -19.03691 -18.97581 -5.30251 -5.29795 -5.29504

.

.

Beta virt. eigenvalues -- 2.27530 2.39890 2.41167 2.44024 2.54778
 Beta virt. eigenvalues -- 2.56315 2.58295 2.63355 2.69171 3.11300
 Beta virt. eigenvalues -- 3.22159 3.23421

Condensed to atoms (all electrons):

		1	2	3	4	5	6
1	H	0.692854	-0.010127	-0.000067	-0.000078	0.000018	0.000000
2	H	-0.010127	0.694888	-0.000106	-0.000094	0.000000	0.000000
3	H	-0.000067	-0.000106	0.671425	0.000000	0.000150	-0.000063

.

.

22	O	0.369732	0.285670	-0.009719	8.021088	-0.020436	0.000005
23	O	0.001505	0.283892	-0.010110	-0.020436	8.042494	0.000014
24	O	-0.000007	-0.024351	0.750376	0.000005	0.000014	7.309498

Mulliken atomic charges:

1	
1	H -0.021871
2	H -0.020478
3	H 0.004839

.

.

22	O -0.586526
23	O -0.591986
24	O 0.010565

Sum of Mulliken charges= 0.00000

Atomic charges with hydrogens summed into heavy atoms:

1	
1	H 0.000000
2	H 0.000000
3	H 0.000000

.

.

22	O -0.586526
23	O -0.591986
24	O 0.010565

Sum of Mulliken charges= 0.00000

Atomic-Atomic Spin Densities.

		1	2	3	4	5	6
1	H	-0.001263	-0.000016	-0.000023	0.000021	0.000000	0.000000
2	H	-0.000016	0.000754	-0.000009	-0.000018	0.000000	0.000000
3	H	-0.000023	-0.000009	0.043209	0.000000	-0.000045	0.000051

.

.

.

```

22 O    0.002464 -0.028064 -0.001103  0.072536  0.000189  0.000001
23 O    0.000386 -0.024576 -0.003074  0.000189  0.065566  0.000003
24 O    0.000033  0.004674 -0.022670  0.000001  0.000003  0.320169
Mulliken atomic spin densities:
      1
1 H    -0.000556
2 H     0.000480
3 H     0.031374
.
.
22 O    0.045404
23 O    0.041377
24 O    0.258965
Sum of Mulliken spin densities=  2.00000
Electronic spatial extent (au): <R**2>= 13816.3675
Charge=  0.0000 electrons

```

In link 716 the forces acting on the nuclei in the current structure are calculated.

Based on this information and extrapolated second derivatives, the geometry of the system is then optimized.

```

Dipole moment (field-independent basis, Debye):
X=  -1.1949   Y=  -3.6322   Z=  -0.3149   Tot=    3.8366
Quadrupole moment (field-independent basis, Debye-Ang):
XX= -144.4356  YY= -170.6914  ZZ= -145.9753
XY= -14.6396  XZ=  -2.1017  YZ=  -6.7256
Traceless Quadrupole moment (field-independent basis, Debye-Ang):
XX=   9.2651  YY= -16.9906  ZZ=   7.7255
XY= -14.6396  XZ=  -2.1017  YZ=  -6.7256
Octapole moment (field-independent basis, Debye-Ang**2):
XXX= -629.2157  YYY= -1642.3646  ZZZ= -559.1831  XYY= -300.4322
XXY= -527.3560  XXZ= -181.7506  XZZ= -221.5762  YZZ= -529.1159
YYZ= -230.2137  XYZ= -29.5500
Hexadecapole moment (field-independent basis, Debye-Ang**3):
XXXX= -4298.3983  YYYY=-13438.7596  ZZZZ= -3339.2862  XXXY= -2229.0299
XXXZ= -767.6104  YYYY= -2646.7614  YYYZ= -2166.1740  ZZZX= -867.5263
ZZZY= -2035.6036  XYYX= -3041.4153  XXZZ= -1276.1823  YYZZ= -2888.0082
XXYZ= -690.3738  YYXZ= -481.6349  ZZXY= -850.6601
N-N= 1.911760870533D+03  E-N=-1.052403736265D+04  KE= 2.798035909220D+03
Isotropic Fermi Contact Couplings
      Atom
      a.u.      MegaHertz      Gauss      10(-4) cm-1
1 H(1)      -0.00012      -0.26082      -0.09307      -0.08700
2 H(1)       0.00016       0.36726       0.13105       0.12251
3 H(1)       0.00964       21.55067       7.68981       7.18853
.
.
22 O(17)      0.05858      -17.75587      -6.33574      -5.92272
23 O(17)      0.05212      -15.79840      -5.63726      -5.26978
24 O(17)      0.05180      -15.70185      -5.60281      -5.23757

```

```

-----
Center      ---- Spin Dipole Couplings ----
            3XX-RR      3YY-RR      3ZZ-RR
-----
1 Atom      -0.000051      0.000947      -0.000895
2 Atom       0.000187      0.001831      -0.002018
3 Atom      -0.002328      0.003961      -0.001633
.
.
22 Atom     -0.071605      0.069397      0.002207
23 Atom     -0.049814      0.063602      -0.013788
24 Atom       0.053542      0.290091      -0.343633

```

		XY	XZ	YZ
1	Atom	0.001181	0.000838	0.001238
2	Atom	0.002070	-0.000158	0.000002
3	Atom	-0.002765	0.001309	0.002136
.
22	Atom	0.053535	-0.029846	-0.049940
23	Atom	0.057857	-0.041620	-0.103531
24	Atom	-0.632678	-0.099642	0.034107

 Anisotropic Spin Dipole Couplings in Principal Axis System

Atom		a.u.	MegaHertz	Gauss	10(-4) cm-1	Axes		
1 H(1)	Baa	-0.0016	-0.839	-0.299	-0.280	-0.2430	-0.3336	0.9108
	Bbb	-0.0008	-0.445	-0.159	-0.148	0.8282	-0.5602	0.0158
	Bcc	0.0024	1.284	0.458	0.428	0.5050	0.7582	0.4124
2 H(1)	Baa	-0.0020	-1.089	-0.389	-0.363	0.1406	-0.0758	0.9872
	Bbb	-0.0012	-0.639	-0.228	-0.213	0.8151	-0.5571	-0.1589
	Bcc	0.0032	1.728	0.616	0.576	0.5620	0.8270	-0.0166
3 H(1)	Baa	-0.0047	-2.528	-0.902	-0.843	0.7352	0.3727	-0.5662
	Bbb	-0.0006	-0.334	-0.119	-0.112	0.6104	-0.0008	0.7921
	Bcc	0.0054	2.862	1.021	0.955	-0.2948	0.9279	0.2281
	Baa	-0.0020	-1.061	-0.379	-0.354	-0.1667	0.7020	-0.6924
.
22 O(17)	Bbb	-0.0244	1.763	0.629	0.588	-0.0151	0.4767	0.8789
	Bcc	0.1160	-8.394	-2.995	-2.800	0.3105	0.8378	-0.4491
	Baa	-0.0857	6.204	2.214	2.069	0.0932	0.5426	0.8348
23 O(17)	Bbb	-0.0739	5.350	1.909	1.785	0.9421	-0.3193	0.1023
	Bcc	0.1597	-11.554	-4.123	-3.854	0.3221	0.7769	-0.5410
	Baa	-0.4929	35.664	12.726	11.896	0.7338	0.5774	0.3580
24 O(17)	Bbb	-0.3295	23.845	8.508	7.954	-0.2294	-0.2854	0.9305
	Bcc	0.8224	-59.508	-21.234	-19.850	-0.6395	0.7650	0.0770

Center Number	Atomic Number	Forces (Hartrees/Bohr)		
		X	Y	Z
1	1	0.001146096	0.000418453	0.002297002
2	1	0.000438619	0.000309862	-0.002321601
3	1	-0.000917556	0.012633446	-0.000046790
.
22	8	-0.004878416	-0.006357674	-0.002443661
23	8	0.000940840	-0.011682918	-0.002452035
24	8	0.774765502	0.846384629	1.262745525

 Cartesian Forces: Max 1.262745525 RMS 0.282001930

Each subsequent step of the optimization is delimited by lines like these:

 Grad

Berny optimization.

Internal Forces: Max 0.021671785 RMS 0.018595738

Search for a local minimum.

Step number 1 out of a maximum of 20

All quantities printed in internal units (Hartrees-Bohrs-Radians)

Swaping is turned off.

Second derivative matrix not updated -- first step.

lowest eigenvalue of the Hessian is 0.1414 .

RFO step: Lambda= 8.34629057D-04.

Linear search not attempted -- option 19 set.

Iteration 1 RMS(Cart)= 0.03412487 RMS(Int)= 0.00111569


```

222 basis functions, 378 primitive gaussians, 222 cartesian basis functions
82 alpha electrons 80 beta electrons
nuclear repulsion energy 1893.1559509431 Hartrees.
NAtoms= 24 NActive= 24 NUniq= 24 SFac= 1.00D+00 NATFMM= 60 Big=F
One-electron integrals computed using PRISM.
NBasis= 222 RedAO= T NBF= 222
NBsUse= 222 1.00D-06 NBFU= 222
Initial guess read from the read-write file:
<S**2> of initial guess= 2.0134
Requested convergence on RMS density matrix=1.00D-08 within 128 cycles.
Requested convergence on MAX density matrix=1.00D-06.
Requested convergence on energy=1.00D-06.
No special actions if energy rises.
SCF Done: E(UB+HF-LYP) = -2824.26068137 A.U. after 13 cycles
          Conv = 0.3699D-08 -V/T = 2.0106
          S**2 = 2.0134
Annihilation of the first spin contaminant:
S**2 before annihilation 2.0134, after 2.0001
-----
Center Atomic Forces (Hartrees/Bohr)
Number Number X Y Z
-----
1 1 0.000016299 0.000621727 0.002496590
2 1 -0.000687029 0.002187895 -0.003350990
3 1 0.003233696 -0.006125911 0.005663815
.
.
.
22 8 0.000005178 0.000020516 -0.000005388
23 8 0.000022974 -0.000030844 -0.000030268
24 8 0.000003770 0.000015339 -0.000017250
-----
Cartesian Forces: Max 0.044119745 RMS 0.006837095

GradGradGradGradGradGradGradGradGradGradGradGradGradGradGradGradGrad
Benny optimization.
Internal Forces: Max 0.029278539 RMS 0.003303414
Search for a local minimum.
Step number 50 out of a maximum of 144
All quantities printed in internal units (Hartrees-Bohrs-Radians)
Update second derivatives using D2CorX and points 36 37 38 39 40
                                     41 42 43 44 45
                                     46 47 48 49 50
Trust test= 1.30D+00 RLast= 5.15D-03 DXMaxT set to 1.00D+00
Eigenvalues --- 0.00089 0.00372 0.00972 0.01314 0.03277
.
Eigenvalues --- 1000.000001000.000001000.00000

RFO step: Lambda=-3.01087941D-08.
Quartic linear search produced a step of 0.42139.
Iteration 1 RMS(Cart)= 0.00012700 RMS(Int)= 0.00000008
Iteration 2 RMS(Cart)= 0.00000004 RMS(Int)= 0.00000005
Variable Old X -DE/DX Delta X Delta X Delta X New X
          (Linear) (Quad) (Total)
X1 0.00000 0.00121 0.00000 0.00000 0.00000 0.00000
Y1 0.00000 0.00152 0.00000 0.00000 0.00000 0.00000
Z1 0.00000 0.00168 0.00000 0.00000 0.00000 0.00000
X2 0.00000 -0.00008 0.00000 0.00000 0.00000 0.00000
.
D87 -2.10410 0.00012 -0.00053 0.00090 0.00037 -2.10373
D88 2.23848 -0.00026 -0.00070 0.00095 0.00026 2.23874
Item Value Threshold Converged?
Maximum Force 0.000025 0.000450 YES
RMS Force 0.000004 0.000300 YES
Maximum Displacement 0.001274 0.001800 YES
RMS Displacement 0.000127 0.001200 YES
Predicted change in Energy=-2.550445D-08
Optimization completed.
-- Stationary point found.

```

After several steps all four convergence criteria are fulfilled. The structure and the wavefunction information for the converged structure are printed. This information includes the redundant internal coordinate definitions, which are given in the second column of the table. The numbers in parentheses refer to the atoms within the molecule specification. For example, the variable R1, defined as R(2,1), specifies the bond length between atoms 1 and 2. The energy for the optimized structure will be found in the output from the final optimization step, which precedes this table in the output file.

```

-----
!   Optimized Parameters   !
! (Angstroms and Degrees) !
-----
! Name  Definition          Value          Derivative Info.      !
-----
! X1    R(1,-1)              0.0            -DE/DX = 0.0012       !
! Y1    R(1,-2)              0.0            -DE/DX = 0.0015       !
! Z1    R(1,-3)              0.0            -DE/DX = 0.0017       !
.
.
! D85   D(21,20,22,19)       -51.1358       -DE/DX = -0.0006      !
! D86   D(23,20,22,19)       36.8774        -DE/DX = 0.0003       !
! D87   D(21,20,23,16)      -120.5561      -DE/DX = 0.0001       !
! D88   D(22,20,23,16)       128.2555       -DE/DX = -0.0003      !
-----

```

GradGradGradGradGradGradGradGradGradGradGradGradGradGradGradGradGrad

Input orientation:

```

-----
Center   Atomic   Atomic          Coordinates (Angstroms)
Number   Number   Type            X           Y           Z
-----
1         1         0               0.000000   0.000000   0.000000
2         1         0               0.000000   0.000000   2.439200
3         1         0               3.405407   0.000000   1.179228
.
.
22        8         0               0.974438   5.683461   -0.327222
23        8         0               2.579160   3.976724   0.097904
24        8         0               2.745370   5.492015   4.068503
-----

```

Distance matrix (angstroms):

```

      1         2         3         4         5
1  H    0.000000
2  H    2.439200  0.000000
3  H    3.603800  3.631023  0.000000
.
.
24 O    5.399743  3.010877  3.449808  5.529620  3.580723
      21         22         23         24
21 Si   0.000000
22 O    3.369816  0.000000
23 O    2.854058  2.380927  0.000000
24 O    1.624705  4.742915  4.253162  0.000000

```

Symmetry turned off by external request.
 Stoichiometry H12O3Si9(3)
 Framework group C1[X(H12O3Si9)]
 Deg. of freedom 66
 Full point group C1 NOp 1
 Rotational constants (GHZ): 0.3712325 0.3571113 0.3219723

 Population analysis using the SCF density.

 Alpha occ. eigenvalues -- -65.79592 -65.78218 -65.77961 -65.77065 -65.76617
 Alpha occ. eigenvalues -- -65.75838 -65.75411 -65.75241 -65.74816 -19.05796

Beta virt. eigenvalues -- 2.56999 2.58775 2.64011 2.70122 3.04247
 Beta virt. eigenvalues -- 3.07188 3.23086

Condensed to atoms (all electrons):

	1	2	3	4	5	6
1 H	0.696297	-0.010010	-0.000082	-0.000066	0.000013	0.000000
2 H	-0.010010	0.692841	-0.000224	-0.000049	0.000000	0.000000
3 H	-0.000082	-0.000224	0.708613	0.000000	0.000229	0.000320

22 O	0.346186	0.321110	-0.012542	8.006027	-0.025423	0.000000
23 O	0.038052	0.197931	0.010408	-0.025423	8.156629	0.000004
24 O	0.000088	-0.019458	0.475573	0.000000	0.000004	7.869431

Mulliken atomic charges:

1	
1 H	-0.024166
2 H	-0.020714
3 H	-0.014334

22 O	-0.573538
23 O	-0.660483
24 O	-0.310216

Sum of Mulliken charges= 0.00000

Atomic charges with hydrogens summed into heavy atoms:

1	
1 H	0.000000
2 H	0.000000
3 H	0.000000

22 O	-0.573538
23 O	-0.660483
24 O	-0.310216

Sum of Mulliken charges= 0.00000

Atomic-Atomic Spin Densities.

	1	2	3	4	5	6
1 H	-0.000801	-0.000002	-0.000012	0.000008	0.000001	0.000000
2 H	-0.000002	0.000023	0.000009	-0.000003	0.000000	0.000000
3 H	-0.000012	0.000009	0.027041	0.000000	-0.000016	0.000090

22 O	-0.002501	-0.020613	-0.000375	0.058907	0.000493	0.000000
23 O	0.003803	-0.027737	-0.007816	0.000493	0.097992	0.000002
24 O	0.000026	0.002442	-0.036721	0.000000	0.000002	0.787974

Mulliken atomic spin densities:

1	
1 H	-0.000326
2 H	0.000163
3 H	0.015724

```

.
22 O 0.035698
23 O 0.069940
24 O 0.737440
Sum of Mulliken spin densities= 2.00000
Electronic spatial extent (au): <R**2>= 13848.9089
Charge= 0.0000 electrons
Dipole moment (field-independent basis, Debye):
X= -0.4917 Y= -2.9114 Z= -1.8324 Tot= 3.4750

Quadrupole moment (field-independent basis, Debye-Ang):
XX= -142.4744 YY= -166.3022 ZZ= -151.8657
XY= -8.5875 XZ= -8.5891 YZ= -11.8887
Traceless Quadrupole moment (field-independent basis, Debye-Ang):
XX= 11.0731 YY= -12.7548 ZZ= 1.6818
XY= -8.5875 XZ= -8.5891 YZ= -11.8887
Octapole moment (field-independent basis, Debye-Ang**2):
XXX= -619.3850 YYY= -1616.0681 ZZZ= -613.8510 XXY= -264.6661
XXY= -511.9235 XXZ= -215.3116 XZZ= -243.8888 YZZ= -552.9745
YYZ= -254.8585 XYZ= -52.3854
Hexadecapole moment (field-independent basis, Debye-Ang**3):
XXXX= -4196.8582 YYYY=-13371.7449 ZZZZ= -3684.9219 XXXY= -2153.0753
XXXZ= -953.5072 YYYX= -2418.0039 YYYZ= -2329.4342 ZZZX= -1058.3133
ZZZY= -2310.3032 XXYX= -2963.2311 XXZZ= -1377.2064 YYZZ= -3035.5007
XXYZ= -831.3117 YYXZ= -596.1096 ZZXY= -936.1710
N-N= 1.893155950943D+03 E-N=-1.048456408998D+04 KE= 2.794521444675D+03
Isotropic Fermi Contact Couplings
Atom a.u. MegaHertz Gauss 10(-4) cm-1
1 H(1) -0.00005 -0.11278 -0.04024 -0.03762
2 H(1) 0.00006 0.13201 0.04711 0.04404
3 H(1) 0.00471 10.52060 3.75401 3.50930
.
.
.
22 O(17) 0.05724 -17.34952 -6.19074 -5.78718
23 O(17) 0.01157 -3.50666 -1.25126 -1.16970
24 O(17) 0.09758 -29.57505 -10.55311 -9.86517

```

```

-----
Center ---- Spin Dipole Couplings ----
3XX-RR 3YY-RR 3ZZ-RR
-----
1 Atom -0.000200 0.000943 -0.000743
2 Atom -0.000145 0.001681 -0.001536
3 Atom -0.001908 0.003063 -0.001155
.
.
.
22 Atom 0.056015 -0.058041 0.002025
23 Atom -0.027896 -0.023651 0.051547
24 Atom 0.069880 0.863590 -0.933469
-----
XY XZ YZ
-----
1 Atom 0.001059 0.000555 0.000992
2 Atom 0.001623 -0.000070 0.000079
3 Atom -0.001901 0.000789 0.001445
.
.
.
22 Atom 0.060087 -0.086903 -0.039493
23 Atom 0.114981 -0.135505 -0.147065
24 Atom -1.543051 -0.379540 0.271562
-----

```

Anisotropic Spin Dipole Couplings in Principal Axis System

Atom	a.u.	MegaHertz	Gauss	10(-4) cm-1	Axes
Baa	-0.0012	-0.645	-0.230	-0.215 -0.1257 -0.3636	0.9230

1	H(1)	Bbb	-0.0008	-0.443	-0.158	-0.148	0.8732	-0.4821	-0.0710
		Bcc	0.0020	1.088	0.388	0.363	0.4708	0.7971	0.3781
		.							
		.							
		Baa	-1.2095	87.520	31.229	29.194	0.7136	0.4622	0.5265
24	O(17)	Bbb	-0.9160	66.279	23.650	22.108	-0.3428	-0.4250	0.8378
		Bcc	2.1255	-153.799	-54.879	-51.302	-0.6110	0.7783	0.1449

When a Z-matrix was used for the initial molecule specification, this output will be followed by an expression of the optimized structure in that format, whenever possible.

Final structure in terms of initial Z-matrix:

```

H
H,1,r2
H,1,r3,2,a3
.
.
.
O,20,r22,19,a22,12,d22,0
O,20,r23,19,a23,12,d23,0
O,21,r24,18,a24,9,d24,0
  Variables:
r2=2.4392
r3=3.6038
a3=70.9
.
.
.
r24=1.62470532
a24=117.48711308
d24=-32.67810492

```

At the very end of each Gaussian calculation, an archive entry in a very compact format is printed to summarize the results. This archive entry is frequently used as supplemental material in publications of theoretical results.

```

1\1\GINC-THOR\FOpt\UB3LYP\3-21G*\H12O3Si9(3)\PHERRERA\21-Oct-2004\0\#\#
UB3LYP/3-21G* OPT(MODREDUNDANT) NOSYMM\OSISIO2d_3_321.inp\0,3\H,0.,0
.,0.\H,0.,0.,2.4392\H,3.4054068896,0.,1.1792278643\H,-2.3643946794,2.4
634634,4.0085326199,-1.8676148497\H,-1.1265747899,5.5302583028,-0.0337
0145066,4.0685026139\Version=x86-Linux-G03RevB.04\HF=-2824.2606814\S2
=2.013446\S2-1=0.\S2A=2.000087\RMSD=3.699e-09\RMSF=6.837e-03\Dipole=-0
.1934417,-1.1454323,-0.7209343\PG=C01 [X(H12O3Si9)]\@\#

```

From a database of citations, Gaussian prints one entry together with some timing information.

```

WAR ES EIN GOTT DER DIESE ZEICHEN SCHRIEB?
- LUDWIG BOLTZMANN, QUOTING GOETHE, ABOUT MAXWELL'S EQUATIONS.
Job cpu time: 0 days 22 hours 14 minutes 51.5 seconds.
File lengths (MBytes): RWF= 69 Int= 0 D2E= 0 Chk= 11 Scr= 1
Normal termination of Gaussian 03 at Thu Oct 21 07:39:55 2004.

```

APPENDIX C
CALCULATION PROTOCOL FOR INITIAL GEOMETRY FOR GEOMETRY
OPTIMIZATIONS

It is not practical to start a geometry optimization calculation using directly the UB3LYP/6-311++G(2d,p) model chemistry, since it would be computationally very demanding and time consuming. Instead, a computational protocol (summarized in Table C-1) that uses molecular mechanics and semi-empirical methods followed by DFT/UB3LYP calculations with small basis sets is used to obtain initial structures that are very close to the one that corresponds to the optimized geometry of the clusters.

Table C-1. Calculation protocol used to determine the best initial geometry for the geometry optimization, transition state search and frequency calculations.

Step	Description	Software required	Input file	Output file
1	Draw initial sketch of structure Options: modify a stored calculation result or start from scratch	HyperChem 7	None or .hin	.hin
2	Molecular mechanics optimization	HyperChem 7	.hin	.hin
3	AM1 [132] semi-empirical optimization	HyperChem 7	.hin	.hin
4	Generate internal coordinates matrix	Babel	.hin	.zmt
5	Generate the Gaussian03 input file from .zmt file	Text editor	.zmt	.inp
6	Density functional theory optimization using the UB3LYP/3-21G* model chemistry	Gaussian03	.inp	.log

The calculation protocol starts with HyperChem 7 where a new structure is built using the software, or one already available in the calculation database is modified. When the initial draft of the structure is finished, the hydrogen atoms are labeled with their respective numbers in the molecule matrix to impose constraints. These atoms are

fixed at their positions by modifying their force constants from the default value of 7 to an arbitrary value of 5000, a change necessary in HyperChem 7 to guarantee that the hydrogen remain fixed during calculations. Once the boundary conditions and constraints are specified the structure is ready to undergo the geometry optimization process. The molecular mechanics (MM+) calculation is run first, and once it is done it is immediately followed by an AM1 optimization [132]. The resulting HyperChem 7 output file (in .hin long format) is changed with the Emacs text file editor into a .hin short file, converted into a .zmt file using Babel and modified again to insert an input section to generate the Gaussian03 input file (Figure A-7A). This file is used by Gaussian03 [71] to run the UB3LYP/3-21G* calculation and the Gaussian log file is read using Molden. In this visualization program, the user has the option to generate a .xyz file of the final structure. This .xyz file is transformed into a .zmt and a .hin short file using Babel. While the .zmt file is used to generate a Gaussian03 input file for the actual 6-311++G(2d,p) calculation, the .hin file is used to generate an image of the initial structure.

APPENDIX D CALCULATION PROTOCOL FOR INITIAL GEOMETRY FOR TRANSITION STATE SEARCHES

We used Gaussian03 options OPT(QST2) and OPT(QST3) to search for transition state structures [71]. (Here OPT stands for Optimization calculation). Both methods search for a transition structure using the synchronous transit-guided quasi-Newton (STQN) method [74, 82] and require at least the reactant and product structures in the input file. OPT(QST3) requires a third structure, corresponding to an initial guess for the transition state. It is imperative that the atoms in all the structures are labeled exactly in the same order. All the transition state calculations are run with the UB3LYP/3-21G* level of theory to speed the convergence process. We specified OPT(NoEigen) so the simulation did not stop after two iterations. This option overrides the default option OPT(Eigen), which searches for the number of negative eigenvalues after each iteration. Given the structural configuration of the Si₉H₁₂ clusters, and the constraints imposed on them, the initial iterations of this STQN method always result in more than one negative eigenvalue. OPT(CalcAll) is used to calculate the Hessian matrix after each iteration. We do not update the Hessian (as we do with the geometry optimization calculations because of computation economy) because it is required that the description of the force fields be as accurate as possible so the transition state structure can be located more precisely [71].

OPT(QST2) is generally straight forward. Having optimized structures for the reactant and the product of the reaction of interest, it is simple to combine the two in a Gaussian03 input (.inp) file and run the calculation.

```

%Mem=450MB
#ub3lyp/3-21G* Opt (ModRedundant,CalcAll,QST2,NoEigen) Nosymm

OxSIOsIOd_OsIOsIO_3_TS321.inp Reactant: OxSIOsIOd_3_631.log

  0 3
  H
  H   1 r2
  H   1 r3   2 a3
  H   1 r4   2 a4   3 d4

d23= 302.33
r24= 1.6282
a24= 107.78
d24= 166.77

  1 B
  2 B
  3 B
  4 B
  5 B
  6 B
  7 B
  8 B
  9 B
 10 B
 11 B
 12 B
 * F

Product: OsIOsIO_3_631.zmt

  0 3
  H
  H   1 r2
  H   1 r3   2 a3
  H   1 r4   2 a4   3 d4

d23= 157.37
r24= 1.5739
a24= 101.30
d24= 34.13

  1 B
  2 B
  3 B
  4 B
  5 B
  6 B
  7 B
  8 B
  9 B
 10 B
 11 B
 12 B
 * F

```

Reactant structure
(Z-Matrix)

Reactant constraints
(Notice that they are
exactly the same as
those of the product).

Product structure
(Z-matrix)

Product constraints
(Notice that they are
exactly the same as
those of the reactant).

Figure D-1. Input file for a transition state search that uses the OPT(QST2) option. In this case, there was not need to reorder the atoms in the structures.

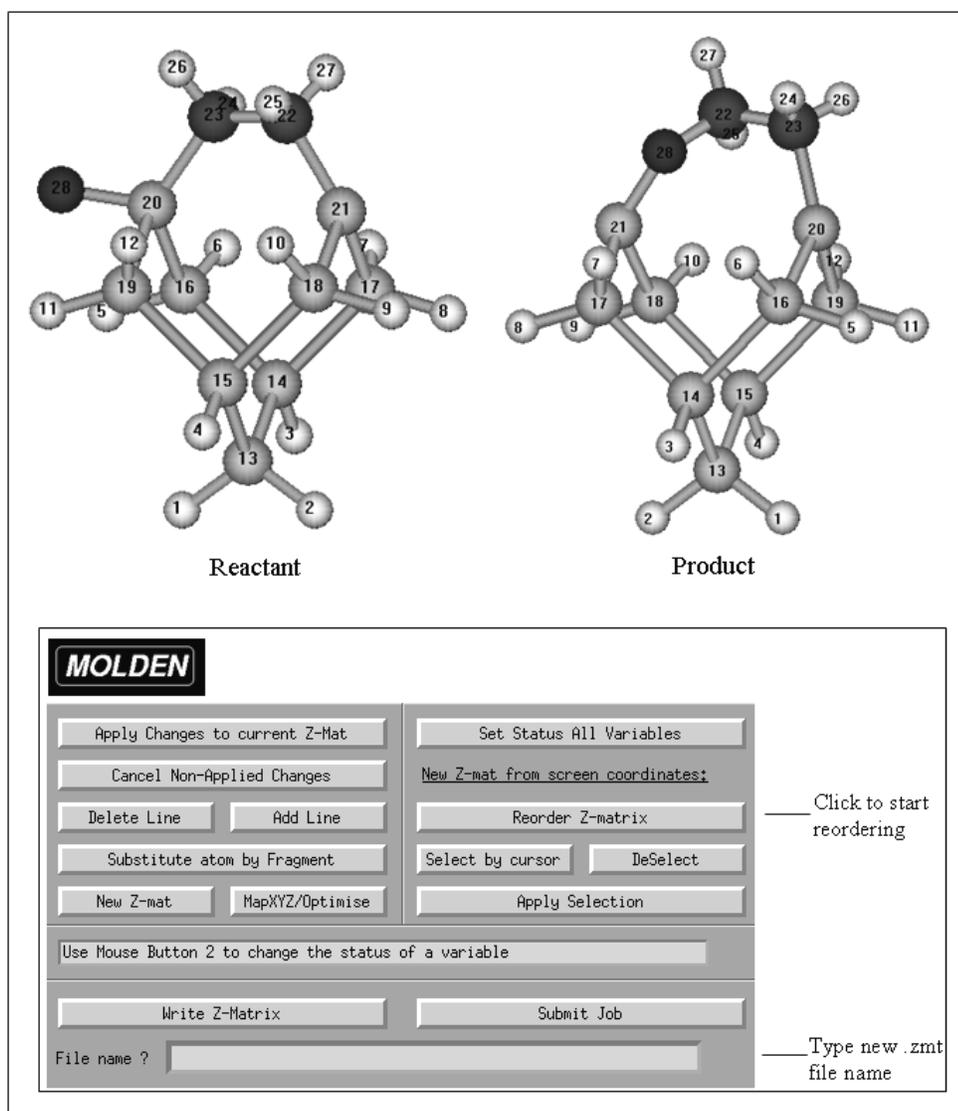


Figure D-2. Diagram of the structures of reactant and product used to search for a transition state structure using OPT(QST2) or OPT(QST3) in Gaussian03. Since the atom order is different for the two structures, one of them must be reordered using Molden. Insert: Molden commands used to change the Z-matrix order for the structures.

Sometimes, however, the bonds being broken (or formed) must be increased by approximately 1.5 times so both the reactant and product initial structures are closer to the estimated transition state geometry (Figure D-1). In some cases, the order of the atoms (especially that of the adsorbed atoms) differs considerably between the reactant and the product. In such cases, the program Molden is used to visualize both structures

and reorder one of them so its atom sequence matches that of the other structure, by using the powerful Z-matrix command of this visualization software. Notice that the latter the file depicted in Figure D-3 is analogous to the sample file presented in Figure A-5 and that the only difference is the notation used to specify the variables. One may refer to the notation used to name the variables in Figure A-5 as the Babel notation, while the one used in Figure D-3 would be the Molden notation. Finally, the result is a Gaussian03 input file that has the reactant (product) structure expressed in Babel notation and the product (reactant) expressed in Molden Notation (Figure D-4).

o					
si	1	sio2			
si	1	sio3	2	siosi3	
h	3	hsi4	1	hsio4	2 dih4
h	3	hsi5	1	hsio5	2 dih5
h	2	hsi6	1	hsio6	3 dih6
h	1	ho7	3	hosi7	4 dih7
h	3	hsi8	1	hsio8	2 dih8
h	2	hsi9	1	hsio9	3 dih9

Molecular structure matrix

sio2	1.644612
sio3	1.644300
siosi3	145.707
hsi4	1.478621
hsio4	108.261
dih4	171.833
hsi5	1.483160
hsio5	110.581
dih5	51.850
hsi6	1.493849
hsio6	110.091
dih6	-56.308
ho7	3.191454
hosi7	94.752
dih7	52.642
hsi8	1.482527
hsio8	110.177
dih8	-68.454
hsi9	1.488440
hsio9	107.834
dih9	-176.147

Variables

Figure D-3. Z-matrix (.zmt) file generated by Molden. This file is completely analogous to the Z-matrix presented in Figure A-5. The only difference the two files is the notation used for the variables. While the Babel notation used in Figure A-5 is based on the number of bond length, bond angle or dihedral angle, the Molden notation is based on the atomic symbol of the atoms involved in the bond length, bond angle or dihedral angle.

```

#sub3lyp/3-21G* Opt (QST2,Noeigen,CalcAll,ModRedundant)
Reactant: structure in "Babel notation"
0 1
Si
H 1 r2
H 1 r3 2 a3
O 1 r4 2 a4 3 d4
Si 4 r5 1 a5 2 d5
H 5 r6 4 a6 1 d6
H 5 r7 4 a7 1 d7
H 1 r8 2 a8 3 d8
H 5 r9 4 a9 1 d9
Variables:
r2= 1.4560
r3= 1.4551
a3= 109.16
r4= 1.7264
a4= 111.49
d4= 240.04
r5= 1.7263
a5= 153.16
d5= 359.44
r6= 1.4554
a6= 107.59
d6= 180.28
r7= 1.4558
a7= 110.51
d7= 60.54
r8= 1.4551
a8= 109.16
d8= 120.05
r9= 1.4558
a9= 110.53
d9= 300.03

2 B
3 B
4 B
* F

Product: structure in "Molden notation"
0 1
o
si 1 sio2
si 1 sio3 2 sios13
h 3 hsi4 1 hsio4 2 dih4
h 3 hsi5 1 hsio5 2 dih5
h 2 hsi6 1 hsio6 3 dih6
h 1 ho7 3 hos17 4 dih7
h 3 hsi8 1 hsio8 2 dih8
h 2 hsi9 1 hsio9 3 dih9

sio2 1.644612
sio3 1.644300
sios13 145.707
hsi4 1.478621
hsio4 108.261
dih4 171.833
hsi5 1.483160
hsio5 110.581
dih5 51.850
hsi6 1.493849
hsio6 110.091
dih6 -56.308
ho7 3.191454
hos17 94.752
dih7 52.642
hsi8 1.482527
hsio8 110.177
dih8 -68.454
hsi9 1.488440
hsio9 107.834
dih9 -176.147

2 B
3 B
4 B
* F

```

Gaussian03 commands

Reactant structure
Babel notation

Product structure
Molden notation

Figure D-4. Gaussian03 input file for a transition state search where the product structure had to be reordered using Molden. This file is analogous to the Gaussian03 input file presented in Figure D-1.

The OPT(QST3) calculations are performed when the OPT(QST2) initialization does not converge. OPT(QST2) has initial convergence problems when the reactant and product structures differ significantly. In this case, an intermediate structure is generated using HyperChem 7. The reactant and product structures are merged in HyperChem 7, where either one of them is labeled as the reactant and the other, as the product. Once the structures are labeled, the option Reaction Map is used to match the atom numbers in both structures. The user must match pairs of atoms individually, making sure that their positions in space have meaning for a reaction path following algorithm.

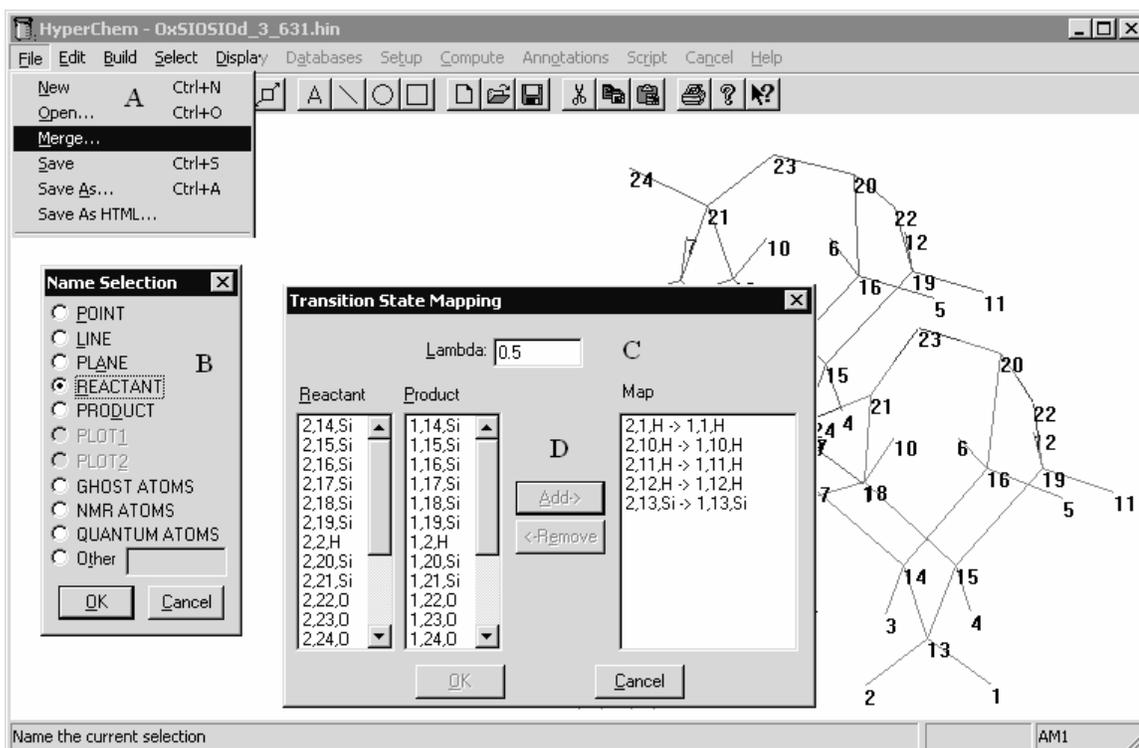


Figure D-5. Process used to generate an initial guess for the transition state search using OPT(QST3) in Gaussian03. HyperChem 7 is the visualization software used. A) Reactant structure is opened and merged with the product. B) Each structure is selected and named as either REACTANT or PRODUCT. C) A Reaction Map is created by mapping the two structures. The factor lambda tells Hyperchem 7 how close the structure will be to that of the reactant (lambda = 0) or the product (lambda = 1). D) The atoms are matched one by one. At the end of the process, Hyperchem 7 generates the TS structure.

As in the case of OPT(QST2), the order of the atoms must be exactly the same in both structures. After the reaction map is completed, HyperChem automatically generates the structure of the transition state. The end structure must be saved in a different .hin file, that will be transformed into a .zmt file with Babel. The typical Gaussian03 input file that uses OPT(QST3) is similar to that which uses OPT(QST2), but with a third structure following that of the product. One must be aware that the same constraints must be imposed on the same atoms in both the reactant and product. These constraints, however, are not accepted for the transition state structure in the Gaussian03 calculation. Nonetheless, since Gaussian03 [71] would not run the calculation until some constraint are specified for the transition state structure (because OPT(ModRedundant) is specified), we added a fixed atom constraint for all our transition state structures. The atom chosen was the first one specified in the Z-Matrix of the Gaussian03 input file, since by keeping it fixed, we do not alter the calculation.

LIST OF REFERENCES

- [1] R. E. Schlier, and H.E. Farnsworth, *J. Chem. Phys.* **30** (1959) 917.
- [2] H. Over, J. Wasserfall, W. Ranke, C. Ambiatello, R. Sawitzki, D. Wolf and W. Moritz, *Phys. Rev. B* **55** (1997) 4731.
- [3] E. Landmark, C. J. Karlsson, Y.-C. Chao and R. I. G. Uhrberg, *Phys. Rev. Lett.* **69** (1992) 1588.
- [4] R. I. G. Uhrberg, G. V. Hansson, J. M. Nicholls and S. A. Flodström, *Phys. Rev. B* **24** (1981) 4684.
- [5] R. D. Bringans, R. I. G. Uhrberg, M. A. Olmstead and R. Z. Bachrach, *Phys. Rev. B* **34** (1986) 7447.
- [6] F. J. Himpsel and Th. Fauster, *J. Vac. Sci. Technol. A* **2** (1984) 815.
- [7] P. Martensson, A. Cricenti and G. V. Hansson, *Phys. Rev. B* **33** (1986) 8855.
- [8] R.J. Hamers and U.K. Köhler, *J. Vac. Sci. Technol. A* **7** (1989) 2854.
- [9] R.J. Hamers, R.M. Tromp, and J.E. Demuth, *Surf. Sci.* **181** (1987) 346.
- [10] Y. Widjaja and C. B. Musgrave, *Phys. Rev. B* **64** (2001) 205303.
- [11] D.D. Eley and E.K. Rideal, *Nature* **146** (1940) 401.
- [12] J. Gadsby, C.N. Hinshelwood and K.W. Sykes. *Proc. Royal Soc. London A* **187** (1946) 1009.
- [13] J. Harris and B. Kasemo, *Surf. Sci. Lett.* **105** (1981) L281.
- [14] M. Litorja and S.A. Buntin, *J. Vac. Sci. Technol. A* **20** (2002) 76.
- [15] A. Dinger, C. Lutterloh and J. Küppers, *Chem. Phys. Lett.* **311** (1999) 202.
- [16] A. Kubo, Y. Ishii, and M. Kitajima, *J. Chem. Phys.* **117** (2002) 11336.
- [17] D. D. Koleske, S. M. Gates, and J. A. Schultz, *J. Chem. Phys.* **99**, 5619 (1993).
- [18] D. D. Koleske, S. M. Gates, and B. Jackson, *J. Chem. Phys.* **101**, 3301 (1994).

- [19] W. Widdra, S. I. Yi, R. Maboudian, G. A. D. Briggs and W. H. Weinberg, *Phys. Rev. Lett.* **74** (1995) 2074.
- [20] M. C. Flowers, N. B. H. Jonathan, A. Morris and S. Wright, *Surf. Sci.* **396** (1998) 227.
- [21] U. Hansen and P. Vogl, *Phys. Rev. B* **57** (1998) 13295.
- [22] P. Kratzer, *J. Chem. Phys.* **106** (1997) 6752.
- [23] P. Kratzer, *Chem. Phys. Lett.* **288** (1998) 396.
- [24] S.A. Buntin, *Chem. Phys. Lett.* **278** (1997) 71.
- [25] S.A. Buntin, *J. Chem. Phys.* **108** (1998) 1601.
- [26] M. P. D'Evelyn, M. M. Nelson and T. Engel, *Surf. Sci.* **186** (1987) 75.
- [27] J. R. Engstrom, M. M. Nelson and T. Engel, *J. Vac. Sci. Technol. A* **7** (1989) 1837.
- [28] J. R. Engstrom, D. J. Bonser and T. Engel, *Surf. Sci.* **268** (1992) 238.
- [29] J. R. Engstrom, D. J. Bonser, M. M. Nelson and T. Engel, *Surf. Sci.* **256** (1991) 317.
- [30] J.R. Engstrom and T. Engel, *Phys. Rev. B* **41** (1990) 1038.
- [31] T. Engel, *Surf. Sci. Repts.* **18** (1993) 93.
- [32] W. Orellana, A.J.R. da Silva and A. Fazzio, *Phys. Rev. Lett.* **90** (2003) 016103.
- [33] M. L. Green, E. P. Gusev, R. Degraeve and E. L. Garfunkel, *J. Appl. Phys.* **90** (2001) 2057.
- [34] M. K. Weldon, K. T. Queeney, J. Eng Jr., K. Raghavachari and Y. J. Chabal, *Surf. Sci.* **500** (2002) 859.
- [35] J. T. Yates, Jr., *Science*, **279** (1998) 335.
- [36] S. F. Bent, *Surf. Sci.* **500** (2002) 879.
- [37] A. Avila, I. Montero, L. Galán, J. M. Ripalda and R. Levy, *J. Appl. Phys.* **89** (2001) 212.
- [38] B. Schneider, A. Guette, R. Naslain, M. Cataldi and A. Costecalde, *J. Mater. Sci.* **33** (1998) 535.
- [39] M. R. Wang, E. Rusli, J. L. Xie, N. Babu, Y. Li, and K. Rakesh, *J. Appl. Phys.* **96** (2004) 829.

- [40] P. M. W. Gill, *Density Functional Theory*, in *Encyclopedia of Computational Chemistry*, P. von Ragué Schleyer, ed., (John Wiley & Sons Ltd, New York, 1998). p. 678.
- [41] P. Hohenberg and W. Kohn, *Phys. Rev.* **136** (1964) B864.
- [42] W. Kohn and L.J. Sham, *Phys. Rev.* **140** (1965) 1133.
- [43] R.G. Parr and W. Yang, *Density-Functional Theory of Atoms and Molecules* (Oxford University Press, New York, 1989).
- [44] W. Kohn, A.D. Becke and R.G. Parr, *J. Phys. Chem.* **100** (1996) 12974.
- [45] C.J. Cramer, *Essentials of Computational Chemistry*, (John Wiley & Sons Ltd, New York, 2003).
- [46] L. H. Thomas, *Proc. Cambridge Phil. Soc.* **23** (1927) 542.
- [47] E. Fermi, *Z. Physik* **48** (1928) 73.
- [48] S. H. Vosko, L. Wilk and M. Nusair, *Can. J. Phys.* **58** (1980) 1200.
- [49] A.D. Becke, *Phys. Rev. A* **38** (1988) 3098.
- [50] C. Lee, W. Yang and R. G. Parr, *Phys. Rev. B* **37** (1988) 785.
- [51] R. Colle and O. Salvetti, *Theoret. Chim. Acta* **37** (1975) 329.
- [52] B. Michlich, A. Savin, H. Stoll and H. Preuss, *Chem. Phys. Lett.* **157** (1989) 200.
- [53] A. D. Becke, *J. Chem. Phys.* **98** (1993) 5648.
- [54] J. K. Kang and C. B. Musgrave, *J. Chem. Phys.* **115** (2001) 11040.
- [55] R. D. Adamson, P. M. W. Gill and J. A. Pople, *Chem. Phys. Lett.* **284** (1998) 6.
- [56] C. Y. Lin, M. W. George and P. M. W. Gill *Aust. J. Chem.* **57** (2004) 365.
- [57] D. E. Woon and T. H. Dunning Jr., *J. Chem. Phys.* **98** (1993) 1358.
- [58] J. A. Pople and R. K. Nesbet, *J. Chem. Phys.* **22** (1954) 571.
- [59] J. S. Binkley, J. A. Pople and W. J. Hehre, *J. Am. Chem. Soc.* **102** (1980) 939.
- [60] J. A. Pople and W. J. Hehre, *J. Comp. Phys.* **27** (1978) 161.
- [61] W. J. Hehre, R. F. Stewart and J. A. Pople, *J. Chem. Phys.* **51** (1969) 2657.

- [62] W. J. Hehre, R. Ditchfield, R. F. Stewart and J. A. Pople, *J. Chem. Phys.* **52** (1970) 2769.
- [63] W. J. Hehre, R. Ditchfield and J. A. Pople, *J. Chem. Phys.* **56** (1972) 2257.
- [64] W. J. Hehre and J. A. Pople, *J. Chem. Phys.* **56** (1972) 4233.
- [65] J. D. Dill and J. A. Pople, *J. Chem. Phys.* **62** (1975) 2921.
- [66] J. S. Binkley and J. A. Pople, *J. Chem. Phys.* **66** (1977) 879.
- [67] M. M. Francl, W. J. Pietro, W. J. Hehre, J. S. Binkley, M. S. Gordon, D. J. DeFrees and J. A. Pople, *J. Chem. Phys.* **77** (1982) 3654.
- [68] M. S. Gordon, J. S. Binkley, J. A. Pople, W. J. Pietro and W. J. Hehre, *J. Am. Chem. Soc.* **104** (1982) 2797.
- [69] R. Ditchfield, W. J. Hehre and J. A. Pople, *J. Chem. Phys.* **54** (1971) 724.
- [70] B. Schlegel, *Geometry Optimization: 1*, in *Encyclopedia of Computational Chemistry*, P. von Ragué Schleyer, ed., (John Wiley & Sons Ltd, New York, 1998). p. 1136.
- [71] M. J. Frisch, G. W. Trucks, H. B. Schlegel, G. E. Scuseria, M. A. Robb, J. R. Cheeseman, J. A. Montgomery Jr., T. Vreven, K. N. Kudin, J. C. Burant, J. M. Millam, S. S. Iyengar, J. Tomasi, V. Barone, B. Mennucci, M. Cossi, G. Scalmani, N. Rega, G. A. Petersson, H. Nakatsuji, M. Hada, M. Ehara, K. Toyota, R. Fukuda, J. Hasegawa, M. Ishida, T. Nakajima, Y. Honda, O. Kitao, H. Nakai, M. Klene, X. Li, J. E. Knox, H. P. Hratchian, J. B. Cross, C. Adamo, J. Jaramillo, R. Gomperts, R. E. Stratmann, O. Yazyev, A. J. Austin, R. Cammi, C. Pomelli, J. W. Ochterski, P. Y. Ayala, K. Morokuma, G. A. Voth, P. Salvador, J. J. Dannenberg, V. G. Zakrzewski, S. Dapprich, A. D. Daniels, M. C. Strain, O. Farkas, D. K. Malick, A. D. Rabuck, K. Raghavachari, J. B. Foresman, J. V. Ortiz, Q. Cui, A. G. Baboul, S. Clifford, J. Cioslowski, B. B. Stefanov, G. Liu, A. Liashenko, P. Piskorz, I. Komaromi, R. L. Martin, D. J. Fox, T. Keith, M. A. Al-Laham, C. Y. Peng, A. Nanayakkara, M. Challacombe, P. M. W. Gill, B. Johnson, W. Chen, M. W. Wong, C. Gonzalez, and J. A. Pople, *Gaussian03, Revision A.1*, (Gaussian, Inc., Pittsburgh, 2003).
- [72] H. B. Schlegel, *J. Comp. Chem.* **3** (1982) 214.
- [73] P. Y. Ayala and H. B. Schlegel, *J. Chem. Phys.* **107** (1997) 375.
- [74] C. Y. Peng, P. Y. Ayala, H. B. Schlegel and M. J. Frisch, *J. Comp. Chem.* **17** (1996) 49.
- [75] H. B. Schlegel, *Theor. Chim. Acta* **66** (1984) 333.
- [76] T. H. Fischer and J. Almlöf, *J. Phys. Chem.* **96** (1992) 9768.

- [77] J. Baker and W. J. Hehre, *J. Comp. Chem.* **12** (1991) 606.
- [78] J. Baker, *J. Comp. Chem.* **14** (1993) 333.
- [79] J. M. Bofill and M. Comajuan, *J. Comp. Chem.* **16** (1995) 1326.
- [80] T. A. Halgren and W. N. Lipscomb, *Chem. Phys. Lett.* **49** (1977) 225.
- [81] J. Baker, *J. Comp. Chem.* **7** (1986) 385.
- [82] C. Peng and H. B. Schlegel, *Israel J. Chem.* **33** (1994) 449.
- [83] P. Pulay, G. Fogarasi, F. Pang and J. E. Boggs, *J. Am. Chem. Soc.* **101** (1979) 2550.
- [84] G. Fogarasi, X. Zhou, P. W. Taylor and P. J. Pulay, *J. Am. Chem. Soc.* **114** (1992) 8191.
- [85] I. J. R. Baumvol, *Surf. Sci. Rep.* **36** (1999) 1.
- [86] D. Mathiot, A. Straboni, E. Andre and P. Debenest, *J. Appl. Phys.* **73** (1993) 8215.
- [87] B. C. Smith and H. H. Lamb, *J. Appl. Phys.* **83** (1998) 7635.
- [88] A. Khandelwal, H. Niimi, G. Lucovsky and H. H. Lamb, *J. Vac. Sci. Technol. A* **20** (2002) 1989.
- [89] K. Watanabe and T. Tatsumi, *Appl. Phys. Lett.* **76** (2000) 2940.
- [90] A. G. Schrott, Q. Su and S. C. Fain, *Surf. Sci.* **123** (1982) 223.
- [91] F. Bozso and Ph. Avouris, *Phys. Rev. B* **38** (1988) 3937.
- [92] W. J. Hehre, L. Radom, P. V. R. Schleyer and J. A. Pople, *Ab Initio Molecular Orbital Theory* (Wiley, New York, 1986).
- [93] Chabal, Y.J, *Phys. Rev. B* **29** (1984) 3677.
- [94] Y. J. Chabal and K. Raghavachari, *Phys. Rev. Lett.* **53** (1984) 282.
- [95] K. Raghavachari, Y. J. Chabal and L. M. Struck, *Chem. Phys. Lett.* **252** (1996) 230.
- [96] B.B. Stefanov and K. Rachavachari, *Surf. Sci. Lett.* **389** (1997) L1159.
- [97] Y. Widjaja, M. M. Mysinger and C. B. Musgrave, *J. Phys. Chem. B* **104**, (2000) 2527.
- [98] Y. Widjaja, A. Heyman and C.B. Musgrave, *J. Phys. Chem. B.* **106** (2002) 2643.
- [99] Y. Widjaja and C. B. Musgrave, *Surf. Sci.* **469** (2000) 9.

- [100] Y. Widjaja and C. B. Musgrave, *J. Chem. Phys.* **116** (2002) 5774.
- [101] L. T. Ueno and F. R. Ornellas, *Surf. Sci. Lett.* **490** (2001) L637.
- [102] S. Pai and D. Doren, *J. Phys. Chem.* **98** (1994) 4422.
- [103] C. Yang, S. Y. Lee and H. C. Kang, *J. Chem. Phys.* **107** (1997) 3295.
- [104] R. Konečný and D. J. Doren, *J. Chem. Phys.* **106** (1997) 2426.
- [105] Y. Saito, *Appl. Phys. Lett.* **68** (1996) 800.
- [106] M.G. Blain, *J. Vac. Sci. Technol. A* **17** (1999) 665.
- [107] A. L. Gerrard, J.-J. Chen and J. F. Weaver, *J. Chem. Phys.* **122** (2005) 1248.
- [108] C. H. F. Peden, J. W. Rogers Jr., N. D. Shinn, K. B. Kidd and K. L. Tsang, *Phys. Rev. B* **47** (1993) 15622.
- [109] X. Xu, S.-Y. Kang and T. Yamabe, *Phys. Rev. Lett.* **88** (2002) 076106.
- [110] J. W. Kim, H. W. Yeom, K. J. Kong, B. D. Yu, D. Y. Ahn, Y. D. Chung, C. N. Whang, H. Yi, Y. H. Ha and D. W. Moon, *Phys. Rev. Lett.* **90** (2003) 106101.
- [111] K. Ohmori, H. Ikeda, H. Iwano, S. Zaima and Y. Yasuda, *Appl. Surf. Sci.* **117-118** (1997) 114.
- [112] A. Redondo and W.A. Goddard III, *J. Vac. Sci. Technol.* **21** (1982) 344.
- [113] B. B. Stefanov, A. B. Gurevich, M. K. Weldon, Y. J. Chabal and K. Raghavachari, *Phys. Rev. Lett.* **81** (1998) 3908.
- [114] M. K. Weldon, K. T. Queeney, Y. J. Chabal, B. B. Stefanov and K., Raghavachari, *J. Vac. Sci. Technol. B* **17** (1999) 1795.
- [115] E. Fattal, M. R. Radeke, G. Reynolds and E. A. Carter, *J. Phys. Chem. B* **101** (1997) 8658.
- [116] P. J. Stephens, F. J. Devlin, C. F. Chabalowski and M. J. Frisch, *J. Phys. Chem.* **98** (1994) 11623.
- [117] N. C. Norman, *Periodicity and the s- and p-block Elements*, (Oxford University Press, Oxford, 1997).
- [118] A. Bongiorno and A. Pasquarello, *Phys. Rev. B* **62** (2000) 16326.
- [119] D. R. Hamann, *Phys. Rev. B* **61** (2000) 9899.

- [120] L. Clemen, R. M. Wallace, P. A. Taylor, M. J. Dresser, W. J. Choyke, W. H. Weinberg and J.T. Yates Jr., *Surf. Sci.* **268** (1992) 205.
- [121] P. A. Taylor, R. M. Wallace, C. C. Cheng, W. H. Weinberg, M. J. Dresser, W. J. Choyke and J. T. Yates Jr., *J. Am. Chem. Soc.* **114** (1992) 6754.
- [122] W. Widdra, A. Fink, S. Gokhale, P. Trischberger and D. Menzel, *Phys. Rev. Lett.* **80** (1998) 4269.
- [123] J.-H. Cho, L. Kleinman, C. T. Chan and K. S. Kim, *Phys. Rev. B* **63** (2001) 073306.
- [124] J.-H. Cho, L. Kleinman, C. T. Chan and K. S. Kim, *Phys. Rev. B* **64** (2001) 199902.
- [125] R. Konečný and D. J. Doren, *Surf. Sci.* **417** (1998) 169.
- [126] R. B. Woodward and R. Hoffmann, *The Conservation of Orbital Symmetry*, (Academic Press, New York, 1970).
- [127] M. A. Phillips, N. A. Besley, P. M. W. Gill and P. Moriarty, *Phys. Rev. B* **67** (2003) 035309.
- [128] W. Pan, T. Zhu and W. Yang, *J. Chem. Phys.* **107** (1997) 3981.
- [129] Y. Imamura, Y. Morikawa, T. Yamasaki and H. Nakatsuji, *Surf. Sci.* **341** (1995) L1091.
- [130] D. R. Lide, *CRC Handbook of Chemistry and Physics*, (CRC Press LLC, Boca Raton, 2004).
- [131] M. Ford, *The Miracles of Chemistry*. (Abril, Buenos Aires, 1947).
- [132] M. J. S. Dewar, E. G. Zoebisch, E. F. Healy and J. J. P. Stewart, *J. Am. Chem. Soc.* **107** (1985) 3902.

BIOGRAPHICAL SKETCH

Paulo Emilio Herrera-Morales was born on April, 13, 1971, in Guatemala City, Guatemala. He is the son of Victor Manuel Herrera and Emma Morales de Herrera. After graduating from high school in 1988, he pursued his studies at Universidad de San Carlos de Guatemala, and earned a bachelor's degree in chemical engineering in 1994. After graduating, he worked in industry in Guatemala. From 1995 to 1999, he was a faculty member in the Universidad Rafael Landívar College of Engineering in Guatemala. Paulo Emilio was very involved in academic and extracurricular activities in Universidad de San Carlos and Universidad Rafael Landívar, becoming the President of Chemical Engineering Students in 1992, and Faculty Advisor of the Fifth Latin-American Chemical Engineering Student Meeting Executive Board in 1999.

In 1999, he received an overseas assistantship from the University of Florida (UF), and he began his Ph.D. degree in surface science technology in the Chemical Engineering Department at the UF under the supervision of Dr. Jason F. Weaver. He spent four semesters in Gainesville taking classes before he began his research in the Surface Science Laboratory, at the Nuclear Sciences Building. He worked as a graduate assistant and as a teaching assistant while at UF.

Paulo Emilio is engaged to Sonia María García, whom he plans to marry, once he finishes this Ph.D.